Generic Interferometric Synthetic Aperture Radar Atmospheric Correction Model and Its Application to Co- and Post-Seismic Motions

Chen Yu

Thesis submitted for the degree of

Doctor of Philosophy

School of Engineering

Newcastle University

June 2019

Abstract

The tremendous development of Interferometric Synthetic Aperture Radar (InSAR) missions in recent years facilitates the study of smaller amplitude ground deformation over greater spatial scales using longer time series. However, this poses more challenges for correcting atmospheric effects due to the spatial-temporal variability of atmospheric delays. Previous attempts have used observations from Global Positioning System (GPS) and Numerical Weather Models (NWMs) to separate the atmospheric delays, but they are limited by (i) the availability (and distribution) of GPS stations; (ii) the time difference between NWM and radar observations; and (iii) the difficulties in quantifying their performance.

To overcome the abovementioned limitations, we have developed the Iterative Tropospheric Decomposition (ITD) model to reduce the coupling effects of the troposphere turbulence and stratification and hence achieve similar performances over flat and mountainous terrains. High-resolution European Centre for Medium-Range Weather Forecasts (ECMWF) and GPS-derived tropospheric delays were properly integrated by investigating the GPS network geometry and topography variations. These led to a generic atmospheric correction model with a range of notable features: (i) global coverage, (ii) all-weather, all-time usability, (iii) available with a maximum of two-day latency, and (iv) indicators available to assess the model's performance and feasibility.

The generic atmospheric correction model enables the investigation of the small magnitude co-seismic deformation of the 2017 Mw-6.4 Nyingchi earthquake from InSAR observations in spite of substantial atmospheric contamination. It can also minimize the temporal correlations of InSAR atmospheric delays so that reliable velocity maps over large spatial extents can be achieved. Its application to the post-seismic motion following the 2016 Kaikoura earthquake shows a success to recover the time-dependent afterslip distribution, which in turn evidences the deep inactive subduction slip mechanism. This procedure can be used to map surface deformation in other scenarios including volcanic eruptions, tectonic rifting, cracking, and city subsidence.

Declaration

I declare that the thesis has been composed by myself and that the work has not been submitted for any other degree or professional qualification. I confirm that the work submitted is my own, except where work which has formed part of jointly-authored publications has been included. My contribution and those of the other authors to this work have been explicitly indicated below. I confirm that appropriate credit has been given within this thesis where reference has been made to the work of others.

The work presented in Chapter 3 was previously published in "Yu, Chen, Nigel T. Penna, and Zhenhong Li. Generation of real-time mode high-resolution water vapour fields from GPS observations. Journal of Geophysical Research: Atmospheres 122.3 (2017): 2008-2025." The dissertation author is the primary researcher and conducted all the experiments and analyzes of this paper, whilst the co-authors listed are the main author's supervisors, who directed the research, structured the Introduction, helped to design the logic flow of the paper, and fine-tuned the English.

Chapter 4 is reformatted from the paper "Yu, Chen, Zhenhong Li, and Nigel T. Penna. Interferometric synthetic aperture radar atmospheric correction using a GPS-based iterative tropospheric decomposition model. Remote Sensing of Environment 204 (2018): 109-121." The dissertation author is the primary researcher who designed the whole methodology and conducted all the experiments and analyzes of this paper. The co-authors listed are the main author's supervisors, who directed the research, refined the presentation and structure of the paper, contributed discussions for the results interpretation and fine-tuned the English.

Parts of Section 5.2, 5.3, 5.4, 5.5 and 5.7 are reformatted from the paper "Yu, Chen, Zhenhong Li, Nigel T. Penna, and Paola Crippa. Generic atmospheric correction model for Interferometric Synthetic Aperture Radar observations. Journal of Geophysical Research: Solid Earth 123.10 (2018): 9202-9222." The dissertation author is the primary researcher and conducted all the experiments and analyzes of this paper. The second and third authors are the main author's supervisors, who directed the research, refined the presentation and structure of the paper,

shared constructive suggestions on the methodology presentation, helped with enhancement of the discussion and fine-tuned the English. The fourth author provided the scripts to decode the high-resolution ECMWF data.

Chapter 6 is a reformatted version of the paper “Yu, Chen, Zhenhong Li, Jiajun Chen, and Jyr-Ching Hu. Small Magnitude Co-Seismic Deformation of the 2017 Mw 6.4 Nyingchi earthquake Revealed by InSAR Measurements with Atmospheric Correction. Remote Sensing 10.5 (2018): 684.” The dissertation author is the primary researcher and conducted all the experiments and analyzes of this paper. The second author is the main author’s supervisor and directed and supervised the research. The remaining authors contributed constructive discussions on the background tectonic activity of the Tibetan Plateau and the GPS velocity field.

Chen Yu

June 2019, Newcastle upon Tyne

Acknowledgements

This work was supported by a Chinese Scholarship Council studentship. Part of this work was also supported by the UK NERC through the Centre for the Observation and Modelling of Earthquakes, Volcanoes and Tectonics (COMET).

First of all, I would like to express my special appreciation and thanks to my supervisors, Prof. Zhenhong Li and Dr Nigel Penna. It is their great patience and encouragement that guided me to grow as a research scientist. Their constant support and professional comments always remind me of "doing the top research" and "looking at the big picture", which are determinant for the accomplishment of my project. Prof. Li is always a positive thinking advisor, delivering inspirations and confidence to conquer tough researches. Dr Penna always reminds me that "God is in the detail", which is essential to improve my scientific writing skill and the quality of research presentations. All these are my lifelong benefits.

Great thanks to a few individuals whose contribution to this project is in some way immense. Thanks to Dr Ian Martin and Dr Jing Guo for their demonstration of the PANDA software and its fundamental equations. Dr Maorong Ge and Dr Xingxing Li also deserve great thanks for their contributions on validating my PANDA results. I benefited enormously from their knowledge, expertise and experience. I am additionally grateful to Dr Paola Crippa for her generosity to provide me with the codes for decoding high resolution ECMWF products, and Dr Neil Harris for developing the web interface for our GACOS system. Without their help, the GACOS system would never be successful. I also gratefully acknowledge Prof. Jyr-Ching Hu for his suggestions on earthquake modelling and geology background interpretation. Sincere thanks also go to COMET who offered me great opportunities to meet and discuss with researchers throughout the UK. I have enjoyed all the student and science meetings and learnt a lot from the workshops held at Newcastle University and Leeds University. Last but not least, thanks to Prof. Peter Clarke and Prof. Philip Moore. Being my panel of experts, they have provided constructive comments and forward-looking suggestions on my reports and research progress.

Special mention must go to Prof. Yibin Yao, my former supervisor at Wuhan University, for arousing my initial interest in precise point positioning and introducing me to Newcastle University.

Thanks to all the generous data providers. The GPS data sets and orbit/clock products used in this paper were gratefully obtained from the UNAVCO PBO (pbo.unavco.org), NERC BIGF (www.bigf.ac.uk), RING (http://ring.gm.ingv.it/), GeoNet (http://www.geonet.org.nz/) and JPL/IGS (www.igs.org). Sentinel-1 images were provided freely by ESA's Sentinels Scientific Data Hub. Thanks to Geoff Blewitt at the University of Nevada, Reno for his GPS time series products (http://geodesy.unr.edu/magnet.php). We acknowledge European Centre for Medium-Range Weather Forecasts for their operational high resolution tropospheric products.

Finally, I reserve my most heartfelt appreciation and thanks for my family for all of the sacrifices they have made on my behalf. Their prayer for me was what sustained me thus far. In the end, I would like to express appreciation to my beloved wife Qin for all the sleepless nights. She has been an inspiration and motivation for continuing to improve my knowledge and move my career forward.

Chen Yu
June 2019, Newcastle upon Tyne

Table of Contents

List of Figures

List of Tables

Chapter 1. Introduction

The Interferometric Synthetic Aperture Radar (InSAR) technique has experienced a tremendous development during the past 10 years that enables research for mapping the Earth's surface movements at larger scales and with smaller amplitudes than ever before. Apart from already in orbit satellites such as Sentinel-1A/B, Gaofen-3 and ALOS-2, many more have been scheduled for the period from 2018 to 2025 (e.g., Sentinel-1C/D, Gaofen-3B/C, RADARSAT Constellation). One of the most critical challenges when utilizing these data, hampering all techniques that require microwaves passing through the Earth's atmosphere, is to mitigate their atmospheric effects due to the spatial and temporal variations of water vapour. This effect may dominate over large scales and completely mask the actual displacement due to tectonic or volcanic deformation. Accordingly, the aim of this thesis is to provide a generic atmospheric correction model through an operational high-resolution numerical weather model, the Global Positioning System (GPS), and/or their combination, with particular application to co- and post-seismic studies.

1.1 Background

Catastrophic events such as major earthquakes occur when the Earth's crust fails in response to accumulated deformation, caused by ongoing processes such as aseismic deformation of the subcrustal rock associated with relative plate motions. Geodetic measurements document the crustal deformation leading to and resulting from these failures, and provide a unique insight into the physical processes involved (Massonnet et al., 1994). As a result, for a range of natural events including earthquakes, aseismic fault motions and volcanic eruptions, geodetic measurements have been widely applied to constrain the physical models behind such phenomena.

Among all geodetic techniques, GPS and InSAR have received massive developments during the past 20 years for widespread applications. GPS provides accuracies of millimetre level in static post-processing and centimetres in Real Time Kinematic (RTK) for measuring ground movements (e.g., Teunissen et al., 2014), approximately 1 mm for troposphere water vapour

estimates in post-processing (e.g., Ning et al., 2016) and 1-2 mm in real-time (e.g., Li et al., 2015), and 2-8 units for the ionosphere Total Electron Content (TEC) (e.g., Spits and Warnant, 2011). Therefore, it has shown its successes in the global reference frame definition (e.g., Altamimi et al., 2002), meteorology (e.g., Bevis et al., 1992), real-time geohazard monitoring (e.g., Genrich and Bock, 2006), precision agriculture (e.g., Stafford, 2000) and so on. It is one of the key geodetic inputs for geophysical models including co-seismic offsets (e.g., Anzidei et al., 2009), post-seismic ground motion time series (e.g., Tong et al., 2010), inter-seismic strain rates (e.g., Serpelloni et al., 2005) and slow slip motions (e.g., Li et al., 2016). Apart from deformation, an important by-product of GPS is the tropospheric delay from which high-resolution tropospheric delay or water vapour fields can be generated in real-time (e.g., Li et al., 2015).

Compared with GPS, InSAR provides a better spatial resolution and measures the positions of millions of points over large spatial extents. The concept of InSAR was first introduced by Rogers and Ingalls (1969) who mapped the surface reflectivity of Venus by radar interferometry, using amplitude fringes with a wavelength of 3.8 cm. Zebker and Goldstein (1986) extended this concept with an airborne platform to produce a topographic map using both the amplitude and phase information recorded by the SAR sensors. Under this technique, the interferograms from two or more SAR images taken at different acquisitions inevitably contain both the signature of the Earth's topography and ground deformation. It was after Massonnet et al. (1993), who subtracted the topographic contribution by a Digital Elevation Model (DEM) thus led to a pure co-seismic displacement field for the Landers earthquake, that repeat-pass InSAR has been extensively used in the geophysical field. Using the same method, Massonnet et al. (1995, 1994) produced the post-seismic deformation for the Landers earthquake and long-term volcanic deformation for Mount Etna. Rosen et al. (1998) measured a wide-area distribution of an aseismic fault creep by the ERS-1 radar, which was relatively easy to be detected due to the creep being discontinuous. Further progress was made by Wright et al. (2001b) who stacked an interferogram time series to enhance the crustal strain signal relative to atmospheric and orbital errors and produced a deformation velocity field of only 17-32 mm/year over a 70 km wide region. Since then, InSAR time series analysis methods have been intensively developed,

such as the small baseline (Mora et al., 2002) and persistent scatters (Hooper et al., 2004), which eventually enable a wide range of applications such as groundwater pump responses (e.g., Bell et al., 2008), landslide monitoring (e.g., Liu et al., 2012), and post-mining activities (e.g., Samsonov et al., 2013). Without doubt InSAR will continue to grow substantially for a wide range of scientific, engineering, and commercial uses.

1.2 New Era of InSAR

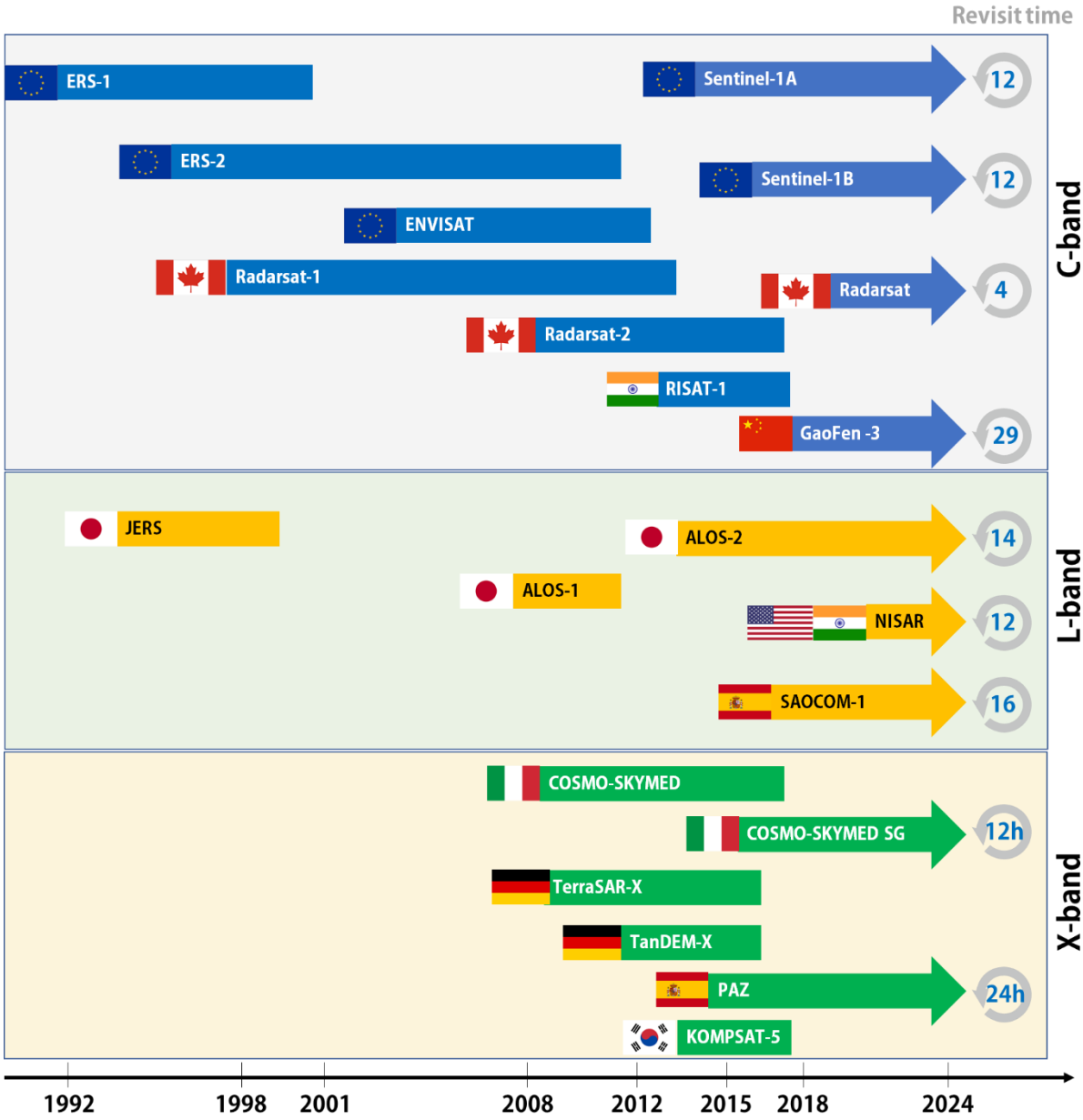

Figure 1.1 An overview of SAR satellites with interferometry capacity, including historic, current and planned missions. The revisit time is in days, except for X-band satellites which can be in hours.

With the success of mapping the Earth's surface movements, InSAR has undergone a

tremendous development during the past decade, with emerging missions such as Sentinel-1A/1B, ALOS-2, TerraSAR-X/TanDEM-X, COSMO-SkyMED, RADARSAT-2, Gaofen-3, as well as their successors planned for launch during 2018-2025. Figure 1.1 shows an overview of SAR satellites with interferometry capabilities, including historic, current and planned missions. As of 2018, there have been at least eight operational SAR missions and a whole 25 years of InSAR data time series for major tectonic and volcanic regions.

Among all current missions, ESA's Sentinel-1 provides for the first-time global coverage images, systematically and frequently every 12 (one satellite) or six days (two satellites), freely available to the public, and therefore it is believed to have opened a new era for the InSAR community. The mission has a long duration, with future launches planned to extend the time series to at least 20 years. Since the launch of Sentinel-1A, a fruitful number of Earth observation applications have been studied with very promising results (e.g., Feng et al., 2016; Lau et al., 2018; Shirzaei et al., 2017). As a result, more and more researchers are gathered to look at the Earth with unprecedented details from a SAR point of view, which in turn positively impacts future SAR missions.

1.3 Atmospheric Effects on InSAR Measurements

InSAR phase measurements can be contaminated by several error sources such as the orbital error due to inaccurate satellite state vectors, the error introduced by the external DEM, the unwrapping error, the decorrelation error, the ionospheric and tropospheric delays. The tropospheric effect is conventionally named as the atmospheric effect among InSAR communities, although the realistic atmospheric error is a combined effect that comes from both the troposphere and the ionosphere. This thesis regards the tropospheric effect as the atmospheric effect, ignoring any contribution from the ionosphere whose effect is specifically referred as the ionospheric delay. In this context, we will not distinguish between the atmospheric delay and the tropospheric delay.

The atmospheric effect represents one of the major error sources of InSAR which may mask actual displacements due to tectonic or volcanic deformation. It has become increasingly

problematic recently, as the new wide coverage, fine spatial-temporal resolution datasets, with precise orbital controls and free data distribution policies, facilitate the studies of small amplitude ground deformation, over long time periods and across great spatial scales (e.g., Lau et al., 2018; Shirzaei et al., 2017).

1.3.1 Definition of atmospheric effects

The atmospheric (tropospheric) delay is generated when the microwave signal passing through the Earth's troposphere in the presence of water vapour, with also substantial relationships with the temperature and air pressure. It can be represented conveniently at the zenith direction (ZTD, Zenith Tropospheric Delay) and then mapped onto a Line of Sight (LOS) direction. There are two components of the ZTD in a physical sense, the Zenith Wet Delay (ZWD) and Zenith Hydrostatic Delay (ZHD), which are distinguished mainly by their relations to humidity (Saastamoinen, 1972). Water vapour can be retrieved from the ZWD when ground meteorological measurements (pressure and temperature), or, more precisely, their vertical profiles, are provided (Bevis et al., 1992; Jolivet et al., 2011).

The absolute ZTD is one of the key error sources in techniques such as GPS. However, since the InSAR measurement is spatial-temporally differenced, it is only the spatial-temporal difference between ZTDs of different acquisitions and pixels that affects InSAR-derived surface displacements and causes errors comparable in magnitude to those associated with crustal deformation (Hanssen, 1998; Walters et al., 2013; Webley et al., 2002; Williams et al., 1998).

There are a variety of different features of the atmospheric delay in InSAR measurements. Firstly, the usage of the ZHD and ZWD is not realistic as most of the ZHD component has been cancelled by differencing, leaving the atmospheric effect in InSAR measurements to be more sensitive to the variations in the water vapour. As a result, the atmospheric delay in InSAR is often divided into a stratified component (or an elevation dependent component) which is highly correlated with topography, more disturbing over mountainous areas, and a turbulent component resulting from tropospheric turbulence. Both the two components are spatial-temporally variable and may be indistinguishable from ground motions. Secondly, the

atmospheric delay signal shares a broad spectrum, with the short wavelength coming from, for example, the rapidly changing turbulent component and/or the stratified component at substantially variated topographies, and with the long wavelength resulting from, for example, a slow-moving weather front over a large spatial extent and representing as ramps on the interferogram.

The magnitude of InSAR atmospheric errors can be substantial. Zebker et al. (1997) reported 10-14 cm errors in SIR-C/X-SAR displacement measurements from only a 20% variation in the water vapour, which is large enough to mask actual ground motions caused by a landslide (e.g., Luzi et al., 2004), urban subsidence (e.g., Crosetto et al., 2002) and permafrost (e.g., Short et al., 2014). There were 0.5 to 3.6 cm atmospheric delay RMS values among a series of 26 ERS tandem SAR interferograms in the Netherlands studied by Hanssen, (1998), which could result in 2.3 phase cycles for the observed phase values. Every interferogram in Hanssen's study displayed a completely different atmospheric behaviour and it was thus problematic to detect them from other errors including satellite orbit errors. Jolivet et al. (2014) showed that the stratified atmospheric delay degraded the unwrapping performance over rough terrain and made it indistinguishable between the long wavelength deformation signal and different noise sources.

1.3.2 Impact on co-seismic modelling

Atmospheric delays are typically ignored in co-seismic modelling under the hypothesis that the magnitude of co-seismic signals is much greater than that of tropospheric delays (e.g., Gualandi et al., 2017; Hamling et al., 2017; Polcari et al., 2017; Simons et al., 2002). However, for earthquakes with small magnitude surface displacements, tropospheric delays can be of the same order or even larger than ground motions. For example, co-seismic signals for three Mw 5.2–5.6 2004 Huntoon Valley earthquakes (Lee et al., 2017) and the Mw 5.5 2007 Ghazaband earthquake (Fattahi et al., 2015) were completely masked by atmospheric errors, causing difficulties to determine the source parameters and to resolve the fault slip distribution. Even for some large events such as the Mw 8.3 2015 Illapel earthquake, Feng et al. (2016) found serious atmospheric contaminations. A few attempts have been made to address this issue, however, they failed in the presence of tropospheric turbulence (e.g., Fattahi et al., 2015), had

a delayed response due to the data availability (e.g., Lee et al., 2017), and were limited to certain radar satellites (e.g., Feng et al., 2016).

1.3.3 Impact on velocity mapping

Post- or inter-seismic process modelling typically utilizes a series of SAR image stacks and relies on spatial-temporal filters to minimize the atmospheric noise to achieve millimetre level velocity mapping accuracies. However, since water vapour is spatial-temporally correlated, the atmospheric effect may be enlarged in large spatial extent interferograms or long time series as the InSAR measurement is spatial-temporally differenced (e.g., Simons and Rosen, 2007; Massonnet et al., 1994; Hooper et al., 2012). For example, Elliott et al. (2008) showed that the strain rate measured over short time scales was dominated by orbital and atmospheric errors along the Altyn Tagh Fault, and standard stacking techniques could not remove topographically correlated atmospheric delays. Jung et al. (2014) found that the stratified atmospheric errors were substantially correlated with time and sometimes severely contaminated the quality of deformation estimation for volcanic activities, hence preventing the use of the high-pass filter in traditional time series methods. Non-steady deformation time series is also hard to distinguish from atmospheric errors, making it challenging to detect time-varying processes such as creep (e.g., Jolivet et al., 2015; Hussain et al., 2016) or slow slip events (e.g., Cavalié et al., 2013; Bekaert et al., 2016).

1.4 Reviews of InSAR Atmospheric Correction Techniques

Based on the dynamic nature of the troposphere, numerous attempts have been made on the quantification and mitigation of InSAR tropospheric effects which are usually divided into two categories: internal correction methods which are mostly statistical correlation analyzes based on phase measurements, and external data-based correction methods which rely on external atmospheric delay datasets.

1.4.1 Internal correction methods

One of the most popular approaches used to mitigate atmospheric effects on InSAR

measurements is correlation analysis, which seeks to capture the spatial-temporal properties of water vapour and attempts to separate the tropospheric noise from the ground motion signal without any external information (e.g., Williams et al., 1998; Fruneau and Sarti, 2000; Ferretti et al., 2001; Hooper et al., 2004). Hanssen (2002) noticed that the atmospheric delay signal generally follows a power law spectrum in its frequency domain, and therefore is estimable from the phase observations. Only one exponential parameter can be estimated per interferogram making it unsuitable for large spatial extent data, and the performance was much poorer at long wavelengths than short wavelengths in his study area. Bekaert et al. (2015a) proposed a new power law-based correction model in the space domain of measurements that allows for a spatial variability of exponent parameters. A large interferogram can be divided into smaller pieces whose power law spectrums are estimated independently. However, other contamination signals such as orbit errors cannot be handled and manual interactions are required, such as *a priori* information about the spatial extent of deformation throughout time for the selection of the non-deforming band (Bekaert et al., 2015b). There are also methods which simulate the stratified atmospheric delay by a linear (or exponential) relation between the phase and elevation across the whole region (e.g., Elliott et al., 2008; Shirzaei and Bürgmann, 2012), or, such as Béjar-Pizarro et al. (2013), by a piece-wise linear correlation over multiple adjacent windows to allow for the spatial variation of the stratified delay component.

Overall, this type of approach is straightforward to implement. However, the disadvantages are, firstly, there is inevitably a risk of removing actual ground motions, such as those induced by volcanic activities which may exert a similar topographic pattern with the stratified atmospheric delay. Secondly, the extraction of atmospheric delays from phases can be biased by ground motions or other error sources. Furthermore, it is sometimes impossible to quantify their performance.

1.4.2 External data-based correction methods

Since atmospheric delays are non-dispersive, we can utilize the external datasets which provide atmospheric delay or water vapour products from instruments other than SAR. There are three main types of external data sources, i.e. space-based instruments, ground-based instruments and

weather models.

The space-based instruments used for InSAR atmospheric corrections include NASA's Moderate Resolution Imaging Spectroradiometer (MODIS, (e.g., Li et al., 2009b, 2005)) and ESA's Medium Resolution Imaging Spectrometer (MERIS, (e.g., Li et al., 2006b; Li et al., 2012)). MERIS is ideal for Envisat since their measurements were taken simultaneously, but both have been expired since 2012. MODIS provides a 1.0-1.2 mm RMS water vapour agreement with radiosondes at ~1 km spatial resolution (Gao and Kaufman, 2003) but is restricted to daytime cloud-free conditions. For some newly launched SAR satellites (e.g., Sentinel-1 and ALOS-2), there may be a large time difference between SAR and MODIS acquisitions (typically > 5 hours) which severely degrades its correction performance.

Ground-based instruments such as GPS and meteorological stations can be used to estimate atmospheric delays continuously (e.g., every 5 minutes) under all-weather conditions and are capable of capturing small features of tropospheric turbulence (e.g., Li et al., 2006a; Onn and Zebker, 2006; Williams et al., 1998). Standard deviations between pointwise GPS water vapour estimates and those from radiosondes and microwave radiometers are about 1–3 mm (Koulali et al., 2012; Li et al., 2003; Mears et al., 2015) depending on the atmospheric water vapour content, with Glowacki et al. (2006) finding the errors were 8–10%. These pointwise estimates must be spatially interpolated to generate high-resolution maps for InSAR atmospheric corrections. Li et al. (2006a) proposed a GPS topography-dependent turbulence model based on the space structure function (Williams et al., 1998) and a linear height scaling function. An overall improvement of 50% after correction using the ERS Tandem Data over the Los Angeles Southern California integrated GPS network area was obtained. However, the interpolator requires a predefined parameter which is sensitive to the local environment and is thus difficult to determine. Onn and Zebker (2006) used a frozen-flow air assumption plus an exponential function for modelling GPS ZWDs, which improved the interferograms by 43% in terms of phase variations. Reuveni et al. (2015) also applied an exponential function but with different scale factors for the hydrostatic and wet components of ZTD which corrected, on average, 17% of the interferogram tropospheric noise. All these GPS-based correction models are applied

blindly to InSAR measurements without any assessment of their applicability or qualities, which may lead to increased noise after correction (Chen et al., 2010). Furthermore, few previous models have accounted for both the stratified and turbulent components of the tropospheric delay and therefore may fail if there are large topographic variations (Houlie et al., 2016).

Popular weather models include the ECMWF Re-Analysis Interim (ERA-Interim, 6 hourly, 0.75 degree horizontal resolution, e.g., Doin et al., 2009; Jolivet et al., 2011) and the Weather Research and Forecasting model (WRF, e.g., Bekaert et al., 2015b; Nico et al., 2011). Jolivet et al. (2011) demonstrated the use of ERA-Interim for atmospheric correction with only the stratified atmospheric delay component being considered. It is, therefore, less accurate over coastal areas, where the temporal fluctuation of atmospheric turbulence is usually stronger. Furthermore, Bekaert et al. (2015b) applied ERA-Interim over Mexico and Italy and reported a 1.7 cm RMS displacement error of the corrected interferograms, which was insufficient to capture both topographic correlated tropospheric signals and local weather turbulent variations. Jung et al. (2014) showed that the WRF model can reduce the seasonal variation of the stratified atmospheric delay and make the displacement related to volcanic activities being dominant. In general, weather models are often released with a latency of several months and tend to be more accurate to predict stratified atmospheric delays. Nevertheless, they are typically insensitive to turbulent components due to their coarse spatial-temporal resolution.

There have also been attempts to integrate multiple external data sources as compensations for each other. For example, Li et al. (2005) interpolated GPS estimates to fill up the cloudy pixels in MODIS water vapour maps and to reduce their time difference effects. Löfgren et al. (2010) combined both GPS and ERA-Interim data to generate atmospheric correction maps. However, they simply used GPS to calibrate ERA-Interim ZTDs instead of properly weighting and integrating them. Should there be fewer GPS stations, or the network exhibits poorer geometry, their approach may fail.

1.5 Aims and Objectives

Despite the success achieved by the abovementioned methods for InSAR atmospheric correction, researchers have increasingly been aware of their inherent limitations. This thesis will address some of the limitations which include, (i) the coupling effect of the tropospheric stratification and turbulence; (ii) the low spatial-temporal resolution of weather models; (iii) the lack of quality control indicators. The overall aim of this thesis is to develop a generic InSAR atmospheric correction model to be capable to deal with the challenges arising from the vast development of InSAR data and techniques, such as the larger spatial extent and longer time series interferograms, higher offset or velocity mapping accuracy requirement and near real-time monitoring applications.

The key objectives are summarized as follows:

O1. To develop a generic InSAR atmospheric correction model by integrating GPS and high-resolution ECMWF. An Iterative Tropospheric Decomposition (ITD) model for generation of high-resolution water vapour fields and integration of GPS and ECMWF will be developed. The key purposes of the generic correction model are to provide atmospheric correction maps that comprise features of: (i) global coverage, (ii) all-weather, all-time usability, (iii) available with a short time latency (less than two days), and (iv) with performance indicators.

O2. To model the small magnitude co-seismic deformation of the 2017 Mw 6.4 Nyingchi earthquake by atmospheric corrected InSAR measurements. The developed atmospheric correction model will be used to extract the co-seismic displacement related to a buried fault located south of the Jiali fault in Tibet from the atmospheric error contaminated InSAR measurement. The resulting displacement map will be used to determine the fault plane geometry and the slip distribution, providing insights into the oblique convergence of the Indian-Eurasian plates.

O3. To model the triggered afterslip on the southern Hikurangi subduction slab following the 2016 Kaikoura earthquake from InSAR time series addressing atmospheric

corrections. An InSAR time series analysis method, aiming to mitigate spatial-temporally correlated atmospheric errors over large spatial extents, will be developed. The method is expected to be less dependent on atmospheric delay spatial correlations, suitable for large areas, and is able to degrade atmospheric delay temporal correlations before filtering. The corrected InSAR interferograms will be used to model the triggered afterslips on the inactive southwestern Hikurangi subduction slab which is probably accommodating regional plate motions, with the time-varying afterslip distribution being retrieved to investigate the potential co-seismic slip on the subduction interface.

1.6 Outline

The thesis is structured as follows:

Chapter 2 is a concise introduction to InSAR principles, error sources, and features of the atmospheric error on interferograms.

Chapter 3 introduces and validates real-time mode GPS tropospheric delay estimates, after which an Iterative Tropospheric Decomposition (ITD) model is proposed. The model is carefully evaluated through internal cross tests and against the high-resolution (1 km) MODIS water vapour map.

Chapter 4 develops a framework to routinely use GPS to reduce tropospheric effects on InSAR measurements. The method is validated on five Sentinel-1A interferograms in Southern California (with a 10–20 km station spacing network) and Southern England (with a 50–80 km station spacing network). The impact of the station spacing on the model performance is evaluated.

Chapter 5 develops a generic InSAR atmospheric correction model by tightly integrating the high-resolution ECMWF product and GPS ZTD pointwise estimate using the ITD model. The model's performance is tested using eight globally-distributed Sentinel-1 interferograms under

various environments. Performance indicator metrics for quality control and model applicability are developed. A Generic Atmospheric Correction Online Service (GACOS) is developed based on the main methodology of this chapter which automatically generates correction maps per user request.

Chapter 6 applies GACOS atmospheric correction maps to co-seismic interferograms, and successfully extracts co-seismic surface displacements for the 2017 Mw 6.4 Nyingchi earthquake. The buried fault geometry located south of the Jiali fault and its slip distribution are investigated.

Chapter 7 recovers the time-dependent afterslip distribution on the southwest Hikurangi Subduction Zone by two tracks of Sentinel-1 data after mitigating the spatial-temporally correlated atmospheric errors. This gives insights into reviewing the co-seismic slip sources, the present status of the inactive subduction plate and future seismic hazards.

Chapter 8 highlights the major innovations and the conclusions of this thesis.

Chapter 2. SAR Interferometry and Error Analysis

SAR is a microwave remote sensing technique that comprises advantages, compared to an optical sensor, such as the cloud-penetrating capability, all day and all climate availability and high interferometric measurement accuracy. A typical SAR system has three main components: it transmits a microwave signal from the satellite to the Earth's surface, receives a portion of the reflected energy as backscatter, and then observes the strength and time delay of the returned signal. Each pixel in a SAR image encodes a complex number whose amplitude corresponds to the intensity of the returned signal energy and whose phase represents a fraction of one complete wavelength. The amplitude measurement, similar to a single band optical image, can be used to invert for the surface's roughness, i.e. the vertical and horizontal irregularity of the surface, or to retrieve the first order ground motion by pixel offset tracking (e.g., Michel et al., 1999). The phase measurements contain information on the ground target altitude and the displacement between acquisitions, from which a DEM map and a deformation field can be respectively generated. Addressing the atmospheric effect for measuring ground motions, this thesis will focus on the portion of phase measurements that is solely related to the deformation signal.

2.1 Principles of SAR Interferometry

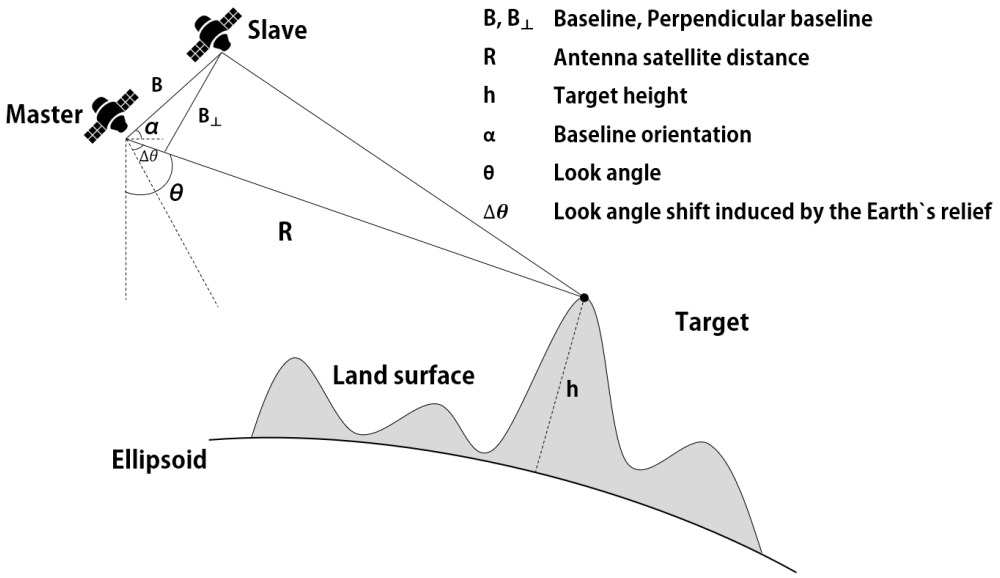

Figure 2.1 The geometry of repeat-pass InSAR.

Phases in a SAR image may be random between adjacent pixels and reflect complicated scattering features of the Earth's surface. However, when one image is multiplied by the

conjugate value of another image (a process known as interferometry), the resulting interferometric phase can be interpreted as the ground movement during these two acquisitions along the LOS direction.

2.1.1 Two-pass interferometric phase

For a typical repeat two-pass InSAR geometry (Figure 2.1), the interferometric phase measurement can be written as (Ding et al., 2008):

$$\varphi = -\frac{4\pi}{\lambda} B_{\perp} \Delta\theta - \frac{4\pi}{\lambda} \frac{B_{\perp}}{R \sin\theta} h + \frac{4\pi}{\lambda} d_{LOS} + \varepsilon_{noise} \qquad \text{(Equation 2.1)}$$

where λ is the wavelength of the radar signal, **B** is the baseline length with $\mathbf{B}_{\perp}$ the perpendicular component; **R** is the distance between the satellite and the ground target with a height of **h**; α is the orientation of the baseline and **θ** is the look angle, which is shifted due to the Earth's relief by **Δθ**. The first term on the right-hand side of Equation 2.1 is the so-called flattened phase, resulting from the elevation variation of the Earth's surface and which can be calibrated according to the baseline length (i.e. the flat-Earth phase removal). The second term relates to the target altitude from which a DEM can be generated. The third term relates to the ground deformation between the master and slave acquisitions. ε represents the phase noise that could come from atmospheric delays, orbital determination errors and so on.

Equation 2.1 implies that the altitude related phase is sensitive to the perpendicular baseline. Therefore, if we consider solely the second term and ignore the other contributions, the standard deviation of the generated DEM has a relationship with the phase measurement as:

$$\sigma_h = \frac{\lambda R \sin\theta}{4\pi \cdot B_{\perp}} \sigma_{\varphi} \qquad \text{(Equation 2.2)}$$

while the phase standard deviation σ_{φ} is affected by the baseline length, with shorter baselines producing higher qualities, resulting in the retrieval of an accurate DEM inherently requiring a long baseline separation. Hence a compromised decision on the geometry has to be made. For example, the C-band Shuttle Radar Topography Mission (SRTM) has a fixed 60 m baseline, and the X-band TerraSAR-X add-on for Digital Elevation Measurement (TanDEM) has baselines varying from 250 to 500 m.

2.1.2 Deformation related phase component

In the situation that DEM information is known, the first two terms of Equation 2.1 are determined, leaving a pure phase component that can be interpreted as ground deformation. In this scenario, the geometry is usually carefully designed to ensure a small baseline separation to minimize the impact of DEM uncertainties. The phase measurement is much more sensitive to deformation than to elevations (e.g., a 2.8 cm ground motion along the LOS direction could generate a 2π interferometric phase variation for C-band InSAR), so we can achieve at least a centimetre level accuracy of deformation, compared to the metre level DEM accuracy.

The InSAR derived displacement is only a projected portion of the actual ground motion along the LOS direction, resulting in InSAR measurements being insensitive to surface movements along certain directions (Dawson and Tregoning, 2007). A possible solution for this is to combine multiple platforms of InSAR measurements with different geometries and look angles and to resolve 3D displacement vectors (e.g., Samieie-esfahany et al., 2010).

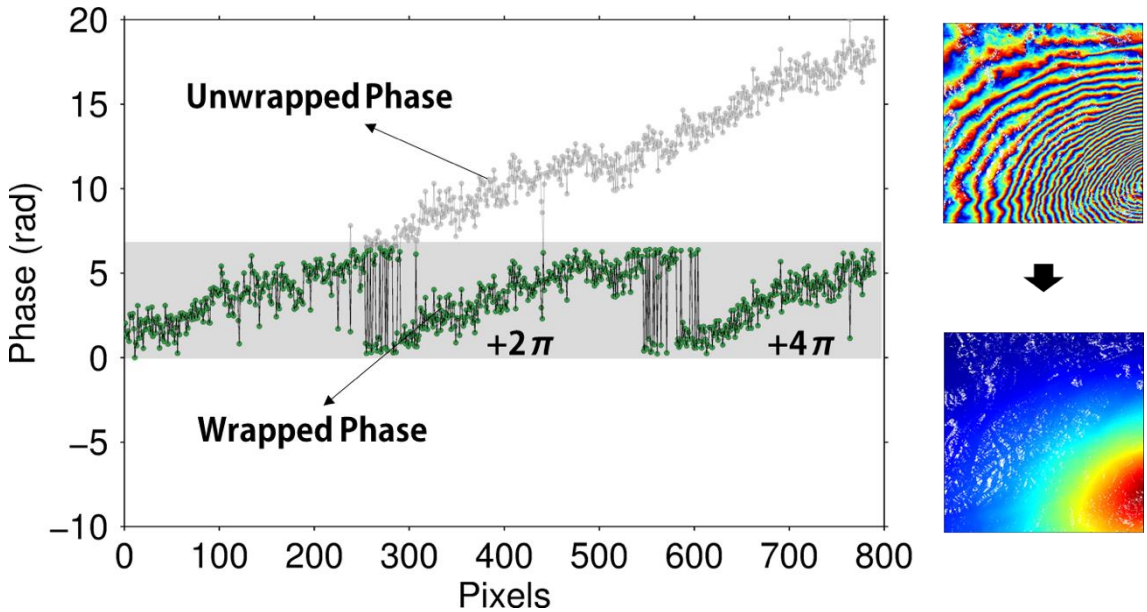

Figure 2.2 Wrapped and unwrapped 1D/2D phase measurements.

Another key feature related to the phase measurement is that it is wrapped between (-π, π) and hence only provides an ambiguous measurement of the ground motion. A 2π-multiple integer must be adjusted to recover the continuous displacement, leading to a process which is known as phase unwrapping. Figure 2.2 is an illustration of the unwrapping process for 1-dimensional

and 2-dimensional InSAR phase measurements, respectively. The fundamental hypothesis behind the process is that the gradient between adjacent pixels is less than π. Disobeying this will result in an unwrapping failure, which is typical when the magnitude of ground deformation or noise such as the atmospheric delay, depending on the signal's wavelength, is large enough.

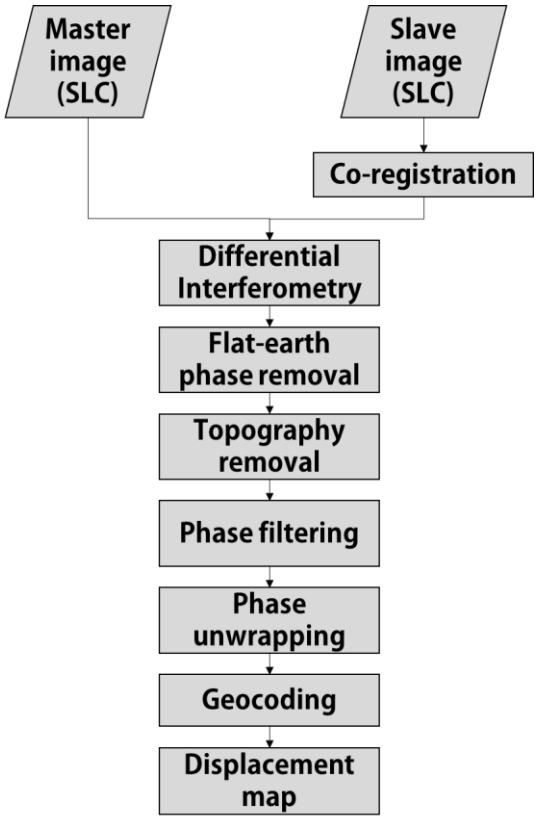

Figure 2.3 Flow chart of standard repeat-pass InSAR processing.

Figure 2.3 is a standard repeat-pass InSAR processing procedure. The Single Look Complex (SLC) images are multi-looked (i.e. averaged) to increase the signal to noise ratio and to improve the computing efficiency. Precise orbit information (recently from onboard GPS receivers) is needed to remove the flat-Earth and topographic phase components (see Equation 2.1). An adaptive filter is applied to the interferometric phase to further reduce the noise level and to minimize the loss of signal. The final displacement map is generated after phase unwrapping and then geocoded from the SAR geometry to geographic geometry. Several tools have been developed to process InSAR data, such as the commercial GAMMA Remote Sensing and Consulting AG (https://www.gamma-rs.ch) and the open source InSAR Scientific Computing Environment (ISCE) software (https://winsar.unavco.org/software/isce). For a full theory of SAR interferometry, readers can refer to (Hanssen, 2001).

The measured deformation related interferometric phase is influenced by a series of factors. To extract accurate deformation signals, contributions except actual ground deformation should be quantified and mitigated. These contributions are interpreted as noise (i.e. error sources) in Equation 2.1, and can be extended as follows:

$$\varepsilon_{noise} = \delta_{atmosphere} + \delta_{ionosphere} + \delta_{DEM} + \delta_{orbit} + \delta_{unwrapping} + \delta_{coherence} + \delta_{instrument} \quad \text{(Equation 2.3)}$$

The terms of the right-hand side are the atmospheric delay, ionospheric delay, DEM error, orbit error, unwrapping error, low coherence effect and instrument error, respectively. These error sources may exert different behaviour but are, to some extent, correlated with each other and are affecting the phase measurement in an integrated way. Although being listed as error source, there are situations where they can be regarded as useful information, such as when using InSAR to sense water vapour content. The following sections will discuss them in detail.

2.2 Atmospheric Effects

Microwaves are delayed when passing through the atmosphere, firstly due to the ionosphere electron density which leads to a dispersive delay dependent on the microwave frequency (i.e. the ionospheric delay), and secondly due to the troposphere which leads to a non-dispersive delay dependent on the atmospheric pressure, temperature and water vapour (i.e. the tropospheric delay). We will start with the tropospheric delay in this section and introduce the ionospheric delay in the following section.

2.2.1 Quantification of the total tropospheric delay

The tropospheric effect on the measurement of satellite-Earth distance has already been well documented (e.g., Hopfield, 1971). The ZTD can be computed from the integral between the surface elevation z_0 and the top of the electrically neutral atmosphere along the zenith direction (Askne and Nordius, 1987):

$$ZTD = 10^{-6}\int_{z_0}^{\infty} N dz = 10^{-6}\left[\frac{k_1 R_d}{g_m}P(z_0) + \int_{z_0}^{\infty}\left(k_2^{'}\frac{e}{T} + k_3\frac{e}{T^2}\right)dz\right] \quad \text{(Equation 2.4)}$$

where, $P(z_0)$ is the surface pressure in Pa; N is the refractive index; g_m is the gravitational acceleration averaged over the troposphere in m s^{-2}; e is the water vapour pressure in Pa; T is the temperature in K. The remaining terms are constants: $k_1 = 0.776$ K Pa^{-1}, $k_2' = 0.233$ K Pa^{-1},

k_3=3.75 ×103 $K^2\,Pa^{-1}$, R_d= 287.05 $J\,kg^{-1}\,K^{-1}$.

Saastamoinen (1972) showed that the total tropospheric delay can be partitioned into (i) a hydrostatic delay component which can be precisely determined with surface pressure (ZHD), and (ii) a wet delay component which is a function of water vapour distribution (ZWD). The hydrostatic delay includes a combined contribution from dry air and water vapour, whilst the wet delay is produced solely by atmospheric water vapour. These components can be approximated by:

$$\begin{cases} ZHD = (2.2779 \pm 0.0024)P(z_0) / (1 - 0.00266\cos\varphi - 0.00028h) \\ ZWD = 10^{-6}[k_2' \int (e / T)dz + k_3 \int (e / T^2)dz] \end{cases} \quad \text{(Equation 2.5)}$$

where, φ is the latitude and h is the elevation in km. In order to project the ZTD to the radar LOS direction, i.e. to produce the Slant Tropospheric Delay (STD), mapping functions for the ZHD and ZWD are needed as (e.g., Boehm et al., 2006):

$$STD_{LOS} = M_H(\theta) \cdot ZHD + M_W(\theta) \cdot ZWD \quad \text{(Equation 2.6)}$$

M_H *and* M_W are the mapping functions at elevation angle θ for the ZHD and ZWD, respectively.

Equation 2.5 reveals that the estimation of the ZHD can be accomplished from only surface measurements, whilst it may be unrealistic for the ZWD where a whole vertical profile of meteorological measurements is needed (Berrada Baby et al., 1988). In practice, the wet delay is measured by launching radiosondes or WVRs, or alternatively derived from stochastic or other forms of parametric models using the GPS data themselves (Bevis et al., 1992).

Equation 2.5 defines the absolute value of the tropospheric delays. Tropospheric effects in SAR interferograms, however, are mainly due to the spatial-temporal variations in atmospheric pressure, temperature and water vapour between two acquisitions. The variations could lead to, depending on the spatial extent, 10–20 cm errors on an interferogram and can often be greater than the tectonic signals of interest (Jolivet et al., 2014; Williams et al., 1998). Based on geometrical configurations of the repeat-pass SAR interferometry, the interferometric phase can be written as (Zebker et al., 1997):

$$\Delta\phi = \phi_1 - \phi_2 = \frac{4\pi}{\lambda}(\mathbf{r}_1 - \mathbf{r}_2) - \frac{4\pi}{\lambda}(\Delta L_1^{LOS} - \Delta L_2^{LOS}) \quad \text{(Equation 2.7)}$$

where λ is the wavelength of the radar signal; $\mathbf{r_1}$ and $\mathbf{r_2}$ are the slant ranges corresponding to the first and second acquisitions, respectively; ΔL_1^{LOS} and ΔL_2^{LOS} are atmospheric propagation delays of radar signals along the LOS (differenced from Equation 2.6). Equation 2.7 reveals that atmospheric delay can be easily interpreted as deformation signals.

Since it is only the spatial-temporally differenced tropospheric delay that matters in InSAR measurements, if the tropospheric profiles at two acquisitions remained the same, the tropospheric effect would disappear, and if the tropospheric delay was constant for all the resolution cells in an area of interest, the tropospheric effects would also be cancelled. However, in practice, these situations are rare to happen, given the fact that water vapour varies substantially over periods of a few hours or shorter and has strong local turbulence.

2.2.2 Tropospheric turbulence

Two types of atmospheric signal can be identified based on their physical origin, (i) a turbulent component resulting from turbulent processes in the atmosphere which causes spatial heterogeneities in the refractivity during both SAR acquisitions, affecting both flat and mountainous terrain and behaving as both short wavelength and long wavelength signals; (ii) a vertically stratified component, resulting from different vertical refractivity profiles during the two SAR acquisitions, which is highly correlated with topography.

The turbulent signal is a result of different tropospheric processes such as (i) local weather conditions amid strong water vapour variations, which lead to turbulent fluctuations of the atmosphere's temperature and humidity (Tarayre and Massonnet, 1996); (ii) scintillations, vertical wind shear forces or strong convective effects due to thin turbulent layers in cumulus clouds (Anber et al., 2014); (iii) changes of local land covers and ecosystems that result in localized variations of surface temperature and humidity (Mahmood et al., 2014). Tarayre and Massonnet (1996) reported that a 150 mm/h rainfall can create a 1.8 cm phase shift whilst a shear turbulence extending vertically over 2 km can cause a 4.4 cm shift. Although the tropospheric refractivity for microwaves is mainly dependent on temperature, pressure, and water vapour, for a SAR image coverage (e.g., 250 km by 250 km), however, it is mainly the

water vapour that causes the atmospheric signal due to its great spatial-temporal variability.

There are several mathematical models to describe the behaviour of the tropospheric turbulence, such as the power spectral function, covariance function, structure function, and fractal dimension model. The power spectral function is effective to recognize the scaling properties of the data or to distinguish different scaling regimes (Bekaert et al., 2015a). The covariance function is similar to the power spectrum, nevertheless, it is more suitable to be applied to irregularly spaced data (Li et al., 2004). The structure function provides a quantitative expression for the variance of the differenced atmospheric delay between two points separated by a specific distance and is useful for data quality description (Williams et al., 1998). Finally, the fractal dimension model evaluates the roughness and scaling characteristics of the turbulent signal (Lancaster, 1989). Among these models, the spatial structure function $D_x(L)$ provides the simplest and most robust measure of the variability in the delay signal in the case of isotropic turbulence in three dimensions:

$$D_x(L) = E((x(r_0, L) - x(r_0))^2) = CL^{\alpha} \quad \text{(Equation 2.8)}$$

where, E(·) denotes an ensemble average; $x(r_0)$ represents a random function (i.e. the phase measurement of InSAR) and $x(r_0+L)$ is the same random function at a point separated from r_0 by the vector L. The structure function can be further described as a power law process where C characterizes the roughness or scale of the process and α is the power index, which expresses the rate at which the random function loses correlation with increasing distance. Based on Equation 2.8, several tropospheric turbulent delay correction models have been developed (e.g., Li et al., 2006a, 2007).

2.2.3 Tropospheric stratification

Atmospheric stratification is another important feature of the InSAR atmospheric effect, which addresses the variation of the atmospheric delay in line with the topography. This effect is seriously identified especially in volcanic deformation studies (e.g., Delacourt et al., 1998; Tarayre and Massonnet, 1996), but could also be substantial on other terrain with high topographic variations (e.g., Walters et al., 2013).

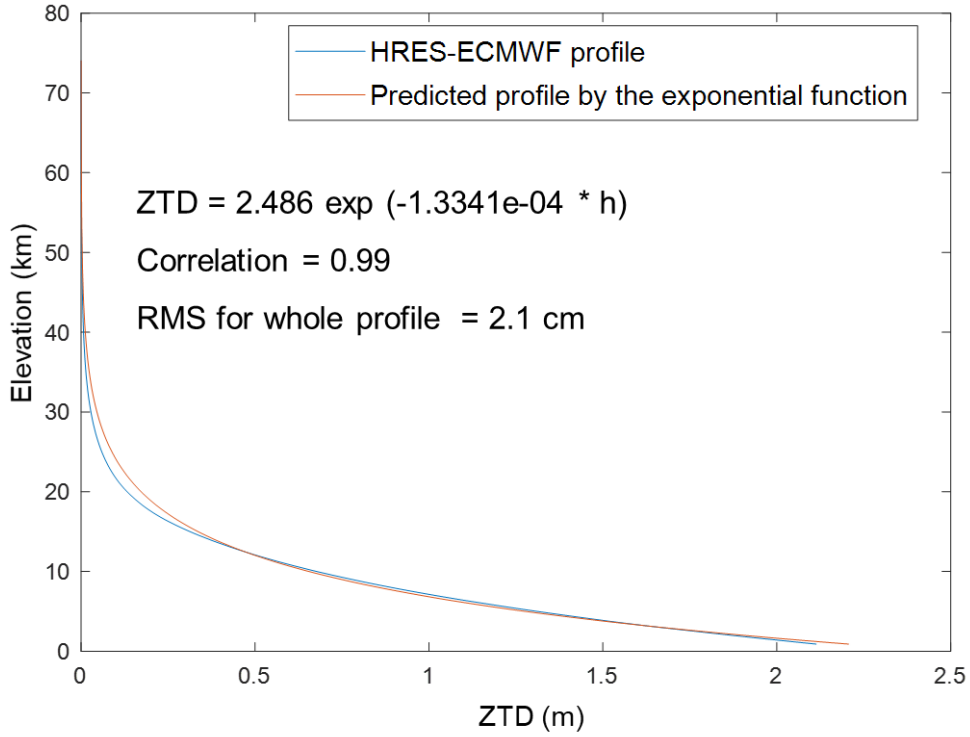

Figure 2.4 Comparison of the ECMWF vertical profile and the exponential profile.

The stratified atmospheric delay S can be modelled by an exponential function:

$$S(h_k) = L_0 e^{-\beta h_k} \qquad \text{(Equation 2.9)}$$

where h is the elevation at point k; β and L_0 are estimated exponential coefficients for the region considered. To assess this simple model, we estimated the exponential parameters in Equation 2.9 using the ECMWF atmospheric delays from a whole 137-level vertical profile at a point in California (38.125N, 119.75W). Their difference, shown in Figure 2.4, culminates at 3-4 cm, occurring between 15 and 35 km in elevation, with an overall RMS difference of 2.1 cm for the whole profile. At low elevations where the InSAR measurement is taken, the exponential function agrees with the actual profile better (1.8 cm RMS for layers below 10 km and 2.3 cm for those above 10 km). However, it should be noted that the phase measurement on an interferogram is differenced between two dates and the stationary atmospheric contributions (mostly come from the upper layers) are cancelled. This will result in the exponential law being disturbed due to the dynamic interaction between the lower troposphere and the ground surface at the atmospheric boundary layer. To conclude, it is the lower troposphere and its dynamics that most affect the InSAR measurement and the atmospheric error correction.

2.2.4 Examples of InSAR atmospheric effects

The InSAR atmospheric effect in flat regions can be quite different from those observed in mountainous regions due to the vertical stratification or the "static" effect of the troposphere in mountainous regions. For example, Ding et al. (2008) applied the Radon transformation (Wood and Barry, 1992) on the phase measurement and derived substantially different properties of the atmospheric effect anisotropy on flat and mountainous regions. Li et al. (2007) used both the Jarque-Bera (Jarque and Bera, 1980) and the Hinich (Hinich and Wilson, 1990) methods to test the atmospheric signals over Shanghai and confirmed that the atmospheric signals in all the interferograms are non-Gaussian. Goldstein (1995) also pointed out that atmospheric signals in a SAR interferogram generally follow a power law distribution, however, the power exponent varies on an interferogram and requires high-resolution external data for quantification.

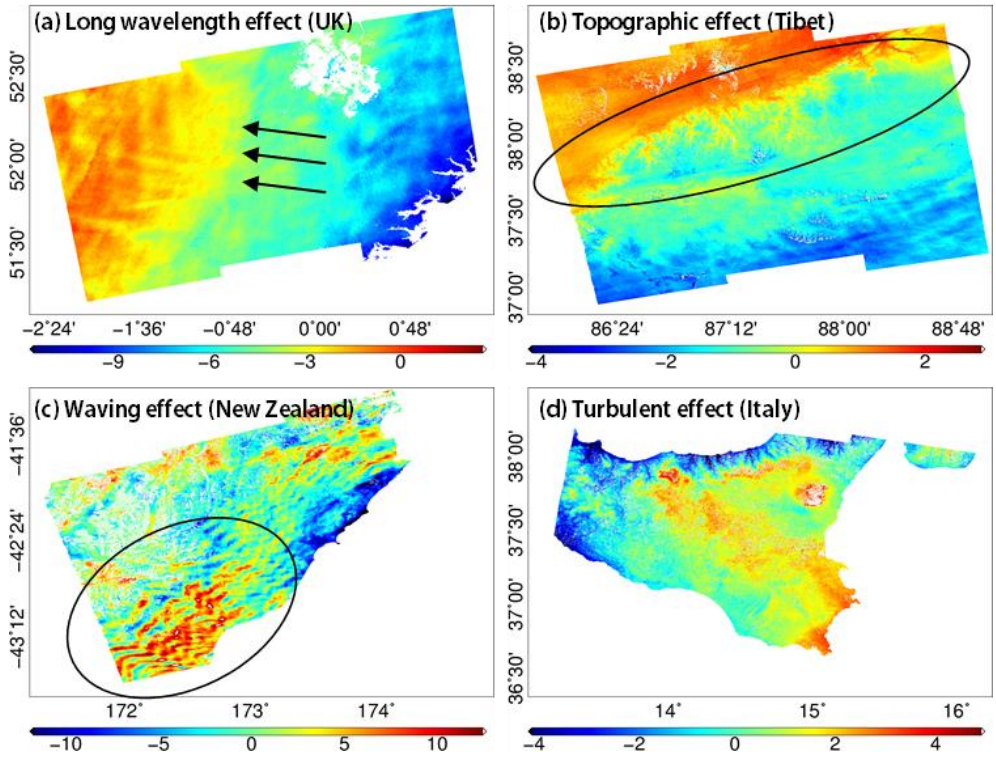

Figure 2.5 Examples of different types of InSAR atmospheric effects on Sentinel-1 interferograms. Unit: radians.

Figure 2.5 shows some different types of InSAR atmospheric effects on some Sentine1-1 interferograms. Figure 2.5a exhibits a substantial long wavelength effect with a clear gradient from southeast to northwest, behaving similarly to an orbital ramp. Figure 2.5b experiences serious topographic related atmospheric errors due to its steep topography along numerous

mountain chains. Rapid changing topography can also lead to ripple-like atmospheric signals, as shown in Figure 2.5c, as a result of water vapour propagation over mountains. The turbulent atmospheric effect, however, can be random in space regardless of topography, such as the eastern and northern coasts in Figure 2.5d. Due to the complex interactions between water vapour above ocean and land areas, atmospheric effects in coastal areas are inevitably severe and hard to mitigate.

2.3 Ionospheric Effect

The free electrons in the ionosphere interact with electromagnetic waves as a dispersive medium, inversely proportional to the frequency, and so exert stronger effects at lower frequencies. The free electron density variation introduces interferometric phase gradients and range registration offsets, which sometimes fail the co-registration. Gray et al. (2000) presented observations of C-band (RadarSAT) and L-band (JERS-1) interferometric pairs, showed substantial azimuth shifts in the fringes that are correlated with ionospheric activity, and confirmed that larger phase offsets and azimuth shifts were observed at long wavelengths with up to several resolution cells at L-band. Due to the shape of the Earth's magnetic field, peak electron concentrations and spatial variations occur mainly in polar and tropical regions. As a result, ionospheric effects are generally negligible for short wavelength SAR satellites (e.g., the C-band Sentinel-1) at least over temperate zones, but more serious for long wavelength SAR satellites (e.g., the L-band ALOS-1/2), particularly over polar and tropical regions (e.g., tectonic and volcanic activities in Taiwan or Indonesia (Zhang et al., 2018)). However, Gomba et al. (2017) pointed out that for C-band SAR interferograms spanning large spatial extent such as Sentinel-1, the ionospheric effect is also observable under extreme ionosphere turbulence.

Several methods have been proposed to mitigate ionospheric effects. The Faraday rotation method, which derives the phase distortion induced by the ionosphere from Faraday rotation estimates, requiring full polarization data and an accurate magnetic field (Kim et al., 2015; Pi et al., 2011); Alternatively, Raucoules and De Michele (2010) investigated the sensitivity of the azimuth offset to small-scale variations in the ionosphere, but it may fail because of spatial

discontinuities. The most recent promising method adopts the split-spectral technique which benefits from the dispersive nature of the ionosphere and separates the ionospheric delay component from the interferometric phase (Gomba et al., 2016). It has received great successes and correction performance improvements, particularly on Sentinel-1 and ALOS-2 interferograms due to their wide beam antennae. Accordingly, this method has been implemented into the standard interferometry processing procedure in software such as GAMMA and ISCE.

2.4 Decorrelation

InSAR phase decorrelations occur due to massive surface changes, particularly in vegetated areas, which produce low correlation ground targets and prevent the recovery of unwrapped phase measurements. Typically, longer wavelength signals enable coherent phase recoveries over much longer time intervals than shorter wavelength signals, making the wavelength one of the key factors when choosing SAR data for different areas of interest. For example, L-band SAR is more suitable in the tropical areas than C-band SAR due to heavy vegetation.

There are many independent factors causing the InSAR decorrelation, such as the Doppler centroid difference, imaging geometry, temporal change, thermal noise, and atmospheric effects. The interferometric decorrelation can be statistically reflected by the phase coherence, computed as a complex cross-correlation index between two complex SAR images (e.g., Jiang et al., 2014). Given a window of N pixels, the coherence can be estimated as (Seymour and Cumming, 1994):

$$\rho = \frac{\left| \sum_{n=1}^{N} z_1 z_2^* \right|}{\sqrt{\sum_{n=1}^{N} |z_1|^2 \sum_{n=1}^{N} |z_2|^2}} \qquad \text{(Equation 2.10)}$$

where z_1 and z_2 are the complex measurements of the master and slave SAR images, respectively. Zebker and Villasenor (1992) demonstrated that decorrelation effects are multiplicative and hence a single coherence value accounts for all potential decorrelation phase error sources. Moreover, a proper estimation of phase coherence guarantees a successful phase unwrapping

and subsequent time series analysis. Figure 2.6 shows some examples of phase decorrelation for C-band Sentinel-1 interferograms, with the phase measurement retaining high coherence at a 12-day interval but gradually decreasing until a complete coherence loss after 168 days over vegetated areas.

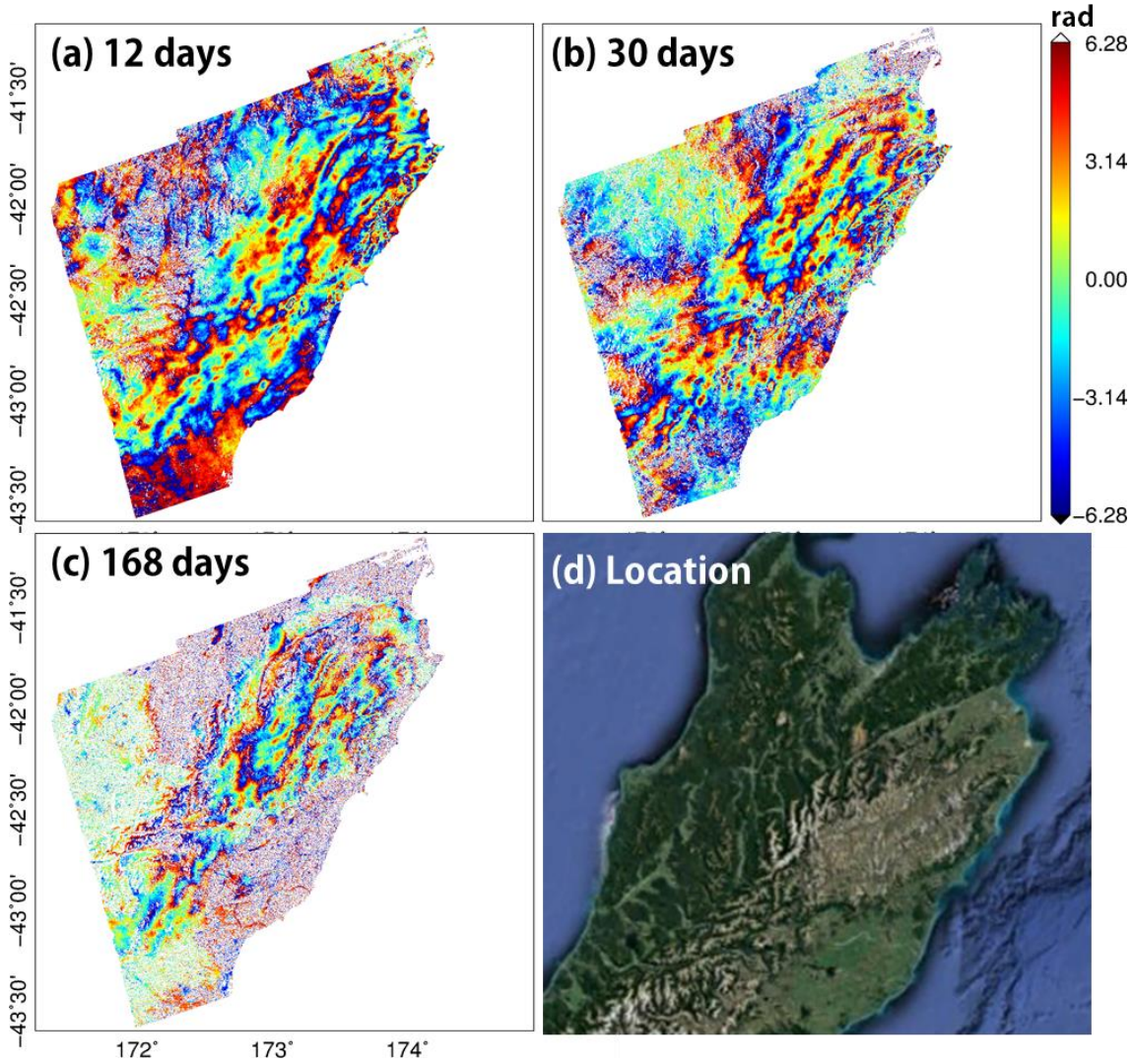

Figure 2.6 Temporal decorrelation of Sentinel-1 interferograms over New Zealand. (a) 20161115-20161127; (b) 20161115-20170114; (c) 20161115-20170601. (d) Location of the interferograms from Google Earth, showing vegetation and topography.

The relationship between the phase standard deviation and coherence can be set up statistically, under the hypothesis that the reflection for a given interferogram pixel can be modelled as the sum of many randomly and independently oriented sub-reflectors. An empirical expression is given by Rodriguez and Martin (1992) when the multi-look factor is large enough:

$$\delta^2(\varphi) = \frac{\lambda}{4\pi}\frac{1-\rho^2}{2\rho^2} \qquad \text{(Equation 2.11)}$$

where δ is the standard deviation of the phase φ along LOS; ρ is the coherence between 0 and 1; λ is the phase wavelength.

2.5 Geometric Related Errors

Geometric related errors are those dependent on InSAR satellite geometries, especially the perpendicular baseline, including the DEM error and the orbital error.

2.5.1 DEM error

Recalling Equation 2.1, the extraction of ground displacement requires the separation of the phase components due to the Earth's curvature and topography, which is accomplished by applying an external DEM (e.g., Shuttle Radar Topography Mission (SRTM) or Advanced Spaceborne Thermal Emission and Reflection DEM (ASTER-GDEM)). Therefore, an inaccurate DEM, including actual vertical shifts between the target height and nearby DEM posting values (González and Fernández, 2011), will inevitably introduce phase residuals that are baseline-dependent (Bürgmann et al., 2000). The phase standard deviation related to the DEM error can be expressed as:

$$\sigma^2(\varphi) = (\frac{4\pi B_\perp}{\lambda R \sin\theta})^2 \sigma^2(h) \qquad \text{(Equation 2.12)}$$

Please refer to Equation 2.1 for symbols. Due to the linear dependence between the topographic phase and the perpendicular baseline, longer baseline separations will produce greater height errors (see examples in Figure 2.7). This provides a criterion to optimize the interferogram selection in a time series, i.e. pairs with short baselines should be chosen in priority to reduce the impact of height errors, leaving the long baseline interferograms only necessary to connect the network. The linear relationship also enables the estimation of the height error in a time series with variable perpendicular baseline lengths (e.g., Li et al., 2009a).

In practice, it is the height difference between the reference pixel and the pixel under consideration that matters to the phase measurement accuracy. As a result, spatial correlations in the data, for example as introduced by the atmosphere, need consideration. In this case, adjacent cells will experience small DEM errors since the atmospheric contributions for both

resolution cells are nearly identical. For two resolution cells with a large spatial separation, the variance of the height difference will be large, as the atmospheric contribution for both resolution cells will be almost uncorrelated. A detailed methodology to minimize the DEM error is described in Fattahi and Amelung (2013).

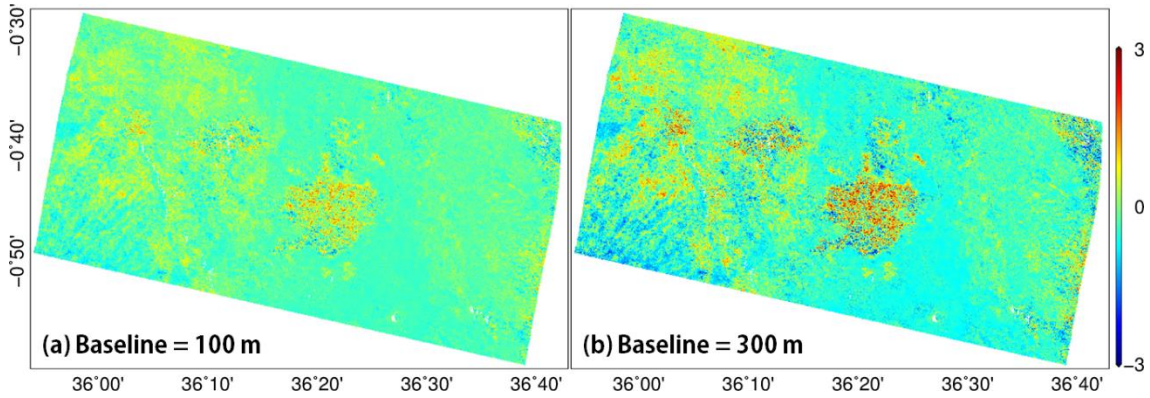

Figure 2.7 Examples of DEM errors at different baseline lengths. Unit: m.

2.5.2 Orbital error

Orbital ephemerides are sometimes not accurate enough to retrieve precise satellite state vectors, introducing long wavelength orbital errors onto phase measurements (Massonnet and Feigl, 1998), as shown in Figure 2.8. They are indistinguishable from long wavelength atmospheric delays and/or deformation signals, hence limiting InSAR for measuring widespread displacements. Massonnet and Feigl (1998) showed orbital errors, at least the first order, on an interferogram can be simply simulated as a best-fit linear or quadratic surface. A more advanced method was proposed by Biggs et al. (2007) who considered a network of interferograms to estimate a consistent surface fitted to all the interferometric phases. A review of these methods and their pro and cons is summarized in Fattahi and Amelung (2014).

Orbital errors may propagate to DEM errors due to an inaccurate perpendicular baseline length estimate. Their relationship can be described as (Lancaster, 1989):

$$dH = H^0 \frac{-n_\perp}{B_\perp^0} \qquad \text{(Equation 2.13)}$$

where H^0 is the initial height derived using the available orbit information, $B_\perp^0$ is the perpendicular baseline derived from observed state vectors, $n_\perp^0$ is the residual (error)

perpendicular baseline caused by the error in satellite state vectors. Equation 2.13 reveals that orbital errors result in an erroneous scaling of the topographic height.

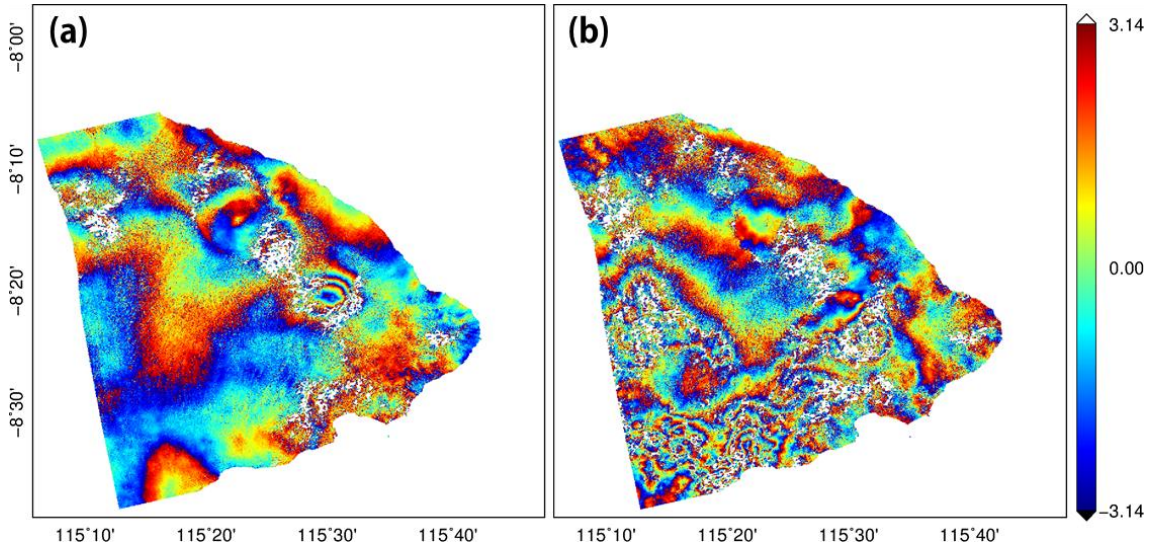

Figure 2.8 Examples of orbital ramps over Indonesia. (a) 20171105-20171117. (b) 20171105-20180221. Unit: rad.

In general, geometric related errors are problematic for some old SAR missions (e.g., ERS-1/2 and JERS-1) due to inaccurate orbit geometry determination. However, this has been largely improved by onboard GPS receivers on modern SAR satellites (e.g., TerraSAR-X, Sentinel-1 and ALOS-2), leaving their geometric errors typically being negligible. For precise velocity mapping, their effects can still be further reduced using interferogram time series and precise orbit information.

2.6 Phase Unwrapping Error

Unwrapping an interferogram with noise contamination can be problematic as the errors may introduce phase jumps of a multiple of 2π and thus seriously degrade the accuracy of InSAR derived displacements. The fundamental assumption in phase unwrapping is that gradients between adjacent pixels (the difference between them) have no ambiguities, therefore, the unwrapped phase could be recovered by integrating the wrapped phases pixel by pixel along an arbitrary path. However, this assumption is quite optimistic because most of the interferograms have gradients large enough to cause discontinuities. One of the origins of these discontinuities comes from the interferometric decorrelation and can be averted by filtering, but with a compromise of losing resolution. Regions with steep phase gradients or cracks (e.g., a ruptured

fault) could also lead to discontinuities, resulting in InSAR only being capable of measuring small magnitude deformation (dependent on wavelength). Figure 2.9 shows a simple method to detect unwrapping errors within a closed loop. Should unwrapping errors occur in any of the three interferograms, there will be a large jump in the residual map.

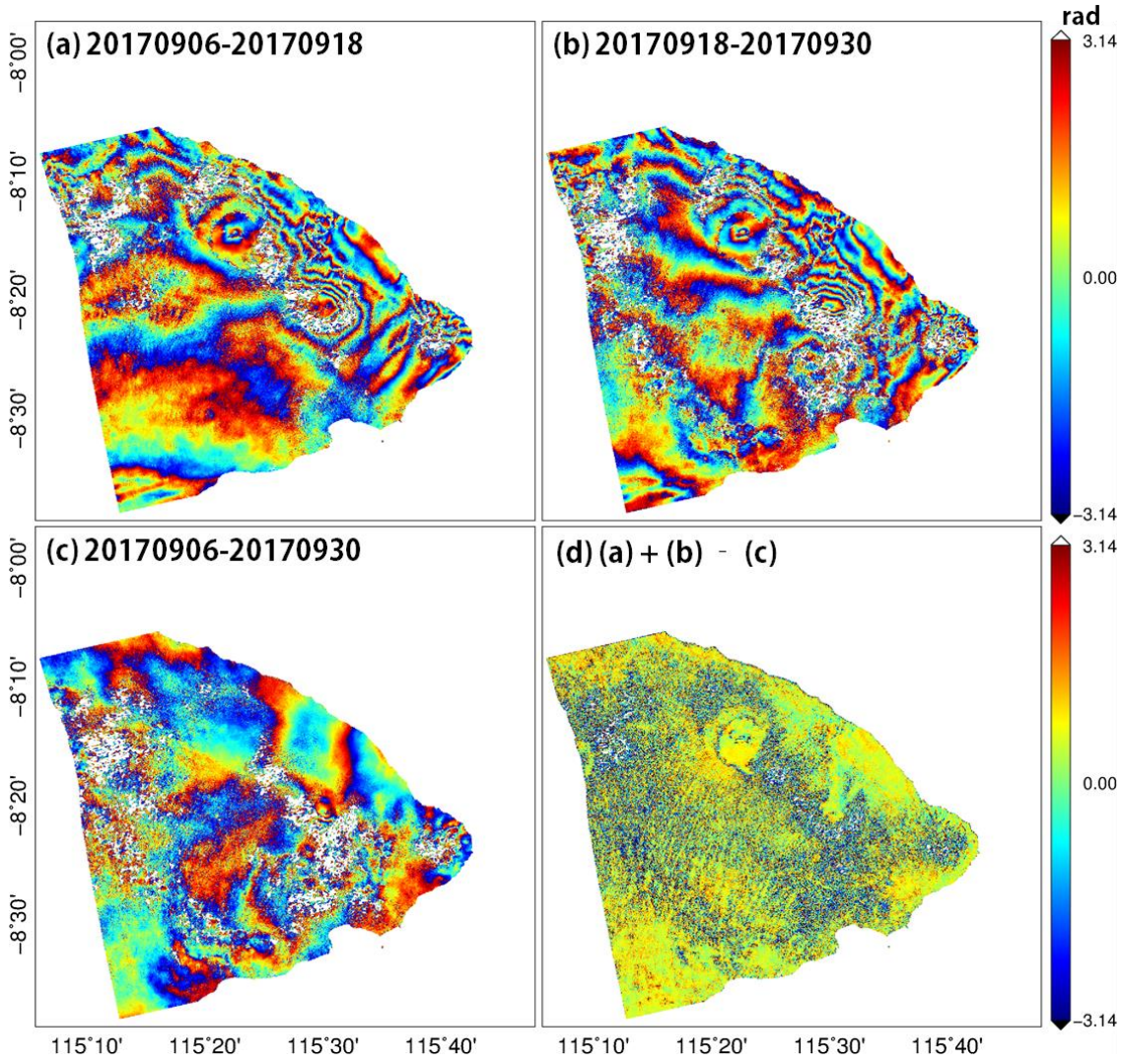

Figure 2.9 Unwrapping error check schedule. (a), (b) and (c) are Sentinel-1 interferograms in the same area. (d) is the residual map by (a + b - c).

There are several ways to avoid unwrapping error with compromises on resolutions and/or accuracies. For example, by the pixel offset tracking method (Hu et al., 2014) or the split-band method (Libert et al., 2017). With new SAR missions become increasingly available, it will be possible to combine multiple satellites with different frequencies to improve the unwrapping accuracy (Ding et al., 2017).

2.7 Discussion

Among all error sources discussed above, the atmospheric error remains one of the most crucial sources in whatever the spatial extent or time span. There are various types of SAR satellites with different wavelengths for users to balance the temporal decorrelation, ionospheric effect and accuracy. The geometric related error is currently negligible because of the precise orbit control, except for the applications which require extreme high-resolution deformation maps in developing cities or when the topography changes rapidly due to volcanic flows, where the DEM error is still problematic. The phase unwrapping error can be detected and removed, although manually, during data processing, or reduced by rejecting poor quality interferograms (e.g., those with low coherence or frequent phase discontinuities). The atmospheric error has been left as the most important and unavoidable error source that has to be corrected in order to achieve reasonable deformation maps.

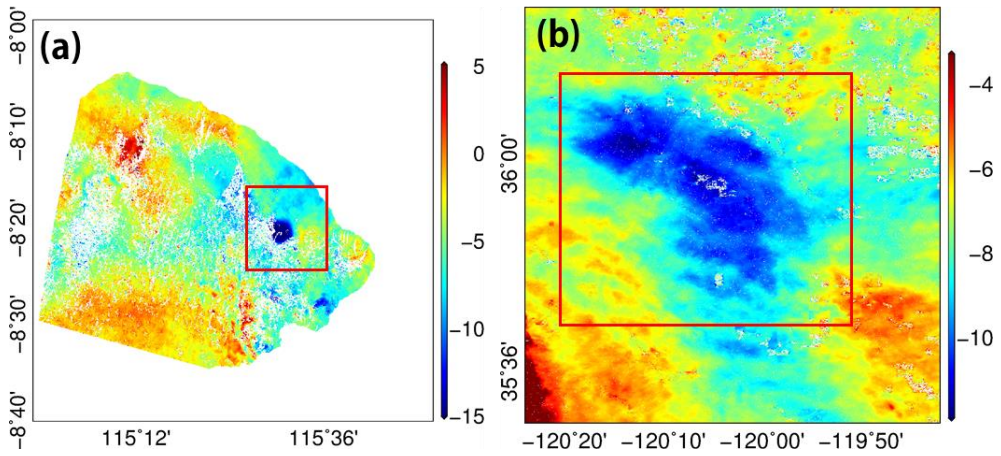

Figure 2.10 Atmospheric error examples that could be interpreted as ground motions. (a) is in Indonesia around Agung volcano (red box). (b) is in Central California. Unit: rad.

Atmospheric errors can be easily interpreted as ground motions. We demonstrated this in Figure 2.10 with two Sentinel-1 interferograms with 12-day temporal baselines to exclude the effect of actual ground motions. Volcanic edifices always have strong topographic variations which may experience atmospheric errors in the same pattern with volcanic deformation (red box in Figure 2.10a). An extreme rainfall on either acquisition of an interferogram may introduce strong localized atmospheric errors which may resemble ground subsidence (red box in Figure 2.10b). As a result, the atmospheric correction is vital for InSAR to achieve authentic and

accurate ground motion measurements, particularly for small magnitude and long-term slow-moving deformation series.

The magnitude of atmospheric effects ranges from 5 to 20 cm (Bekaert et al., 2015b) but is subject to the spatial extent of the interferogram. Though typically increasing with the spatial extent, atmospheric errors can be substantial on small interferograms. Figure 2.11 shows some examples of atmospheric errors on different spatial extents. The small landslide has serious topographic related errors mainly due to its large elevation variation (from 0.1 to 3 km), with a similar magnitude of a long wavelength atmospheric error being observed on the New Zealand interferogram across ~250 km.

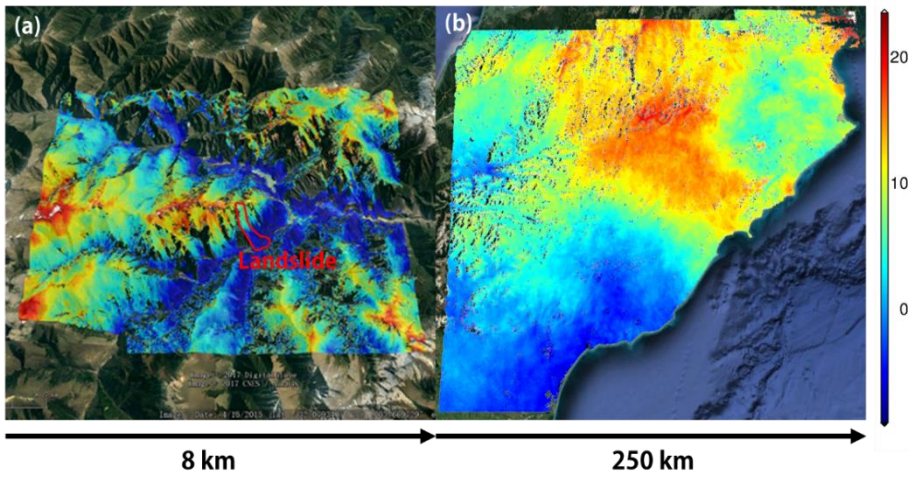

Figure 2.11 Atmospheric errors at interferograms over different spatial extents. (a) is around a small landslide in China; (b) is in the South Island of New Zealand. Unit: rad.

2.8 Summary

In this chapter, the basic knowledge of SAR interferometry is described, and the most important error sources are analyzed. The atmospheric error, identified as the most important error source of InSAR, varies spatial-temporally and contributes substantially to the variance and covariance of the phase. The ionospheric error, dependent with the frequency, exerts mostly long wavelength signals over great spatial extents and is particularly serious over polar and tropical regions. The phase noise can be mathematically related to the coherence (Equation 2.10) and DEM error (Equation 2.12). However, their relationships are only effective to estimate an upper bound for coherence and a lower bound for phase variance, since the influence of temporal decorrelation is often spatially variable and difficult to assess (Lancaster, 1989). A combined

variance matrix of atmospheric, ionospheric, temporal decorrelation and geometric errors can lead to a priori prediction of the phase variance, even before the data is scanned, which is a useful information for data selections or satellite scanning time allocations.

Chapter 3. GPS Based Iterative Tropospheric Decomposition (ITD) Model

Pointwise GPS measurements of tropospheric ZTD should be interpolated to provide high-resolution water vapour maps in order to be used for correcting InSAR measurements, as well as for numeral weather prediction and for correcting GPS observations in network RTK. To achieve this, numerous efforts have been attempted, with emphasis on the importance of the elevation dependency of water vapour, but it remains a challenge to model the elevation-dependent tropospheric delay in the presence of tropospheric turbulence. To overcome this, we present an iterative tropospheric decomposition interpolation model that decouples the elevation and turbulent tropospheric delay components to retrieve high resolution water vapour maps, with both the tropospheric stratification and turbulence being considered.

3.1 Real-time GPS Tropospheric Delay

In this section, we introduce the method for estimating ZTDs from GPS observations in real-time mode and validate them internally and against the post-processed solutions.

3.1.1 Real-time mode GPS precise point positioning method

The pointwise ZTD values were estimated using real-time mode GPS Precise Point Positioning (PPP) processing. We used a PPP software which is a highly self-modified version of RTKLIB (www.rtklib.com), employing an extended Kalman filter (Haddad, 1976) to estimate in the state vector the constant ambiguities and time varying receiver coordinates, receiver and satellite clocks (considered as white noise), whilst the ZWD was estimated as a random walk parameter as a correction to an a priori ZTD from the UNB3 global empirical model (Leandro et al., 2006), employing the Global Mapping Function (Boehm et al., 2006), and east-west and north-south tropospheric gradients were estimated. We used the ionospherically-free pseudorange and carrier phase observables and applied absolute IGS satellite and receiver antenna phase centre offset corrections. We also applied corrections for antenna phase wind up (Beyerle, 2009), relativistic effects (Kouba, 2009), pseudorange differential calibration delays, Earth tide (McCarthy, 1996) and ocean tide loading effects using FES2004 coefficients obtained from

http://holt.oso.chalmers.se/loading. Uncalibrated phase and pseudorange hardware delays were assumed to be absorbed by the (float) ambiguity parameters and estimated receiver clocks, respectively.

PPP relies on highly accurate satellite orbits and clocks (Zumberge et al., 1997), which are usually held fixed in post-processed PPP. For our real-time mode processing, we used fixed real-time satellite orbits from the International GPS Service (IGS) Real-time Service, which were generated by decoding the IGC01 solution streams (products.igs-ip.net) every 15 seconds to match the GPS observation sampling rate of the Plate Boundary Observation (PBO, http://pbo.unavco.org/data/gps) stations used. However, the satellite clocks have unpredictable behaviour which makes their real-time prediction challenging (Li et al., 2014), so we did not fix these to the real-time product values but estimated corrections to them using satellite clock parameters with the Gundlich and Koch (2002) robust estimation method. Additional constraints were introduced to overcome the rank deficiency of the normal equations, namely:

$$\begin{cases} dt_k - dt_{k,RTS} = 0 \\ res(dt_k) = dt_k - dt_{k,RTS} \end{cases} \qquad \text{(Equation 3.1)}$$

where $dt_{k,RTS}$ is the initial value of the satellite clock given by the real-time product and acts as a pseudo-observation; $res(dt_k)$ and dt_k are the satellite clock residual and value, respectively. The satellite clock parameters were estimated as white noise parameters with a sigma of 0.001 ns, and the error messages contained in the real-time satellite clock product were used to determine the weights of the pseudo-observations in Equation 3.1. An iterative process was used to identify some clock outliers which were hence ignored or assigned less weight in subsequent iterations (Gundlich and Koch, 2002).

3.1.2 Validation of real-time mode GPS pointwise ZTDs

To validate our real-time mode PPP (RTPPP) method, we processed the data for the 41 stations in a 150 km x 150 km California study region (Figure 3.1) from 1 January to 31 December 2015 per GPS station in daily, discrete 24-hour batches in real-time mode, with an elevation angle cut-off of 10º. The tropospheric delay was estimated every 5 minutes using a process noise of 5.0e-8 km s^{-1}, as per the GIPSY solutions. To enable the fastest PPP solution convergence and

separation of the ambiguities from the other estimated parameters, which is particularly problematic when using real-time satellite orbits and clocks (e.g., Yao et al., 2014), we applied loose constraints (1000 times lower than the phase observation) to a priori receiver coordinate values obtained from the PBO GPS Station Position Time Series. Nearly 70% of daily solutions converged within 30 minutes (convergence time here means, from the beginning epoch to an epoch whose horizontal component bias is less than 10 cm and height component bias is less than 15 cm, and the overall standard deviation of its next 20 consecutive epochs also satisfies this requirement), with 90% of daily solutions converging within 50 minutes. The results presented hereafter are based only on the ZTD values after convergence was attained, according to these criteria.

The real-time mode PPP (RTPPP) GPS ZTD estimates was compared with post-processed 'truth' values computed by the Geodesy Laboratory at Central Washington University using the NASA JPL / Caltech GIPSY software version 6.2 and made available at ftp://data-out.unavco.org/pub/products/troposphere/. The truth values were estimated every 5 minutes using the PPP technique, fixing IGS final orbits and clocks, using the VMF1 gridded tropospheric mapping function together with ECMWF gridded a priori ZHDs and ZWDs (Boehm et al., 2006), whilst estimating the ZWD and tropospheric gradients (east-west and north-south), applying process noise values of 5.0e-8 km s^{-1} and 5.0e-9 km s^{-1}, respectively. We computed the differences between our RTPPP and GIPSY ZTDs at the common 5-minute epochs, excluded all the outliers greater than three times the standard deviation, then for each station computed per day the mean difference and the Root Mean Square (RMS) of the differences to assess the quality of the real-time mode processing. These are shown for a sample day (2 September 2015) in Figure 3.1, chosen as it is indicative of the median differences for all days of 2015. The mean of the per station differences across the whole network is 1.9 mm for the sample day, indicating that no large systematic error exists between the RTPPP and GIPSY ZTDs, including stations in mountainous areas. The mean RMS is 10.1 mm and more than 80% of the stations have an RMS value smaller than 12 mm, which is deemed sufficient quality for assimilation into real-time meteorological models (Shoji et al., 2011).

Apart from considering the spatial distribution of the differences, it is also important to assess the RTPPP performance over time. We therefore in Figure 3.2 show the 5-minute RTPPP ZTDs plotted against the common epoch 5-minute GIPSY ZTDs, from all 41 stations for the entire year, and plot the differences as a histogram. A linear regression fit gave: GIPSY ZTD = 0.989(±0.002) × RTPPP ZTD + 0.024(±0.003), and the correlation coefficient between them was 0.99, demonstrating high consistency between the RTPPP and GIPSY ZTDs not just spatially but also temporally. About 82% of solutions show differences smaller than 15 mm with 73% below 12 mm. The RMS difference is 12.5 mm, commensurate with the spatial RMS difference and further indicating an RTPPP ZTD precision of about 1 cm, which is commensurate with previous real-time studies (e.g., Ahmed et al., 2016; Li et al., 2014).

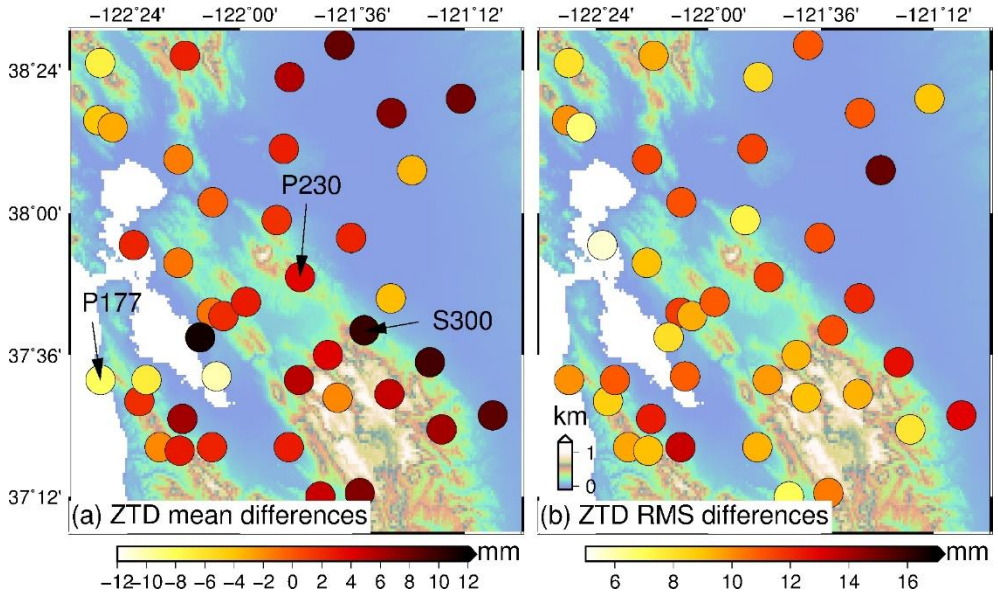

Figure 3.1 Mean (a) and RMS (b) differences per station between RTPPP and GIPSY ZTDs, estimated every 5 minutes on 2 September 2015 for all 41 GPS stations in the California study region. For all stations, the mean difference and the mean RMS difference are 1.9 mm and 10.1 mm respectively, with this day being indicative of the median differences for all days of 2015. The white area represents the Pacific Ocean and San Francisco Bay, and the background shows the elevation. Stations P177, P230 and S300 are labelled as they are considered in Figure 3.9.

The time-varying ZTD is estimated per receiver using the GPS data alone, and then the ZHD (which may be accurately modelled using surface pressure data, obtained from ftp://data-out.unavco.org/pub/rinex/met) is subtracted to leave the ZWD, which is spatially and temporally much more variable. The ZWD may then be readily converted to Precipitable Water Vapour (PWV) using estimates of the mean temperature of the atmosphere, based on surface

temperature measurements (Bevis et al., 1992). GPS hence provides a means of obtaining PWV with continuous temporal resolution without any cloud or weather dependence, albeit at discrete points where the GPS receivers are located. The pointwise GPS PWV measurements agree to those from radiosondes and microwave radiometers with standard deviations of about 1-2 mm (e.g., Ohtani and Naito, 2000; Liou et al., 2001; Li et al., 2003), and may then be interpolated to provide PWV fields, which has been attempted using different models.

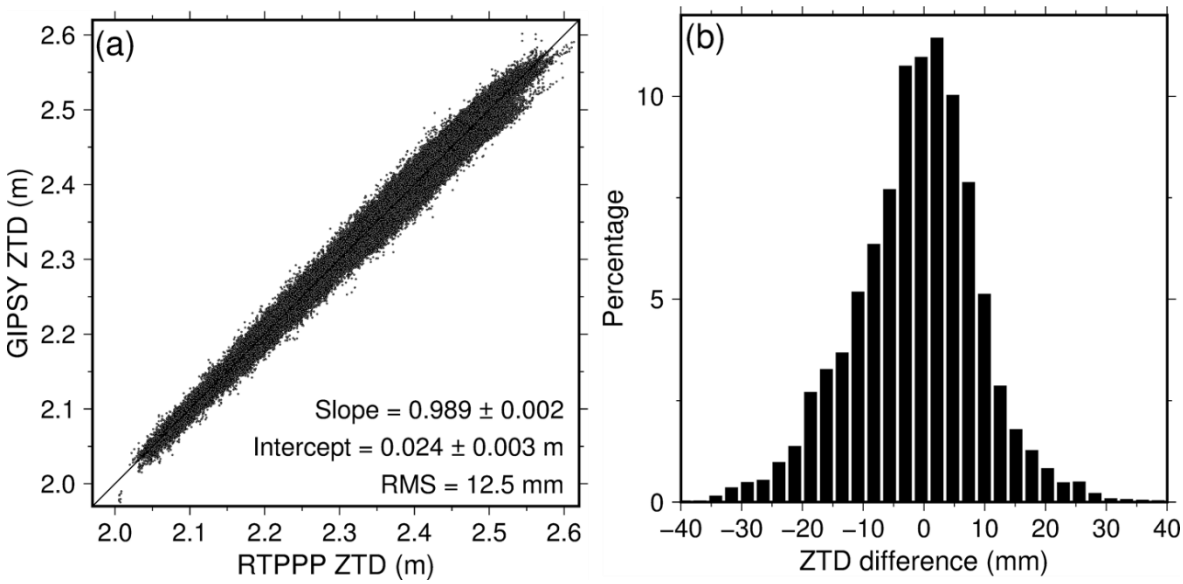

Figure 3.2 Comparison between RTPPP and GIPSY ZTDs for all 41 GPS reference stations in California, from 1 January to 31 December 2015 at an interval of 5 minutes. (a) Correlation analysis with a linear model: GIPSY ZTD = Slope × RTPPP ZTD + Intercept, and (b) Histogram of the differences.

3.2 Iterative Tropospheric Decomposition (ITD) Model

The pointwise ZTD/PWV samples will need to be interpolated into fields (maps) in order to be used in meteorological nowcasting, including the identification of events dominated by horizontal advection (Benevides et al., 2015); for assessing moisture transport in the lower troposphere (e.g., Mengistu Tsidu et al., 2015); for relating humidity fields to precipitation events (e.g., Boniface et al., 2009); for assessing the severity of tropical cyclones (e.g., Shoji et al., 2011); for assessing the impact of new assimilated observations for forecasting precipitation (Yan et al., 2009). Such maps are also essential for correcting SAR images for atmospheric effects to enable small (and long wavelength) geophysical signals to be measured, including inter-seismic strain accumulation and post-seismic motion, observations of which not only give insight into the mechanics of a fault, but also play key roles in estimating the likelihood of

future earthquakes (Fialko, 2006; Gourmelen and Amelung, 2005; Wright et al., 2004). Dense ZTD fields also enable GPS network RTK observations to be corrected for signal delays due to water vapour on propagating from space through the Earth's neutral atmosphere to a ground-based receiver. Such corrections are essential for centimetre level positioning, particularly heights, and enable (subject to sufficient GPS base station coverage) Network RTK to be used for geophysical and engineering applications that have normally only used local base station RTK, such as river channel mapping (e.g., Notebaert et al., 2009), glacier flow and debris mapping (e.g., Paoli and Flowers, 2007), coastal erosion (e.g., Thomas et al., 2010), crustal deformation and structural monitoring (e.g., Genrich and Bock 2006), precision farming (e.g., Pérez-Ruiz et al., 2011), embankment instability and landslide monitoring (e.g., Gili et al., 2000). The ZTD, ZWD and PWV shares similar characteristics when being dealt with by interpolators, although ZWD/PWV are more turbulent than the dry components. All the models we mentioned and proposed hereafter can be applied on all of them, so that we may introduce the model in terms of ZTD but validate the model on PWV or ZWD whatever data is available.

3.2.1 Review of atmospheric delay interpolation techniques

To interpolate the GPS pointwise ZTD, Jarlemark and Emardson (1998) evaluated a gradient model, a linear regression in time model that ignored observational directions, and a turbulence model that yielded at least 10% improved RMS error than the other two models. Williams et al. (1998) used a structure function to model the water vapour variation in space, but with respect to a reference value, whilst Janssen et al. (2004) found that Inverse Distance Weighted (IDW) and Ordinary Kriging (OK) interpolation models perform better than spline interpolation, but also only considered double differenced ZTDs as they were considering InSAR atmospheric corrections only. A deficiency of all these models is that they did not consider the terrain elevation dependence of water vapour and hence the interpolated values may contain large errors in regions with highly varying topography (Walters et al., 2013).

To deal with the atmospheric stratification, Emardson and Johansson (1998) incorporated a height scaling function with a best linear unbiased estimator and suggested an interpolated ZWD accuracy of about 1 cm, but only one station in Sweden was considered and the height

variation across the network was only about 200 m. Li et al. (2006a) proposed a GPS topography-dependent turbulence model (GTTM) but reported that interpolation models should be applied to ZTD/ZWD values differenced in time rather than the absolute ZTD/ZWD values themselves, as this can reduce the influence of topographic effects on the ZTD/ZWD variations. For interpolating undifferenced GPS ZWD point values, Onn and Zebker (2006) utilized a frozen flow hypothesis to model the water vapour variation in time. Then Xu et al. (2011) showed that incorporating this height scaling function approach with an interpolator model based on the estimator of simple Kriging with varying local means (we will refer to this model as SKlm+Onn) improved the ZWD interpolation RMS accuracy by 29% compared with using the Berrada Baby et al. (1988) semi-empirical height scaling function. In a different approach to account for variations with topography, Bekaert et al. (2015a) employed an InSAR phase observation-based power law correction model which used a fixed reference at the relative top of the troposphere, and described how the phase delay varies with altitude. To separate deformation and tropospheric signals, a frequency band insensitive to deformation is required. Benevides et al. (2016) also attempted to constrain GPS PWV with InSAR-derived PWV maps containing the topography signal. However, these models did not take into account that the InSAR measurements themselves have uncertainties of up to several centimetres and are susceptible to not detecting geophysical signals such as volcano inflation/deflation and inter-seismic slip rate (Williams et al., 1998). Hence, we consider the SKlm+Onn model to represent the current state-of-the-art for the generation of PWV maps.

3.2.2 Description of the ITD model

Several previous studies have noticed the coupling effect of the tropospheric turbulence and terrain elevation dependency (e.g., Treuhaft and Lanyi 1987; Li et al., 2006a; Xu et al., 2011; Benevides et al., 2016). However, in the presence of strong atmospheric turbulence, the previous models are inadequate for correcting SAR images to be used for sub-centimetre level ground motion monitoring (e.g., Walters et al., 2013; Fattahi et al., 2015), or for the highest network RTK positional precisions when such variations are not eliminated by data differencing. The aim of our proposed ITD model is therefore to improve the accuracy of GPS interpolated tropospheric water vapour maps by accounting for the coupling effect of both the terrain

elevation dependency and tropospheric turbulence, demonstrate this over varying terrain, and compare with the current state-of-art SKlm+Onn model (see Section 3.2.1).

The ITD model can effectively separate the turbulent and elevation dependent ZTD components by decoupling the ZTD into a stratified delay and a turbulent delay, as described in Section 2.2, which enables the more accurate interpolation of dense ZTD fields from pointwise values from a set of GPS reference stations across a region. It is defined mathematically as:

$$ZTD_k = S(h_k) + T(x_k) + \varepsilon_k \qquad \text{(Equation 3.2)}$$

where, for the *ZTD* at location *k*, *T* represents the turbulent component and x_k is the station coordinate vector in the local topocentric coordinate system; *S* represents the stratified component correlated with height *h*. ε represents the remaining unmodeled residual errors, including unmodeled stratified and turbulent signals. The stratified component in Equation 3.2 can be fitted with a modified exponential function (Emardson and Johansson, 1998; Xu et al., 2011):

$$S(h_u) = L_0 \exp\{-\beta(h_u - h_{\min}) / (h_{\max} - h_{\min})\} \qquad \text{(Equation 3.3)}$$

where, β is the exponential coefficient and L_0 is, for the region considered, the stratified component delay at sea level. The height has been scaled to local minimum and maximum. L_0 and β can be estimated by regression analysis if the stratified delays on a set of GPS stations are known. However, instead of using the stratified delay, previous researchers (e.g., Doin et al., 2009; Li et al., 2006a; Xu et al., 2011) used total ZTDs to regress the parameters in Equation 3.3 since the stratified and the turbulent components are coupled together (see Equation 3.2) and hard to distinguish from each other. In this case, the stratification regression could be biased by strong turbulence processes.

The turbulent component which is driven by tropospheric convective water vapour variance and/or local rainfall processes usually consists of medium-to-long wavelength signals (Tarayre and Massonnet, 1996). It is sensitive to a variety of geophysical variables including, but not limited to, location and topography, climate, time and land covers. Janssen et al. (2004) investigated several interpolators and found that the IDW and OK perform comparatively

effective. Hence, in this thesis, we choose IDW. Suppose n GPS stations are used as references, the IDW model reads as:

$$\begin{cases} T_u = \sum_{i=1}^{n} w_{ui} T_i(\mathbf{x_i}) \\ w_{ui} = \dfrac{\delta_{ui} d_{ui}^{-2}}{\sum_{k=1}^{n} \delta_{ui} d_{uk}^{-2}} \\ if\,(d_{ui} \le d_{\max}), \delta_{ui} = 1; else, \delta_{ui} = 0 \end{cases} \quad \text{(Equation 3.4)}$$

where w_{ui} denotes the interpolation coefficient; u and i are indices for the image pixels and the reference stations, respectively; $\mathbf{x}$ represents the station coordinate vector in the local Plane Coordinate System. d_{ui} represents the horizontal distance from the user to reference station. Reference stations with a distance larger than ~100 km (d_{max}), according to Jarlemark and Emardson (1998), were excluded since they show limited correlations with the user station.

Under the above definition, the total delay is mathematically divided into two parts: the stratified part which is completely correlated with the elevation whereas the turbulent part has no correlation with the elevation. We use their linear summation in Equation 3.2 as we treat them as independent parameters, under the assumption that the tropospheric delay is a sum of the stratified component and the turbulence component (e.g., Doin et al., 2009; Emardson et al., 2003; Hanssen, 2001). As a result, there will be no cross term in Equation 3.2 and the two components can be separated by iteration.

Both the stratified and turbulent delays can account for a substantial amount in the total delay but behave very differently. The main procedures for separating these two components are summarized as:

(i) The total delays are used to estimate the initial exponential coefficient β and L_0. This is done on a pixel by pixel basis, i.e. for each pixel, the surrounded data samples within the defined maximum distance are used, resulting in a lateral variation of the coefficients as a consequence of the data sampling;

(ii) The residuals, which are the summation of unmodelled errors and the turbulent component, are computed by subtracting per station the stratified delay (as modelled by the estimated

exponential coefficients) from the ZTD;

(iii) Extract the turbulent component of all reference stations from the residuals by forming an IDW function:

$$\begin{bmatrix} T_1 \\ T_2 \\ \cdots \\ T_n \end{bmatrix} = \begin{bmatrix} 0 & w_{12} & \cdots & w_{1n} \\ w_{21} & 0 & \cdots & w_{2n} \\ \cdots & \cdots & 0 & \cdots \\ w_{n1} & \cdots & w_{n,n-1} & 0 \end{bmatrix} \begin{bmatrix} \varepsilon_1 \\ \varepsilon_2 \\ \cdots \\ \varepsilon_n \end{bmatrix} \quad \text{(Equation 3.5)}$$

where w_{ij} is the j_{th} coefficient when interpolating station i using the remaining stations in IDW model (see Equation 3.4).

(iv) Consider the output of Equation 3.5 as the new turbulent component and subtract it from the total delay to produce a new input for Equation 3.3. A new set of exponential coefficients is obtained.

(v) Repeat (ii) – (iv) until stable coefficients are obtained. The final outputs are exponential coefficients (L_0, β) for the given region, the turbulent part and residuals on each reference station.

(vi) Both the final turbulent delay components and residuals from all stations are used to interpolate to each grid cell. The stratified delay is then computed per grid cell using the final values for the exponential coefficients, and the two are summed to produce the ZTD per grid cell.

It should be noted that the assumption of the ITD model is that the turbulent component obeys the IDW interpolation law and the stratified component obeys the exponential law and, importantly, that these two components are not tightly coupled together. We later show that the two components are indeed separable, and the convergence state can be reached rapidly. Although here we present the ITD model by ZTDs in zero difference mode, it is also suitable for interpolating differenced ZTD or PWV/ZWD.

3.3 Validation of the ITD Model

In this section, we validate the ITD model using the real-time mode ZTDs processed in Section 3.1 and demonstrate that the decoupled interpolation model generates improved high-resolution tropospheric delay maps compared with previous tropospheric turbulence and elevation

dependent models.

3.3.1 Cross validation of the interpolated ZTDs at GPS stations

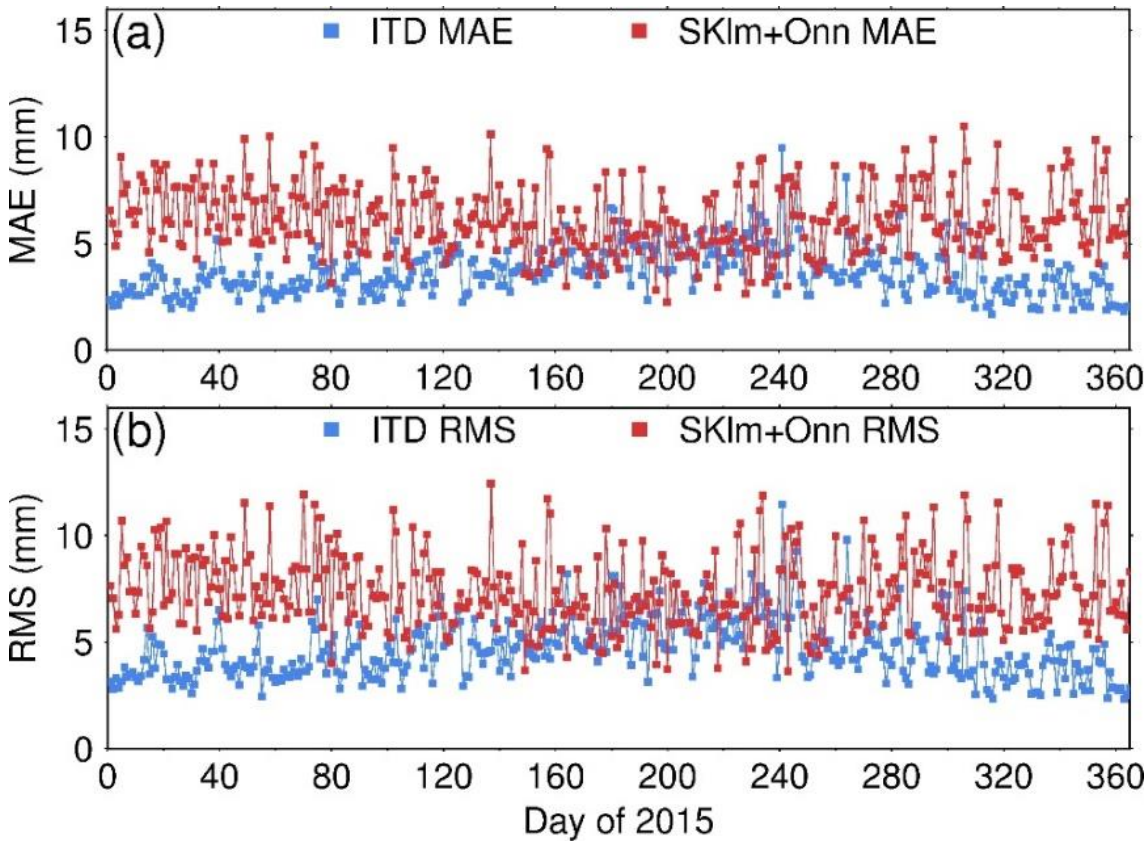

Figure 3.3 Time series of cross validated daily MAE and RMS differences, based on 14:00 Pacific Standard Time (i.e. local time) RTPPP interpolation at all 41 GPS stations using the ITD and SKlm+Onn models, and comparing with RTPPP ZTDs. The annual mean MAE values are 3.2 mm for ITD and 6.2 mm for SKlm+Onn, whilst the annual mean RMS differences are 4.1 mm for ITD and 7.4 mm for SKlm+Onn.

Cross validation was used to evaluate the performance of the ITD model for interpolating ZTDs and compared with the SKlm+Onn model. In this, one point from the whole network of GPS stations was excluded and the ZTD values from the other points used to determine the ZTD at the particular point considered. This procedure was repeated for all stations and the cross-RMS difference computed between the interpolated and original ZTD values. Whilst Xu et al. (2011) applied the SKlm+Onn model to ZWD, as ZWD also dominates the spatiotemporal variations of ZTD (with the ZHD being readily determined with surface pressure) we may also apply it to ZTD interpolation. Since the dry and wet components are both crucial for applications such as InSAR atmosphere corrections (Elliott et al., 2008; Jolivet et al., 2014), it is then recommended to use total delays rather than just the wet component. To provide an indication of the ZTD

quality used for single epoch SAR corrections, and to be commensurate with subsequent MODIS validations, we adopted the approach of Xu et al. (2011) and used one ZTD value per day (that at 14:00 Pacific Standard Time, i.e. local time, the approximate time of day when the troposphere is most active (Gendt et al., 2004; Wang et al., 2005), although this is not an all-encompassing rule and diurnal variations of PWV can differ from location to location) per station for the whole of 2015. The RTPPP ZTDs were interpolated for each GPS station in turn, with the 40 other GPS station ZTD values providing the input. Hence for ITD, per epoch, L_0 and β of Equation 3.3 were estimated for the network and the turbulent component estimated per station. Validation was carried out by comparing the interpolated ZTDs with the RTPPP ZTD estimates themselves at 14:00 local time and computing the RMS difference and Mean Absolute Error (MAE) for all stations for each day. This was repeated using interpolation with the SKlm+Onn model.

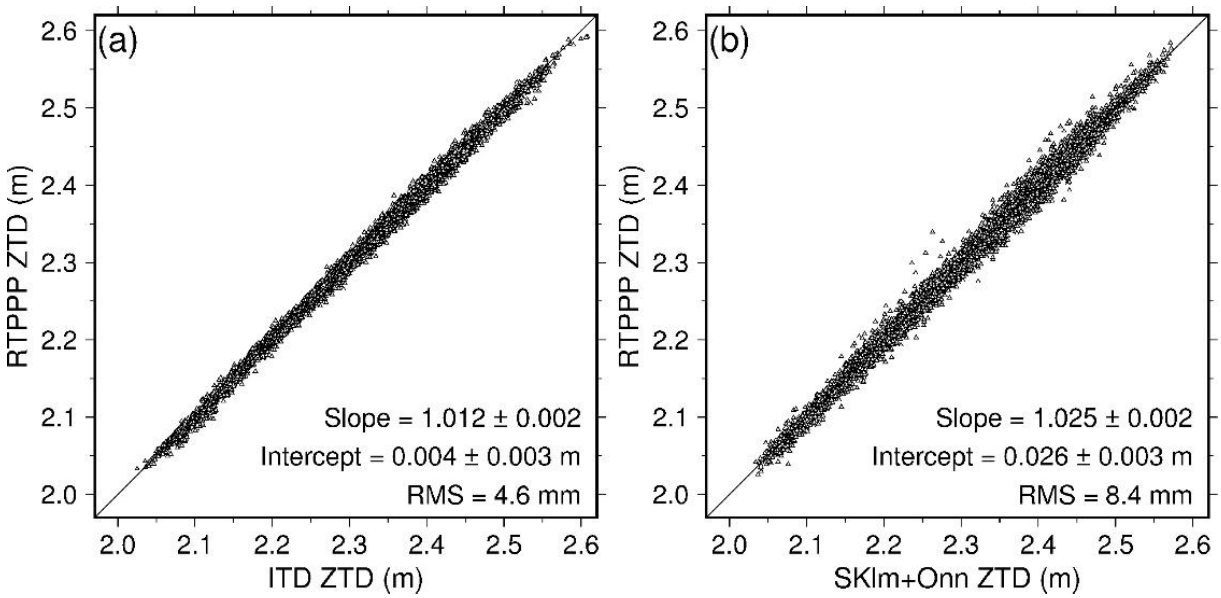

Figure 3.4 Cross validation of (a) ITD and (b) SKlm+Onn RTPPP ZTDs daily at 14:00 local time for 1 year for all the 41 GPS stations. Linear model (Initial RTPPP ZTD = Slope×Interpolated RTPPP ZTD + Intercept) was also applied.

Time series of the cross validated daily MAE and RMS differences from the ITD and SKlm+Onn ZTD interpolation models are shown in Figure 3.3. It is clear that the ITD model leads to both lower annual mean MAE and RMS difference values than SKlm+Onn, i.e. the MAE and RMS reduce from 6.2 mm to 3.2 mm and 7.4 mm to 4.1 mm, respectively. It can also be seen from Figure 3.3 that the improvement of ITD is greater than that of Sklm+Onn in colder

seasons (e.g., between days 0 to 100 and 280 to 365), when the medium-to-long wavelength and elevation-dependent signals dominate and can be effectively modelled by ITD. The performance of the two models is more similar in the summer (i.e. from around day of year 150 to 220), indicating that short wavelength water vapour effects are substantial and variable and cannot be fully mitigated by either model.

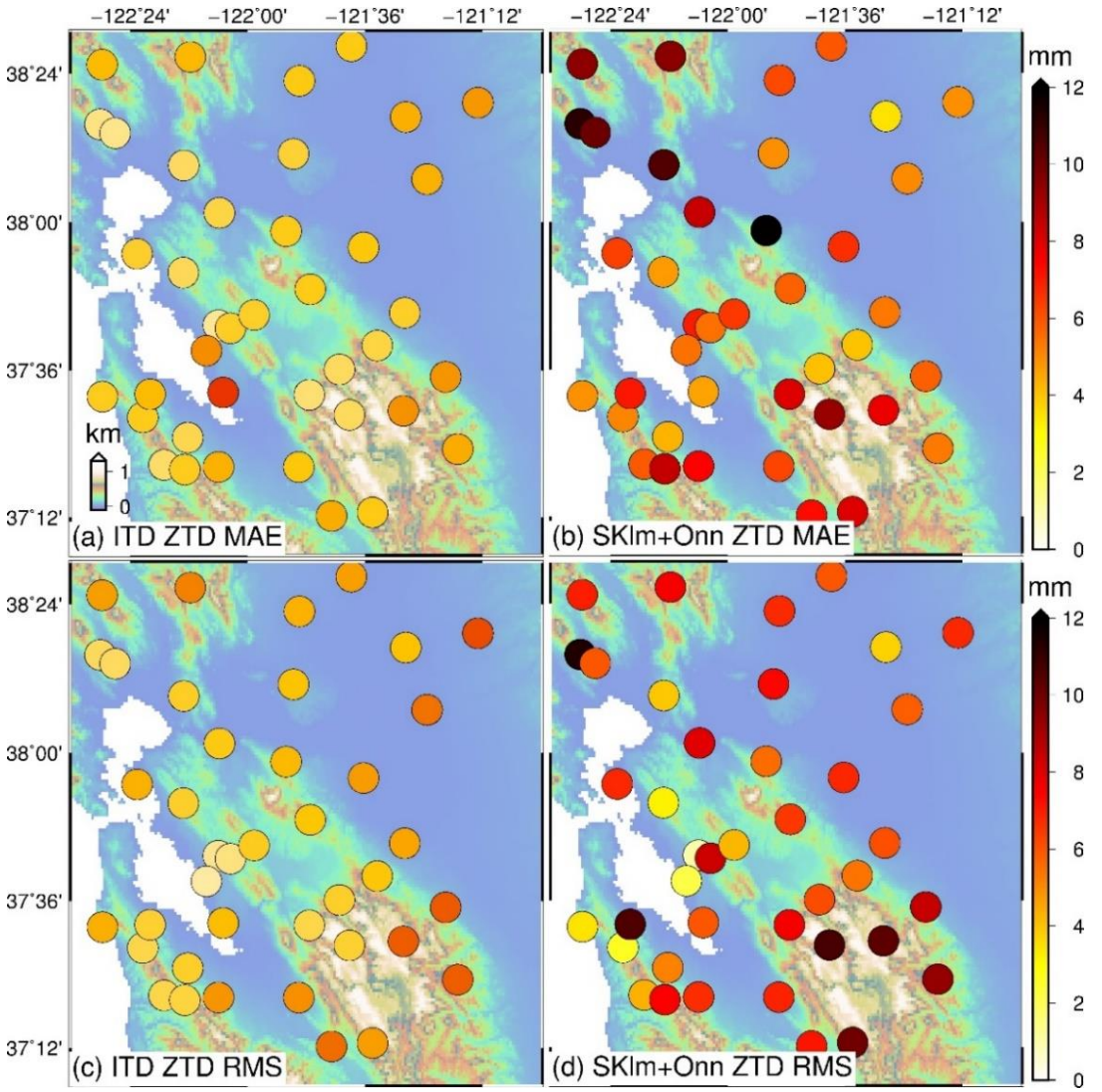

Figure 3.5 Spatial distribution of cross validation ZTD results, showing MAE and RMS of daily (14:00 local time) differences of interpolated versus RTPPP ZTDs, computed over all of 2015 per GPS station. (a) MAE using ITD, with an overall mean of 3.6 mm; (b) MAE using SKlm+Onn, with overall mean of 6.1 mm; (c) RMS using ITD, with an overall RMS of 4.6 mm; (d) RMS using SKlm+Onn, with an overall RMS of 8.4 mm.

Cross comparisons of the daily interpolated ZTD values are shown in Figure 3.4 for both the ITD and SKlm+Onn interpolation models, for all 41 stations for all of 2015. As for the time

series, substantial reductions in the scatter is observed for ITD compared with SKlm+Onn, i.e. the RMS difference decreases from 8.4 mm to 4.6 mm. Improved correlations and linear fits are also obtained with ITD compared with SKlm+Onn. Furthermore, the proportion of differences under (magnitude) 10 mm increases from 61% for SKlm+Onn to 89% for ITD, and increases from 32% to 69% for the proportion under 5 mm magnitude.

When considered for all stations for the entire year, the ITD interpolation model has been shown to substantially improve on the SKlm+Onn model. However, in the cross validation, some large differences occurred (more than 2 cm magnitude for both models), which suggests that the interpolation result is influenced by the GPS reference station distribution. To investigate this, the annual MAE and RMS differences per station are plotted in Figure 3.5, for both the ITD and SKlm+Onn models. It can be seen that the smaller MAE and RMS differences occur where the station coverage is denser, but the SKlm+Onn MAE and RMS values show substantial degradation compared with ITD in the north-west of the region where there are fewer stations, e.g., ~12 mm MAE for SKlm+Onn compared with ~5 mm for ITD. Meanwhile, the largest RMS value for any station is only ~8 mm for ITD, improved from ~12 mm for SKlm+Onn (Table 3.1). In terms of terrain effects on the MAE and RMS, for the ITD model, stations in the mountainous areas show approximately comparable precision with those at lower altitudes, whereas with SKlm+Onn larger MAE and RMSs arise, and the same applies in coastal areas. This is mainly attributed to the variability of the turbulent component and the coupling effect of the turbulent and elevation dependent components.

In conclusion, fewer gross errors are observed in Figure 3.4a than Figure 3.4b, revealing that outliers in GPS estimates or strong and irregular turbulent signals could impact the interpolation results. One immediate benefit of ITD is its robust estimation capability through iterations even with relatively low quality real-time data and/or variable tropospheric environments. Another essential benefit is to separate medium to long wavelength turbulent signals from others, which in turn makes it efficient to determine stratified delays using regression analysis. In other words, ITD can better handle stratified signals as well as the medium to long wavelength turbulent signals, and hence produces lower RMS values, especially in the winter and spring seasons

dominated by medium and long wavelength turbulent signals (Figure 3.3). This is particularly useful in areas with strong topography variations, illustrated here by the big improvements in Figure 3.5 across mountain areas.

3.3.2 Validation of the interpolated PWV maps with MODIS water vapour products

To provide further validation of the ITD interpolation model and its improvement over the SKlm+Onn model, including a detailed spatial resolution assessment, and to provide an accuracy assessment with an independent data set, the RTPPP GPS pointwise ZTD values at the MODIS acquisition time (19:00 UTC) were converted to PWV, interpolated to 1 km pixels across the entire study region and compared with the MODIS near-IR PWV product. Pressure and temperature data at 5-minute temporal resolution from co-located meteorological sensors were available at four of the 41 GPS stations and obtained from unavco.org. These were supplemented by 10 meteorological stations which were located up to 10 km outside the study region. The meteorological data were first interpolated to all 41 stations using the Li et al. (2003) differential models and, according to their cross tests, the resulting pressure and temperature errors should be less than 1 hPa and 2 K, respectively. The interpolated pressure measurements at each GPS station were used to directly compute ZHD using the Saastamoinen (1972) model and subtracted from the RTPPP ZTD estimates, with the resulting ZWD pointwise values converted to PWV using the Bevis et al. (1992) model, inputting the interpolated surface temperature measurements. To enable the comparisons, 1 year of MODIS Level 2 data from the Terra satellite were obtained across the study region, providing one PWV map at the Terra orbit track time of each day (during daytime, about 10:30 local time). The Level 2 data were generated at the 1-km spatial resolution of the MODIS instrument using the near-IR algorithm (Gao and Kaufman, 2003). About 30% of days had severe cloud conditions so we excluded them as only a few grids can be obtained. Areas with cloud conditions or above water were also masked and only the cloud free land areas were used in the comparison.

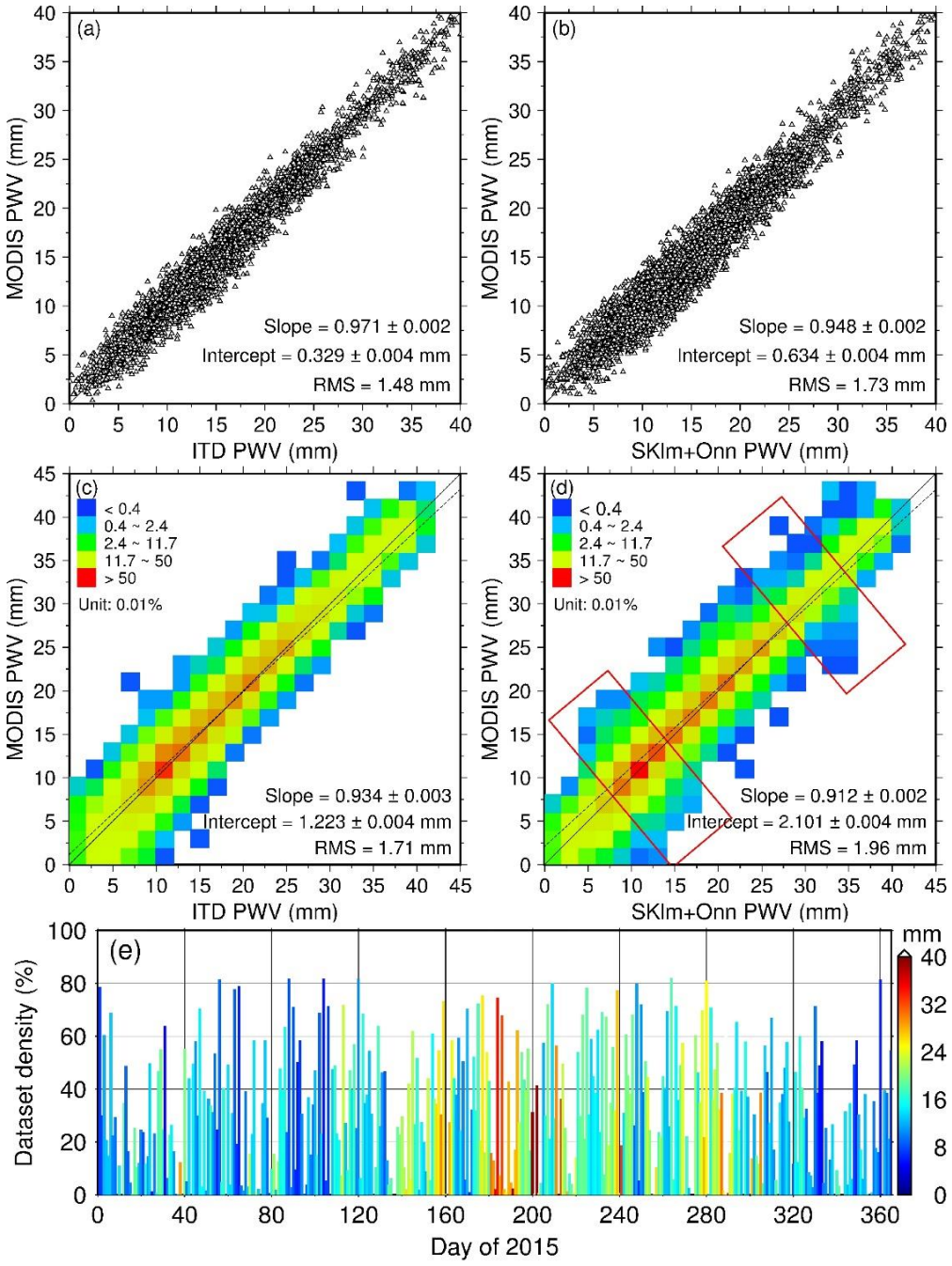

Figure 3.6 Cross validation of (a) ITD and (b) SKlm+Onn interpolated RTPPP GPS PWV with MODIS, using daily values at MODIS acquisition time on all 41 GPS stations for all of 2015. (c) and (d) displays all the available pixels between MODIS PWV and ITD/SKlm+Onn PWV maps for year 2015. The colour scale represents the density of occurrence. The daily cloud free MODIS PWV pixel density is displayed by (e) in which the vertical bar represents the total available pixel numbers divided by the maximum amount. The colour scale represents the average daily PWV of all available pixels.

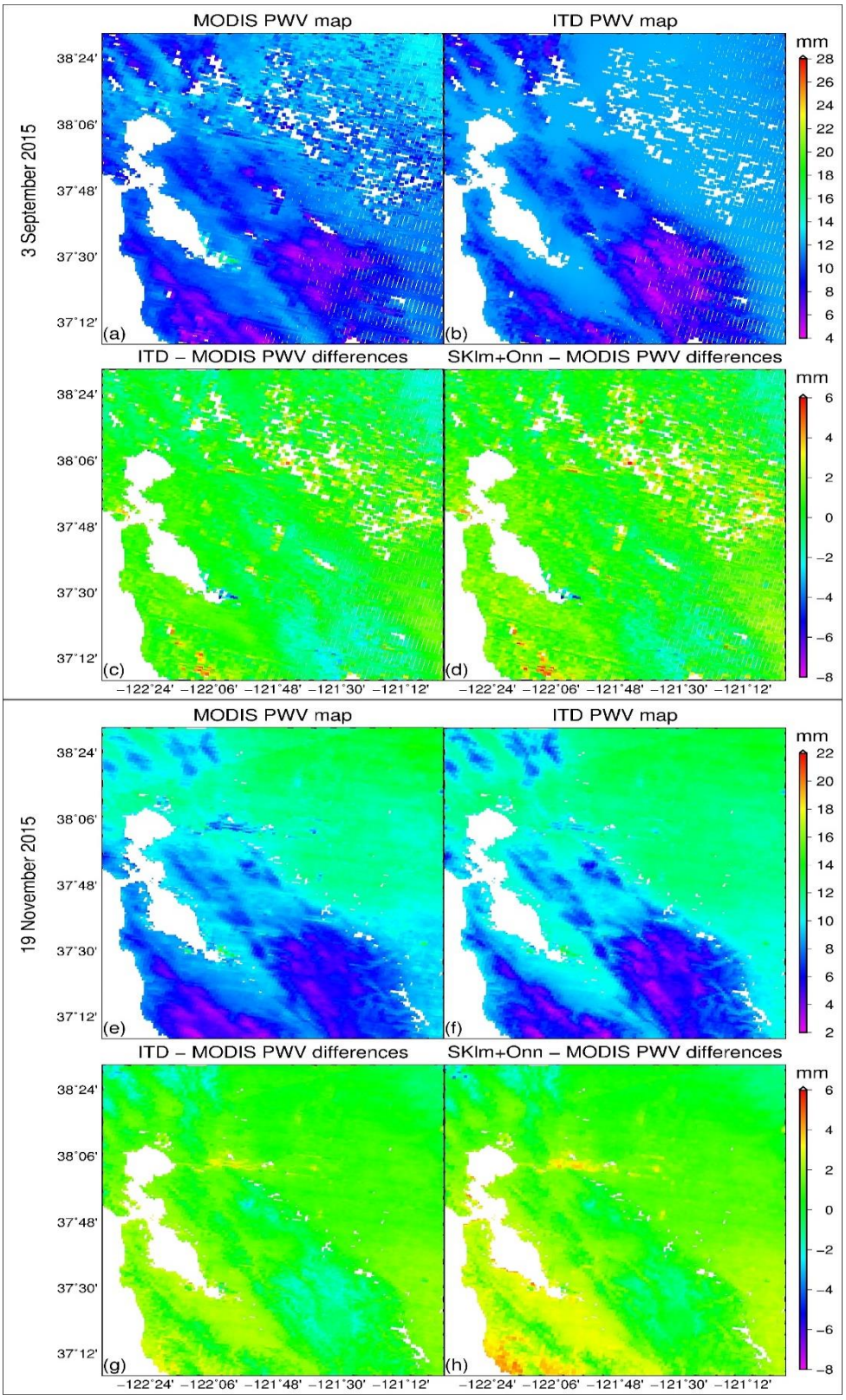

Figure 3.7 MODIS PWV and ITD RTPPP GPS PWV maps and RTPPP GPS minus MODIS PWV difference maps at 1 km spatial resolution, for both ITD and SKlm+Onn interpolations. (a,b,c,d) are for 3 September 2015 and (e,f,g,h) for 19 November 2015. (a) and (e) are MODIS maps, (b) and (f) are ITD maps, (c) and (g) are ITD difference maps, (d) and (h) are SKlm+Onn difference maps. The large differences (red pixels) in the north east of (c) and (d) are likely due to the presence of thin clouds which are not labelled in the cloud mask product.

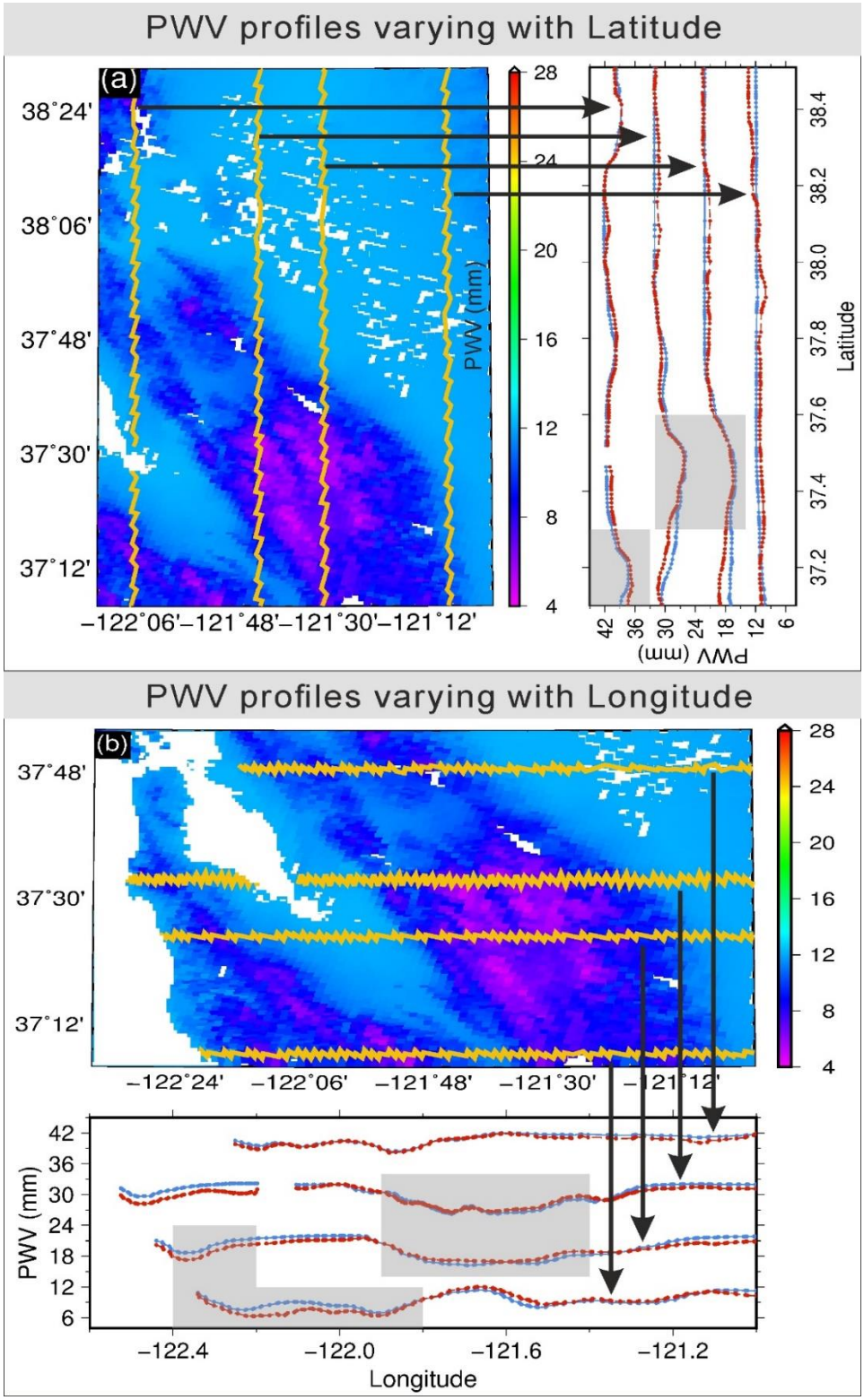

Figure 3.8 ITD RTPPP map and MODIS PWV (red line) and ITD RTPPP PWV (blue line) profiles along certain latitudes and longitudes, after shifting a constant number, for 3 September 2015. The PWV profile series are in the same order as the line segments in the PWV map, and are averaged by a tenth average window. The gray polygon areas represent the mountain area. The overall RMS difference between MODIS and ITD PWV along the eight profiles is 1.51 mm and the RMS difference for the mountainous (gray polygon) and flat areas are 1.57 mm and 1.47 mm, respectively.

As the first step, cross validation was carried out at each GPS reference station, using one GPS PWV value per day per station, taken at the MODIS acquisition time. We used MODIS PWV as 'truth' values to validate the interpolated PWV at each GPS station (cross test), and the MODIS PWV values were averaged over boxes of 3 × 3 pixels centred on the GPS station's location if the centred pixel was missing. PWV cross comparisons for all daily values available for each GPS station for the whole of 2015 are shown in Figure 3.6, with the RMS of the differences being 1.48 mm for the ITD model and 1.73 mm for SKlm+Onn, as also listed in Table 3.1. The ITD model also results in a better linear regression fit, with a slope of 0.97 and intercept of 0.33 mm compared with respective values of 0.95 and 0.63 mm with the SKlm+Onn model, and the correlation coefficient increased from 0.97 to 0.98. The height scaling model works under the assumption that the turbulent delays are small and of short-wavelength compared with stratified delays, therefore the height scaling would be easily biased when strong tropospheric turbulence with medium-to-long wavelength signals occurred. In Figure 3.3 a clear improvement of ITD against SKlm+Onn, in terms of both mean and RMS differences, can be observed in cold seasons (between late autumn and early spring). Similarly, substantial improvements can be observed in mountainous areas (Figure 3.5). Figures 3.6a and 3.6b also suggest that when PWV values are low (e.g., 0-10 mm), the improvements of ITD are greater. This is because ITD takes into account the turbulence effects which in turn benefit to estimate the height scaling and separate the topography-dependent and turbulent components.

The interpolated RTPPP PWV values and resulting maps were then compared spatially with the MODIS PWV maps, with the results (RTPPP GPS minus MODIS) shown in Figure 3.7 for MODIS images acquired on 3 September and 19 November 2015, chosen as they are sample days which are virtually free from cloud conditions across the whole study region. The height for each grid cell was resampled by the 30 m Shuttle Radar Topography Mission DEM. Some large differences are visually apparent, mostly across the areas with frequent cloud masks and near San Francisco Bay, but MODIS PWVs above water areas also involve a different retrieval algorithm compared to those above the land, resulting in differences and discontinuities at the land edge. Furthermore, any values over water areas have been removed since PWVs above water (bay, lake or ocean) share different characteristics from PWVs over land areas which

cannot be well-described by the interpolation model (Sobrino et al., 2003). On average, the mountainous areas give more negative differences than flat terrain, showing that MODIS tends to overestimate PWV compared with GPS with increasing altitude (i.e. small PWV values), as previously found by Li et al. (2003). It can also be seen in Figure 3.7 that edge areas with fewer GPS stations produce larger differences than central areas, confirming as discussed in Section 3.3.1 that improved GPS station coverage will improve the quality of interpolated PWV maps. The ITD model produces smoother difference maps than SKlm+Onn and has a lower percentage of large differences. ITD also performs much better than SKlm+Onn in coastal areas where the PWV is more changeable and gives more complicated turbulent components.

Table 3.1 Summary of ITD and SKlm+Onn Model Interpolation Performance from Cross Validation of all ZTDs and all Common Epoch RTPPP and MODIS PWVs for all of 2015.

X[1]	Y[1]	No. Data Points	Slope[2]	Intercept[2]	Correl. Coeff.	RMS (mm)
ITD ZTD	RTPPP ZTD	14883	1.012 ± 0.002	0.004 ± 0.003 m	0.99	4.6
SKlm+Onn ZTD	RTPPP ZTD	14883	1.025 ± 0.002	0.026 ± 0.003 m	0.98	8.4
ITD PWV	MODIS PWV[3]	8523	0.971 ± 0.002	0.329 ± 0.004 mm	0.98	1.48
SKlm+Onn PWV	MODIS PWV	8523	0.948 ± 0.002	0.634 ± 0.004 mm	0.97	1.73
ITD Map	MODIS Map[4]	288 million	0.934 ± 0.003	1.223 ± 0.004 mm	0.97	1.71
SKlm+Onn Map	MODIS Map	288 million	0.912 ± 0.002	2.101 ± 0.004 mm	0.96	1.96

[1]The linear model is Y = Slope * X + Intercept
[2]Uncertainties are 95% confidence
[3]MODIS PWV pixels with co-locate GPS stations for year 2015
[4]All available MODIS pixels

Figure 3.6c and 3.6d display the correlation statistics between all MODIS and ITD/SKlm+Onn PWV maps in 3D view for all available pixels. The colour scale represents the density of occurrences. Pixels outside the GPS station coverage (i.e. the edge area) were excluded as the performance would decrease after extrapolating. Overall, most PWV pairs are located along the 1:1 line, implying a good correlation between the GPS based PWV and MODIS PWV maps. The SKlm+Onn map exhibits greater differences compared to the ITD PWV map and the scatters were distributed more unsymmetrically (red rectangle) especially for when PWV

amounts fell between 5-15 mm and 30-35 mm.

To illustrate the finer spatial detail of PWV and the performance of interpolated RTPPP PWV, in Figure 3.8 we plot ITD-based PWVs over mountainous areas, shown as (a) from 37º 09’ to 38º 30’ in latitude and -122º 12’ to -121º 00’ in longitude, and (b) from 37º 09’ to 37º 50’ in latitude and -122º 30’ to -121º 00’ in longitude, for 3 September 2015. In Figure 3.8 we include PWV profiles (smoothed using a tenth averaging window) for both ITD RTPPP and MODIS along lines of constant latitude and longitude, over both mountainous and flat areas, which enable detailed comparisons of the ITD PWV gradients with respect to topography. The ITD PWV profiles change in a similar tendency with MODIS and share similar gradients. The overall RMS difference between MODIS and ITD PWV for the eight profiles considered is 1.51 mm and the RMS differences for mountain (gray polygon in Figure 3.8) and flat areas are 1.57 mm and 1.47 mm, respectively. These agreements demonstrate that the ITD model is capable of retrieving detailed water vapour distributions over a wide region, thereby showing its potential application for monitoring local extreme weather events.

3.4 Discussion on Tropospheric Turbulence

The principal aim of the ITD model is to separate the elevation dependent ZTD/PWV component from the turbulent component, which is the most variable and uncertain part, and can easily bias the vertical ZTD scaling, making the separation of the two components challenging. Due to the constraints of the density of GPS stations, only medium-to-long wavelength turbulent signals are expected to be successfully modelled using ITD. To illustrate the size and variation of the turbulent component, and the importance of iterating the solution until convergence arises, a sample three GPS stations were considered: P177, P230 and S300 (Figure 3.1), which are in different parts of the study region, are at different elevations, and are at varying distances from the nearest other GPS reference stations. P177 is near the ocean, whilst S300 and P230 are in mountainous areas with elevations of ~500m and ~700m, respectively. Three epochs, from different seasons (spring, summer and autumn) were considered, and the variation of the turbulent component and its convergence with the number

of iterations is illustrated in Figure 3.9.

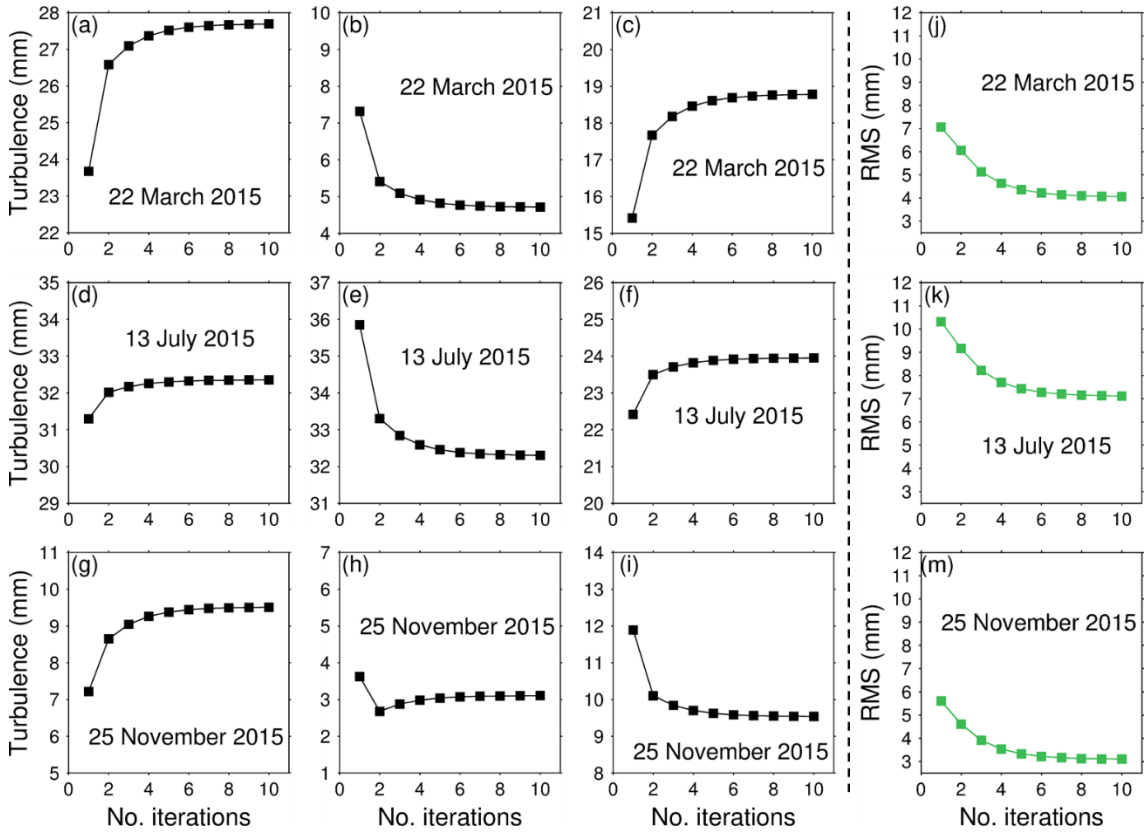

Figure 3.9 RTPPP ZTD turbulent component separated by ITD at each iteration step. The first, second and third columns represent stations P177, P230 and S300, respectively, and the fourth column represents the ZTD cross validation RMS difference for all 41 stations on the corresponding day. Shown for sample days in each of spring, summer and autumn.

It is clear from Figure 3.9 that the turbulent ZTD component can reach several centimetres and can be efficiently separated from the elevation dependent component. Although the first iteration enables the majority of the turbulent component to be determined, the subsequent iterations are needed for robust estimation. The far righthand column in Figure 3.9 further indicates the performance improvement with increasing number of iterations, with the RMS difference (computed through the RTPPP ZTD cross validation from all 41 stations at the corresponding epoch of each row) becoming smaller and tending towards convergence. Around six iterations are typically needed for convergence, after which sub-millimetre RMS changes arise.

As the most important feature of the ITD model, the convergence tendency in Figure 3.9 reveals that the turbulence effect can be reduced by separating the stratified and turbulent components

through iteration. The decoupling procedure acts very similarly to robust estimation, in which the ZTDs from stations exhibiting strong turbulence will contribute less in height scaling but account for more in the turbulent delay interpolation. In this way, the systematic patterns of turbulence resulting from local weather conditions or topography (Betts et al., 2007; Cho et al., 2003) can be better modelled. The iteration also allows for the detection of ZTD outliers, which is a not uncommon occurrence in real-time PPP due to the unpredictable behaviour of the satellite clocks. Consequently, the ITD model enables both fitting of the tropospheric vertical profiles and also models the turbulence processes. As the fourth column in Figure 3.9 suggests, successfully accounting for this results in the overall RMS difference of the cross validation test reducing and converging.

3.5 Summary

In this chapter, an iterative tropospheric decomposition model has been developed to interpolate pointwise GPS ZTDs and to generate high-resolution water vapour maps, without any data differencing. For a California study region of around 150 km x 150 km, the approach of decoupling the terrain elevation dependency and the tropospheric turbulence contribution to ZTD in an iterative procedure (typically 4-6 iterations were required) led to improved accuracy interpolated tropospheric water vapour maps over those based on previous studies, such as the tropospheric turbulence and elevation dependent model SKlm+Onn of Xu et al. (2011). To be applicable to not only post-processed SAR atmospheric corrections, i.e. to also facilitate SAR for rapid response to monitoring earthquakes and volcanoes, network RTK positioning and meteorological forecasting, we used real-time mode PPP GPS ZTD values estimated every 5 minutes (which were validated with post-processed GIPSY ZTDs with an overall RMS difference of 12.5 mm for all 41 stations for all of 2015) to generate the tropospheric maps. Cross validation of the GPS ZTD values resulted in 4.6 mm RMS differences using the ITD model compared with 8.4 mm using the SKlm+Onn model, using one value per station per day (14:00 local time) for all of 2015. Whereas the SKlm+Onn interpolation model has degraded performance over mountainous areas, the cross validation ITD model RMS and mean differences are similar for both mountainous and flatter terrain, and also similar for both coastal and inland areas. The cross validation improvements using ITD are smallest in the summer

months. Spatially, we generated PWV values for 1 km pixels for all land-covered parts of the region and compared with daily MODIS PWV near-IR product values, with the RMS difference for the year being improved from 1.73 mm using the SKlm+Onn model to 1.48 mm using ITD. Furthermore, the spatial PWV gradients using the ITD model and MODIS across a variety of topography were nearly identical to each other. The overall RMS difference between MODIS and ITD PWV profiles is 1.51 mm and the RMS differences for mountainous and flat areas are 1.57 mm and 1.47 mm, respectively. Hence the ITD PWV fields are also able to reveal detailed water vapour information over varying terrains.

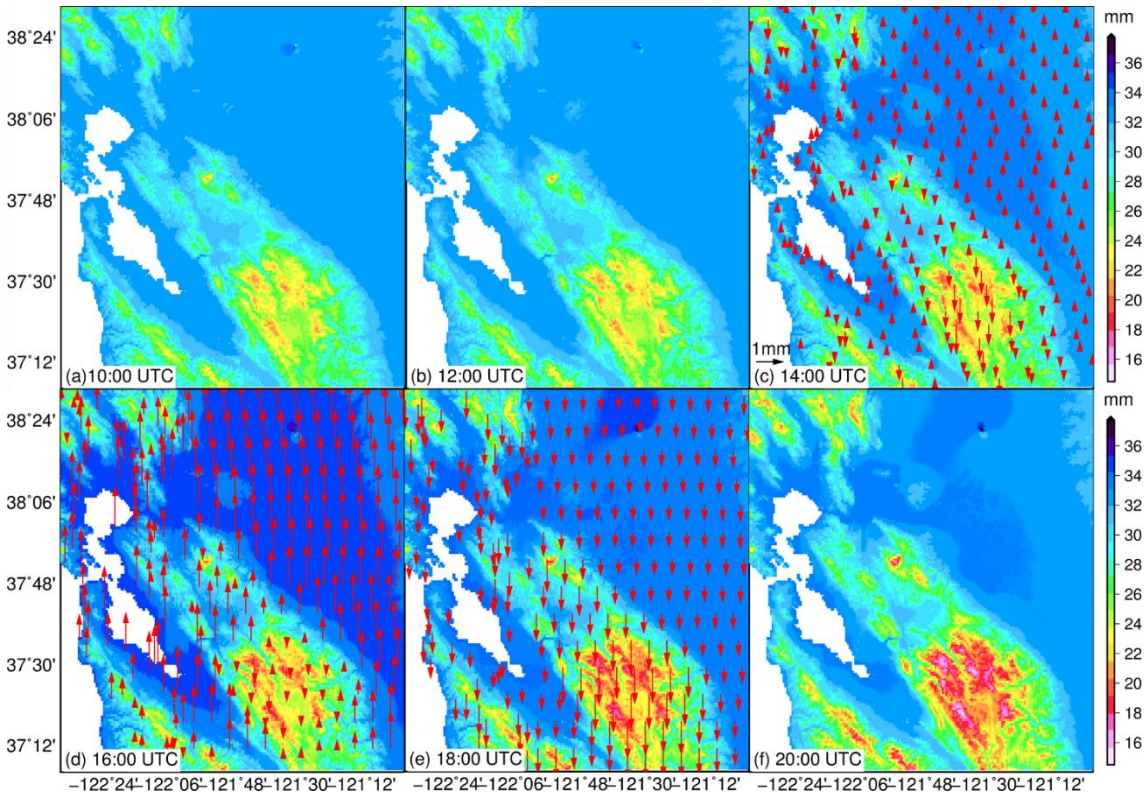

Figure 3.10 RTPPP PWV fields across the California study region every 2 hours on 2 November 2015 during a rainfall process from (a) 10:00 to (f) 20:00 UTC. Arrows represent PWV increasing (upwards) or decreasing (downwards) during the preceding 2 hours.

To provide an indication of the potential of the real-time mode ITD model interpolated tropospheric maps for meteorological and geodetic applications, including revealing detailed information of local weather processes, we show in Figure 3.10 the detailed 2-hourly PWV information during a rainfall process over the study region on 2 November 2015 (10 am to 8 pm UTC). Arrows represent the PWV increasing (upwards) or decreasing (downwards) during each preceding two hours. One important fact is that the PWV over mountainous areas

decreased during the whole rainfall process, but other areas experienced increasing and decreasing PWV before and after the rainfall, respectively. We do not explain the patterns further as the focus of this chapter is on showing the quality of RTPPP ZTD and PWV maps.

The generated spatially-dense PWV fields with continuous, high (5 minute) temporal resolution are not only suitable for correcting atmospheric effects in SAR images at the instant of acquisition, but they also will ensure the identification of water vapour variation from ground motion between image acquisition times (Foster et al., 2006). What is more, the high performance of the dense PWV maps using the ITD model is especially useful for mitigating the effects of water vapour for SAR measurements in mountainous areas, which usually suffer from vertical stratification and turbulent mixing due to the orography (Wadge et al., 2002).

Chapter 4. GPS Based InSAR Atmospheric Correction Model

The growing number of continuous GPS networks in different regions/countries with increasing densities, although still variable from place to place, has inspired and facilitated the utilization of GPS for InSAR atmospheric correction. Chapter 3 has provided a method for generating high-resolution atmospheric delay maps from these pointwise GPS data. In this chapter, we evaluate this method by applying it to reduce atmospheric effects on radar measurements, addressing also the impact of station spacing on the model performance. This GPS-based atmospheric correction model produces high temporal resolution (5 minute) atmospheric correction maps and can be used routinely in a systematic, automatic way.

4.1 Atmospheric Effects Modelling for Repeat-pass InSAR

The atmospheric effects in repeat-pass InSAR derived surface displacements are, in dimensions of length, caused by the relative tropospheric delay occurring between two image acquisitions (see Equation 2.7). Hence GPS-based tropospheric corrections should be provided as high spatial resolution maps of LOS relative delays to enable pixel by pixel correction. This is obtained by interpolating pointwise relative ZTDs (differenced per GPS station between image acquisitions) from the continuously operating GPS stations across and around the area of the interferogram, then mapping to LOS. The ITD model proposed in Chapter 3 for the interpolation of undifferenced ZTDs is used and validated for the interpolation of relative ZTDs, including the separation of the stratified and turbulent components.

4.1.1 Interpolation of the differenced GPS ZTD

The ITD model considers the relative ZTD between image pair *i* and *j* at pixel *k* with coordinate vector **x** to be represented as:

$$\Delta L_{ij}^{k} = S(h_k) + T(\mathbf{x}_k) + \varepsilon \qquad \text{(Equation 4.1)}$$

where S represents the stratified component correlated with height h, T represents the turbulent component and ε is the unmodeled residual. The stratified component in Equation 4.1 can be fitted with a modified exponential height scaling function as in Equation 3.3.

The main procedure of ITD is to iteratively estimate the height scaling function and find the optimal exponential coefficients. The turbulent part is horizontally interpolated and then removed from the total delay. In order to apply the ITD model to InSAR atmospheric correction, we apply a constant value to the relative ZTDs input, and then map to LOS using a tropospheric mapping function. The constant applied will not affect the final result after shifting back but provides the advantage of avoiding negative values in the exponential function regression. We must also consider which GPS reference stations ZTD values are needed in order to interpolate to the pixel of interest. This depends on the network density, i.e. for a dense network a smaller distance is used, however, for a sparse network, a larger distance is used to ensure that more stations are employed. While Chapter 3 used a maximum distance of 100 km, this was for a dense California network, but as we need to consider both dense and sparse networks, we use a maximum distance of 200 km from the particular pixel here. This ensures sufficient stations in the sparse network are included, but not those that would be completely uncorrelated with the user station.

4.1.2 Cross validation of interpolated differenced GPS ZTDs

To assess the capability of the ITD model for handling relative ZTDs, a cross validation was applied to the ITD interpolated values from two different GPS networks. The first is a subset of the PBO network, selecting the Southern California region (32º 40′ to 34º 40′ N, 116 to 119º W) of around 250 x 250 km, i.e. about the size of a Sentinel-1A image. It comprises 294 continuous GPS (CGPS) stations, thus providing a very dense network with a station spacing of typically 10-20 km, exhibits large topography variations (from sea level to 3500 m) and experiences a variety of weather/climate conditions in winter and summer seasons. The second is a relatively sparse network, comprising all (up to 141) stations from the UK British Isles continuous GNSS Facility (BIGF: www.bigf.ac.uk) network, which has a typical station spacing of 50-100 km and is more representative of the CGPS station spacing in many countries than the dense Southern California spacing. It also exhibits only limited topography variations (from sea level to 1300 m, but with median elevation only 120 m), and is a cooler atmosphere that can hold less water vapour than Southern California.

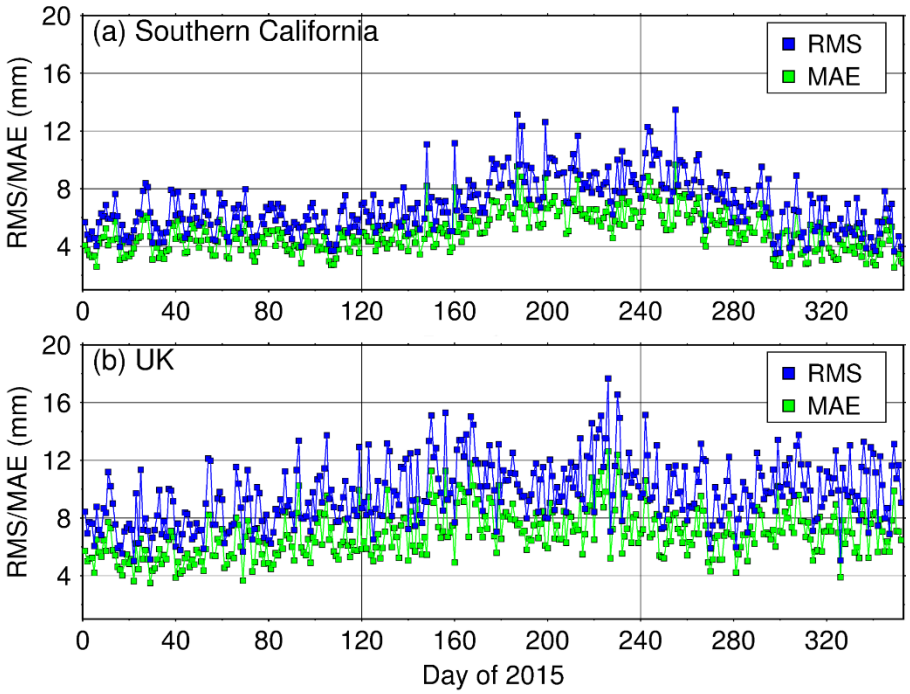

Figure 4.1 Daily RMS (blue) and MAE (green) of the 12-day ITD model interpolated relative ZTDs in 2015 compared with the actual relative ZTDs. (a) Southern California GPS network. (b) UK GPS network. The horizontal axis represents the first day that the ZTD is differenced, i.e. day 1 represents the relative ZTD between days 1 and 13.

All available GPS data from the stations of the Southern California and UK networks for all of 2015 were processed separately per day using the PANDA software package (Liu and Ge, 2003) in Precise Point Positioning mode, with JPL 'repro2' satellite orbits and 30 second clocks, obtained through the IGS, held fixed. A least squares adjustment was used for the daily parameter estimation, which comprised constant (float) ambiguities, one set of station coordinates, receiver clocks (estimated as a white noise parameter), and the tropospheric ZWD estimated per 5 minutes epoch as a random walk parameter with a process noise of 5.0e-8 $km/s^{1/2}$, as well as east-west and north-south tropospheric gradients. We used the ionospherically-free carrier phase and pseudorange observables, employed the Global Mapping Function (GMF: Boehm et al. (2006)), applied models for satellite and receiver antenna phase centre models (from the IGS), Earth tide (McCarthy, 1996), ocean tide loading (FES2004, from http://holt.oso.chalmers.se/loading), phase wind up (Beyerle, 2009), relativistic effects and pseudorange Differential Calibration Delays (Kouba, 2009).

All PANDA-derived GPS ZTDs at 14:00 local time per day were firstly differenced by every 12 days (i.e. between days 1 and 13, 2 and 14, 3 and 15, etc.) in year 2015. We chose 12-day

ZTD time differencing to match the repeat cycles of Sentinel-1A, and 14:00 local time provided daily estimates sampled when tropospheric activity and water vapour content was typically greatest. These relative ZTDs were then used for cross validation, repeating for all sampled points, i.e. all stations from both the Southern California and UK networks for the whole of 2015.

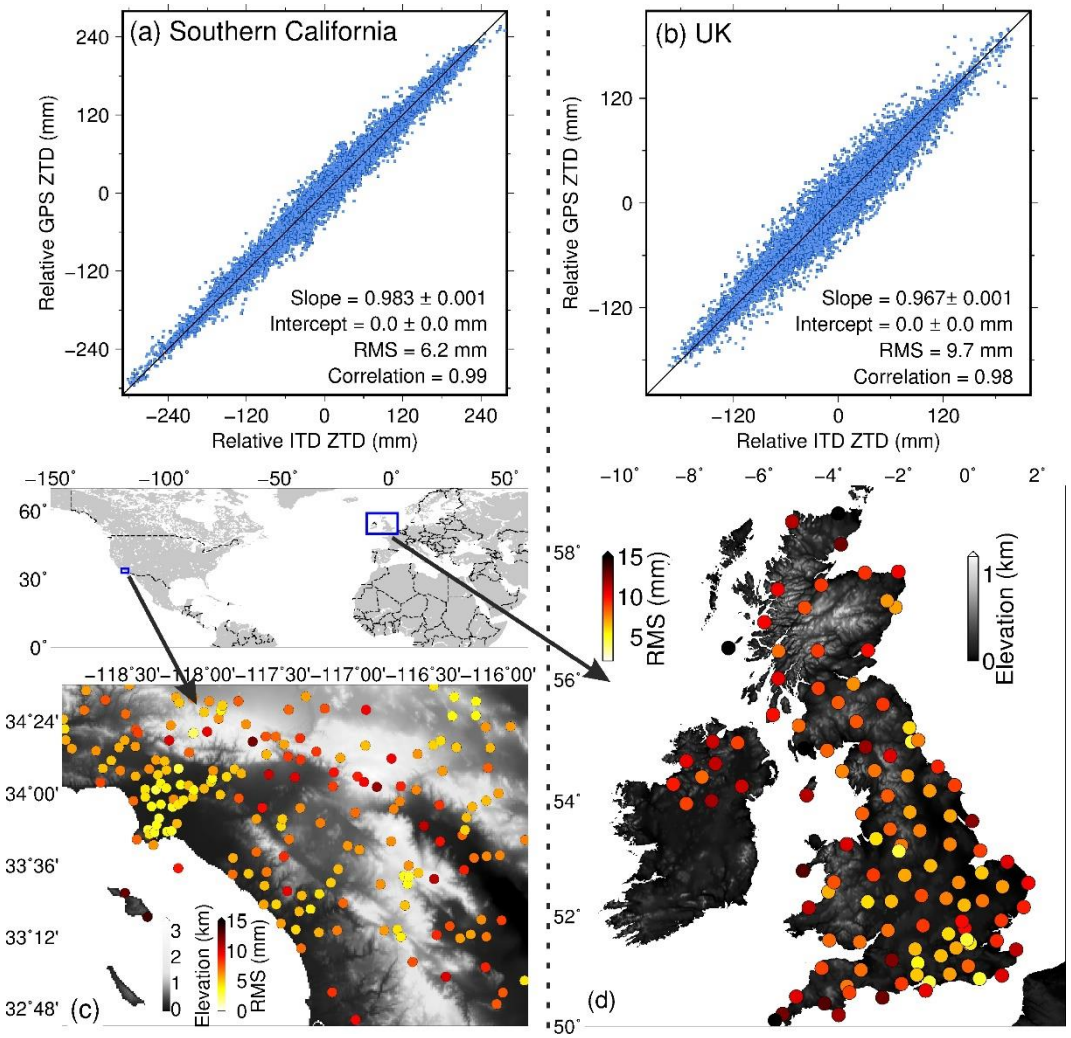

Figure 4.2 Cross validation of 12-day ITD model interpolated relative ZTDs for all of 2015 for Southern California (10-20 km station spacing) and UK (50-100 km station spacing) GPS networks, compared with the actual relative ZTDs. The linear model in (a) and (b) is GPS-ZTD = Slope × (Interpolated ZTD) + Intercept. (c) and (d) show the average RMS errors for all of 2015 per station. Note the different map scales.

The difference between the interpolated and actual 12-day relative ZTDs was computed per station for each of the two GPS networks at 14:00 local time on each day, and the RMS and MAE computed per network per day. These cross validation results, for the whole of 2015, are shown in Figure 4.1. For the Southern California network, 94% of the RMS values and 99% of

the MAE values are below 1 cm, indicating a high performance of the ITD model interpolator. The overall mean RMS and MAE are 6.9 mm and 5.2 mm, respectively. The ITD model performed better in colder seasons (i.e. between days 0 to 160 and 280 to 365), which we attribute to medium-to-long wavelength and elevation-dependent signals dominating and which were effectively modelled. However, the RMS/MAE are fairly high between day 160 and 280, i.e. the summer months of June to September when the water vapour content is high, implying that the short-wavelength water vapour effects were large and variable during this period and cannot be fully mitigated by the ITD model. It can be seen from Figure 4.1 that the performance was slightly lower in the UK compared with Southern California because of its greater station spacing. 60% of the RMS values and 95% of the MAE values are below 1 cm and the overall RMS and MAE values are 9.7 mm and 6.9 mm, respectively. These results are however still promising for InSAR atmospheric correction which typically aims for (sub-) cm-level precision (Li et al., 2006a; Onn and Zebker, 2006). The seasonal signal was not as substantial for the UK as for Southern California due to different climate features, for example, the precipitation in the UK is nearly stationary during the year whilst the water vapour content in summer is typically 2~3 times higher than winter in Southern California.

The ITD model interpolation performance was also assessed using a correlation analysis between the interpolated relative ZTDs and the original values, which are plotted for all stations for 14:00 local time for all of 2015 in Figure 4.2. The overall cross validation RMS differences of the 12-day relative ZTDs is only 6.2 mm for the Southern California network and 9.7 mm for the UK network. The slopes are close to one with an intercept of zero for both networks, implying that there is no substantial deviation after interpolation. Figures 4.2c and 4.2d show the RMS distribution of ITD model interpolated relative ZTD of each station for both networks. One clear pattern is that more precise interpolated relative ZTDs are generated in areas with a denser station distribution. In terms of terrain effects on the RMS difference, stations in mountainous areas show approximately comparable precision with those in flat areas, indicating that the performance of the ITD model is nearly independent of height for these networks. The different performance between Southern California and the UK provides an indication of the impact of station distribution as well as the different climate conditions on the

ITD model's performance.

4.2 Validation of GPS Derived Atmospheric Correction Map

In order to evaluate the suitability of the GPS based ITD model for InSAR atmospheric correction, five Sentinel-1A interferograms (three over Southern California, USA, and two over Southern England, UK, see Table 4.1) were selected. We chose these interferograms to sample different climate and weather conditions in summer and winter seasons, cool and warm atmospheres, as well as different station densities and topography variations. The interferogram processing was undertaken using the GAMMA software (http://www.gamma-rs.ch), with precise orbit data from the European Space Agency (ESA) used to reduce baseline errors and assist image co-registration and flat Earth phase removal. The topographic phase contribution was removed using a 1-arcsec (~30 m) DEM from the Shuttle Radar Topography Mission (Farr et al., 2007). The interferometric pairs were processed by multi-looking operation with ten pixels in the azimuth direction and two pixels in the range direction, and then unwrapped by the branch-cut method with the coherence threshold set to 0.5 (Goldstein et al., 1988). The ITD model was utilized to generate relative ZTD maps for all the five interferograms; the relative ZTDs were projected to the LOS direction of the InSAR observations with the GMF mapping function, and then applied as the interferogram atmospheric corrections per pixel (one point every ~30 m). It should be noted that the unwrapped phase (in radians) was converted to range changes (in meters) in the LOS where a negative range change indicates the Earth's surface is moving away from the satellite (or an increase in the delay of radar propagation due to the atmosphere). Since the ITD model is able to separate stratified delays from the turbulent component, stratified delay maps were also generated to investigate the impact of tropospheric turbulence on InSAR observations.

To assess the performance of the ITD model, two metrics were used. The LOS range change standard deviation (hereafter called StdDev) across the entire interferogram was computed to assess the precision, which assumed there was negligible ground movement between the two image acquisitions (12-156 days). As a large StdDev could also result from actual ground

movements such as inter-seismic slip or ground water extraction (e.g., Argus et al., 2005), to account for this and assess the accuracy, the InSAR displacements at each GPS station location were compared with independent 3D GPS-derived displacements provided by the Nevada Geodetic Laboratory at the University of Nevada, Reno (Blewitt et al., 2016). Both InSAR and GPS-derived displacements were converted to LOS, differenced for all GPS stations in the interferogram, and the RMS displacement difference computed. Note that all stations (within the defined 200 km decorrelation range limit) from the GPS networks were used to generate the correction maps for interferograms, but only the stations located inside the interferogram were used when computing the StdDev and RMS differences. We hereafter categorise stations with displacement improvements greater than twice the RMS difference (2RMS) per corrected interferogram as substantial improvements.

Table 4.1 Sentinel-1A interferograms (denoted as IFG) used in this Chapter.

IFG	Orbit	Date 1	Date 2	Δt (days)	Location	Geographical extent
IFG1	Ascending	26/05/2015	29/10/2015	156	Southern California	32-35N, 116-119W
IFG2	Ascending	13/07/2015	25/07/2015	12	Southern California	32-35N, 116-119W
IFG3	Descending	16/12/2015	21/03/2016	96	Southern California	33-36N, 116-119W
IFG4	Ascending	30/01/2015	07/03/2015	36	Southern England	51-54N, 1-3W
IFG5	Ascending	01/01/2016	25/01/2016	24	Southern England	50-53N, 2W-2E

4.2.1 Atmospheric correction using the dense GPS network in Southern California

Figure 4.3 shows the three Southern California interferograms with and without the GPS-based ITD model atmospheric correction. IFG1, which spans a time interval of 156 days from 25 May 2015 (dry season) to 29 October 2015 (rainy season), shows in its raw form (Figure 4.3a, with no atmospheric correction) a range increase (up to 6.4 cm, i.e. the Earth surface moving towards the radar sensor) around San Bernardino National Forest, together with a range decrease (up to -4.9 cm, i.e. the Earth surface moving away the radar sensor) around Palm Desert. After correcting with the stratified delays only (Figure 4.3b) and then the ITD model total (stratified

and turbulent) delays (Figure 4.3c), both clustering features still exist, but their magnitudes decrease, with the StdDev reducing from 1.69 cm to 1.45 cm and 1.05 cm, respectively. At the GPS stations, the RMS displacement difference reduced from 1.66 cm to 1.47 cm after applying the stratified correction only, and further to 0.92 cm after applying the total delay correction, indicating that the ITD model reduced the large variances around San Bernardino National Forest and Palm Desert mainly by modelling the troposphere turbulence. 72% of stations exhibited substantial (> 2RMS) improvements after correcting with total delays compared to 57% with the correction using the stratified part only. Moreover, accounting for the tropospheric turbulence reduced the percentage of stations with deteriorated performance from 11% to 3%. Note that Sneed et al. (2014) reported that the Coachella Valley (close to Palm Desert) is subsiding due to reduced groundwater-levels, as observed both by InSAR and GPS methods, which may be associated with the remaining LOS displacement signal in the corrected map of Figure 4.3c.

IFG2 was obtained from images 12 days (one orbital period) apart in July, i.e. the summer, when the atmosphere can hold most water vapour. A prominent long wavelength signal was observed across the whole raw interferogram (Figure 4.3d), with an inhomogeneous pattern with clear gradients towards the middle of the area, and troughs around the Palm Desert and the Anza-Borrego Desert. The RMS displacement difference was 3.85 cm and the phase StdDev was 3.72 cm, indicating substantial tropospheric noise contamination. After applying the ITD model total delay (Figure 4.3f), the RMS difference reduced to 0.84 cm and the StdDev to 1.75 cm. Overall, 63% of stations exhibited RMS improvements greater than 2RMS after correcting with the total delays compared to 23% with the stratified part only. Moreover, accounting for the tropospheric turbulence reduced the percentage of stations at which deterioration arose (after applying the tropospheric corrections compared with applying none) from 14% with stratified delays only, to 2%. Unlike for IFG1, the major improvement came from the turbulent delay correction (RMS difference reduction from 3.85 cm to 0.84 cm with the total delays, but only reduced to 2.67 cm with the stratified delays) and the GPS stations which exhibited > 2RMS improvements only arose after correcting with the total delays (and not with the stratified part only), indicating that substantial atmospheric turbulence occurred during this short 12 day

time-differencing interval. These strong turbulent signals are most likely caused by conditions when the 23 July 2015 radar image was acquired, since a rainfall event was reported during 18-21 July 2015 (www.wunderground.com/).

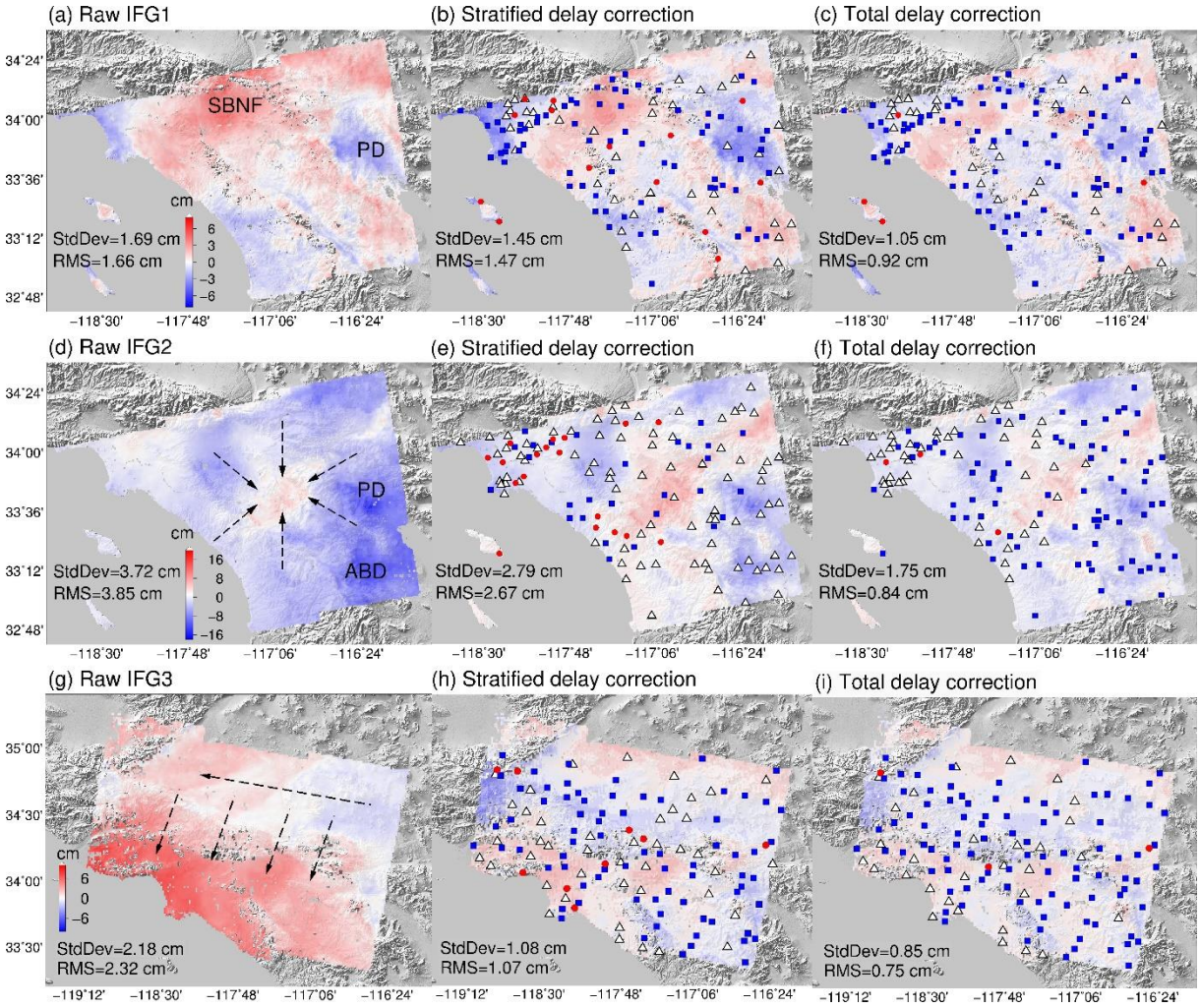

Figure 4.3 Southern California Sentinel-1A interferograms. (a, d, g) Raw; (b, e, h) corrected only by the stratified delays from the ITD model; (c, f, i) corrected by the total delays from the ITD model. SBNF: San Bernardino National Forest; PD: Palm Desert; ABD: Anza-Borrego Desert. The LOS range change StdDev and the RMS difference between GPS and InSAR displacements are listed per interferogram per tropospheric correction approach. White triangles, blue squares and red solid circles in (b, e, h) and (c, f, i) represent GPS stations with displacement improvement < 2RMS, > 2RMS, and deterioration, after correction, respectively. Note the different colour bars.

IFG3 was obtained from two images in rainy seasons with a time interval of 96 days. As can be seen from Figure 4.3g, the phase measurements exhibit a clear long wavelength pattern along the southwest to northeast direction, which is probably due to atmospheric errors considering the relatively short time span. The RMS displacement difference reduced by 68% from 2.32 cm

to 0.75 cm after correcting with the total delays and by 54% to 1.07 cm with only the stratified delays, respectively. The long wavelength pattern seen in Figure 4.3g has been mostly eliminated on correcting with only the stratified delays, but a further 14% improvement was achieved when correcting using the total delays. 74% of the GPS stations experienced greater than 2RMS displacement improvements after correcting with total delays compared with 59% on only correcting with the stratified component delays. Moreover, accounting for the troposphere turbulence reduced the percentage of stations at which deteriorations occurred from 7% to 2%. Similarly, the LOS range change StdDev was reduced from 2.18 cm for the raw interferogram, to 1.08 cm on correcting with the stratified delays only, to 0.85 cm when using the total delays, i.e. respective 50% and 61% improvements (Table 4.2).

Table 4.2 Performance of ITD model stratified and total delay atmospheric corrections on the interferograms. Unit: cm. Numbers in parentheses indicate the percentage improvement, (Raw – Corrected) / Raw.

Interferograms	**Phase StdDev**			**Displacement RMS**		
	Raw IFG	Stratified correction	Total delay correction	Raw IFG	Stratified correction	Total delay correction
IFG1	1.69	1.45 (14%)	1.05 (38%)	1.66	1.47 (11%)	0.92 (45%)
IFG2	3.72	2.79 (25%)	1.75 (53%)	3.85	2.67 (31%)	0.84 (78%)
IFG3	2.18	1.08 (50%)	0.85 (61%)	2.32	1.07 (54%)	0.75 (68%)
IFG4	2.56	1.50 (41%)	0.90 (65%)	2.72	1.79 (34%)	0.80 (71%)
IFG5	4.76	1.30 (73%)	0.98 (79%)	2.42	1.45 (40%)	0.97 (59%)
Mean	**2.98**	**1.62 (46%)**	**1.11 (63%)**	**2.59**	**1.69 (35%)**	**0.86 (67%)**

To further consider the improvement obtained for the InSAR-derived displacements at the GPS stations after applying the atmospheric corrections in all three interferograms, the differences between InSAR and GPS displacements in the LOS direction at 127 GPS stations for all three interferograms IFG1-3 are shown in Figure 4.4, with no tropospheric corrections (raw), correcting with the stratified delays only, and correcting with the total delays. The overall RMS difference between InSAR and GPS displacements improved from 3.79 cm with no atmospheric corrections, to 1.86 cm on correcting with stratified delays only, to 0.87 cm on correcting with the total delays. It can be seen from Figure 4.4 that differences of around 7 cm still arise in some instances if only the stratified delay is applied, further illustrating the need to consider and successfully correct both the stratified and turbulent components.

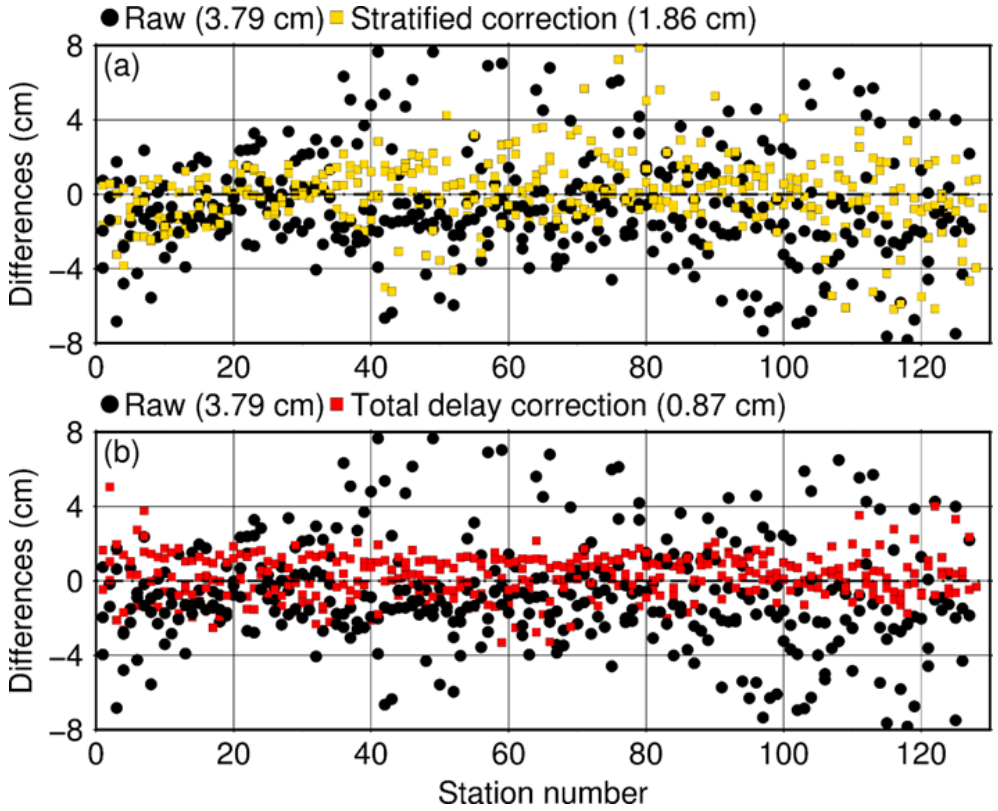

Figure 4.4 Differences between InSAR and GPS LOS displacements after ITD model atmospheric correction with (a) stratified delays and (b) total delays, respectively, collated for all three Southern California interferograms. Numbers in parentheses indicate the overall RMS differences. The horizontal axes represent the 127 stations.

4.2.2 Atmospheric correction using the sparse GPS network in Southern England

To assess whether the substantial improvements obtained on correcting the Southern California interferograms (with the dense 10-20 km GPS station spacing) are also obtained for a sparser GPS network, we applied the ITD atmospheric corrections to two Southern England interferograms, with a station spacing of 50-80 km. The maximum spacing of 80 km for this part of the UK network is slightly less than the 100 km maximum spacing that arises in some parts of the UK network. For both interferograms (IFG4 and IFG5 in Figure 4.5), the LOS range change StdDev was reduced to below 1 cm after correcting with the total delays (from a StdDev of 2.56 cm and 4.76 cm for the respective two raw interferograms, representing improvements of 65-79%), whilst applying the stratified delay corrections only led to StdDev values of 1.3-1.5 cm. Similarly, the RMS LOS displacement differences were improved from 2.72 cm and 2.42 cm (raw) to 1.79 cm and 1.45 cm respectively on applying the stratified delays only, to 0.80 cm and 0.97 cm when applying the total delays, representing improvements of about 60-70% (Table 4.2).

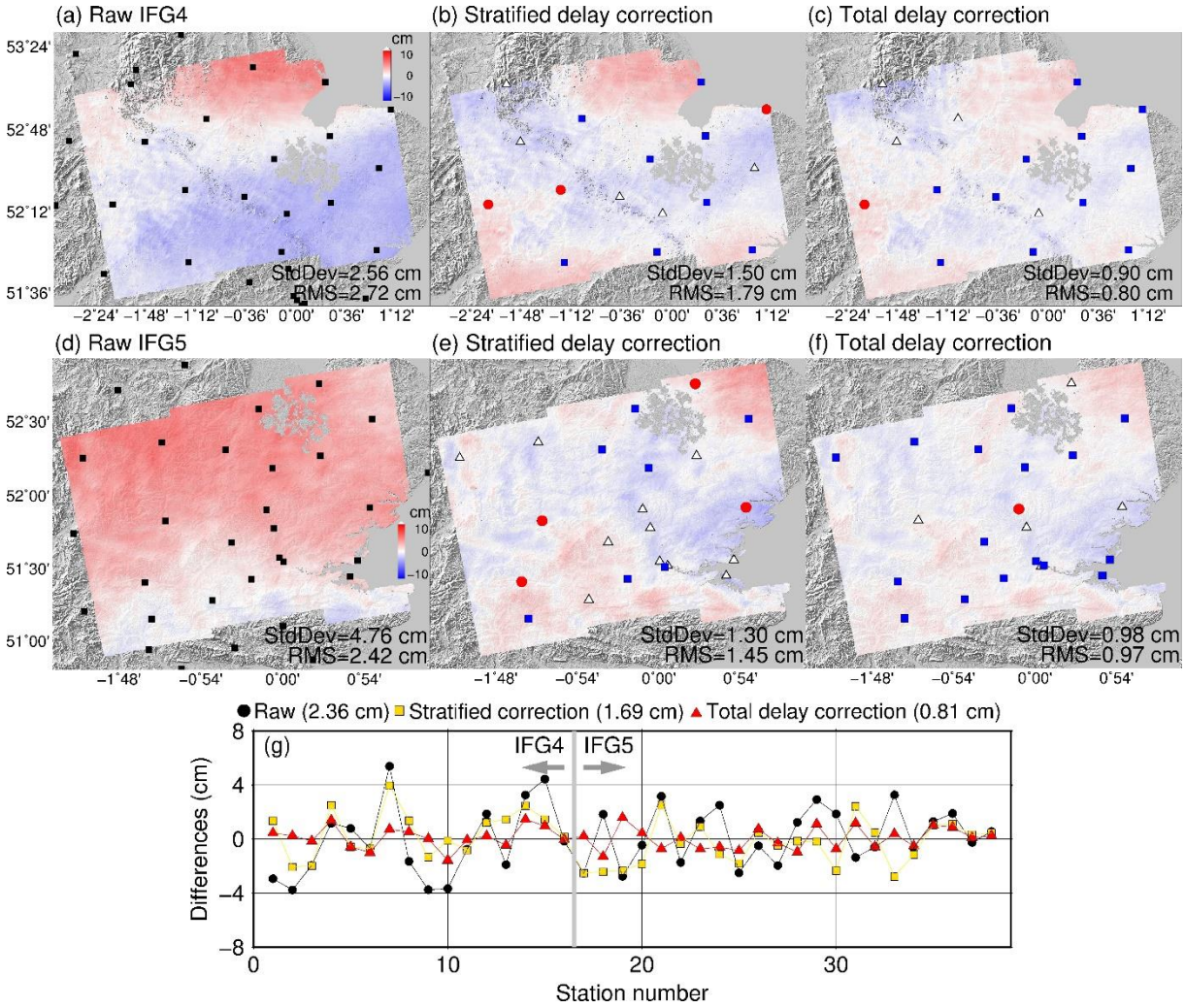

Figure 4.5 Southern England Sentinel-1A interferograms. (a, d) Raw; (b, e) corrected only by the stratified delays from the ITD model; (c, f) corrected by the total delays from the ITD model. The LOS range change StdDev and the RMS difference between GPS and InSAR displacements are listed per interferogram per tropospheric correction approach. White triangles, blue squares and red solid circles in (b, e) and (c, f) represent GPS stations with displacement improvement < 2RMS, > 2RMS, and deterioration, after correction, respectively. Note the different colour bars. (g) Collated differences for both interferograms.

The short time intervals of 24 and 36 days between the image acquisitions used for the two interferograms means that actual ground movements should be negligible, and the atmosphere-corrected maps confirm this hypothesis more strongly than the raw interferograms, as can be seen from Figure 4.5. Figure 4.5 also show that the proportion of GPS stations with more than 2RMS displacement difference improvements increases from 32% and 50% on correcting with the stratified delays only, to 73% and 69% on correcting with the total delays. Finally, the raw and corrected displacement differences are collated for both interferograms in Figure 4.5g, with the raw overall RMS displacement difference reducing from 2.36 cm to 1.69 cm and 0.81 cm

on applying the stratified delays and total delays, respectively. These statistics illustrate the capability of the ITD model to be applied to relatively sparse GPS networks, which are commonly distributed globally. The impact of GPS station density is further considered in Section 4.3.

4.2.3 Features of tropospheric turbulence

Substantial improvements to InSAR displacement maps have been obtained after applying atmospheric corrections with both dense and sparser GPS networks. In theory, a denser network can reveal topography-related tropospheric signals better and capture the turbulence features in greater detail, especially in mountainous areas. Most likely due to a lack of high-resolution ZTD maps, turbulent signals have previously commonly been considered as a random process with a Gaussian distribution and either reduced by averaging or stacking (e.g., Fruneau and Sarti, 2000; Ferretti et al., 2011) or simply ignored (Doin et al., 2009; Elliott et al., 2008). However, our experiments show that turbulent delays can exhibit non-random patterns in space and account for a large proportion (e.g., up to 72% for IFG2) of the total delays. This is especially true given the fact that the atmospheric effects on repeat-pass InSAR observations are differenced (between two image acquisitions) and part of the stratified components can be cancelled out, leaving the turbulence effects as dominant. In Section 4.2.1 and 4.2.2, we have demonstrated the presence of turbulent signals and the improvements arising to interferograms if atmospheric corrections using the total delays, not just the stratified delays, are applied. Here we further discuss the turbulent signal features and their impact on InSAR atmospheric corrections.

Figure 4.6 shows the stratified and turbulent components of relative ZTD for all GPS stations in the three Southern California interferograms. For IFG1, the average percentages of the total delay made up by the turbulent and stratified components are nearly identical (49% against 51%, Fig. 6a) and there is no clear pattern for the turbulent part. However, a strong turbulent pattern can be observed for IFG2 with the turbulent component contributing on average 72% of the total delay (Figure 4.6b). A clear turbulent pattern can also be seen in Figure 4.6c where some of the stations suffer from substantial atmospheric delay increases while others exhibit

substantial decreases. We attribute this mainly to the crowded tropospheric delays in the shore area where the turbulence behaviour is completely different from that in the inland area. On correcting with the stratified delays only, such as would be obtained via correlation analysis between interferometric phases and elevations (as used by for example Elliott et al. (2008) and Doin et al. (2009)), only limited RMS LOS displacement reductions can be obtained (Figure 4.3). The turbulent part also helped to reduce the tropospheric delay clustering on certain topographies such as the forest and desert in IFG1. It is therefore clear that correcting with only the stratified delay component is far from optimal for mitigating InSAR atmospheric effects.

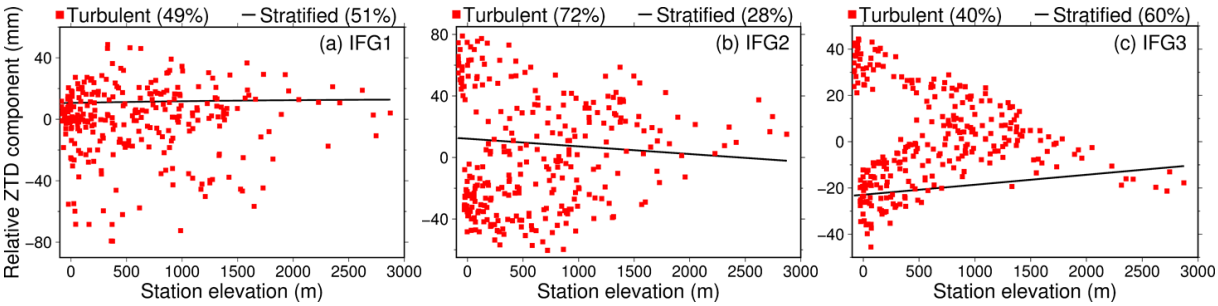

Figure 4.6 Turbulent and stratified components of the relative ZTDs, as separated by the ITD model with all the available GPS stations in the three Southern California interferograms (IFG1-3). The listed percentages denote the average proportion of the total delay contributed by the stratified and turbulent components. Note the different ZTD ranges.

Figure 4.7 shows the spatial distribution of the tropospheric turbulent signals on the Southern California interferograms, and the key features can be summarized as:

1). The turbulent components can have a comparable magnitude to the elevation-dependent component (i.e. stratified delays, see Figure 4.3 and 4.6). This is mainly because the differencing in InSAR weakens the stratification but, to some extent, amplifies the turbulence, especially when the weather conditions on the two days of image acquisition are considerably different and hence the errors tend towards a random distribution.

2). Patterns of the turbulent delays arise, with decreasing delays around the Palm Desert in Figure 4.7a and Figure 4.7b and the Anza-Borrego Desert in Figure 4.7b, and increasing delays around San Bernardino National Forest in Figure 4.7a and the shore areas, as shown in Figure 4.7c. The turbulent delays are sometimes clustered into different groups all with their own peak

values. The distribution of tropospheric turbulence is inhomogeneous, making it challenging to interpret actual deformation signals in InSAR measurements if they are not appropriately mitigated.

3). More variable turbulence can be seen in the summer than in other seasons (see the magnitude scales in Figure 4.7, where IFG2 is in the summer), which is attributed to the atmosphere being able to hold more water vapour and hence also substantial variability.

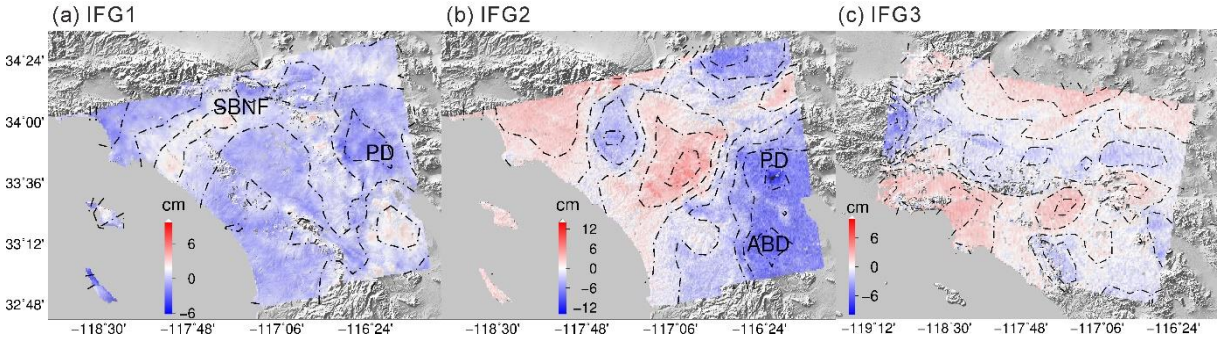

Figure 4.7 Turbulent relative zenith delays estimated using the ITD model for the three Southern California interferograms, IFG1-3. The black dotted lines represent turbulent delay contours of 1 cm; SBNF = San Bernardino National Forest, PD = Palm Desert, ABD = Anza-Borrego Desert. Note the different colour bars.

4.3 Assessment of the Impact of Station Spacing

As shown in Section 4.2, all the five interferograms were improved after applying the ITD model atmospheric corrections. The Southern California interferograms covered a region of varying topography but with a dense GPS network, while the Southern England region had a sparser GPS network but with flatter terrain. In order to assess the impact of station distribution on the ITD model performance, a station spacing test was carried out for the Southern California network. It comprised deleting stations from the (dense) network covered by the interferogram, to form sub-networks with different station spacing. The procedure was as follows: (i) we divided the whole coverage area into uniform grids for a chosen station spacing distance (1 km, 2 km, 3 km, etc.); (ii) for each grid, we selected only one station inside it (the closest one from the grid centre) and all the selected stations were then used to form a new sub-network; (iii) by repeating the previous two steps, we generated a series of sub-networks with different station spacings ranging from 1 km to 70 km. The station spacing here means the size of each grid and, to some extent, represents the average distance between stations. This procedure ensured

resampling of stations as uniformly as possible, leaving the spacing distance as the main variable between the sub-networks.

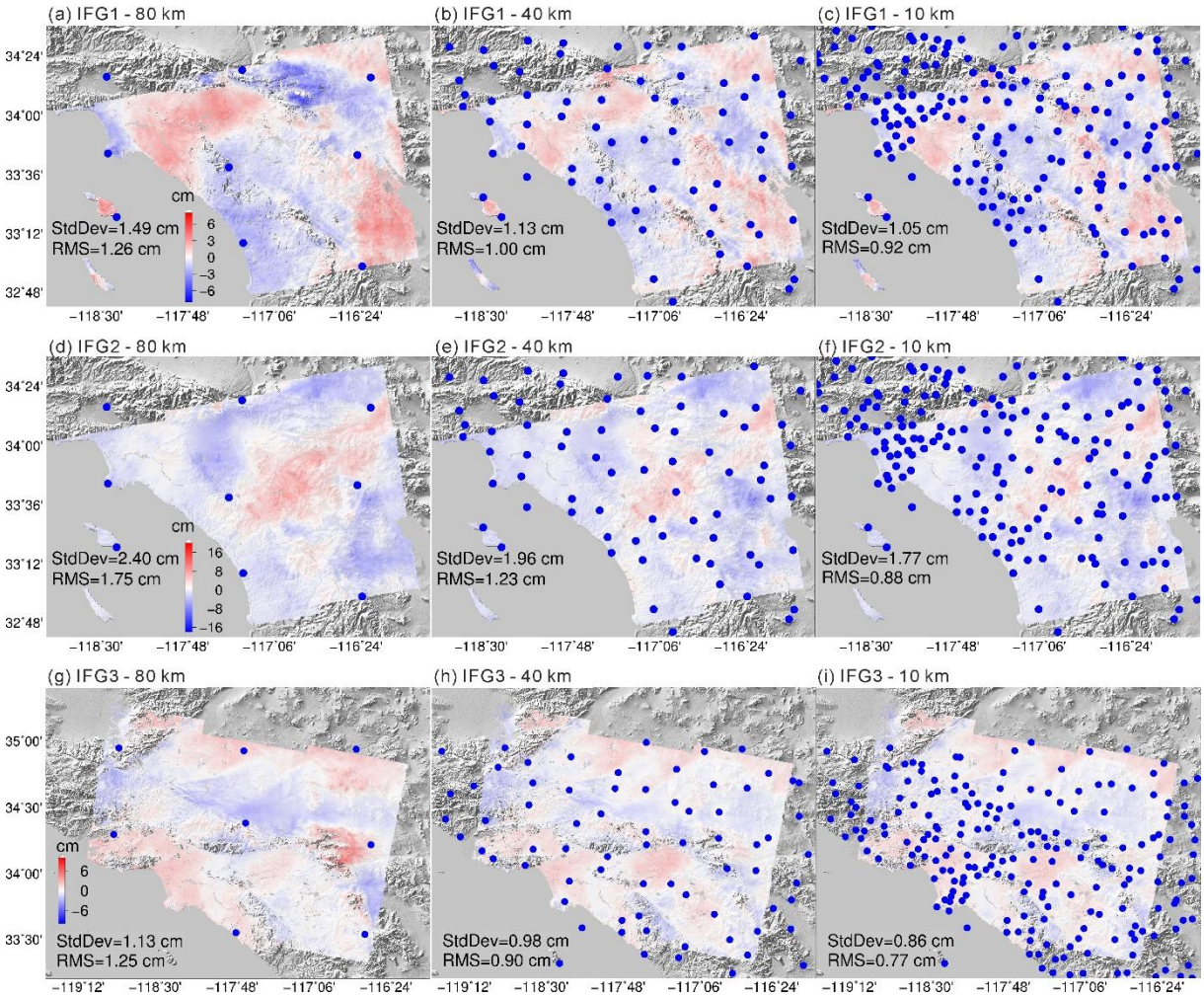

Figure 4.8 GPS station spacing tests on the Southern California interferograms. Three sub-networks were considered with spacing distances of 80 km, 40 km and 10 km, with the blue dots representing the GPS stations used to compute the ITD model total delay corrections applied in each interferogram. The corrected interferograms and the corresponding phase StdDev and RMS displacement difference statistics are also indicated. Note the different colour bars per interferogram.

Figure 4.8 shows some results of the spacing test with three sub-networks used to generate ITD model total delays and applied to the three Southern California interferograms, plotted for station spacing distances of 80 km, 40 km and 10 km. The performance improves dramatically as the spacing decreases from 80 km to 40 km (LOS range change StdDev improving from 1.49, 2.40 and 1.13 cm, to 1.13, 1.96 and 0.96 cm, respectively for interferograms IFG1-3; RMS LOS displacement differences improving from 1.26, 1.75 and 1.25 cm, to 1.00, 1.23 and 0.90 cm, respectively), but little further improvement was attained when further decreasing the spacing

from 40 km to 10 km, as can be seen in Figure 4.8 and Table 4.3. This indicates that some medium-to-long wavelength signals are not handled well by the sparsely distributed pointwise ZTDs, although even this 80 km spacing provides improvements over the raw interferogram, e.g., for IFG2 the StdDev and RMS difference improved from 3.85 and 3.72 cm to 2.40 and 1.75 cm, respectively. By adding stations uniformly until a 40 km spacing was attained enabled the overall tropospheric noise to be modelled as much as possible by the network. A denser network with 10 km distance had a similar performance, revealing that short-wavelength turbulent signals are hard to model even with a very dense GPS network.

Table 4.3 Summary of station spacing tests for the Southern California interferograms. Unit: cm. The number in parentheses indicates the improvement, (Raw – Corrected)/Raw.

Interferograms	Phase StdDev	Displacement RMS
IFG1 - Raw	1.69	1.66
IFG1 – 80 km	1.49 (12%)	1.26 (24%)
IFG1 – 40 km	1.13 (33%)	1.00 (40%)
IFG1 – 10 km	1.05 (38%)	0.92 (45%)
IFG2 - Raw	3.72	3.85
IFG2 – 80 km	2.40 (35%)	1.75 (55%)
IFG2 – 40 km	1.96 (47%)	1.23 (68%)
IFG2 – 10 km	1.77 (52%)	0.88 (77%)
IFG3 - Raw	2.18	2.32
IFG3 – 80 km	1.13 (48%)	1.25 (46%)
IFG3 – 40 km	0.98 (55%)	0.90 (61%)
IFG3 – 10 km	0.86 (61%)	0.77 (67%)

More detailed statistics of the spacing test are shown in Figure 4.9. Figure 4.9a represents the relative ZTD cross validation RMS differences (using the three interferograms) for each sub-network with spacing distance ranging from 2 km to 80 km at a 1 km interval. Figure 4.9b shows the noise reduction level of each sub-network and the improvement percentage, calculated as the LOS range change StdDev and RMS LOS displacement difference reduction divided by the maximum reduction. Limited improvement was obtained on decreasing the spacing from 15 km due to (i) the additional stations were located in areas where the tropospheric delays had already been fully modelled (it should be noted that the station

distribution in our original network is not uniform), so it contributed no further improvement; (ii) the principal component of tropospheric delay signals has already been modelled and the closer distance between stations contributed only limited improvement on modelling short wavelength signals. When the spacing is below 15 km, the performance remains similar to when the principal component of tropospheric delay signals is modelled. However, as the distance increased from 15 km the performance degraded, with the increased spacing distance resulting in fewer stations being available, which made the correction maps less reliable. This can be seen from the more variable performance between 50–80 km, i.e. although some sub-networks have similar spacing, their performance can be totally different.

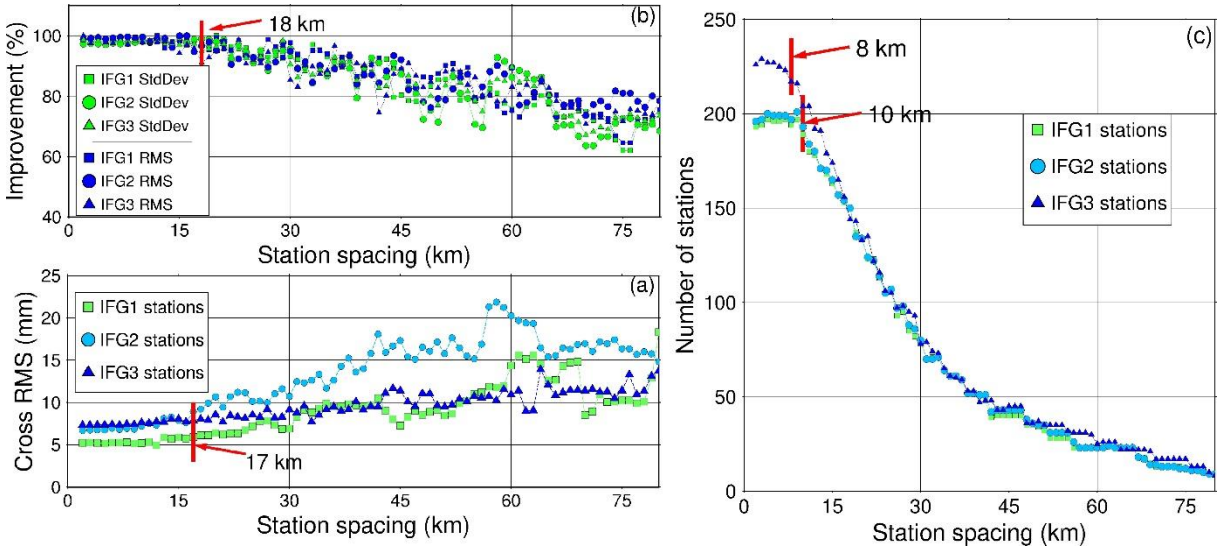

Figure 4.9 Multiple station spacing tests for the three Southern California interferograms, ranging from 2 km to 80 km. (a) Relative ZTD cross validation for each sub-network on every interferogram. (b) Noise reduction using each sub-network stations on every interferogram, for phase (StdDev) and RMS difference between InSAR and GPS LOS displacements. (c) number of stations for each sub-network with different station spacings.

The spacing test serves as an intuitive way to understand the impact of the station distribution on the ITD model performance. A good distribution should be able to model the principal components of tropospheric noise, i.e. as the spacing distance decreases, the ZTD cross validation RMS should converge before the number of stations converges and therefore adding more stations would introduce little improvement. In the case that the stations are distributed rather non-uniformly, the conclusions still hold except that the largest noise reduction will converge to a local optimum, leaving some medium-to-long wavelength noise signal still being uncorrected, especially those areas where few or no stations are available.

4.4 Summary

In this chapter, we have demonstrated GPS-based atmospheric correction model to reduce atmospheric effects on radar measurements. The ITD model was employed to separate the turbulent and stratified delays from the total delays in order to reduce their coupling effects on SAR interferograms. Cross validation and station spacing tests were carried out to serve as indicators of correction performance to inform users whether the correction is applicable and provide insights into the trade-off between station spacing and the achievable accuracy.

After applying our GPS-based tropospheric correction model (using the total delays, i.e. including both the stratified and turbulent components), the RMS differences between InSAR and GPS displacements in the LOS for five Sentinel-1A interferograms in Southern California (10-20 km station spacing) and Southern England (50-80 km station spacing) reduced from 1.66, 3.85, 2.32, 2.72 and 2.42 cm, to 0.92, 0.84, 0.75, 0.80 and 0.97 cm, respectively. These represented improvements of 45-79% for Southern California, and 59-71% for Southern England, and the phase standard deviation improvements for the two test areas were 38-61% and 65-79%, respectively. The importance of correcting for turbulent delays has been emphasized since the time differencing of InSAR can cancel out part of the stratified component and amplify the turbulence effects. The turbulent components can have a comparable magnitude to the stratified component and exhibit larger variations in the summer than in other seasons due to the atmosphere being able to hold more water vapour hence exhibits greater variability. By accounting for both the stratification and turbulence of the troposphere, ~1 cm precision of the corrected interferograms is achievable. This improves the feasibility of using InSAR observations to investigate low-amplitude, long wavelength deformation fields such as those due to inter-seismic strain accumulation and/or post-seismic motion, and to investigate underground human activities in modern cities which plays an important role in ground subsidence monitoring (Chen et al., 2016; Crosetto et al., 2002; Walters et al., 2013). Furthermore, this method does not result in any removal of real deformation signals or require manual interaction, which can arise when using filtering tropospheric mitigation approaches, and unlike using MERIS and MODIS, is applicable in all weathers.

The station spacing test by cross validating the GPS ZTDs provides an assessment of the overall interpolation performance which should be considered as one essential step to assess the feasibility of the ITD model correction. A lower RMS in the cross validation indicates higher ITD model performance, and vice versa (Figure 4.9). Spacing tests served as an intuitive way to understand how the station distribution affects the correction performance, which is especially important when using pointwise GPS ZTDs which may be sparsely or non-uniformly distributed. A network with a greater station spacing is likely to provide higher RMS values and hence poorer correction performance against a denser network. Based on these two indicators, one could decide whether the correction is applicable as well as assessing the expected accuracy of the network considered.

Chapter 5. Generic Atmospheric Correction Model

The GPS based atmospheric correction model is dependent on the availability of sufficiently dense and geometrically sound networks of GPS stations, which are not available everywhere globally. To overcome this, in this chapter we propose a generic InSAR atmospheric correction model whose notable features comprise: (i) global coverage, (ii) all-weather, all-time usability, (iii) correction maps available with a short time latency, and (iv) indicators to assess the correction performance and feasibility. The model integrates operational high-resolution ECMWF data (0.125-degree grid, 137 vertical levels, 6-hour interval) and continuous GPS tropospheric delay estimates (every 5 minutes) using the revised ITD model. Indicators describing the model's performance are developed to provide quality control for subsequent automatic processing, and to give insights of the confidence level with which the generated atmospheric correction maps may be applied.

5.1 High-resolution ECMWF ZTDs

Previously used weather models such as the ERA-Interim are often released with a latency of several months and suffer from coarse temporal and/or spatial resolution and failure in accurately capturing atmospheric turbulence (e.g., Foster et al., 2013; Jolivet et al., 2011; Webley et al., 2002), with Bekaert et al. (2015b) reporting a 1.7-cm RMS displacement error of corrected interferograms over Mexico and Italy, after applying corrections generated from ERA-Interim and WRF. We used the output from the model level operational high-resolution ECMWF analysis product. Specifically, modelled surface pressure, temperature and specific humidity were used to calculate ZTDs and PWV at each 0.125-degree grid point (i.e. spacing of approximately 9-12 km), as described in Jolivet et al. (2011). While forecast products can potentially introduce pluri-annual time series trends when compared with reanalysis products, we expect such effects to be small here as the ECMWF product is not purely forecasted, but computed using a uniform procedure over time, combining short-range forecast data with real observations to produce the best fit to both (Persson, 2015).

We also compared the daily (at 12:00 UTC) ECMWF and GPS ZTDs in California (35-38N,

118-122W) for the whole year of 2016 by interpolating the ECMWF regular grids onto GPS stations. The GPS data was downloaded from the PBO network and processed as in Section 4.1. The result is shown in Figure 5.1. The ECMWF ZTD agrees with the GPS ZTD, with a 9.8 mm RMS difference and a 0.994 linear slope.

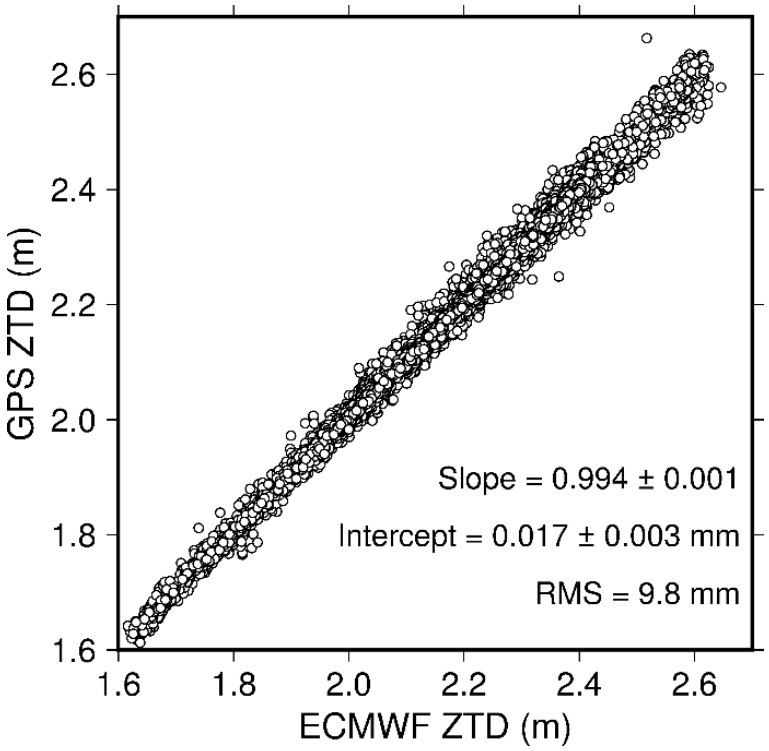

Figure 5.1 Comparisons between the daily GPS ZTD and ECMWF ZTD in California for the whole year of 2016 at 12:00 UTC. The slope and intercept are the parameters in the linear model: GPS ZTD = Slope * (ECMWF ZTD) + Intercept.

5.2 Cross Validation of GPS and ECMWF ZTDs

It is crucial to validate the ZTD interpolation performance and check the GPS network distributions before generating and applying atmospheric correction maps for InSAR. For validation purposes, in this chapter, we used four networks of continuously operating GPS reference stations located respectively in Central California (CA), North of New Zealand (NZ), Italy and the United Kingdom (UK), each one characterized by different geometry and station density, ranging from an average spacing of 43 km for the UK network, to 12 km for CA (Table 5.1). All GPS data for the whole of the year 2016 from all stations in the four networks were processed in the same way as described in Section 4.1. While in Chapter 4 we used differenced ZTDs to generate correction maps, this may not be achievable as the spatial resolution of ECMWF ZTDs may be different between two acquisitions (i.e. the resolution improved from

~16 km to ~9 km in 2016) where the GPS network is the densest to validate the ECMWF ZTDs. As a result, in this Chapter, we use the absolute ZTD to generate atmospheric delay maps, with the correction map obtaining by differencing.

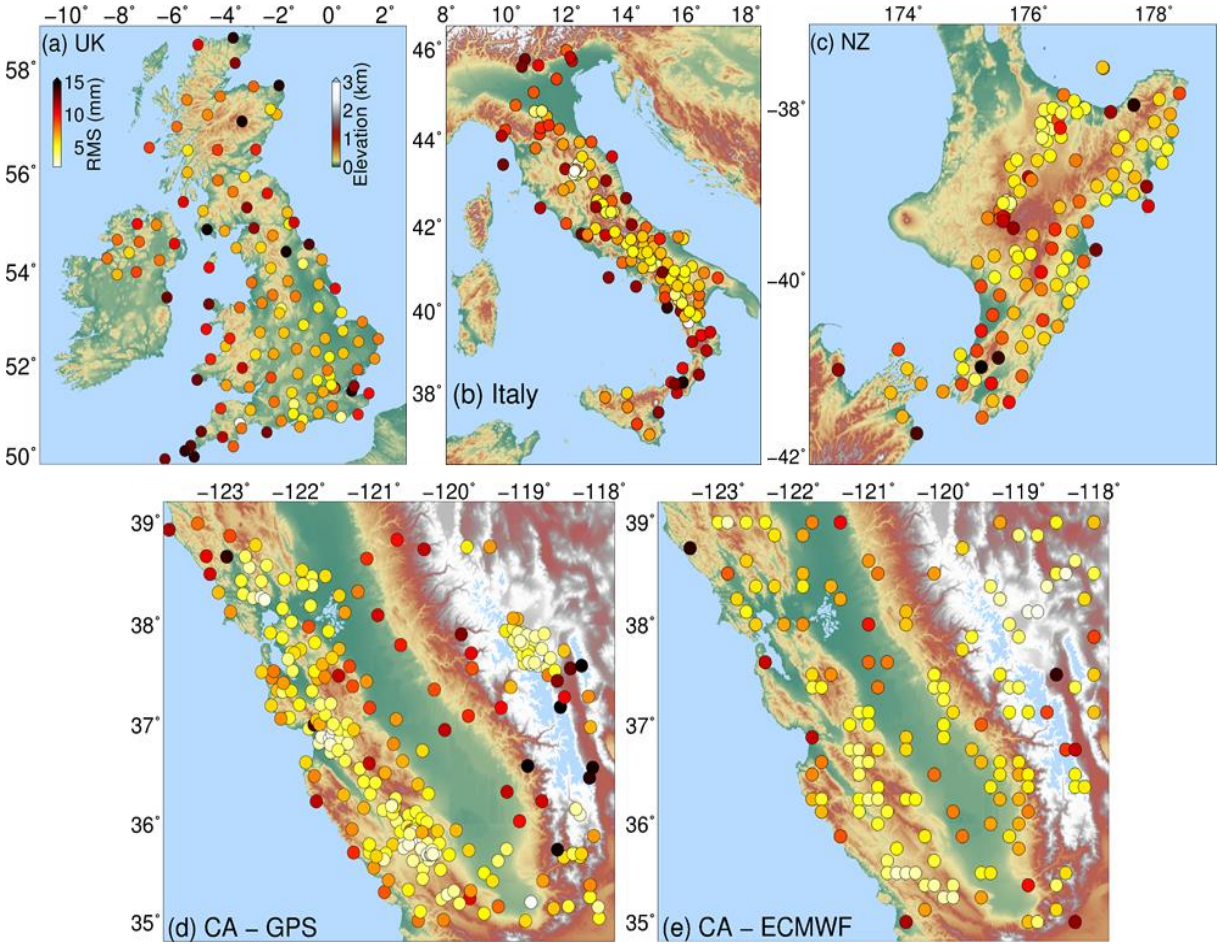

Figure 5.2 Cross validation: mean RMS differences for each station in the four GPS networks and ECMWF in 2016. Note that the 20% of ECMWF points used were selected randomly from the original 0.125-degree spacing grids.

Daily PANDA-derived GPS ZTDs at 14:00 local time for all of 2016 were cross-validated (as described in Section 3.3). It was also undertaken for ECMWF, but because of the small and regular spacing (and therefore high spatial correlation) of the ECMWF ZTD data points, this should only be considered as internal cross validation and will always produce a low RMS difference and not realistically reflect the interpolation performance of the whole area. Hence, we randomly chose 20% of points among the regular 0.125-degree spacing grids to reduce the spatial correlation and then conducted the (internal) cross validation in the same way as for GPS.

Table 5.1 Cross validation for four GPS networks and one ECMWF area using daily values at 14:00 local time for all of the year 2016.

Network	Location	Average spacing (km)[5]	Slope	Intercept (m)	Bias (mm)	RMS (mm)	Correlation	Mean RMS (mm)[6]
BIGF[1]	UK	43	0.973	0.065	0.2	9.8	0.97	9.3
RING[2]	Italy	30	0.993	0.015	0.1	8.5	0.99	8.8
GeoNet[3]	New Zealand (NZ)	17	0.995	0.012	0.2	7.8	0.99	7.7
PBO[4]	California USA (CA)	12	1.000	0.001	0.1	6.6	1.00	6.6
ECMWF[7]	California USA	12	0.997	0.006	0.0	6.3	1.00	5.9

[1] British Isles continuous GNSS Facility (www.bigf.ac.uk/) at 50-59N, 11W-2E;
[2] Rete Integrata Nazionale GPS (ring.gm.ingv.it/) at 37-47N, 8-18E;
[3] Modern geological hazard monitoring system in New Zealand (www.geonet.org.nz/) at 37-42S, 173-179E;
[4] Plate Boundary Observatory (pbo.unavco.org/) at 34-39N, 124-118W;
[5] The spacing is computed as the mean distance between each station and its closest station;
[6] The mean daily RMS differences for the year 2016;
[7] For ECMWF, values were taken at 10:00 or 11:00 local time.

The cross validation RMS differences between the interpolated and actual values for all the GPS networks and, for the case of CA, also internal cross validation of ECMWF, for the year 2016 are summarized in Table 5.1. We fitted a linear model (actual ZTDs = Slope * Interpolated ZTDs + Intercept) for each network including ECMWF. We used the local time 14:00 for all GPS networks, but for ECMWF over CA, we used 18:00 UTC (local time 11:00 during summer and 10:00 during winter) to avoid ECMWF temporal interpolation. The average GPS station spacing decreases from the UK, Italy, NZ to CA networks, and their corresponding RMS differences reduce accordingly: the UK network exhibits the greatest average station spacing (43 km), which leads to an RMS of 9.8 mm compared with 6.6 mm for the 12-km spacing CA network. The ECMWF of CA has a similar spacing to the CA GPS network but a slightly lower RMS, which is attributed to the GPS ZTD capturing more detailed turbulent signals and thus degrading the interpolation performance. The RMS differences per station are plotted in Figure 5.2, which shows that more precise interpolated ZTDs are generated in areas with a denser GPS

network. Larger RMSs mostly arise in areas with fewer stations or on the edge of the networks. However, all regions present a mean correlation coefficient using all stations of at least 0.97 and a bias varying between 0 and 0.2 mm. A summary of multiple statistical metrics that were computed is given in Table 5.1.

5.3 Integration of GPS and ECMWF

To model GPS and ECMWF consistently and capitalize on the high spatial resolution of ECMWF and the high quality of GPS-estimated tropospheric delay, the ITD approach is used to tightly integrate both datasets.

5.3.1 The integrated ITD model

In the ITD model, the exponential function is used to model the stratified delays, and the turbulent part of the delay is constructed by fitting an interpolating scheme based on IDW to the remaining delays. To integrate GPS and ECMWF ZTDs, the total delays are defined as in the same form as in Equation 3.2, but the stratified components are modelled as:

$$S_i = L_0 e^{-\beta h} \Rightarrow \begin{cases} S_m^G = L_0 e^{-\beta h_m} \\ S_n^E = L_0 e^{-\beta h_n} \end{cases}, P_i = \begin{bmatrix} P_G & 0 \\ 0 & P_E \end{bmatrix} \qquad \text{(Equation 5.1)}$$

where the modelled stratified delay S is represented by an exponential function with coefficient (L_0, β), the same symbols are used as in Equation 3.3; P is the weight matrix; G represents GPS and E represents ECMWF. The equation holds within a defined tropospheric decorrelation distance from the point being interpolated. This is a key parameter for GPS-based interpolator which is subject to network density and geometry, with Chapter 3 defining it as 100 km for a dense California network and Chapter 4 using 200 km to avoid discontinuities for a sparse GPS network. In this Chapter, we found 150 km is sufficient for all considered GPS networks and a larger distance may result an over-smoothed interpolation. Furthermore, when including the ECMWF ZTD, this parameter becomes less important and we believe that 150 km is sufficient for any GPS network, since the dense distribution of the ECMWF ZTD ensures a reliable estimation of the exponential coefficients and avoids discontinuities in the interpolated delay maps.

We use all ZTD samples in the region considered to estimate the two coefficients in a least squares algorithm. Extra reference locations are needed outside of the interferogram bounds (up to the defined decorrelation distance) to avoid any need to extrapolate rather than interpolate. The ZTDs used (hereafter called reference location ZTDs) include both the GPS ZTD at position *m* and the ECMWF ZTD at position *n*. The weight matrix *P* is defined according to the different quality of GPS and ECMWF ZTDs, and there are three principal factors that influence this: (i) the quality of GPS ZTD is higher than ECMWF ZTD, especially when there are large time differences between ECMWF and InSAR acquisitions (Bock et al., 2005); (ii) GPS ZTD captures the tropospheric temporal variations better than ECMWF ZTD, which is essential in InSAR atmospheric corrections; (iii) the higher spatial resolution and uniform distribution of ECMWF makes it better than GPS for interpolation. A method based on cross validation is proposed in the next section to automatically determine the relative weights between GPS and ECMWF.

The turbulent part is modelled by a modified IDW to incorporate both ECMWF and GPS ZTDs and reads as:

$$T_u = \sum_{i=1}^{k} w_{ui} T(\mathbf{x}_i), w_{ui} = \frac{p_i d_{ui}^{-2}}{\sum_{i=1}^{k} p_i d_{ui}^{-2}} \qquad \text{(Equation 5.2)}$$

where *u* and *i* are indices for the user and reference locations, respectively. Each turbulent delay at the user location is assigned a weight of w_{ui} which is determined by the horizontal distance from the user to reference location d_{ui} and the weighting p_i for GPS and ECMWF, respectively (the same as in the case of the stratified delays as per Equation 5.1). The detailed integrated ITD implementation steps are the same as in Section 3.2.

The ITD model uses the ZTDs integrated from the layered temperatures, pressures and the partial water vapour pressures from ECMWF (Jolivet et al., 2011) to enable the decomposition of the stratified and turbulent components in a way consistent with the GPS delays, which is critical to integrate them, and a high computing efficiency. Given the fact that the vertical profile of water vapour over large scales varies exponentially (Ehret et al., 1999; Rocken et al., 1997),

ITD seeks a local average vertical profile for each map pixel by its surrounding reference grid nodes and/or reference GPS stations and fit to an exponential function. To avoid over-interpretation, any disturbances on this assumption will drop into the turbulent component which is iteratively handled in the ITD model. In general, the elevation dependent and medium to long wavelength tropospheric delays can be well reconstructed by ITD, but the short wavelength (e.g., a few kilometres) delays require a dense GPS network. While some GPS ZTDs have been assimilated into ECMWF, principally from continuously operating GPS stations in Europe, the integrated ECMWF+GPS ITD approach is still needed because of (i) the coarse temporal resolution (6 hours) of the ECMWF model; and (ii) the GPS data assimilated into ECMWF are used for forecasting, which poses prediction uncertainties compared to the GPS ZTD estimates themselves.

5.3.2 Weight determination

One of the key parameters in the integrated ITD model is the relative weight between GPS and ECMWF. Since the cross validation reflects the ZTD interpolation performance and the GPS network distributions, we utilized the cross validation RMS of the GPS network stations to determine the relative weights between GPS and ECMWF.

For a given GPS network, we calculated its cross validation RMS, but instead of using GPS ZTDs only, we also used the surrounding ECMWF grid nodes to predict ZTDs at each GPS station. This was done by the integrated ITD model described in Section 5.2.1 and using different ECMWF:GPS relative weights ranging from 0.0 to 10 (at a step of 0.1). The optimum ECMWF:GPS weighting for the particular network was considered that which led to the lowest cross RMS. Figure 5.3 shows examples using data from the CA (~12 km GPS station spacing) and UK (~43 km GPS station spacing) networks using one day in winter (7 December 2016) and one in summer (5 July 2016). Clear RMS minima can be seen for all cases, arising when applying ECMWF:GPS relative weights of 0.15 and 0.25 for the denser CA network, and 0.44 and 0.45 for the sparser UK network. A simulation test was also undertaken to show the impact of a network of GPS stations which has a very sparse distribution. We selected five stations from the CA network on 12:00 UTC 1 January 2016 (Figure 5.3e) and repeated the cross

validation analysis. The best relative weight was found to be 3.3 which means that in this simulation case, the correction maps should be mainly dictated by ECMWF due to the sparse GPS station distribution.

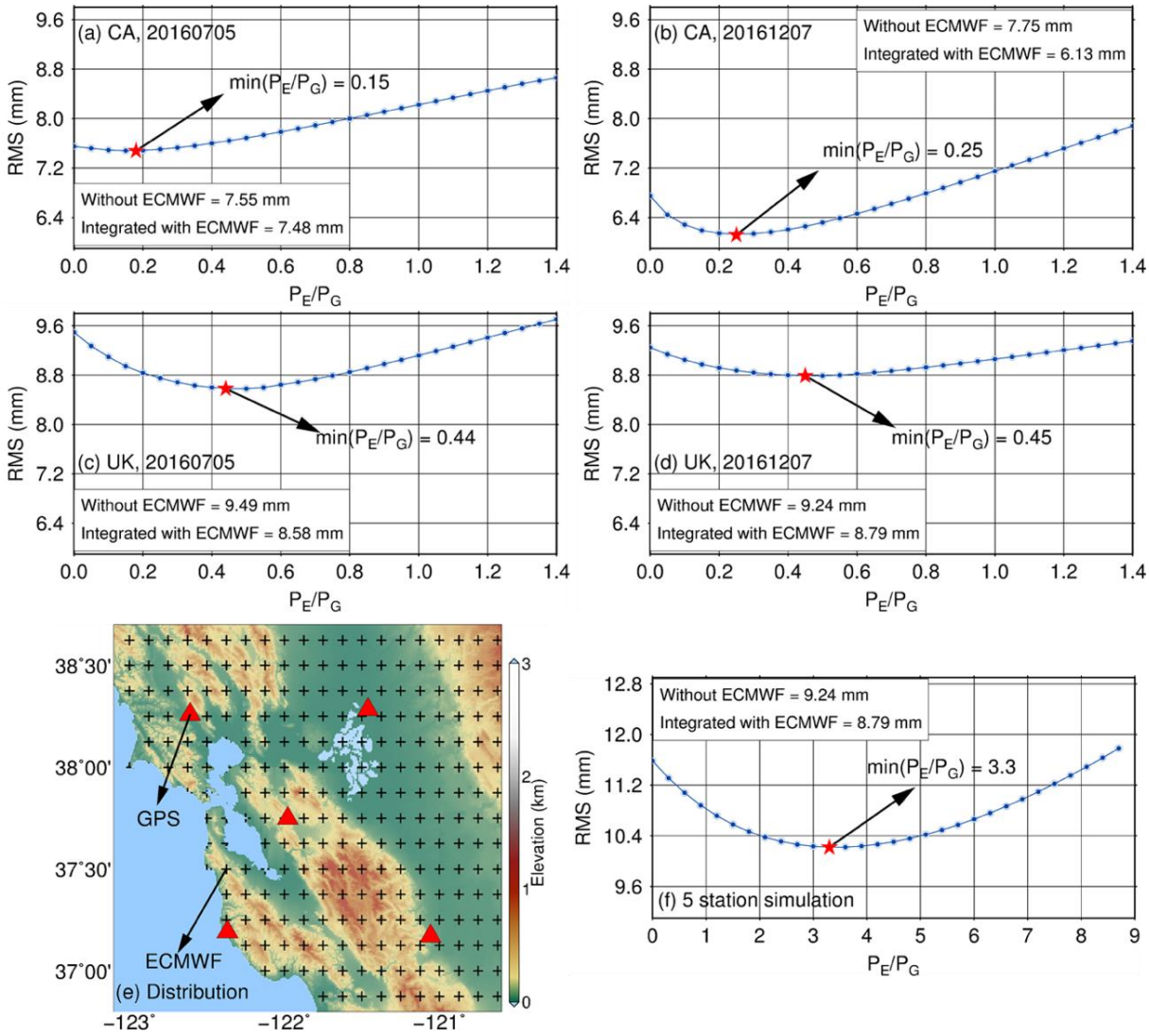

Figure 5.3 Relative weighting between GPS and ECMWF ZTDs on integrating, using the Central California (CA) and UK GPS networks. The y axes represent the cross-RMS for all GPS stations on the dates shown. The horizontal axis represents the relative weighting between ECMWF and GPS.

From the weight determination procedures described above, when the GPS network is sparse, the cross validation RMS will be higher because of missing short wavelength components. The ECMWF:GPS relative weighting will depend on how well the ECMWF ZTDs represent the missing signals from GPS (reflected by the integrated ITD cross validation RMS for the GPS stations). If the ECMWF ZTDs have large time latency (resulting in the ECMWF ZTDs differing substantially from the GPS values), it will not help to improve the cross validation and

hence they will be assigned low weight.

The relative weight from cross validation is a spatial-temporally dependent variable that can be easily determined whenever both GPS and ECMWF data are available, and is essential for automated processing. For the four IFGs used here covered by GPS stations, the relative weights were computed as just described, using all GPS data from stations covered by the IFG and also up to 150 km outside its boundaries. Hence the relative weighting reflects not only the ZTD precision but also the density of the observations, the variation of the topography, and the local tropospheric conditions.

5.4 Generic Atmospheric Correction Model

Based on the integrated ITD model and the determined relative weights for the integration of the ECMWF and GPS ZTDs, ZTD maps were generated and applied to InSAR measurements to correct for atmospheric effects. This leads to a generic atmospheric correction model since it has (i) global coverage, (ii) all-weather, all-time usability, and (iii) correction maps available with a short time latency (two days latency from ECMWF, no latency from GPS).

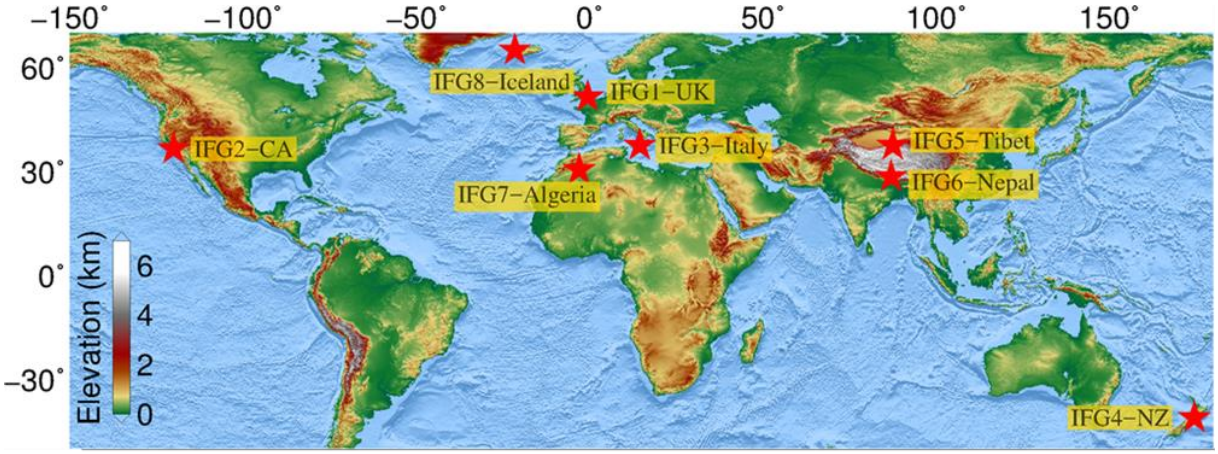

IFG	Date1	Date2	Time of day	Interval (days)	GPS network	Geographical extent
IFG1-UK	20160125	20160206	17:49	12	BIGF	50-53N, 3W-2E
IFG2-CA	20160302	20160326	01:58	24	PBO	35-38N, 118-122W
IFG3-Italy	20160313	20160406	05:04	24	RING	36-39N, 12-17E
IFG4-NZ	20160923	20161017	07:15	24	GeoNet	39-43S, 172-177E
IFG5-Tibet	20160112	20160205	12:08	24	-	36-39N, 85-90E
IFG6-Nepal	20160720	20160813	12:21	24	-	27-30N, 83-87E
IFG7-Algeria	20161001	20161007	06:11	6	-	29-32N, 1-5W
IFG8-Iceland	20160609	20160703	18:58	24	-	63-67N, 18-25W

Figure 5.4 Sentinel-1 interferograms (denoted as IFG) used in this study. All times are in UTC.

We assessed the performance of the generic atmospheric correction model by using it to correct atmospheric effects on the eight globally-distributed interferograms (Figure 5.4), thus testing its suitability in different parts of the world and when there is a range of GPS ZTDs available, from none through to 12 km station spacing. These interferograms represent typical problematic scenarios in InSAR processing such as strong, long wavelength signals caused by water vapour, large topography variations, large time latency of the ECMWF data, and the effect of the different densities of GPS networks, in that they cover the four GPS networks to test the benefit of ECMWF combined with GPS but of various station spacings. They also include four areas of geophysical interest where there are no GPS stations, namely Tibet, Nepal, Algeria and Iceland, in order to test the global applicability of the generic model but in scenarios whereby only ECMWF can be used. For the four interferograms which are covered by GPS networks, we assess and quantify the model's performance when the applied correction is based on GPS ZTDs only, on ECMWF ZTDs only, and from integrated GPS and ECWMF ZTDs. Then, four additional interferograms covering areas without a GPS network are evaluated using ECMWF ZTDs only, to emphasize the global applicability of the model developed. The same decorrelation limit was used per pixel as per the cross validation tests by using only the ECWMF and GPS ZTDs within 150 km of the pixel considered. The metrics used to assess the model's performance are the same as in Section 4.2 (the phase StdDev and the RMS displacement difference between GPS and InSAR).

5.4.1 Validation of the integrated ECMWF and GPS correction maps

Figure 5.5 shows the results for IFG1-UK and IFG2-CA, which represent different station spacings. It appears that both raw interferograms exhibit strong atmospheric effects, with raw phase StdDev values of 2.75 cm and 2.44 cm, respectively. The long wavelength atmospheric effect on IFG1-UK disappeared and the phase StdDev dropped to 0.71 cm after applying the GPS-only atmospheric correction map, to 1.02 cm after ECMWF correction and to 0.69 cm after the integrated correction, as listed in Table 5.2. The displacement RMS differences compared with GPS also decreased dramatically after correction, particularly for the integrated correction, which shows a 71% improvement of 2.23 cm to 0.65 cm. It can be seen from Figure 5.5 that the remaining signals are mostly short wavelength and topography-correlated,

especially after applying the ECMWF correction, indicating that these remaining signals, or at least parts of them, are unmodeled atmospheric delays. Elliott et al. (2008) used a linear fit with height to reduce such effects, but the method fails when the deformation signals are correlated with topography or the relationship between phase and height is not constant throughout the interferogram.

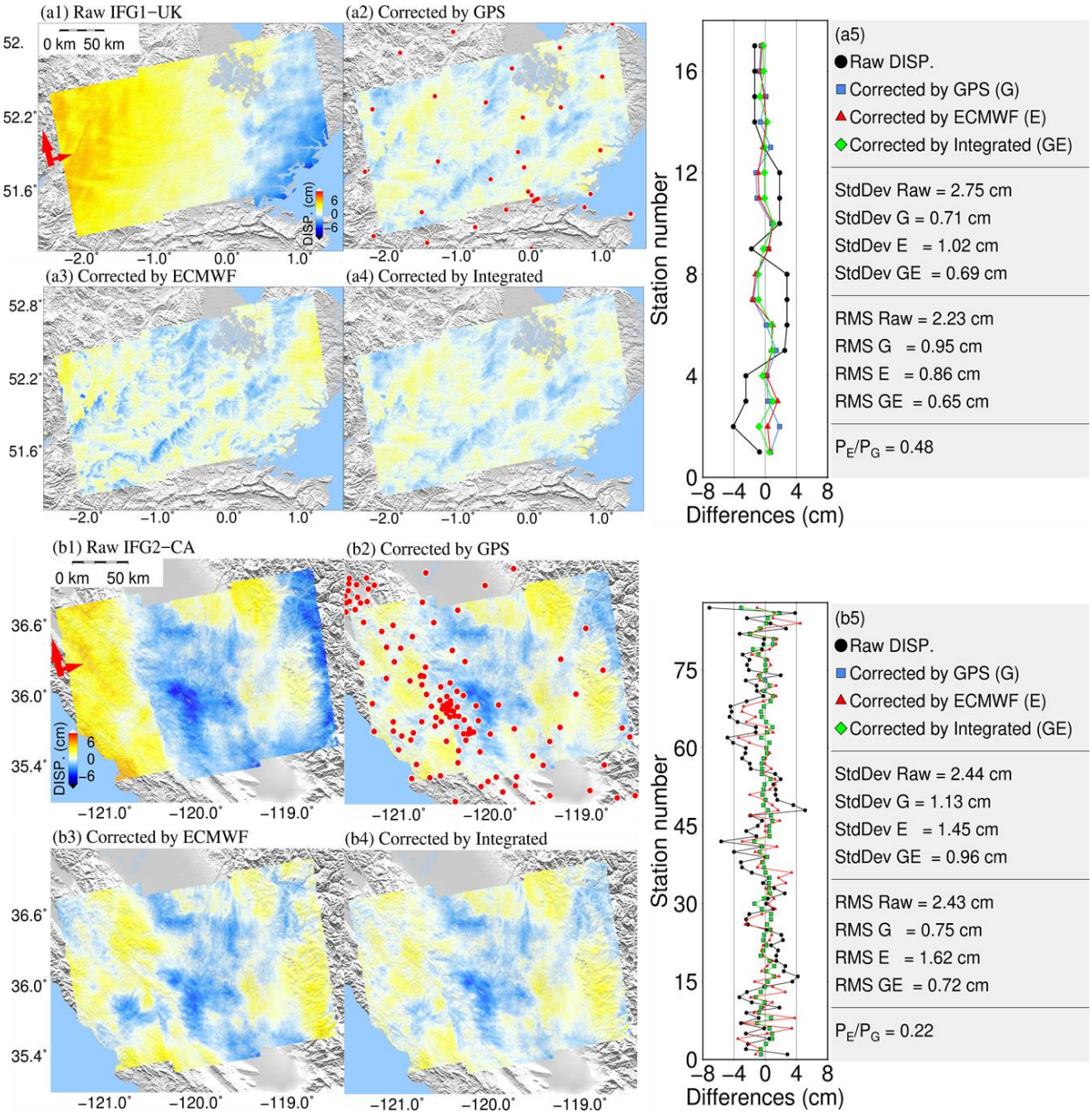

Figure 5.5 InSAR atmospheric corrections using GPS (G), ECMWF (E) and their combinations (GE) for IFG1-UK and IFG2-CA. The first two columns are raw and corrected interferograms. The third column shows the displacement differences between GPS and InSAR per GPS station. Phase StdDev, displacement RMS and automatically-determined ECMWF:GPS relative weight (PE/PG) for each IFG are also listed. The red arrow indicates the radar flight direction and the red circles represent GPS stations. All phases are in LOS direction.

Similar improvements are also observed in Figure 5.5 for IFG2-CA, with 54% improvement in

terms of phase StdDev after GPS correction, 41% after ECMWF correction and 61% after the integrated correction, reducing from 2.44 cm to 0.96 cm. The displacement measurements compared with GPS improved by 70% after the integrated correction, with most of the errors per GPS station falling to below 1 cm as can be seen in Figure 5.5b5, and an RMS displacement error of 0.72 cm. Although the IFG2-CA GPS network is denser than that for IFG1-UK, it is unevenly distributed, resulting in most of the improvements after applying GPS corrections occurring in the west (Figure 5.5b2) where most of the GPS stations are located, whereas improvements on the eastern part of the interferogram are limited. The large topography variation in this area makes it harder to model the atmospheric delays compared with the flatter terrain in the UK, and the lower performance of ECMWF (41% StdDev improvement) compared with IFG1-UK (63% StdDev improvement) reflects this. Hence the different performances of GPS for the two interferograms indicate the dependence on both topography and network geometry.

Table 5.2 InSAR atmospheric correction performance statistics expressed in terms of phase StdDev and displacement RMS for different correction methods applied on eight interferograms. Unit: cm. Percentage improvements over the raw measurements are given in parentheses.

	Phase StdDev				**Displacement RMS**			
IFG	Raw IFG	GPS correction	ECMWF correction	Integrated correction	Raw IFG	GPS correction	ECMWF correction	Integrated correction
IFG1-UK	2.75	0.71 (74%)	1.02 (63%)	0.69 (75%)	2.23	0.95 (57%)	0.86 (61%)	0.65 (71%)
IFG2-CA	2.44	1.13 (54%)	1.45 (41%)	0.96 (61%)	2.43	0.75 (69%)	1.62 (33%)	0.72 (70%)
IFG3-Italy	1.49	0.95 (36%)	0.88 (41%)	0.85 (43%)	1.37	0.70 (49%)	0.61 (55%)	0.47 (66%)
IFG4-NZ	1.97	1.35 (31%)	1.13 (43%)	1.10 (44%)	1.99	1.23 (38%)	1.30 (35%)	1.12 (44%)
IFG5-Tibet	1.15	-	0.45 (61%)	-	-	-	-	-
IFG6-Nepal	1.83	-	1.11 (39%)	-	-	-	-	-
IFG7-Algeria	2.40	-	0.88 (63%)	-	-	-	-	-
IFG8-Iceland	1.76	-	1.05 (40%)	-	-	-	-	-
Mean	**1.97**	**1.04 (47%)**	**1.00 (49%)**	**0.90 (54%)**	**2.01**	**0.91 (55%)**	**1.10 (45%)**	**0.74 (63%)**

IFG3-Italy covers most of the island of Sicily and only incorporates a limited number of GPS stations (11, with average spacing 75 km). Figure 5.6 shows that interferogram atmospheric contamination arises on the west and north coasts, where the raw observations imply substantial ground subsidence, but which is not the case in reality. Applying ECMWF corrections results in a 41% StdDev improvement, compared with 36% for GPS (Table 5.2), with the greater improvement visually apparent in the northeast and southeast of Sicily. The sparse distribution of GPS stations was unable to adequately capture the atmospheric delays around Mount Etna and the greater improvement (where GPS has performed similarly to ECMWF) is found in the west due to its flat topography. As for IFG1-UK and IFG2-CA, the benefit of applying integrated correction maps can be seen from Figure 5.6, with StdDev reductions of 43% obtained (from 1.49 cm to 0.85 cm) and 66% RMS displacement reductions (from 1.37 to 0.47 cm).

The atmospheric correction results for IFG4-NZ shown in Figure 5.6 follow a similar trend to those for IFG3-Italy: ECMWF resulting in a lower phase StdDev and similar RMS displacement than GPS, with ECMWF removing atmospheric effects in the west where GPS correction is less successful because the GPS station distribution is sparse. Whereas in the east, where the GPS station distribution is much denser (15 km spacing), the GPS corrections perform similarly to ECMWF. As for IFG1-UK, IFG2-CA and IFG3-Italy, the integrated correction maps result in the lowest phase StdDev (1.10 cm) and displacement RMS (1.12 cm), equating to improvements over the raw interferogram of 44% and 44% respectively.

To summarize, both the GPS and ECMWF atmospheric correction maps are able to substantially improve raw InSAR measurements: for the four interferograms considered, phase StdDev improvements of up to 74% arise on applying GPS corrections and 63% for ECMWF. When a dense GPS network is available, the GPS maps provide more precise corrections and capture the small magnitude, turbulent atmospheric delays better than ECMWF and thus perform better. However, the performance is highly dependent on the station density and distribution (network geometry), as well as the topography, with the GPS corrections when using a sparse network (e.g., IFG3-Italy in Figure 5.6a2) performing worse than ECMWF. In

all four cases considered, the integration of GPS and ECMWF results in the lowest phase StdDev and RMS displacement values.

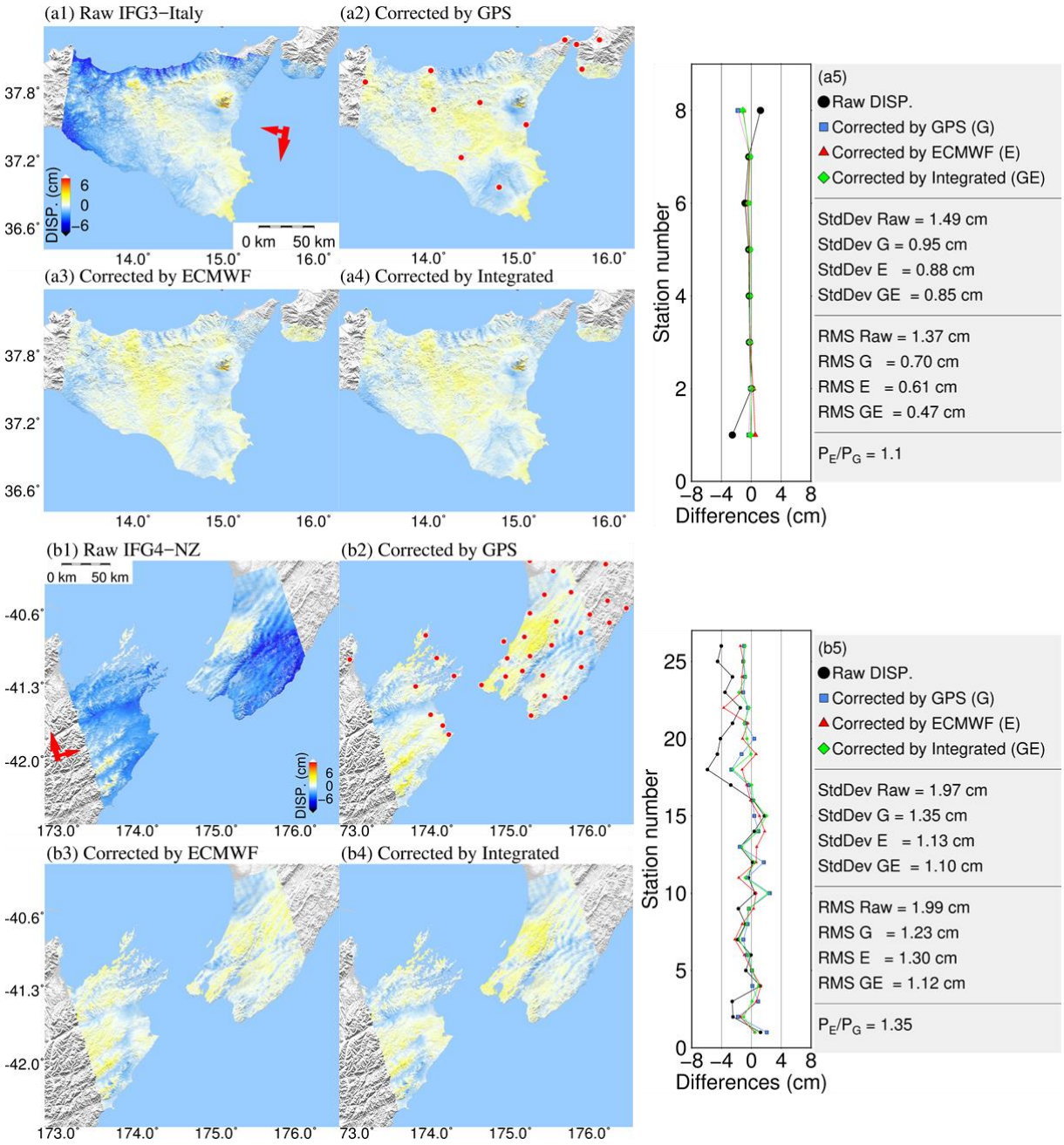

Figure 5.6 InSAR atmospheric corrections using GPS (G), ECMWF (E) and their combinations (GE) for IFG3-Italy and IFG4-NZ. Panel descriptions as for Figure 5.5. All phases are in LOS direction.

5.4.2 Global applicability of ECMWF-based correction maps

To evaluate the global applicability and performance of the model developed, we applied ECMWF atmospheric corrections to the four interferograms that do not contain any GPS stations, namely IFG5-Tibet, IFG6-Nepal, IFG7-Algeria and IFG8-Iceland. The results are

shown in Figure 5.7, displaying the raw and ECMWF-corrected interferograms, and the phase StdDev values are listed in Table 5.2.

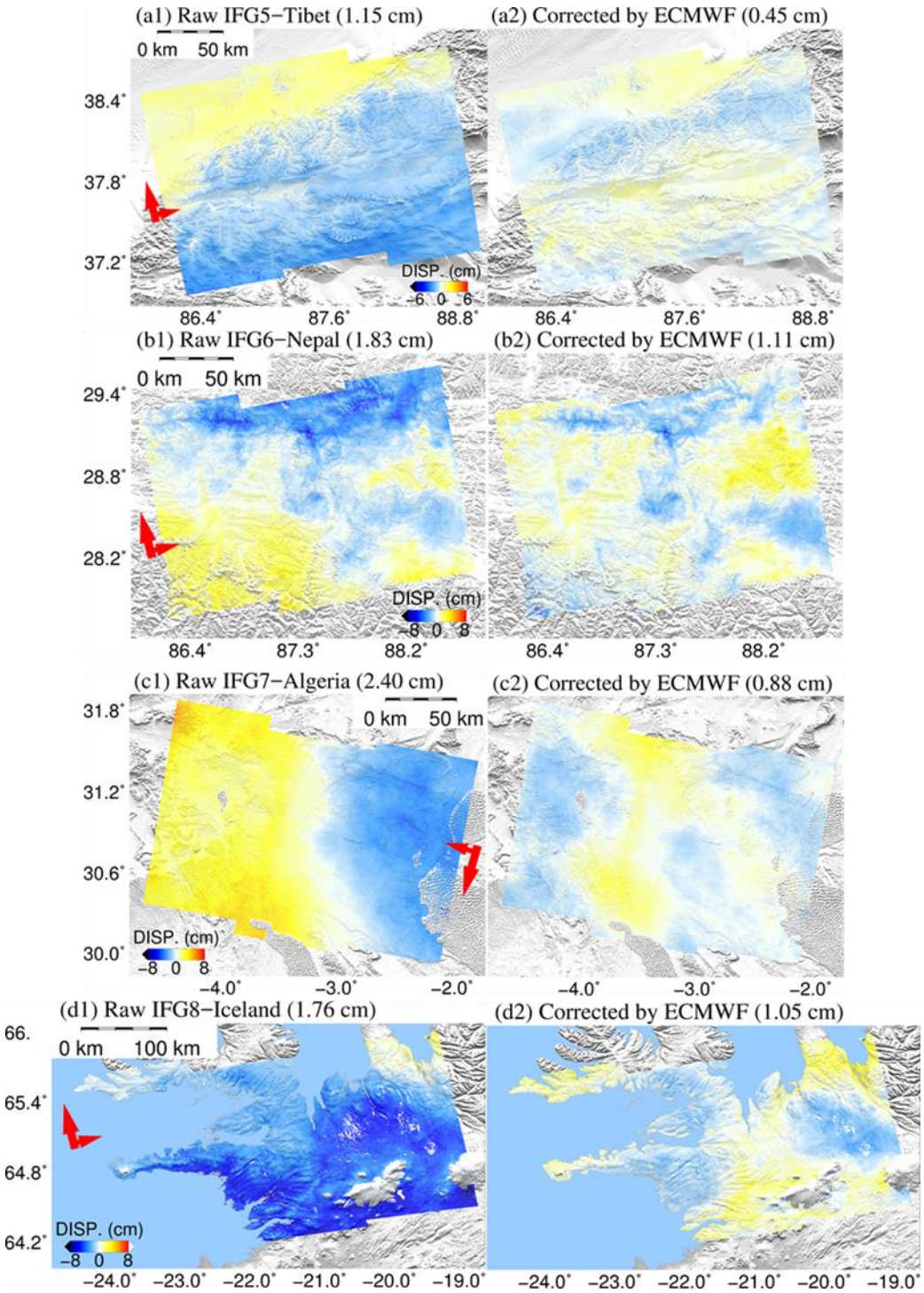

Figure 5.7 InSAR atmospheric correction using ECMWF for IFG5-Tibet, IFG6-Nepal, IFG7-Algeria and IFG8-Iceland. The first and second columns represent the raw and corrected interferograms, respectively. The numbers in parentheses indicate the phase StdDev before and after correction. The red arrow represents the radar flight direction. All phases are in LOS direction.

It is clear that for the mountainous regions (IGF5-Tibet and IFG6-Nepal), the phase errors are mostly topography-correlated and have been corrected by 61% to 0.45 cm StdDev and by 39% to 1.11 cm, respectively. The atmospheric errors on IFG5-Tibet tend to be long wavelength and thus are easier to be captured by ECMWF. The shorter wavelength effects on IFG6-Nepal, mainly due to the high topography variations, cannot be fully removed using the ECMWF model, and the remaining uncorrected errors are likely to be turbulent signals. It should be noted that for a high-altitude region (which means lower water vapour content on average), a strong turbulence effect can also be observed on interferograms (as here for IFG6-Nepal).

IFG7-Algeria is located in a desert region with fairly low altitude and limited topography variations (altitude 0.8 km ~ 1.0 km across the IFG). As shown in Figure 5.7, the magnitude of the atmospheric errors reaches up to ~8 cm (raw phase StdDev of 2.40 cm) but they appear to be mostly associated with a long wavelength signal. After applying ECMWF atmospheric corrections, turbulence errors persist but the phase StdDev has reduced by 63% to 0.88 cm. Conversely, IFG8-Iceland exhibits large topography variations (from 0 km to 1.5 km) and is located close to a polar region, where the water vapour content is lower. It can be seen from Figure 5.7 that the large magnitude (8 cm) atmospheric errors systematically affect the computed displacement across almost the entire interferogram. After correction, the StdDev of the phase errors drops to 1.05 cm (40% improvement) and is partly associated with an elevation dependent signal (the western part where the topography variations are high) and partly with a turbulent behaviour (eastern part). Hence, as for IFG5-Tibet and IFG6-Nepal, the ECMWF based correction model is suitable for obtaining corrected interferograms with a StdDev of ~1 cm or lower.

5.5 Performance Indicator Metrics

The generic atmospheric correction model developed has been evaluated at different locations globally, encompassing a range of topography, climate and GPS station distributions. The model's performance has been evaluated by considering the phase StdDev and also, for areas including GPS stations, the RMS displacement difference between GPS and InSAR. However, in practice, when actual surface movements occur and there are insufficient GPS stations to

cover the whole area, these performance indicators will fail. It is therefore important to develop additional performance indicators to inform users of model applicability, including flagging any instances when the modelled atmospheric corrections should not be applied. In this section, we introduce several additional indicators for model interpolation and atmospheric error correction performance, which include: (i) cross validation RMS of GPS and ECMWF ZTD, (ii) correlation analysis between InSAR phase and tropospheric delays, (iii) the time differences between ECMWF and InSAR acquisitions, and (iv) topography variations.

5.5.1 Indicator 1: ZTD cross validation RMS

In Section 5.2, we have used the cross-test to validate the interpolation performance of GPS and ECMWF ZTDs. The RMS of the cross validation reflects not only the pointwise ZTD interpolation precision, but also the network geometry, especially for GPS where a non-uniform and sparse station distribution often arises. It was shown in Section 5.2 that GPS corrections perform better than ECMWF for the IFG2-CA dense network case, whereas for the IFG3-Italy and IFG4-NZ cases which have sparser GPS station coverage, the ECMWF corrections perform slightly better than the GPS. One exception is for IFG1-UK where there is a sparse GPS network, but the GPS-based corrections perform well. This is mainly due to its flat topography which is another indicator to be discussed later. Section 5.2 also showed that a dense GPS network yields a lower cross validation RMS and vice versa. These results imply that the ZTD cross-RMS may be used as an indicator to reflect the atmospheric correction performance, and that a lower ZTD cross-RMS indicates a better station distribution and more precise atmospheric interpolation map. As a result, the cross-RMS of the GPS and ECMWF ZTDs are calculated for each interferogram before utilizing the corrections (Table 5.3).

5.5.2 Indicator 2: phase versus estimated atmospheric delay correlation

A high correlation between phase measurements and the computed atmospheric corrections suggests that the model is able to capture most of the atmospheric effects, and thus successful InSAR atmospheric error correction is expected. For all eight interferograms, the correlations between the phase and tropospheric delays (using the integrated model for IFG1-4 and ECMWF for IFG5-8, hereafter referred to as the "phase-delay correlation") per pixel are shown in Figure

5.8, with the statistics per interferogram also listed in Table 5.3. A high correlation of 0.86 was observed for IFG1-UK, which corresponds to a 75% improvement in terms of phase StdDev reduction, whereas for IFG5-Tibet a lower 0.57 correlation, corresponding to a 61% improvement, was obtained. The lower correlation for IFG5-Tibet may be due to the smaller magnitude of the raw phase measurements (StdDev=1.15 cm compared with 2.75 cm for IFG1-UK before correction) and therefore the atmospheric errors may not be dominating in magnitude.

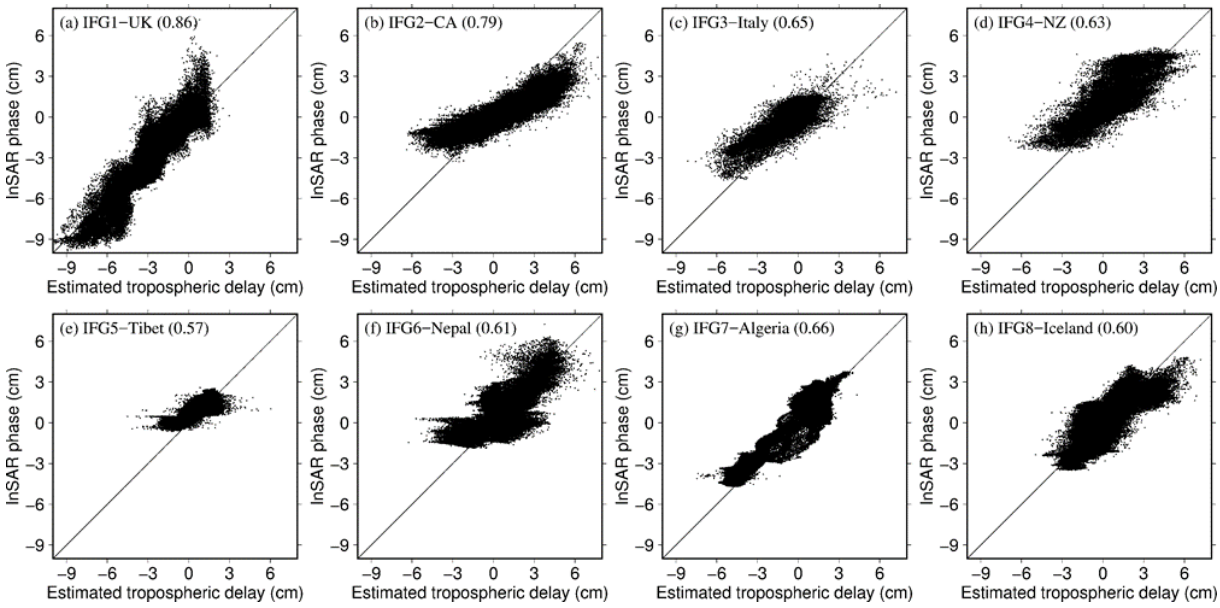

Figure 5.8 Phase and interpolated tropospheric delay correlations for all pixels in the eight interferograms. The linear relationship between phase and estimated tropospheric delay is Phase=Slope×Delay+Intercept. Phase has been converted to raw displacement in cm. Tropospheric delays have been computed using the ECMWF and GPS integrated model for IFG1-4, and ECWMF only for IFG5-8. Correlation coefficients are listed in parentheses.

5.5.3 Indicator 3: ECMWF time difference

The GPS ZTDs are coincident in time with the SAR image acquisitions, but the ECMWF ZTDs are only available every 6 hours, which can lead to time differences between the InSAR measurements and the ECMWF-based atmospheric correction maps. The temporal variation of ZTDs, especially the part due to water vapour during a short time interval (e.g., 2-3 hours) can be substantial but unpredictable and thus may cause the correction to perform poorly (e.g., Fielding et al., 2017; Li et al., 2009a). To investigate the impact of ECMWF and InSAR acquisition time differences, we used continuous GPS ZTD time series (5-minute interval) to

evaluate errors of temporally interpolating the 6-hourly ECMWF ZTDs to the measurement epoch. We used the Central California region covered by IFG2-CA and for each hour of an individual day, we linearly interpolated the nearest 6-hourly ECMWF ZTD values on to all GPS stations and computed the differences against the GPS ZTDs directly estimated at the station and for the hour considered (this approach will hereafter be called 'nearest'). This procedure was then repeated for all days of 2016 and the mean RMS difference per hour was averaged for each hour of day (0, 1, 2, …., 23) over the year. These mean hourly RMS values for the year are shown in Figure 5.9, together with variations (1-sigma), and it can be clearly seen that as the time difference from the ECMWF 6-hourly ZTD times (the model is available at 0, 6, 12 and 18 hours UTC) increases, so does the RMS and the 1-sigma range. The RMSs at hours corresponding to the greatest temporal interpolation have a peak value that is nearly 150% of the RMSs at no time difference: approximately 20 mm compared with 12 mm.

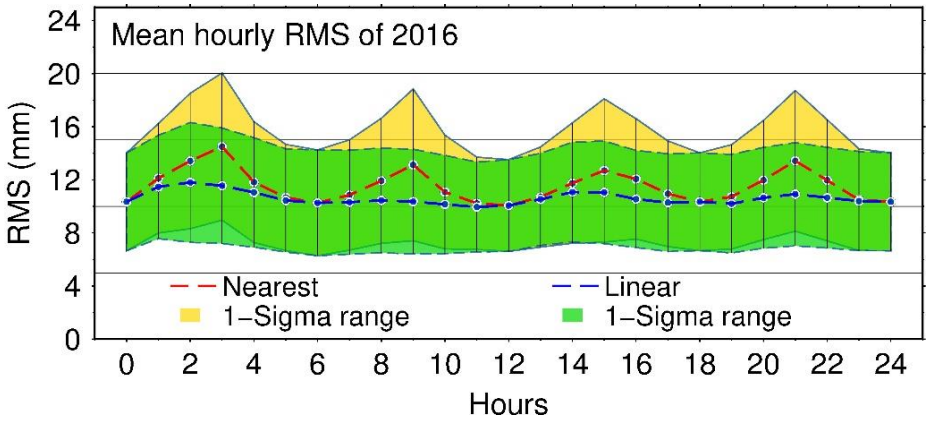

Figure 5.9 Impact of ECMWF time differences. The ECMWF ZTDs were evaluated with GPS ZTDs using one year of data from 2016 in Central California. The red line represents the mean RMS differences using the nearest (in time) data point method with 1-sigma range plotted as yellow shade. The blue line represents the mean RMS differences using linear interpolation to the InSAR observation time, with the 1-sigma range plotted as green shade.

To minimize the impact of the time differences, we applied a linear temporal interpolation in our correction model using the two closest ECMWF ZTD samples. It can be seen from Figure 5.9 that this procedure improves the performance and reduces the peak values from 15 mm to 10 mm, however there are still uncertainties during large time difference periods. As a result, we may use time difference as an indicator to highlight potential uncertainty induced by rapidly-changing atmospheric conditions.

5.5.4 Indicator 4: topography variations

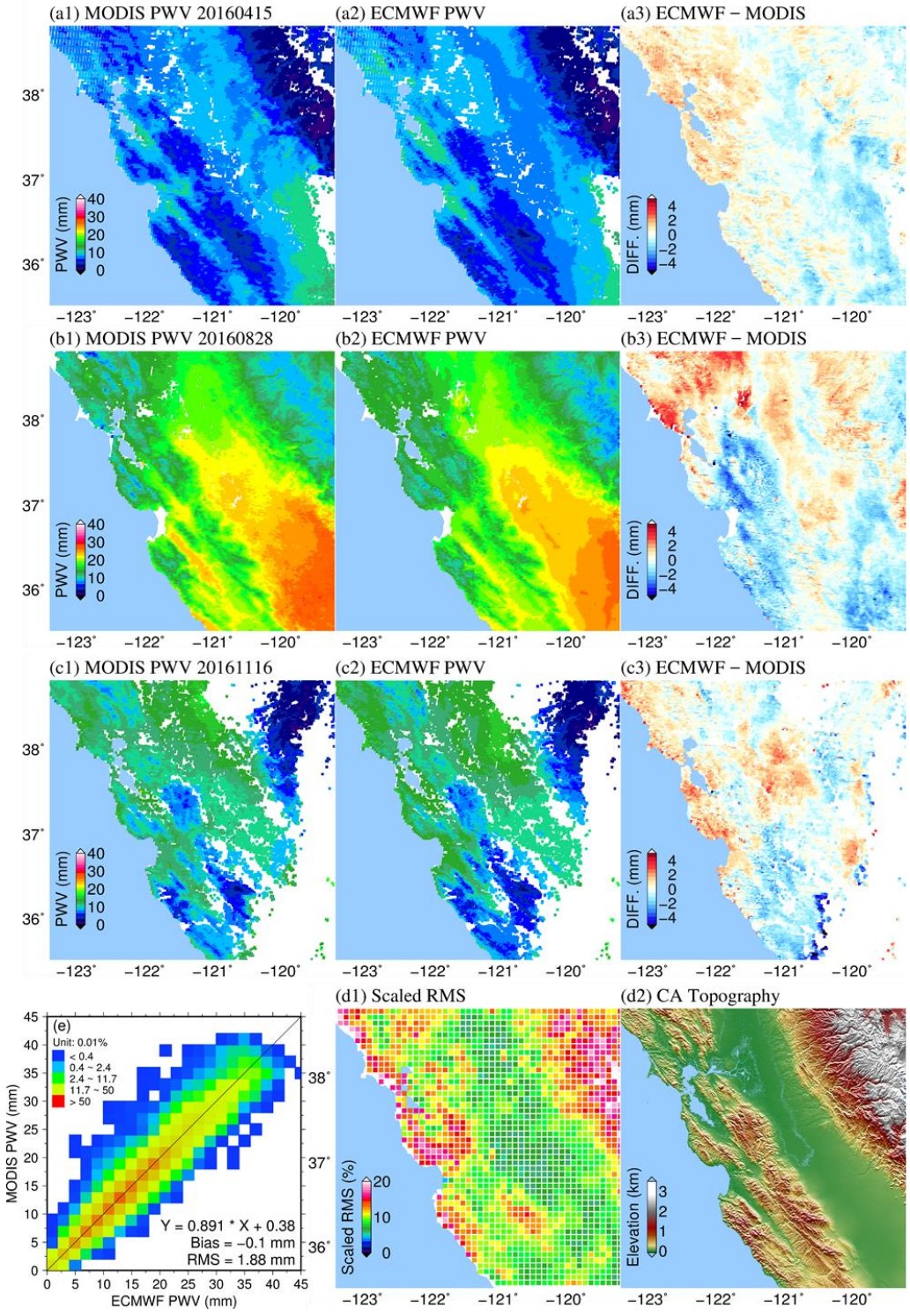

Figure 5.10 Impact of topography variations. Panels a, b and c shows differences in PWV between MODIS and ECMWF on cloud free MODIS grid cells on 20160415 (spring), 20161116 (autumn) and 20160828 (summer): (d1) is the scaled RMS = (averaged RMS of year 2016) / (averaged PWV content of year 2016) for each grid; (d2) is the topography; (e) is a linear fit between ECMWF and MODIS PWV for all available pixels of year 2016; the colour scale represents the density of occurrence.

The ZTD variations and the interpolation performance will all be affected by the topography. To assess this effect, we introduced MODIS near-infrared PWV data as 'truth' and interpolated the ECMWF PWV (with the same 0.125 degree grid distribution throughout the region) on to the MODIS PWV grid. Since MODIS PWV has a higher spatial resolution than ECMWF (~1 km compared with ~9-12 km), it can be used to evaluate the ECMWF-based model's interpolation performance relative to local topography variations. As a test case, we selected the region of Central California since it displays considerable topography variations with high mountains (~3500 m altitude) on the west coast and on the eastern portion of the domain, and nearly flat areas in the middle (under 200 m altitude).

We processed all cloud-free MODIS PWV data during 17:50 ~ 18:10 UTC (i.e. around 10 am or 11 am local time) on each day of 2016, which coincides with the ECMWF 18:00 UTC model output and hence minimizes any time interpolation errors. The elevation of each MODIS PWV grid was bilinearly interpolated to a uniform grid using the 3-arcsec SRTM digital elevation model. The ECMWF PWV was then interpolated on to the MODIS PWV grid using the ITD model, and the ECMWF PWV agreed with the MODIS PWV with an RMS difference of 1.88 mm (Figure 5.10e). Figure 5.10a-b-c show the PWV differences for three dates, from which greater differences between observations and ECMWF-derived PWV can be observed in regions with higher PWV contents. This is consistent with the magnitude of errors in other PWV sensors being proportional to the water vapour content, e.g., as found for GPS by Glowacki et al. (2006) and for MODIS by Li et al. (2003). The differences are greater in the summer and/or over lower altitude flat regions since the average PWV content is higher compared with those in the autumn or over mountain areas. Hence, to better evaluate the impact of topography variations, the RMS was scaled. We first divided the study region into uniform 1 km by 1 km grid cells and computed the RMS differences for each cell using all MODIS samples that were located in that cell during the whole of 2016. Each of the RMS values were then scaled by the average PWV content of the corresponding cell and are displayed in Figure 5.10d1. The scaled RMS appears to be strongly correlated with the topography (Figure 5.10d2), with the higher RMS values occurring over mountains and the lower RMS values over lower, flatter areas. The topography variations cause the PWV to be short wavelength in nature,

meaning it is challenging to fully model, thus making accurate InSAR atmospheric correction more difficult (Bekaert et al., 2015b; Li et al., 2009b; Zebker et al., 1997). In practice, lower performances are often expected over high topography variation areas.

Table 5.3 Model performance indicator metrics for all interferograms.

IFG	ZTD cross validation linear fit (cm)	ρ[1]	Cross RMS of GPS ZTDs (mm)	Cross RMS of ECMWF ZTDs (mm)	IFG-ECMWF time difference (Minutes)	Topography variation
IFG1-UK	Y=1.096X-0.928	0.86	11.5	8.3	11	Low
IFG2-CA	Y=0.699X-0.952	0.79	13.1	9.2	118	High
IFG3-Italy	Y=0.624X+0.217	0.65	12.6	4.8	56	Medium
IFG4-NZ	Y=0.693X+1.014	0.63	12.0	6.4	75	Medium
IFG5-Tibet	Y=0.454X+0.531	0.57	-	1.9	8	High
IFG6-Nepal	Y=0.669X+0.522	0.61	-	7.9	21	High
IFG7-Algeria	Y=0.690X+1.078	0.66	-	5.1	11	Low
IFG8-Iceland	Y=0.718X+0.112	0.60	-	4.8	58	Medium

[1]Phase-delay correlation

5.5.5 Uses of the indicator metrics

The performance indicators presented above are particularly useful for InSAR time series analysis, e.g. severe weather phenomena will cause the troposphere to be more turbulent and result in larger cross RMS values for ECMWF and GPS, which will reduce the correction performance. Figure 5.11a provides an example of the performance indicator matrix for all interferograms in this chapter and it should be noted that (i) the phase-delay correlation, cross RMS and phase StdDev reduction are direct statistics which link to the displacement measurement quality and (ii) ECMWF time difference and topography variation are indirect indicators that should be considered when evaluating the performance. The correction performance cannot be quantified by one indicator solely (e.g. the UK has a larger cross RMS than CA, but higher performance due to the large topography variation in CA) and only the combination of all the indicators can provide a complete picture of the atmosphere condition and the potential correction performance.

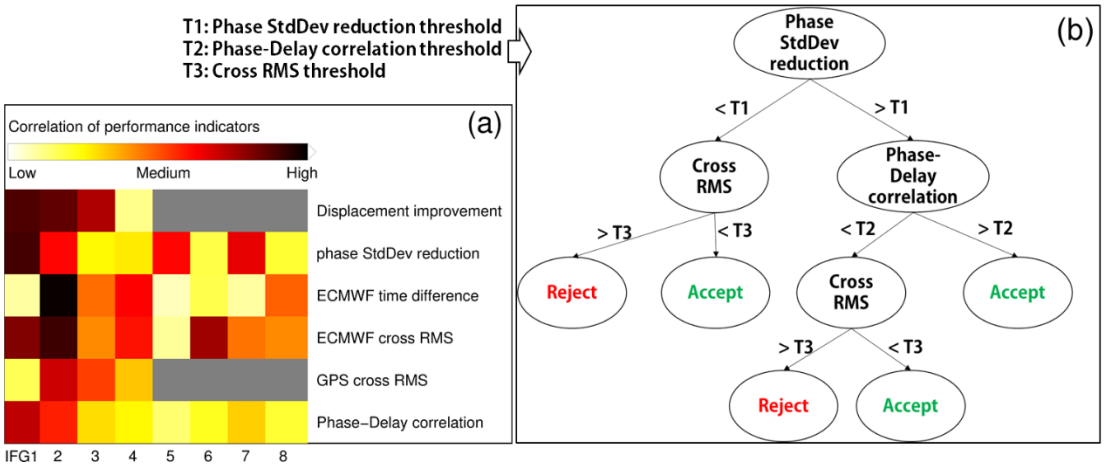

Figure 5.11 Performance indicator metrics. (a) indicators for all eight interferograms in this chapter. (b) A decision tree for the use of the performance indicators.

Figure 5.11b provides a simple decision tree to utilize the proposed statistical indicators, in which thresholds are set to identify the interferograms with large cross RMS, StdDev reduction, and small phase-delay correlation. Particularly, using the cross RMS and the phase-delay correlation statistics, it is possible to identify potential problematic interferograms in a time series. Applying the predefined thresholds (T2 and T3 in Figure 5.11b), which should be defined case by case, interferograms with large cross RMS and low correlation could be excluded to ensure a high correction confidence and hence a better performance. This procedure will be discussed further in Chapter 6 and 7 using real datasets. In this way, an automatic processing chain is possible in order to process a large volume of data or long time series, with all interferograms being quality controlled by the indicators.

5.6 Generic Atmospheric Correction Online Service for InSAR (GACOS)

We released the Generic Atmospheric Correction Online Service (GACOS) based on the proposed generic atmospheric correction model (http://ceg-research.ncl.ac.uk/v2/gacos/) on 6th June 2017. The main interface is shown in Figure 5.11. The current version only includes the ECMWF data, but we will soon release an upgraded version to include the global GPS tropospheric delay products. GACOS aims to provide the InSAR atmospheric correction map, globally with a short delay of two days, in a convenient way, with its performance indicators being processed when requested.

Since releasing, GACOS has received over 15,000 requests from all over the world (until

December 2018), and attracted over 500 identical users for variety InSAR related researches, such as tectonic or volcanic modelling, landslide and city subsidence monitoring. Given the convenience and global availability, it has rapidly responded to events such as the Maoxian Landslide (24 June 2017) and the Xinjiang earthquake (8 August 2017) by correcting interferograms contaminated by serious elevation dependent atmospheric errors. The corrected inteferograms facilitated the detection of surface damages, and aided the rescue and recovery operations, which was reported by over 20 social media and organizations.

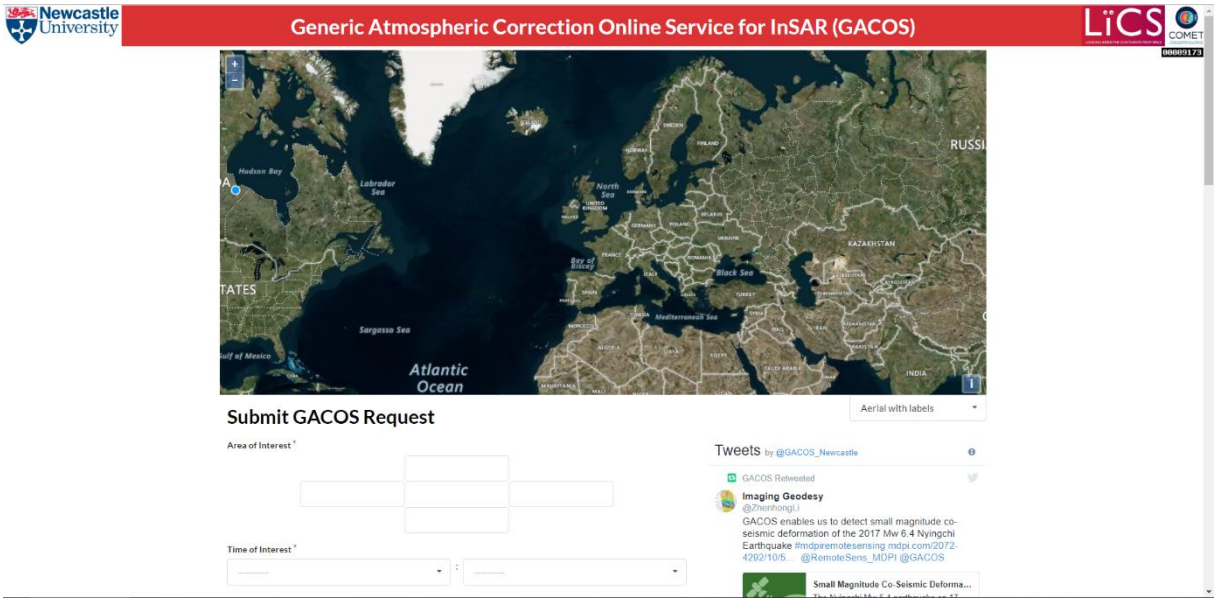

Figure 5.12 Main interface of the GACOS website.

The GACOS service is a major output of this thesis, involving the key innovations and advantages of the proposed generic atmospheric correction model, and will be used in the following co- and post-seismic modelling in Chapter 6 and 7.

5.7 Summary

A generic InSAR atmospheric correction model has been developed in this chapter by using both ECMWF grid model output and GPS ZTD pointwise observations, tightly integrated using the ITD model to produce atmospheric correction maps. The ECMWF data, available globally with a two-day time latency compared to several months for ERA-Interim, provide the basic input of the correction model, which is enhanced using GPS-estimated ZTDs where available, which improve its performance both spatially and temporally. The developed InSAR atmospheric correction model is (i) global and all time useable, including in the presence of

clouds; (ii) potentially near real-time (two days latency from ECMWF, while GPS ZTDs can be generated in real-time or with much lower latencies); (iii) robust and easy to implement automatically, with quality control indicators.

The model developed was evaluated using eight globally distributed interferograms of about 250 km x 250 km spatial extent in flat and mountainous topographies, mid-latitude and near polar regions, monsoon and oceanic climate systems, with or without GPS networks. The average improvements in terms of phase StdDev resulting from the atmospheric correction maps applied were 47%, 49%, 54% for GPS, ECMWF and the integrated corrections, respectively. The corrected InSAR LOS displacements were also compared with the GPS displacements with average RMS improvements for the four interferograms of 55%, 45% and 63% for GPS, ECMWF and the integrated corrections, respectively. Hence the integrated model performs the best, with the combination of different data sources increasing the model's reliability, and the displacement StdDev and RMS difference arising for the corrected interferograms considered is approximately 1 cm.

A set of performance indicator metrics has also been developed to enable the model's suitability for InSAR atmospheric correction application to be assessed, and we recommend their adoption as indicators to inform users when abnormal conditions occur and give insights of the confidence level of the correction results.

The model developed can be used either on an individual interferogram to identify small amplitude ground movements (e.g., city subsidence, small landslide), or on a series of interferograms for larger scale plate movements and longer term monitoring (e.g., post- or inter-seismic motion) which allows for temporal filtering to further reduce the residual atmospheric errors and to achieve mm/year level displacement StdDev. It is believed that the method is particularly beneficial for InSAR time series over mountain areas as the residual atmospheric errors after correction are more likely to be randomly temporally distributed, which allows an easier minimization through time series analysis, and will be discussed further in Chapter 7.

Chapter 6. Co-seismic Model of the 2017 Mw 6.4 Nyingchi Earthquake from Atmospheric Corrected InSAR Measurements

The Nyingchi Mw 6.4 earthquake on 17 November 2017 is the first large event since 1950 at the southeast end of the Jiali fault. It was observed by ESA's Sentinel-1A InSAR measurements, providing the potential to determine the fault plane geometry as well as co-seismic slip distribution, and to understand future seismic hazards. However, due to the limited magnitude of its surface displacements and substantial topographic variations, the derived InSAR co-seismic interferograms were contaminated seriously by atmospheric effects, making it difficult, if not impossible, to determine the source parameters and co-seismic slip distribution. In this chapter, we apply the GACOS atmospheric correction developed in Chapter 5 to the co-seismic interferograms and address the importance of the atmospheric correction for identifying small magnitude earthquake-generated surface displacements.

6.1 Introduction

On 17 November 2017, an Mw 6.4 earthquake hit the Tibetan Plateau, 63 km northeast of Nyingchi, China (Figure 6.1). The epicentre lies on the southeast edge of the Tibetan Plateau where the dominant tectonic movement is driven by the oblique convergence between the Indian and Eurasian plates (Armijo et al., 1986; Tapponnier et al., 1982; Yin and Harrison, 2000). This region has long been characterized as tectonically weak (e.g., Lee et al., 2003; Searle et al., 1998; Weinberg and Searle, 1998) with a limited number of recorded historical events according to the United States Geological Survey (USGS) and the China Earthquake Administration (CEA). Only a limited number of geodetic surveys have been conducted in this region, making this event the first large earthquake captured by one of the modern geodetic techniques: the SAR interferometry with the ESA's Sentinel-1A radar satellite (Malenovský et al., 2012). These InSAR measurements provide high spatial resolution co-seismic surface displacements, which can be used to infer the source parameters of the seismogenic fault, assess future seismic hazards and better understand the activity of seismogenic structures.

In the presence of atmospheric effects, only an accuracy of several centimetres can be reliably

achieved for displacement retrieval even under a relatively quiet atmospheric environment (e.g., Fielding et al., 2017; Jolivet et al., 2011; Parker et al., 2015). However, while being extensively addressed in post- and inter-seismic studies where a millimetre level accuracy of velocity mapping is needed (e.g., Fielding et al., 2017; Hooper et al., 2012; Walters et al., 2013), tropospheric delays are typically ignored in co-seismic modelling under the hypothesis that the magnitude of co-seismic signals is much greater than that of tropospheric delays (e.g., Hamling et al., 2017; Liu et al., 2004; Polcari et al., 2017; Simons et al., 2002). However, for earthquakes with small magnitude surface displacements, tropospheric delays can be of the same order or even larger than ground motions. This is especially true for the Nyingchi earthquake which occurred in a high-altitude region with substantial topographic variations, and the co-seismic signals were substantially masked by the elevation dependent tropospheric delays, making it difficult to determine the source parameters and to resolve the fault slip distribution. To deal with small magnitude earthquakes, Lee et al. (2017) used a stacking method to combine a series of interferograms to reduce tropospheric errors in order to extract small co-seismic signals for three Mw 5.2–5.6 2004 Huntoon Valley earthquakes. However, it has a delayed response to the events and requires additional data before and after the earthquakes, which are not always available. Fattahi and Amelung (2015) utilized the ERA-Interim global atmospheric model to correct tropospheric effects for the co-seismic interferograms of the Mw 5.5 Ghazaband earthquake, with only the stratified component being considered. Feng et al. (2016) employed MERIS water vapour data for correcting the RADARSAT-2 images of the Mw 8.3 Illapel earthquake claiming it would outweigh the ERA-Interim, however, it is not available for recent satellite missions such as Sentinel-1 and ALOS-2 (Li et al., 2009b).

This chapter aims to use GACOS to overcome the disadvantages of the abovementioned correction methods, including (i) a delayed response of 1 ~ 3 months for the event; (ii) low spatial-temporal resolution for capturing the tropospheric turbulence; (iii) incompatibility with newly launched satellites such as Sentinel-1 and ALOS-2.

6.2 Tectonic Setting

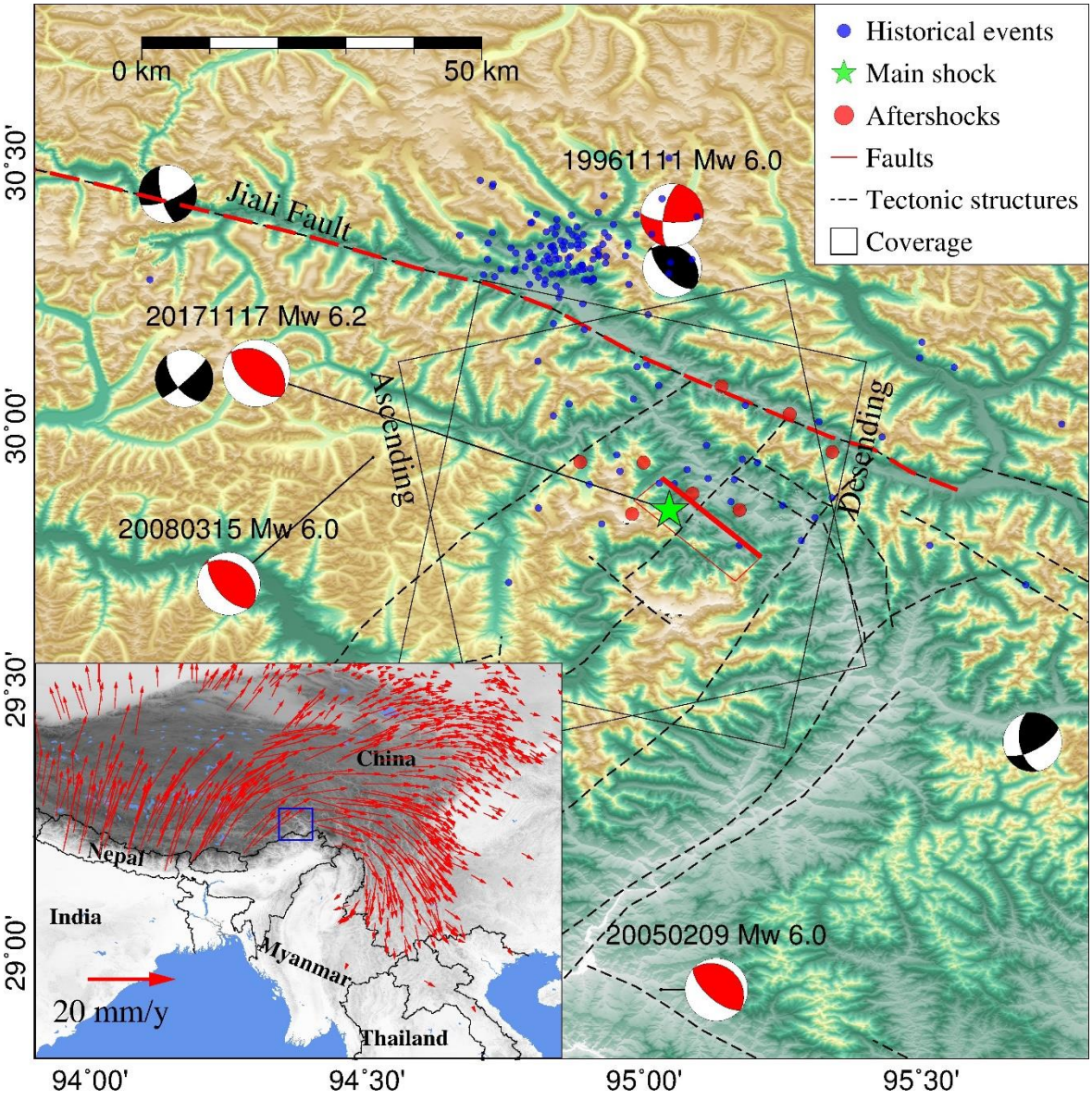

Figure 6.1 Tectonic setting for the Mw 6.4 Nyingchi earthquake. Historical earthquakes recorded by the USGS database from January 1950 to October 2017 are plotted as blue dots, the main shock is indicated by a green star and aftershocks by red dots. Historical major events recorded by the CEA are plotted as a beach ball (red for Mw > 6.0, and black for Mw < 6.0). The GPS velocity field (red arrows) is referenced from Liang et al. (2013). The event was covered by two pairs of Sentinel-1A images with different geometries (solid line boxes). The red solid line is the modelled fault plane projected onto the Earth's surface.

Driven by the northward movement of the Indian plate relative to the Eurasian plate at a rate of ~4 cm/year (Wang et al., 2001), the tectonic activities in southern Tibet are dominated by a mixture of normal and strike-slip faulting (Armijo and Tapponnier, 1989; Lee et al., 2003; Tapponnier et al., 1982), which is in contrast with the thrust faulting along the ranges bordering

the Tibetan Plateau (Molnar and Chen, 1983). Most of the faults are predominantly south-north striking normal faults, although many locations also show oblique displacements, reflecting the eastward tectonic extrusion mostly during ~18-13 Ma (Coleman and Hodges, 1995; Williams et al., 2001). The Karakoram-Jiali strike-slip fault system terminates the normal faulting system at its northern tips and releases part of the collision energy. Lee et al. (2003) suggested that the Jiali fault was initiated during ~18-12 Ma and can be best explained as the accommodation of deformation from the oblique convergence between the India and Eurasian plates. Furthermore, the clockwise rotation of the GPS velocity field from north-eastward to eastward reflects a northeast shortening which is also recorded by several historical events (Figure 6.1).

The Mw 6.4 Nyingchi earthquake occurred on a blind fault in the southeast part of the main Jiali fault, where there were a limited number of recorded historical events. From here, the Jiali fault is divided into several north-south striking faults such as the Puqu fault and the Kumon fault. One Mw 6.0 strike-slip earthquake happened on 11 November 1996 on the north side of the Jiali fault, and another more thrust-slip Mw 6.0 event happened on 15 March 2008 on the south side. Most of the historic small quakes (< Mw 6.0) were centred on the north part of the Jiali fault. The aftershocks were randomly distributed and small in magnitude (< Mw 5.0), suggesting a high percentage of stress release by the main shock.

6.3 Datasets and Atmospheric Delay Mitigation

The event is spatial-temporally covered by two pairs of Sentinel-1A images in descending and ascending geometries, respectively (Table 6.1). The interferograms were generated by the same method as in Section 4.2.

Clear atmospheric effects can be observed in Figure 6.2, especially over mountainous areas. For the descending interferogram, the co-seismic signals were substantially masked by atmospheric delays, making it difficult even to check the pattern of ground motions. The magnitudes of the atmospheric delay and co-seismic signal were comparable, hence decreasing the signal to noise ratio and leading to unreasonable constraints for modelling. These errors can

be largely ignored when dealing with earthquakes with large ground motions as the signal to noise ratio is high, but they become vital when modelling small and/or deeply buried earthquakes with small surface displacements.

Table 6.1 Sentinel-1A interferograms used for the co-seismic modelling and their atmospheric correction results.

	Descending	Ascending
Dates	20171106-20171118	20171111-20171123
Acquisition time (UTC)	23:37	11:41
Temporal Baseline (Days)	12	12
Perpendicular Baseline (m)	9.6	32.9
Raw Phase StdDev[1] (cm)	1.83	1.47
StdDev after Method 1[2] (cm)	0.73	0.80
StdDev after Method 2[3] (cm)	1.13	0.93
StdDev after Method 3[4] (cm)	1.28	0.99

[1] The standard deviation of the observed phases excluding near-field deforming area.

[2] GACOS atmospheric correction.

[3] Conventional removal of signals correlated with altitude.

[4] ECMWF interpolated by bilinear.

To overcome this, we applied the GACOS atmospheric corrections on the Sentinel-1A interferograms to mitigate their atmospheric effects. The iterative separation in the ITD model performs better over mountain areas compared to the traditional models without iteration, and therefore is valuable to this study as the main co-seismic displacements occurred over a high-altitude mountain (over 3 km), where the elevation dependent signal was dominating. The performance of GACOS was also compared against two other methods. The first is a conventional method by removing signals which are correlated with the altitude. This was implemented by fitting the observed phase (excluding the near-field observations) to an exponential function: phase=a*exp(b*h), where a and b are the estimated coefficients, h is the altitude. Phases correlated with altitude are removed after estimating the coefficients. The second method is to use high-resolution ECMWF data but with a simple bilinear interpolator instead of ITD. It is clear in Figure 6.2 that the co-seismic signals stood out with two major displacement lobes after the GACOS correction.

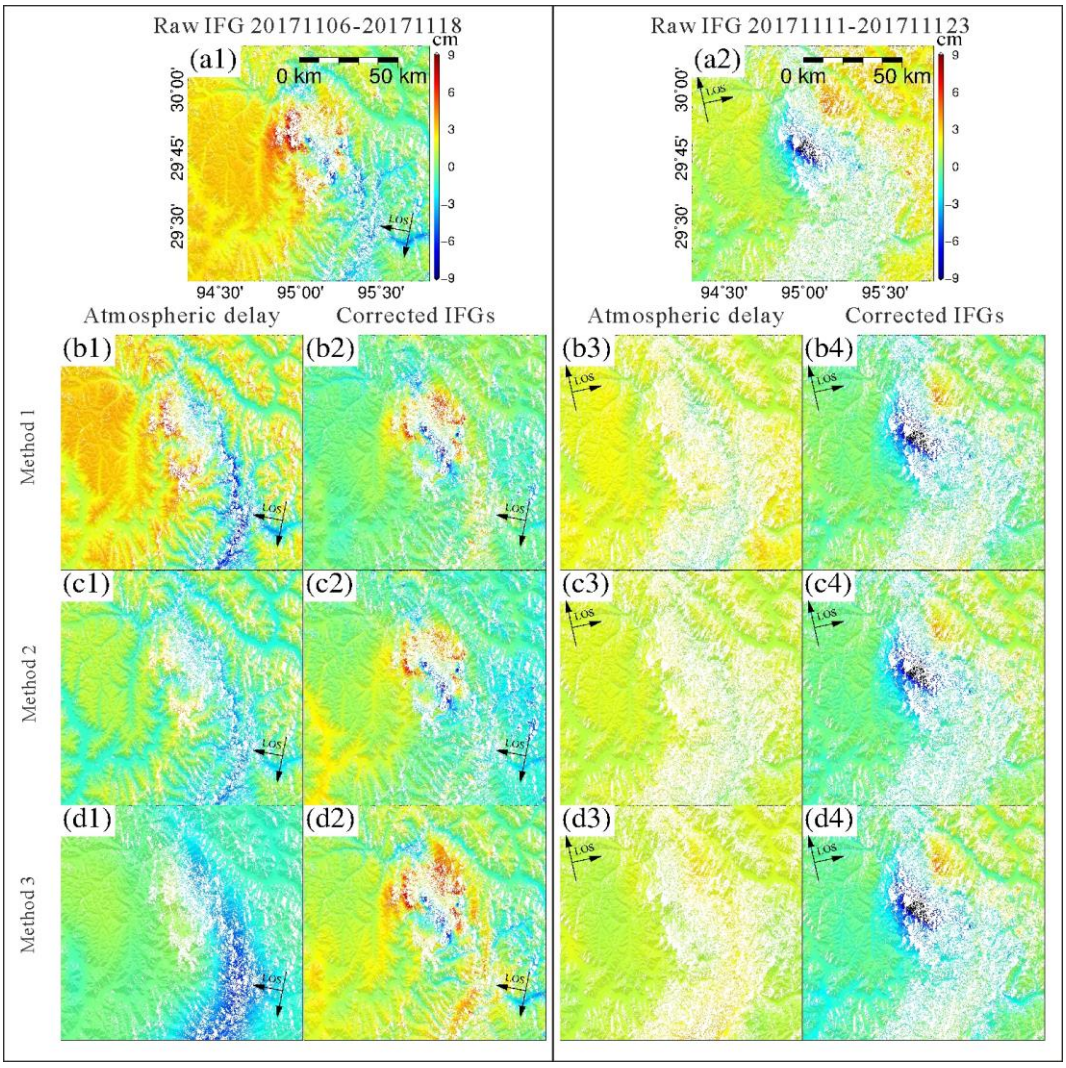

Figure 6.2 InSAR observations and atmospheric corrections. (a1)-(a2) are raw interferograms. Method 1 (b1-b4) is the GACOS correction. Method 2 (c1-c4) is to remove signals correlated with elevation. Method 3 (d1-d4) is to use the bilinearly interpolated ECMWF ZTD. Note the coverage is different from Figure 6.1 as the very far-field data has been excluded.

Table 6.1 lists the statistics for the three methods, among which GACOS presented the best performance, especially for pair 20171106-20171118 as it is more contaminated by atmospheric effects. The phase StdDev after correction for pair 20171106-20171118 reaches 0.8 cm, substantially improved from the elevation dependent signal removal method (1.13 cm) or the bilinear interpolation method (1.28 cm). Although the atmospheric contamination was limited on pair 20171111-20171123, we still see more improvements after the GACOS correction over the northeast and southwest areas, compared to the other two methods. The simple bilinear interpolation performed the worst because the elevation dependency of the tropospheric delay was not considered, leaving the ECMWF data being over-interpreted over some large topographic variation areas (e.g., the valley in the southeast of Figure 6.2d1). Although the

atmospheric contamination in Figure 6.2a was, to some degree, correlated with topography, their correlation may have very localized characteristics and is hard to be described by a single equation across the whole interferogram. The phase-elevation correlation can be shifted due to the effect of water vapour flow (Onn and Zebker, 2006), making the peak delay value to occur not necessarily on the peak altitude. Furthermore, the removal of the elevation dependent signal method has a large potential for removing actual ground displacements.

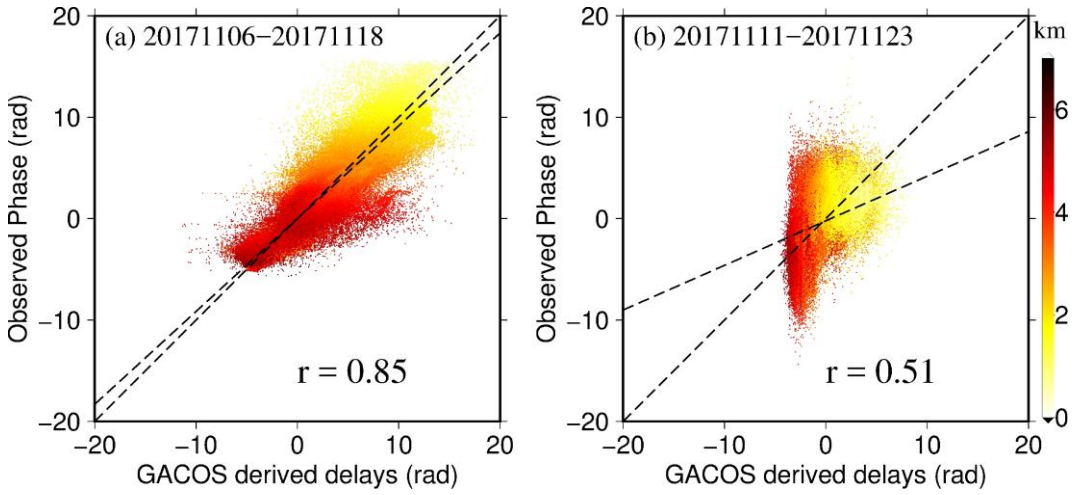

Figure 6.3 Correlations between the observed phase and the GACOS correction for the descending (a) and ascending (b) tracks, respectively. Each dot represents one pixel on the interferograms and the colour scale corresponds to its elevation. r is the correlation ratio.

To further assess the reliability of the GACOS correction, we calculated the correlation between the observed phase observation and the GACOS derived tropospheric delay for all pixels, as was done in Section 5.5.2. A high correlation is found for the descending interferogram in Figure 6.3a, suggesting that GACOS was able to capture most of the atmospheric effects, and therefore resulting in a successful correction. The small magnitude of the tropospheric delay of the ascending interferogram, on the other hand, produced a lower correlation. Another important statistic is the phase StdDev after correction (computed by excluding the near-field co-seismic region), which dropped by approximately 53% after the GACOS correction, compared to 37% for the elevation dependent signal removal method and 31% for the bilinear interpolation method, and reflected the flat phase patterns over the far-field region. All these statistics demonstrate a successful tropospheric correction and ensure a high precision of the corrected data. The signal to noise ratio was improved, making the data more applicable to the

following modelling step.

6.4 Co-seismic Modelling and Results

The GACOS atmospheric correction improved the signal to noise ratio of the interferograms, making the near-field displacement stand out. It reduced the elevation dependent atmospheric error over the far-field and mountainous regions, where the other two methods failed due to the steep topography. The corrected interferograms were then used for the following co-seismic modelling, implemented in two steps, (i) the non-linear fault geometry inversion; and (ii) the linear fault slip distribution inversion. To reduce the high spatial correlation and computation burden of the modelling, pixels with coherence smaller than 0.4 were masked, and the masked, corrected interferograms were then down-sampled using a quadtree quantization algorithm. This led to 1345 input samples on the descending track and 1947 on the ascending track, respectively.

6.4.1 Fault geometry inversion

The first step of the co-seismic modelling is to determine the fault geometry by minimizing the square misfit between the observed and modelled surface displacements, incorporating a uniform slip model on a rectangular fault in a homogeneous elastic half-space (Okada, 1992). An improved particle swarm optimization (Feng et al., 2013) was utilized to solve the non-linear equations, with a downhill simplex method (Nelder and Mead, 1965) searching for the preferred solution and therefore avoiding the convergence at a local minimum. The best-fit fault geometry parameters are 132.8^0 for the strike angle and 59^0 for the dip angle. The optimal rake angle is 115^0, reflecting a combination of right-lateral strike and reverse dip slips. The resolved fault depth is 9 km with a total moment release of 4.84e+18 Nm, corresponding to a magnitude of Mw 6.4. Our model suggests a dip angle of 59^0, larger than the USGS's solution of 36^0, and allows the rake angle to vary from 80^0 to 115^0. The overall explaining ratios (defined as (1-abs(residual)/observation) for the near-field deforming area) are respectively 78% and 82% for the descending and ascending interferograms, corresponding to misfits of 1.12 and 0.95 cm. The residuals on the descending interferogram may be due to a combined contribution of interferometric decorrelation in the near-field and residual atmospheric delays.

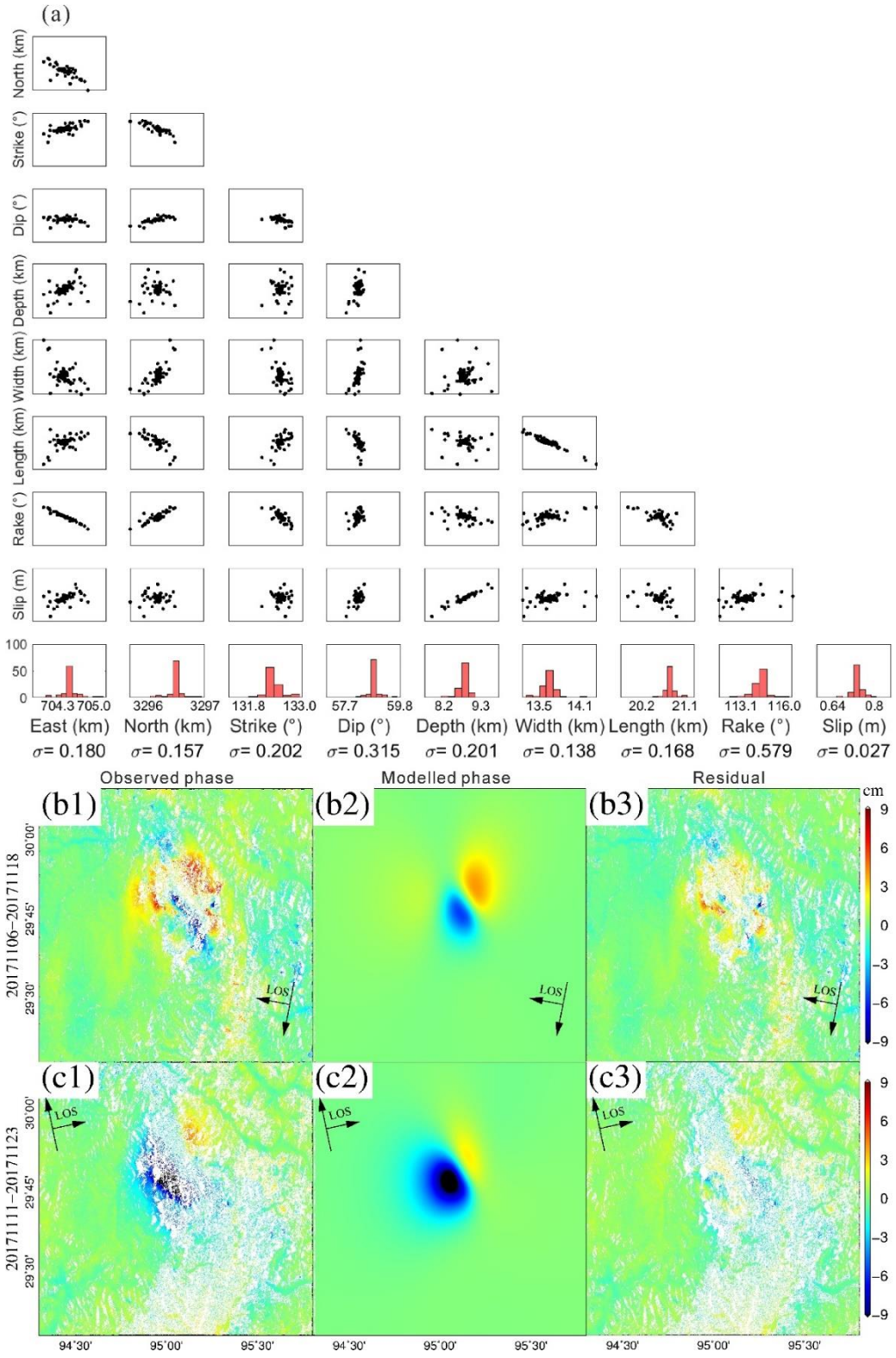

Figure 6.4 Source parameter inversion. (a) Uncertainty analysis by the Monte Carlo test for the non-linear inversion: standard deviation (red histograms) and trade-offs (scatterplots) between the model parameters. The vertical axes of the first column share the same scale with the bottom horizontal axes in (a). The rest figures are, observed observations (b1, c1), modelled displacement maps (b2, c2) and residual maps (b3, c3).

A Monte Carlo test was performed to estimate the uncertainties and trade-offs of the fault

geometry parameters based on the method described in Yokota et al. (2016). The far-field observations were used to construct an approximate variance-covariance matrix (VCM) with which 100 perturbed datasets were generated. These datasets were then used to determine a set of 100 fault geometry solutions, using the same method as described above. The distribution of each model parameter from the Monte Carlo test is plotted in Figure 6.4a as a histogram to visually assess the uncertainty in that parameter, with scatterplots between every two parameters being plotted alongside to assess the trade-offs between those parameters. Most of the parameters were well resolved, appearing as tight clusters in the scatterplots with narrow peaks in the histograms. The overall uncertainties were considered small, revealing a substantial confidence level in the non-linear estimation.

6.4.2 Co-seismic slip distribution inversion

The second step is to linearly resolve the slip distribution by constructing a 15 km × 25 km fault plane and discretizing it into 0.5 km × 0.5 km patches. For each fault segment, the strike and dip slip components are estimated using the green functions defined by the source parameters (Okada, 1986), with its striking angle being fixed to the value of the first step. Meanwhile, the Akaike's Bayesian Information Criterion (ABIC) method (Fukahata and Wright, 2008) is used to search for the optimal smoothing factor and dip angle, simultaneously, by minimizing the ABIC function:

$$ABIC(\alpha^2,\delta) = -2\log\int p(\mathbf{a};\alpha^2,\delta \mid \mathbf{d})d\mathbf{a} + C \qquad \text{(Equation 6.1)}$$

where α^2 is the smoothing factor; δ is the dip angle; p is the probability density function; **a** is the fault slip vector and **d** is the observation vector; C is the constant that is not related to the smoothing factor and dip angle. For detailed equations related to the ABIC, please refer to Fukahata and Wright (2008). Figure 6.5d shows that the fault dip can be well determined from the two tracks of InSAR observations, with the smoothing factor not substantially affecting the data misfit for this small event.

The resolved fault plane slip distribution is shown in Figure 6.5 and can be divided into two regions. Region A was characterized by right lateral slip components with a rake angle of ~115^0 and a maximum slip of 1.9 m. The slips here were concentrated at depths between 5 to 11 km

and peaked at 8 km. Region B occupied nearly pure dip slip components with an averagely smaller magnitude compared to A. The dip slip components were deeper than the strike slip components with its maximum occurring at 10 km. The hypocentre was located at the west of the fault plane, reflecting the eastward propagation of the fault rupture. The fault slipped for a distance of 25 km with varying slip magnitude from 0.3 m to 1.9 m. The transition from the strike slip in the west to the dip slip in the east well reflected the oblique convergence of the Indian plate. In this region, the Tibetan Plateau is pushing out eastwards, resulting in the east-west extension, which may be revealed by the strike-slipping Jiali fault.

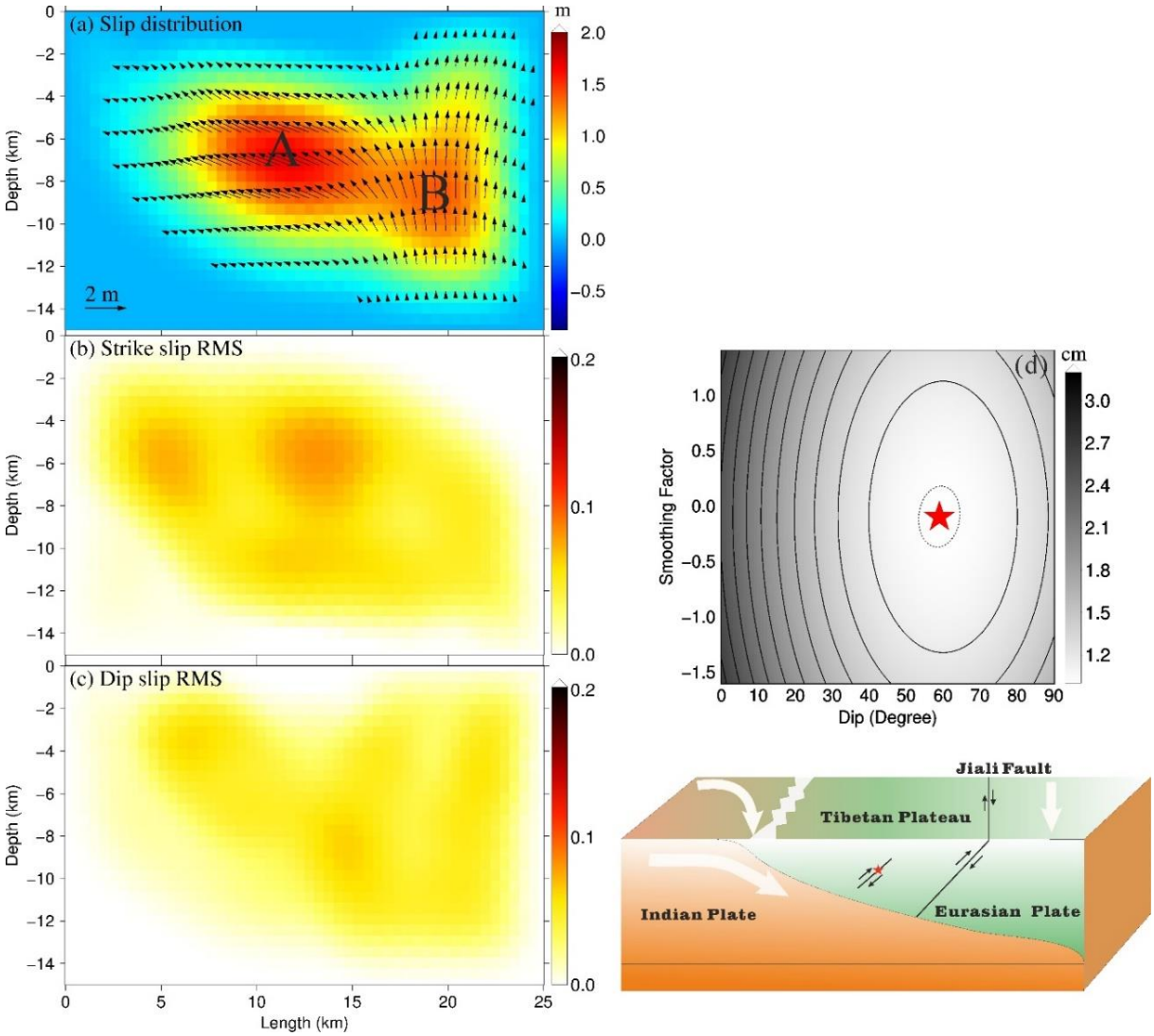

Figure 6.5 The fault plane slip distribution of the Nyingchi Mw 6.4 earthquake (a). (b) and (c) are the slip RMS values by the Monte Carlo test along the strike and dip directions, respectively. (d) is the contour map of the ABIC searching for the optimal smoothing factor and fault dip. The smoothing factor is represented as log(α2) in Equation 6.1. The colour bar indicates the data misfit. The determined optimal values are 0.9 for α^2, 59^0 for the dip angle. The fault geometry is also illustrated with reference to the Jiali fault and the Indian and Eurasian Plates.

To assess the uncertainty and resolution of the best-fit slip distribution, two separate error analysis techniques were employed, the Monte Carlo and the checkerboard tests. The Monte Carlo test was used to estimate the uncertainty of the best-fit slip distribution, in a similar way as for the fault geometry parameter uncertainty estimation. It was implemented by perturbing the observations 1000 times with a spatial noise covariance matrix estimated from the residuals of the best-fit solution. 1000 solutions could be obtained using these synthetic observations in the same way for the best-fit slip distribution and their RMS differences against the best-fit solution were calculated (Figure 6.5b, c). The overall RMS differences were well below 0.2 m, with a mean value of 2.8 cm for the strike slip component and 2.0 cm for the dip slip component, respectively. The greatest RMS difference occurred at a depth of 6 km for the strike slip, while it is 9 km for the dip slip.

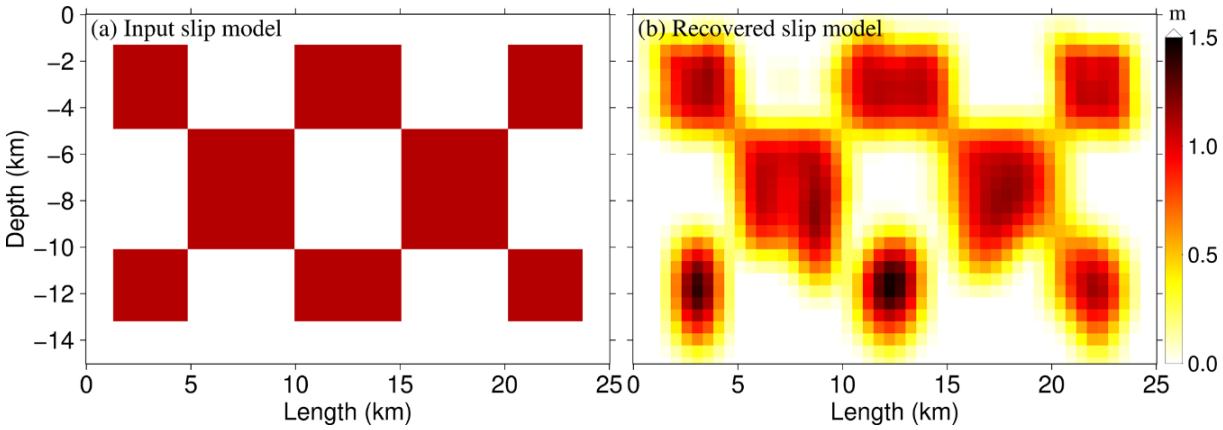

Figure 6.6 Checkerboard test for the slip distribution using the modelled fault geometry and the InSAR observation distributions. The input slip sources are 2 m reverse slips.

To assess the inverted resolution of the fault slip distribution and the reliability of the input observation's distribution, a set of checkerboard-like slip sources on the fault plane were used to generate a set of synthetic observations, spatially co-locating with the original observations. These synthetic observations were used to recover the simulated checkerboard-like slip sources, showing in Figure 6.6 (Yokota et al., 2016). The checkerboard-like slip sources were well recovered, with a shallower source experiencing higher resolution and a deeper source obtaining poorer resolution. This reflects a good distribution of the input observations and a reliable retrieval of the fault slip distribution.

6.5 Summary

In this chapter, we inverted for the fault geometry and the slip distribution of the Nyingchi earthquake using InSAR observations. This is the first time in this region that a large event (> Mw 6.0) was captured by a modern geodetic technique. The observations provide valuable information on the local faulting system and tectonic strain balance induced by the oblique convergence between the Indian and Eurasian plates over southeast Tibet.

After applying GACOS atmospheric corrections, the Sentinel-1A interferograms were able to map the Nyingchi Mw 6.4 earthquake with small ground displacements but substantial atmospheric effects. The elevation dependent atmospheric contamination was largely reduced, which was crucial due to the region's steep topography. The phase StdDev dropped from 1.83 to 0.73 cm for the descending track and 1.47 to 0.80 cm for the ascending track, which outperformed the phase correlation analysis method (1.13 and 0.93 cm after correction respectively for the two orbits) and a simple bilinear interpolation method (1.28 and 0.99 cm after correction respectively for the two orbits). The fault geometry and slip distribution were inverted using the corrected interferograms and a mixture of right lateral and reverse slip distribution was found. The maximum slip on the determined fault was 1.9 m, occurring in the northwest part of the fault plane at a depth of 8 km.

The oblique convergence between the Indian and Eurasian plates results in a wide shear zone and the rocks are intensely folded and faulted parallel to the shear zone with the main steeply dipping right lateral strike-slip Jiali fault. The Jiali fault was most active during ~18-12 Ma, but became quiet after then with limited large events occurring. The Nyingchi Mw 6.4 earthquake is the most powerful event ever recorded in this region since 1950 and the modelled fault slips suggest it released at least part of the cumulated stress induced by the background Indian-Eurasian tectonic motion. The modelled surface fault trace is parallel to the Jiali fault with a small rotation to the northeast. Most of the surface displacements are concentrated on the hanging wall (southwest of the fault trace), consisting with the northeast shortening of the clockwise rotation of the eastern Tibetan Plateau revealed by the GPS velocity (Figure 6.1).

The major contributions of this chapter are (i) to apply the GACOS correction to improve the InSAR capability for measuring small magnitude earthquakes; (ii) to map the buried fault geometry located south of the Jiali fault; (iii) to provide evidence of the oblique convergence between the Indian-Eurasian plates from the modelled fault plane slip distribution. In a similar way, the GACOS atmospheric correction can be applied to large earthquakes, especially to help improve the far-field observations, hence aiding the determination of deep fault slip distributions.

Chapter 7. Afterslip Following the 2016 Kaikoura Earthquake Revealed by InSAR Time Series with Atmospheric Correction

The 2016 Mw 7.8 Kaikoura earthquake represents an extremely complex process involving over 10 major faults and has altered some conventional understanding of multi-fault ruptures. One of the most striking features relates to the potential sliding on the Hikurangi subduction interface which has long been considered as permanently locked. This chapter intends to show the triggered afterslips on the Hikurangi subduction slab beneath southwestern Marlborough using 1 year of GPS and InSAR time series. An InSAR time series atmospheric correction model is developed to reduce the spatial-temporally correlated atmospheric error observed on Sentinel-1 interferograms, combining the generic atmospheric correction model proposed in Chapter 5 with an Atmospheric Phase Screen (APS) filter. The resulting time series are used to precisely locate the origin of the afterslip on the southern Hikurangi interface, and to provide implications of the co-seismic slip source, present status of the inactive subduction plate and future seismic hazards.

7.1 Introduction

The 2016 Mw 7.8 Kaikoura earthquake struck the northern South Island of New Zealand on 13 November 2016 (11:02 UTC) with two people killed, 57 injuries a major economic and fiscal impact. It is considered as one of the most complex earthquakes ever studied, which ruptured over 10 major faults with up to 10 m surface displacements, generated a regional tsunami maximized at ~7 m (Bai et al., 2017), as well as triggering numerous landslides (Massey et al., 2018). Combined geodetic and seismologic datasets immediately after the earthquake were used to constrain the complex multi-fault geometry and co-seismic slip distribution. For example, Hamling et al. (2017) determined the fault geometry by surface rupture surveys and inverted for its slip distribution by a combination of field data, GPS and InSAR observations. At least 20 overriding continental crustal faults in their model had slipped, accompanying a potential deep slip source on the Hikurangi subduction interface, and therefore undoubtedly challenged the traditional assumption about the degree to which earthquake ruptures are controlled by fault segmentation. Xu et al. (2018) showed that the rupture speed was overall

slow (1.4 km/s), by combining InSAR and seismologic data, and several Conway-Charwell fault links have aided in the rupture propagation across the step over from the Humps fault zone to the Hope fault. Holden et al. (2017) proposed some kinematic models based on local strong-motion and high-rate GPS data, in which the rupture propagated from south to north with half of the moment release occurring at the far north, 60 seconds after the origin time.

7.1.1 Poorly resolved afterslip distribution

Active seismic movements along the Marlborough Fault System (MFS) have accommodated most of the plate motions. Consequently, the convergence related to the Hikurangi subduction slab beneath the northern South Island becomes insignificant, with GPS observations reporting a slip rate deficit < 10 mm/year (Wallace et al., 2012), and this part of the slab has long been considered as permanently locked (Reyners, 1998). This assumption, however, has been altered as new evidence indicates that the inactive Hikurangi slab was accommodating plate motions at least after the 2016 Kaikoura event. The first direct evidence is the triggered large Slow Slip Event (SSE) beneath the North Island immediately after the mainshock (Wallace et al., 2017), which include a deep Kapiti SSE which accumulated up to 31 cm of slip, and a shallow (<15 km), moderate (>10 cm) east coast SSE on the Hikurangi subduction interface revealed by GPS observations (Jiang et al., 2018). Through simulating SSE slip distributions near Gisborne according to the rate-and-state friction framework, Wei et al. (2018) pointed out that only a low effective normal stress on the shallow subduction interface is required to trigger the observed SSEs. The second evidence is the afterslip on the subducting slab beneath the MFS, producing widespread surface displacement over the northern South Island (Wallace et al., 2018). However, unlike the SSE events which were covered by a dense GPS network and frequent InSAR observations, the origin of this afterslip is poorly located due to the lack of GPS and InSAR observations in the region. The InSAR data acquisitions used in Wallace et al. (2018) spanned less than 4 months and the ascending track was abandoned due to substantial atmospheric disturbances. Their resolved afterslip, largely distributed beneath the central offshore and northern MFS, would also produce wide surface displacements above the western MFS where there was no data coverage, resulting in a relatively weakly constrained slip model. Jiang et al. (2018) recovered a different but less spreading major slip source located southwest

of those in Wallace et al. (2018) using five months of GPS data, nevertheless, all were located in the east of the MFS. Lacking the surface displacement measurement on the western and southwestern MFS, the precise location of the afterslip origin on the Hikurangi subduction zone, which is crucial to explain in what degree, if any, the southern Hikurangi subduction slab has moved during the co-seismic period, remains unknown. It is therefore important to utilize the ascending Sentinel-1 data, which covers the whole MFS region continuously after the mainshock, to seek for robust constraints for the afterslip model.

7.1.2 Temporally correlated atmospheric error

The obstacle preventing Wallace et al. (2018) from utilizing the ascending Sentinel-1 data is the observed substantial atmospheric disturbance on interferograms, which, as addressed in the previous chapters, may mask actual tectonic displacements. Apart from the proposed models that correct interferograms individually, the atmospheric error can be mitigated in a time series through spatial and temporal filters, with fundamental assumptions of (i) the atmospheric error is spatially correlated; but (ii) temporally random. For example, Ferretti et al. (2001) approximated atmospheric errors by removing a linear deformation component, confined to slow motion targets over small areas where the linear assumption and the constant velocity model held. Hooper et al. (2007) high-pass filtered the phase in time to isolate atmospheric contributions from deformation. Lauknes et al. (2011) modelled atmospheric errors as an additive Gaussian random process with zero mean and 2-10 mm standard deviation. Given the large spatial extent of the interferograms used in this coastal area (over 250 by 250 km), however, these assumptions are threatened. For example, the atmospheric error can hardly be expressed as a single linear or power-law function across the whole interferogram, therefore restricting the use of spatial filters over large spatial extents. Potential temporal correlations of water vapour, such as those induced by a constant landcover or seasonal weather variations (e.g., fog is more prevalent at certain times of the year in coastal areas), decrease the filter performance, bias geophysical signal estimations and introduce unpredictable uncertainties on velocity estimates.

7.2 Tectonic Setting

The oceanic Pacific plate obliquely converges into the continental Australian plate at a rate of 39-49 mm/year and causes tectonic activities throughout New Zealand. Great earthquakes have been documented in the region, including the 1855 Mw 8.2 Wairarapa event (Darby and Beanland, 1992), the 1976 Mw 8.2 Kermadec Island event (Habermann and Wyss, 1984), the 2009 Mw 7.8 Dusky Sound event (Beavan et al., 2010) and the 2016 Mw 7.8 Kaikoura event (Hamling et al., 2017). The margin-parallel component of the plate motion at the North Island is represented largely as the clockwise rotation of the crustal Australian plate at 0.5–3.8 degree per million years (Wallace et al., 2004), while the perpendicular component happened mainly on the Hikurangi subduction interface, therefore releasing high slip rate deficits along the plate margin and beneath the southern North Island. Far to the central and southern South Island, the transpressional Alpine fault accommodates 35.5±1.5 mm/year parallel and 10±1.5 mm/year perpendicular motions relative to itself (Norris and Cooper, 2001) and has resulted in the uplift of the Southern Alps and the exposure of deep-seated crustal rocks during the last few million years (Norris et al., 1990).

In the northern South Island, the transition from the Hikurangi subduction to the strike-slip dominating Alpine fault translates into the MFS, a set of four large dextral strike-slip faults and their splayed structures. Slips on these faults are approximately parallel to the direction of the relative plate motion and decrease north-westerly from 20-25 mm/year on the Hope fault to 3-5 mm/year on the Wairau fault (Bourne et al., 1998; Cowan, 1990). On the eastern side of the MFS, the fault trend swings anticlockwise by about 30 degrees, such as the Jordan thrust with a nearly northerly striking angle and a dominating reverse slip component, and the Kekerengu fault with a dominating dextral strike-slip. Both have ruptured during the 2016 Mw 7.8 Kaikoura earthquake (Figure 7.1). South of the MFS, at the latitude of Canterbury (43W-41W), the oblique plate convergence rate reaches 40 mm/year (DeMets et al., 1990) and is largely accommodated by a number of slowly deforming faults and folds, including the Humps and Hundalee faults (Pettinga et al., 2001). Despite the presence of an underlying subduction interface at depths of 25-30 km (Williams et al., 2013), the crustal MFS accommodates a majority (>75%) of the relative plate motion within the northern South Island according to the

Quaternary evidence and geodetic observations (e.g., Holt and Haines, 1995; Norris and Cooper, 2001; Wallace et al., 2007).

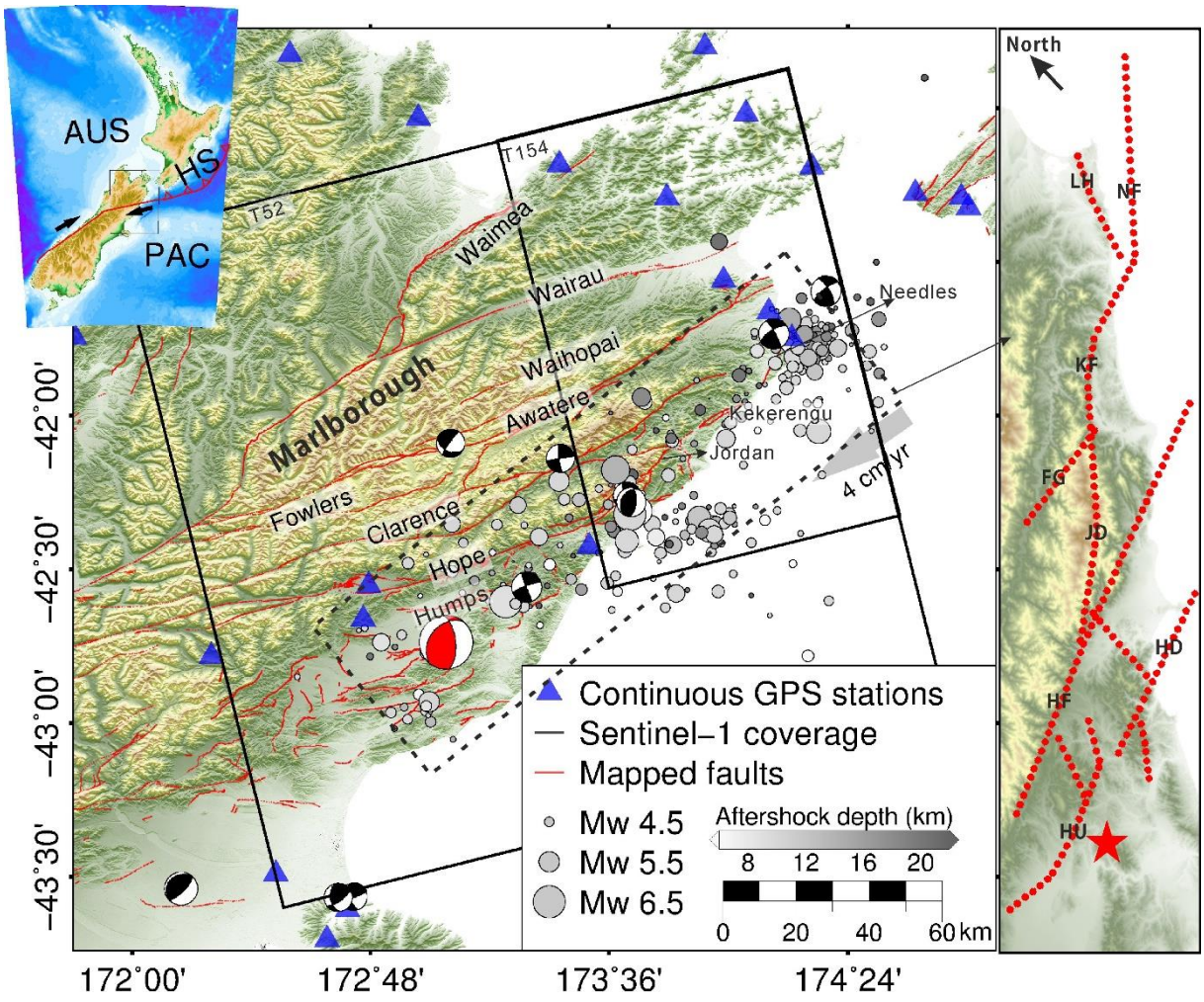

Figure 7.1 The tectonic setting of the southern Hikurangi Subduction (HS) interaction between the Pacific (PAC) and Australian (AUS) plates. Black rectangles represent Sentinel-1 data coverage. Blue triangles are GPS stations. Red lines indicate mapped active fault traces including the MFS from the institute of Geological and Nuclear Sciences (GNS), New Zealand. Red dotted lines are modelled faults which observed major co-seismic slips, HF: Hope Fault; HU: Humps Fault; HD: Hundalee Fault; JD: Jordan Thrust; FG: Fidget; KF: Kekerengu Fault; NF: Needles Fault; LH: London Hills.

The 2016 Mw 7.8 Kaikoura earthquake rupture initiated from the Humps fault zone and the Hundalee fault and propagated to the Hope fault through stepovers. It then splayed further north to the Jordan Thrust, Kekerengu fault and Needles segment. At least 12 major faults were involved in the multi-fault rupture process with various orientations and slip mechanisms, extending along southwest-northeast for about 150 km (Figure 7.1), exhibiting more complexity than most previously studied earthquakes such as the 2012 Mw 8.6 Sumatra event which

ruptured only three orthogonal strike-slip fault branches (Satriano et al., 2012). The stepovers between the Hump and Hope faults transferred from reverse faulting in the south to predominantly strike-slip in the north, whose distances were more than double the threshold for halting a fault rupture. The aftershocks first occurred at the offshore end of the Hope fault with a broad northeast-southwest trend, then stepped approximately northward along the Jordan thrust and Kekerengu fault, and finally clustered at the Needles fault segment (near Cape Campbell and Lake Grassmere). Most of the aftershock origins were shallower than 30 km with a mixture of reverse and strike-slips according to the USGS (Figure 7.1).

7.3 Data

Two ascending tracks of Sentinel-1 data were used with spatial and temporal overlaps making it possible for checking (coverage in Figure 7.1 and spatial-temporal baselines in Figure 7.2). The descending track was excluded since only eight acquisitions were available. Interferograms were generated with the GAMMA software (http://www.gamma-rs.ch), in the same manner as in Section 4.2.

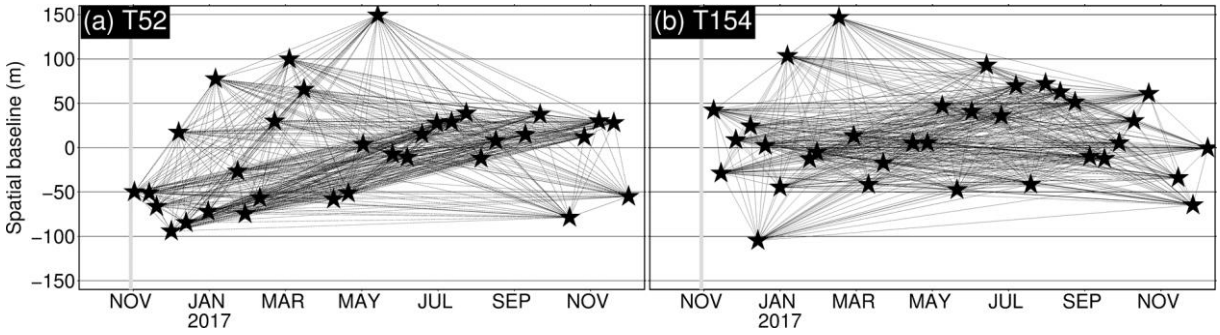

Figure 7.2 Spatial-temporal baselines for tracks 52 and 154. For T52, max=243.5 m, min=0.1 m, standard deviation=49.1 m. For T154, max=251.5 m, min=0.1 m, standard deviation=43.8 m.

There are also several GPS stations from the New Zealand GeoNet network providing continuous observations after the earthquake (Figure 7.3). We utilized their daily position time series from the Nevada Geodetic Laboratory at the University of Nevada, Reno (Blewitt et al., 2016), processed with GIPSY/OASIS-II Version 6.1.1 using final non-fiducial daily JPL orbit products (ftp://sideshow.jpl.nasa.gov/pub/JPL_GPS_Products/Final). The time series are in the IGS08 reference frame and have been corrected for the ocean tide loading using the Finite Element Solutions 2004 (Lyard et al., 2006), and for the solid Earth tides following the

International Earth Rotation and Reference Systems 2010 conventions. The full processing strategy is summarized at http://geodesy.unr.edu/gps/ngl.acn.txt. These GPS time series were then detrended to remove secular inter-seismic deformation (Gualandi et al., 2017) and corrected for annual and semi-annual signals by estimating 0.5 and 1 year period sinusoids (Bevis and Brown, 2014), using 5 years of daily time series prior to the 2016 earthquake.

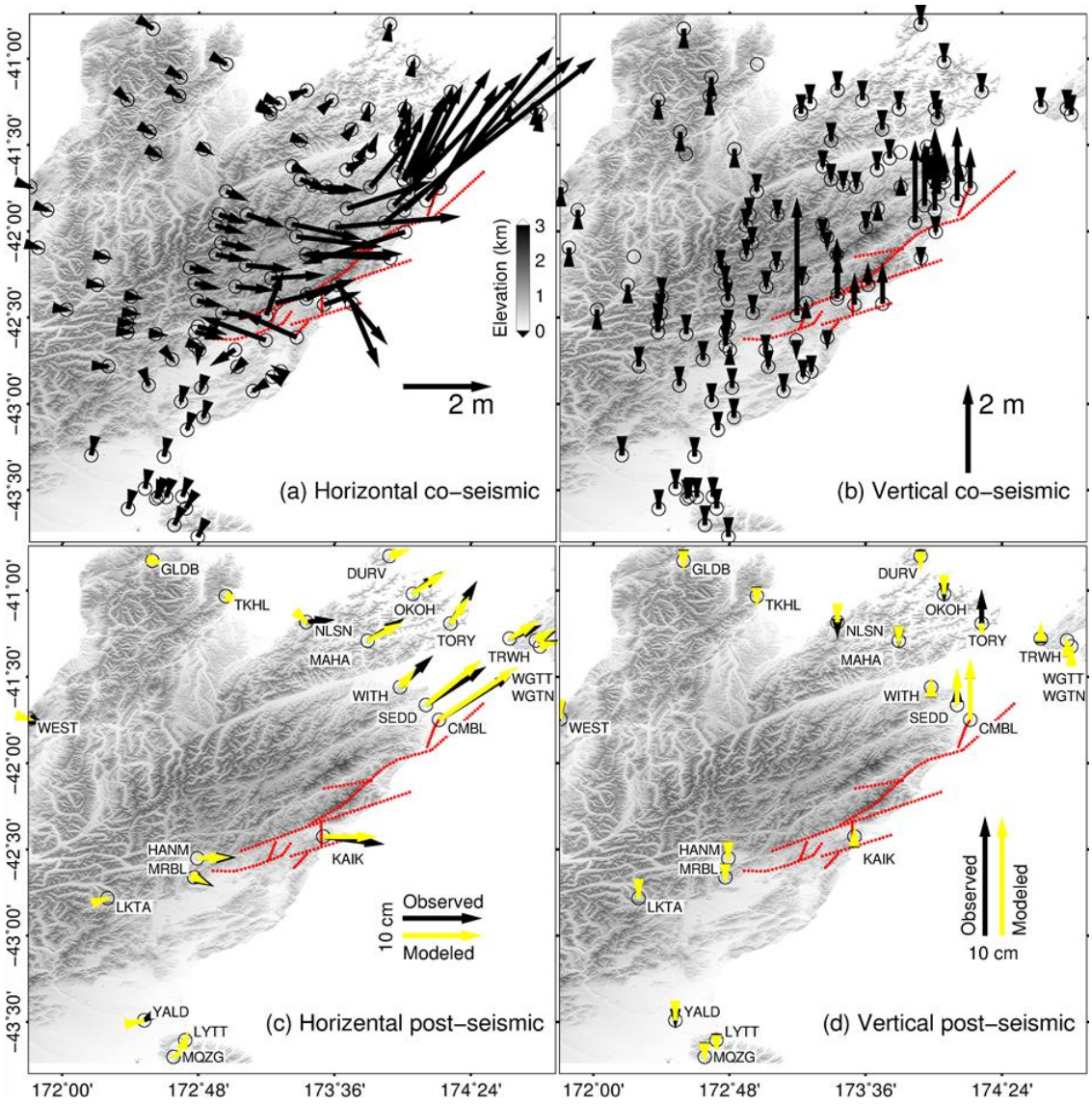

Figure 7.3 Observed co-seismic GPS offsets and 1-year (from 15 November 2016 to 31 December 2017) post-seismic GPS cumulative displacements (black arrows). Modelled post-seismic displacements are denoted by the yellow arrows. Red dotted lines indicate modelled fault surface traces (Hamling et al., 2017).

7.4 Mitigation of Spatial-temporally Correlated Atmospheric Errors

Original interferograms may experience a mixture of topographic correlated and turbulent

atmospheric errors, exhibiting as either short or long wavelength signals, which can degrade the spatial-temporal filtering when extracting deformation signals in InSAR time series analysis. Traditional InSAR time series analysis methods assume the atmospheric error is temporally random (e.g., Hooper et al., 2007), with only spatial correlations being highlighted. However, though they may not be as dominant as the spatial correlations, the atmospheric error temporal correlations should not be neglected, given the fact that the tropospheric moisture content varies seasonally (e.g., fog is more prevalent at certain times of the year in coastal areas) and analogously correlated with the topography. The temporal correlation can completely mask geophysical signals and introduce unpredictable uncertainties on the velocity estimates (Hooper et al., 2007).

7.4.1 Atmospheric correction for individual interferograms with GACOS

As the first step, the GACOS correction was applied to individually mitigate, at least to first order, atmospheric errors, including turbulence as well as the elevation dependent components. Some examples are shown in Figure 7.4, where most of the original interferograms experienced long wavelength signals along northeast-southwest and northwest-southeast directions with a maximum magnitude of over 10 cm and which have been substantially mitigated by GACOS. Meanwhile, topographic correlated errors were substantial on acquisitions, for example, 20161203 and 20170207 but reduced after applying GACOS corrections. The corrected interferograms tended to be random in time with the temporal correlation of the atmospheric error being reduced, therefore satisfying the basic assumptions in the time series analysis and expecting to be better handled through filtering.

To assess the GACOS correction quality, we cross-validated the ECMWF weather model derived atmospheric delays, used by GACOS to produce correction maps, by excluding one point from the whole grid and determining its value from the remaining grid. This was repeated for all the considered grids to obtain a cross-RMS difference between the interpolated and original values. The cross-test RMS for each acquisition date in Figure 7.4 revealed a seasonal variation which peaks in summer and is minimized in winter. For quality control purposes, the dates with large cross-RMS values (more than two standard deviations from the mean) would

reject the use of GACOS corrections on their related interferograms (the overall rejection rate is 5.8%). Those failed corrections probably came from the extreme turbulent troposphere which the weather model was not able to capture.

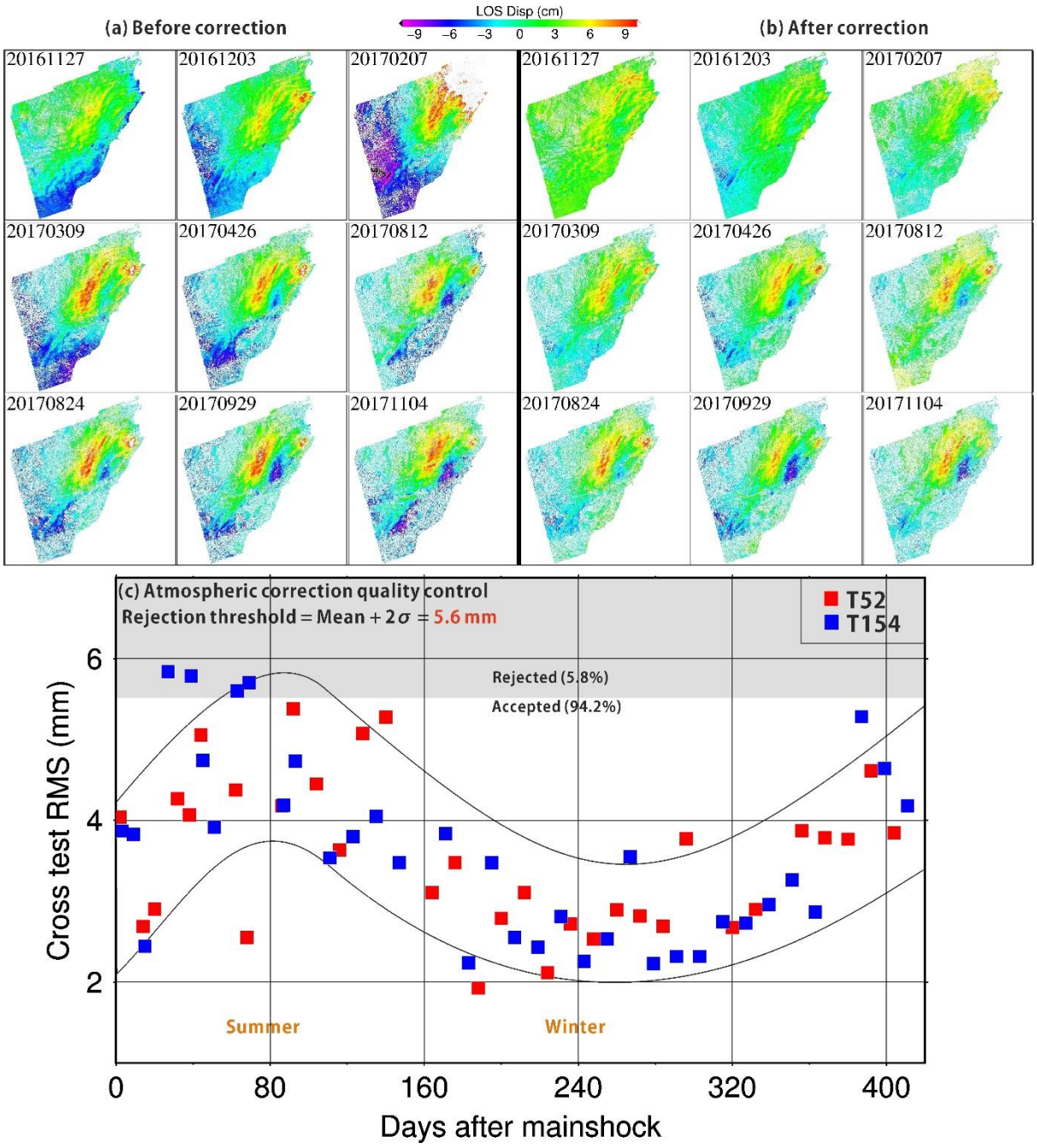

Figure 7.4 Examples of the individual atmospheric correction result (a, b) and the cross-test RMS of the ECMWF data. The master date for all the interferograms is 20161115 and the slave dates are indicated in the figure.

7.4.2 SBAS+APS model

After applying the GACOS atmospheric corrections, a small baseline subset (SBAS) differential algorithm was applied to extract the time-dependent deformation map (Li et al.,

2009a; Mora et al., 2002). For *N* interferograms from *P* identical dates, each map pixel complies with the following equation:

$$\begin{cases} L_{t_m t_s} = \varphi_{t_s} - \varphi_{t_m} + \dfrac{B^{perp}_{t_m t_s}}{r \sin\theta} D + \varepsilon_{t_m t_s} \\ [\underset{N\times 1}{\mathbf{L}}] = [\underset{N\times P}{\mathbf{T}} \quad \underset{N\times 1}{\mathbf{C}}] \begin{bmatrix} \underset{P\times 1}{\varphi} \\ \underset{1\times 1}{D} \end{bmatrix} \end{cases} \qquad \text{(Equation 7.1)}$$

where, L is the original or atmospherically corrected phase observation on an interferogram with a master date of t_m and a slave date of t_s; φ_t is the cumulative displacement from the earthquake rupture time t_0 to t; B^{perp} is the perpendicular baseline; D is the DEM error; r is the satellite-target distance (693 km for Sentinel-1); θ is the satellite incidence angle; ε accounts for the temporal decorrelation, orbital error, thermal noise effect and atmospheric error if not corrected. **T** is the coefficient matrix of the cumulative displacement and **C** is the coefficient matrix of the DEM error. If all the acquisitions are well connected, as was the case for our Sentinel-1 data, Equation 7.1 can be well determined in a least squares sense.

For the interferograms that have rejected GACOS corrections, their atmospheric errors were estimated by extending Equation 7.1 to:

$$\begin{cases} L_{t_m t_s} = \varphi_{t_s} - \varphi_{t_m} + (APS_{t_s} - APS_{t_m}) + \dfrac{B^{perp}_{t_m t_s}}{r \sin\theta} D + \varepsilon^{'}_{t_m t_s} \\ [\underset{N\times 1}{\mathbf{L}}] = [\underset{N\times P}{\mathbf{T}} \quad \underset{N\times (P-1)}{\mathbf{A}} \quad \underset{N\times 1}{\mathbf{C}}] \begin{bmatrix} \underset{P\times 1}{\varphi} \\ \underset{(P-1)\times 1}{APS} \\ \underset{1\times 1}{D} \end{bmatrix} \end{cases} \qquad \text{(Equation 7.2)}$$

where, *APS* is the estimated atmospheric error for the un-corrected interferogram. Equation 7.2 is singular due to the correlation between deformation and *APS* parameters. We therefore introduced a temporal deformation model as a constraint on the deformation parameter. For this post-seismic study, the logarithmic deformation model may be used:

$$\varphi_t = a + b \cdot \log(t - t_0) \qquad \text{(Equation 7.3)}$$

where φ is the phase change between the time t and rupture time t_0; a and b are parameters to be estimated. Substituting Equation 7.3 into 7.2, we obtain:

$$\begin{cases} L_{t_m t_s} = b \cdot \log(\dfrac{t_s - t_0}{t_m - t_0}) + (APS_{t_s} - APS_{t_m}) + \dfrac{B^{perp}_{t_m t_s}}{r \sin\theta} D + \varepsilon'_{t_m t_s} \\ [\underset{N\times1}{\mathbf{L}}] = [\underset{N\times1}{\mathbf{G}} \quad \underset{N\times(P-1)}{\mathbf{A}} \quad \underset{N\times1}{\mathbf{C}}] \begin{bmatrix} \underset{1\times1}{b} \\ \underset{(P-1)\times1}{APS} \\ \underset{1\times1}{D} \end{bmatrix} \end{cases} \quad \text{(Equation 7.4)}$$

Equation 7.4 can be determined with a well-connected acquisition network on a pixel-by-pixel basis. The temporal deformation model in Equation 7.4 requires the *APS* parameter to be random, which was largely satisfied in our situation as only a small portion of acquisitions required an *APS* parameter (<6%). To prevent unphysical oscillatory variations in the *APS* estimation, a spatial filter was performed on the APS parameters. Assuming that the atmospheric effect on each pixel within a given window *W* was identical, the final equation reformed from 7.4 was obtained:

$$\begin{bmatrix} \underset{N\times1}{\mathbf{G_1}} & \underset{N\times(P-1)}{\mathbf{A}_1} & \underset{N\times1}{\mathbf{C}_1} & \underset{N\times1}{0} & \cdots & \underset{N\times1}{0} \\ \underset{N\times1}{\mathbf{G_2}} & \underset{N\times(P-1)}{\mathbf{A}_2} & \underset{N\times1}{0} & \underset{N\times1}{\mathbf{C}_1} & \cdots & \underset{N\times1}{0} \\ \cdots & \cdots & \cdots & \cdots & \cdots & \cdots \\ \underset{N\times1}{\mathbf{G}_{W^2}} & \underset{N\times(P-1)}{\mathbf{A}_{W^2}} & \underset{N\times1}{0} & \underset{N\times1}{0} & \cdots & \underset{N\times1}{\mathbf{C}_1} \end{bmatrix} \begin{bmatrix} \underset{1\times1}{b} \\ \underset{(P-1)\times1}{APS} \\ \underset{W^2\times1}{D} \end{bmatrix} = \begin{bmatrix} \underset{N\times1}{\mathbf{L}_1} \\ \underset{N\times1}{\mathbf{L}_2} \\ \cdots \\ \underset{N\times1}{\mathbf{L}_{W^2}} \end{bmatrix} \quad \text{(Equation 7.5)}$$

where the DEM error for each pixel was introduced as an independent unknown parameter. Equation 7.5 is an overdetermined system and can be easily solved in a least squares sense. Once the APS parameters are estimated, we can obtain a whole network of interferograms corrected for atmospheric delays.

A further refinement was done by resolving Equation 7.5 again using the atmospherically corrected interferograms (either by GACOS or the estimated APS). This time an *APS* parameter was assigned on each acquisition as a residual atmospheric delay, which should be temporally uncorrelated and therefore more separable from deformation signals.

A step by step implementation of the proposed method is shown in Figure 7.5: (i) apply the GACOS correction on each interferogram; (ii) cross-validate and reject corrections with poor ECMWF data qualities; (iii) estimate the APS for interferograms without GACOS corrections by a sub-network of corrected interferograms, and iterate until all interferograms are corrected;

and (iv) estimate the deformation signal together with residual atmospheric delays and DEM errors with least squares and spatial-temporal filters.

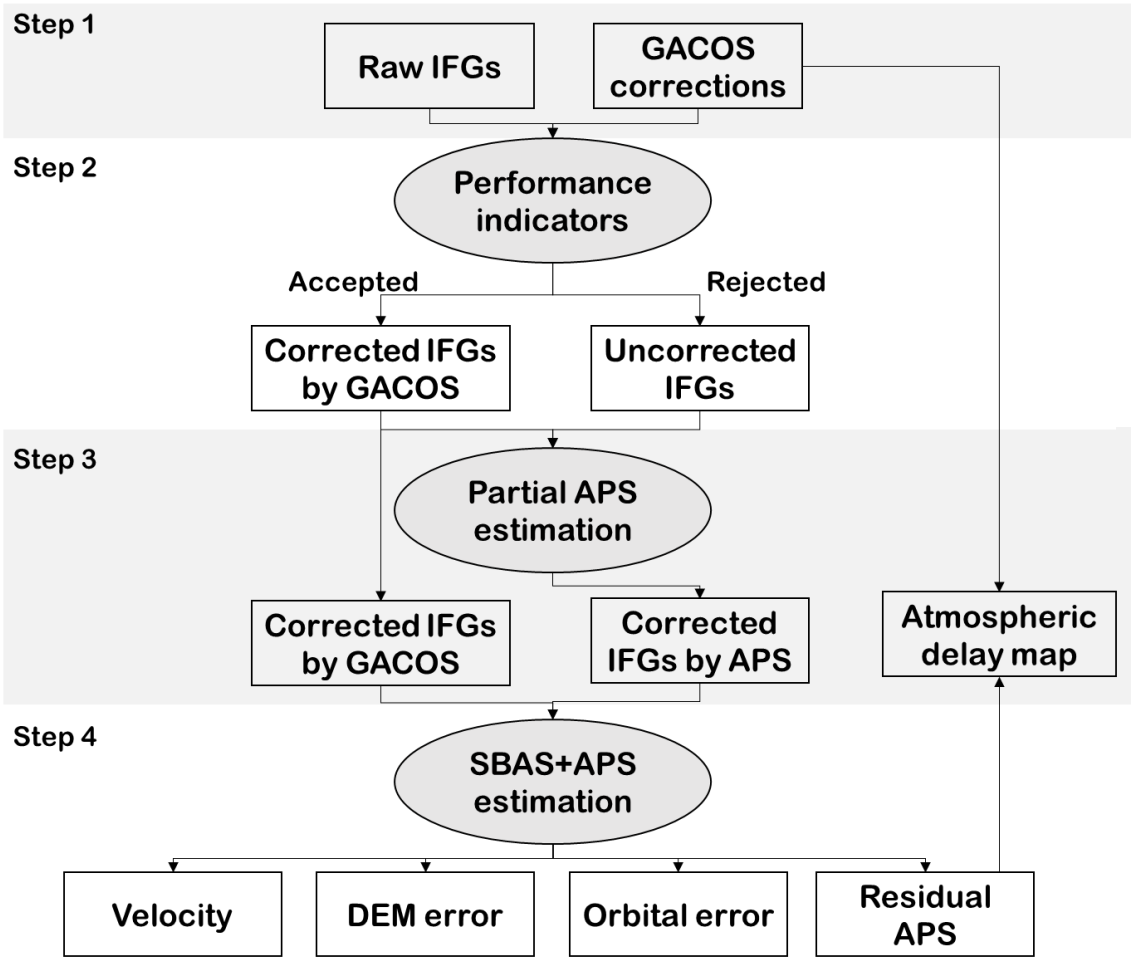

Figure 7.5 A flow chart of the SBAS+APS model and its final outputs.

7.4.3 Results and validations

To evaluate the model's performance, four different time series methods for generating cumulative displacement maps were compared: (i) the traditional SBAS method by interferogram stacking without estimating APS parameters (hereafter called SBAS); (ii) the traditional SBAS method after applying GACOS corrections for each interferogram (hereafter called SBAS-GACOS); (iii) the traditional SBAS method integrated with the APS model (hereafter called SBAS-APS); (iv) our proposed method, i.e. the traditional SBAS method plus the APS model, but after applying GACOS corrections for each interferogram (hereafter called SBAS-GACOS-APS). The major difference between the SBAS-APS and SBAS-GACOS-APS was the APS parameter, where the SBAS-APS estimated the whole APS for all acquisitions,

which could be temporally correlated and exert long wavelength biases to the deformation field. Nevertheless, the SBAS-GACOS-APS only estimated APS residuals using the atmospherically corrected interferograms.

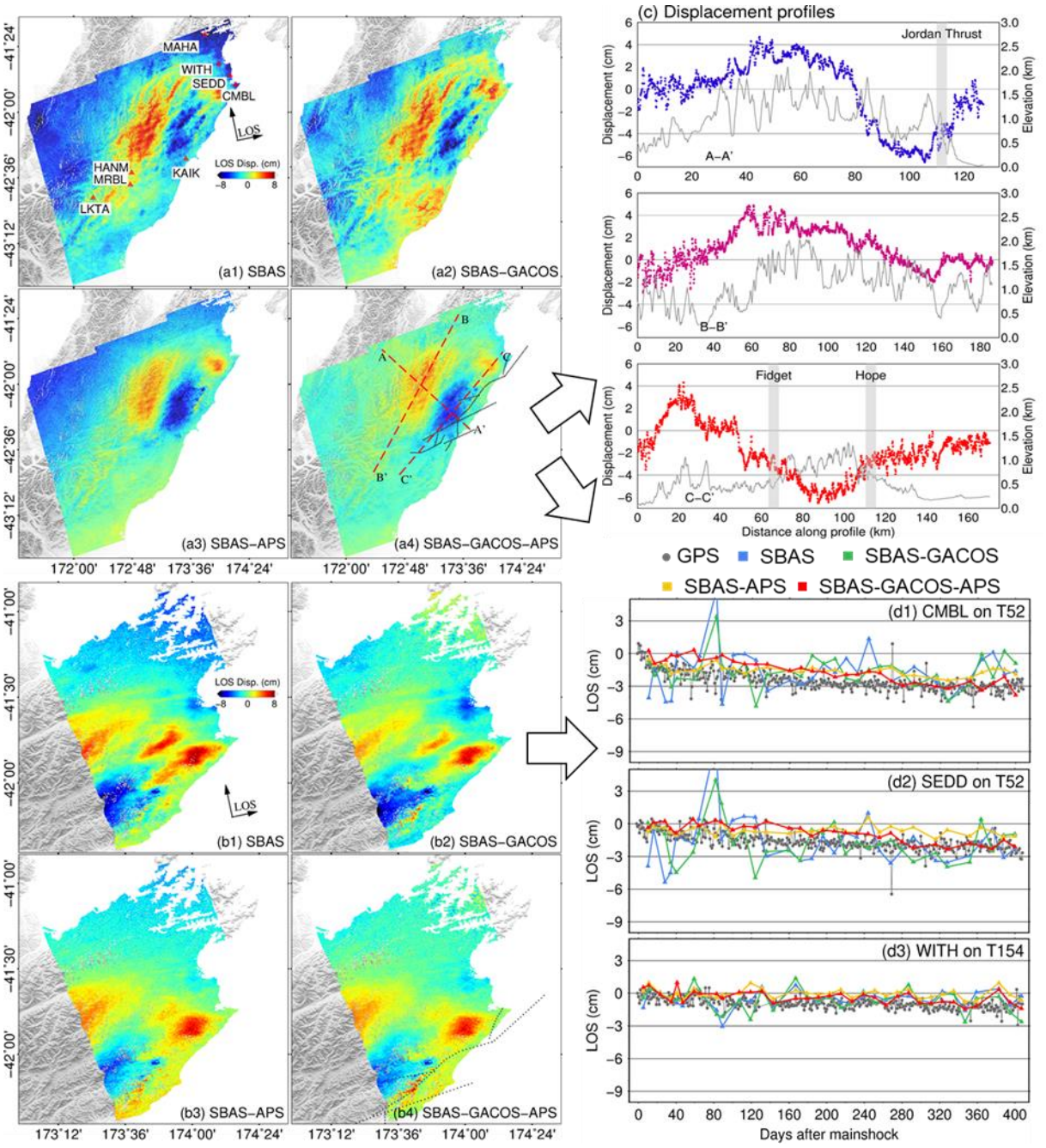

Figure 7.6 Cumulative displacements from the four InSAR time series methods for (a) track 52, 15 November 2015 to 22 December 2017, and (b) track 154, 16 November 2015 to 29 December 2017. Black dots are the projected surface fault traces. (c) The displacement profile from track 52 (coloured) and the elevation profile counterparts (grey lines). (d) Comparisons between InSAR and GPS displacement time series for all methods (station locations in Figure 7.3).

Figure 7.6 shows the InSAR time series results for the two tracks from all four different methods.

A long wavelength signal with a gradient from the northwest to southeast was seen on the uncorrected results (i.e. those without GACOS corrections) from both tracks, probably revealing the fact that the western South Island has more precipitation than the west (over three times) therefore producing strong spatial-temporally correlated atmospheric effects. The temporal correlation prevented the atmospheric error from being distinguishable from the deformation, hence introducing additional long wavelength signals in the final displacement maps. After applying GACOS corrections, the atmospheric effect was largely reduced (see Figures 7.6a2, 7.6b2) with a further weakening after applying the SBAS+APS model (Figures 7.6a4, 7.6b4). Overall, these results demonstrate the importance of the GACOS correction in reducing the spatial-temporally correlated atmospheric errors in InSAR time series.

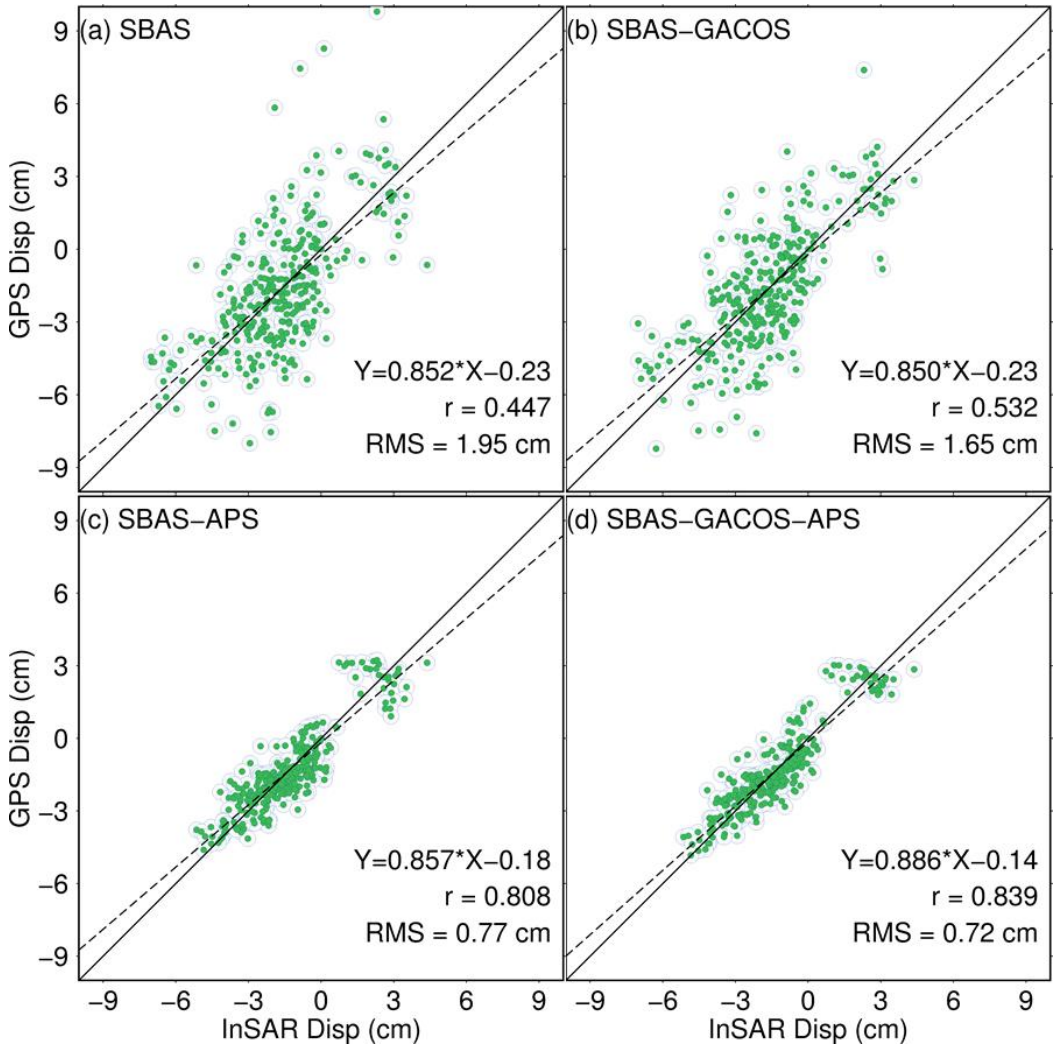

Figure 7.7 Comparisons of displacements between InSAR and GPS for all four InSAR time series methods.

The SBAS-APS and SBAS-GACOS-APS were less noisy after applying the SBAS+APS model.

Figures 7.6d and 7.7 show detailed comparisons between all available GPS stations and all InSAR acquisitions. A 0.72 cm RMS difference was obtained with our SBAS-GACOS-APS model, improved from the SBAS (1.95 cm) and SBAS-APS (0.77 cm), respectively. The RMS difference for the SBAS-GACOS was smaller than the SBAS method, but both were greater than the SBAS-APS and SBAS-GACOS-APS methods, since the short wavelength atmospheric noise was unable to be captured by GACOS. This was also demonstrated by their spectrograms, which were computed by the spatial Fourier transformation of the phase measurement. For track 52, the SBAS-GACOS-APS method had a more centralized spectrum amplitude distribution in all directions, whereas the others show stronger northwest-southeast signals (Figure 7.8). Track 154 was less noisy than track 54 due to its smaller spatial extent, and consequently smaller atmospheric errors, but still has received considerable improvements after applying the GACOS correction and SBAS+APS model.

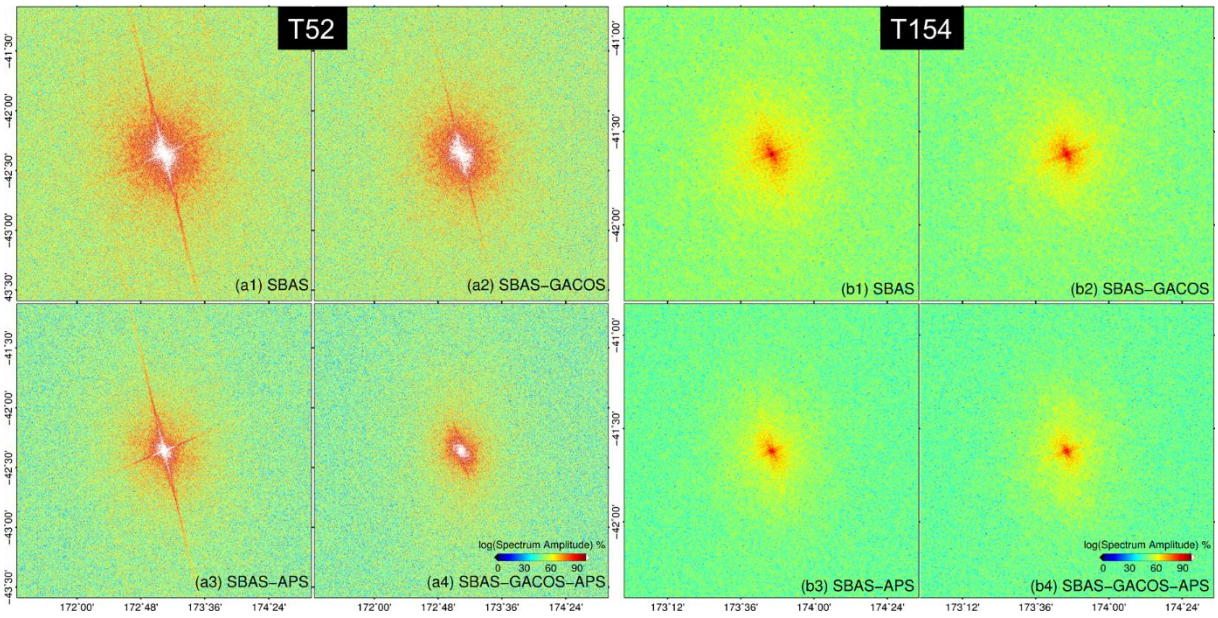

Figure 7.8 Spectrograms computed by the Fourier transformation for both tracks. The spectrum amplitudes are shifted so the low-frequency signals are in the map centre.

7.5 Time-dependent Afterslip Modelling

From the cumulative displacement maps shown in Figure 7.6, there were two major and one minor displacement lobes during the 1-year post-seismic period. An intuitive interpretation is that the northeast lobe was probably related to the crustal Kekerengu and Needles faults and their oceanic extensions. The other two are symmetrical lobes and should originate at a deeper

source because of their far westward location away from the main co-seismic area and the crustal faults. From profiles A and B shown in Figure 7.6c, the western displacement lobe happened over the mountainous area (2–3 km) whereas the eastern lobe occurred mostly over the flat region. There were no sharp surface dislocations on all three profiles, implying the slip sources were dominating at a deep depth (~35 km). As we only used one year of data after the earthquake, we neglected the viscous-elastic effect and confined our model only to afterslips.

We used the SBAS-GACOS-APS InSAR time series results, combining the detrended and seasonal/semi-seasonal signals corrected GPS time series for the time-dependent afterslip modelling. We assumed a logarithmic function to simulate the afterslip time history as (displacement=A+B*log(t)), where A and B are constant parameters estimated by least squares from the displacement time series; t is the epoch time after the mainshock. The misfit standard deviations after fitting this equation were 0.54 cm (East), 0.63 cm (North), and 1.10 cm (Vertical) for GPS and 0.48 cm (LOS) for InSAR, respectively. The optimal relative weight between GPS and InSAR was determined by minimizing their data misfits iteratively.

The location of the western deformation lobes imply that they cannot be explained by the shallow crustal faults, so we utilized the fault geometry from Hamling et al. (2017), in which a subduction interface along with 19 crustal fault segments was included. To minimize the number of free parameters, we included only five major crustal faults (the Humps, Hope, Jordan thrust, Kekerengu and Needles faults), where there were largest co-seismic displacements, and the subduction interface. We discretized the fault planes into 2 by 2 km patches and, for each patch, estimated its strike and dip slip components. The estimation was a linear procedure in a least squares sense, with a spatial smoothing factor being applied whose optimal value was iteratively determined by minimizing the data residuals.

The observations, modelled surface displacements and residuals for the two InSAR tracks and GPS are shown in Figures 7.9 and 7.3, respectively. The major deformation pattern was well explained, including the two major lobes and the northeast minor lobe on both tracks. The GPS displacements were mostly along the horizontal with the most substantial movements being

recorded by stations CMBL, SEDD and WITH, at the coastal end of the Needles fault, and KAIK, at the coastal end of the Hundalee fault. Their directions complied with the local tectonic background where the strike-slips rotate counter clockwise from south to north. Our afterslip model reveals that the movements on CMBL, SEDD and WITH were related to the oceanic extensions of the Needles fault, whose triggered surface displacements were only partially observed by InSAR. There were small residuals along the Jordan thrust surface trace, suggesting the existence of small and shallow reverse slips on the thrust. Northwest of the Jordan thrust, the residuals were probably due to the shallow (6.9 km) Mw 5.3 aftershock on 18 November 2016.

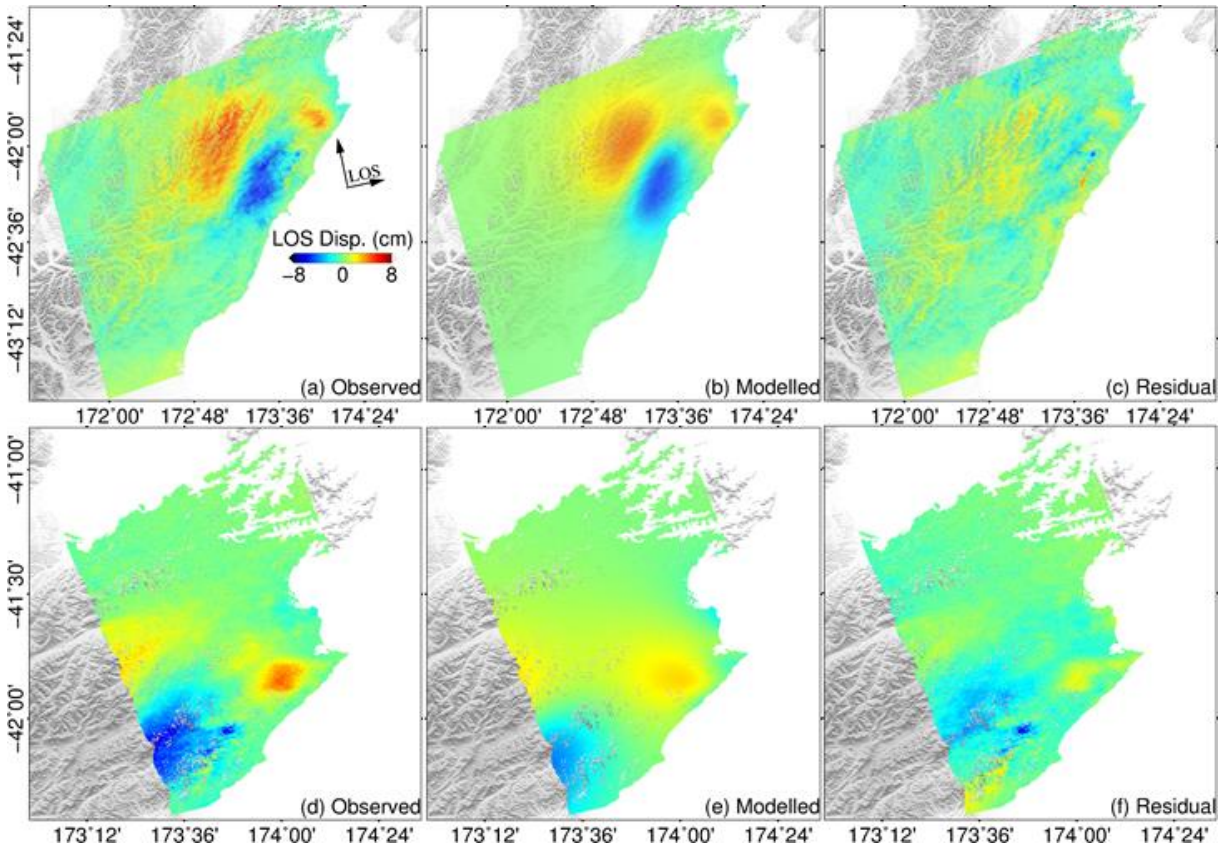

Figure 7.9 Observed, modelled and residual interferograms based on the best fit afterslip model.

The fault slip distribution is shown in Figure 7.10 with two major slip sources. The first one is the oceanic extension of the Needles fault. The afterslip here was right-lateral dominating and has propagated deeper (15-25 km) than the co-seismic slip (5-15 km). The slip on this fault may have propagated further to the north after the mainshock through frequent aftershocks (Figure 7.1), most having 15-20 km depth focal mechanisms (Figure 7.1), and have continued steadily as afterslips. Although this slip source was not well determined due to the lack of observations

above the ocean, the afterslip model reasonably explained the northeast deformation signals from InSAR and GPS.

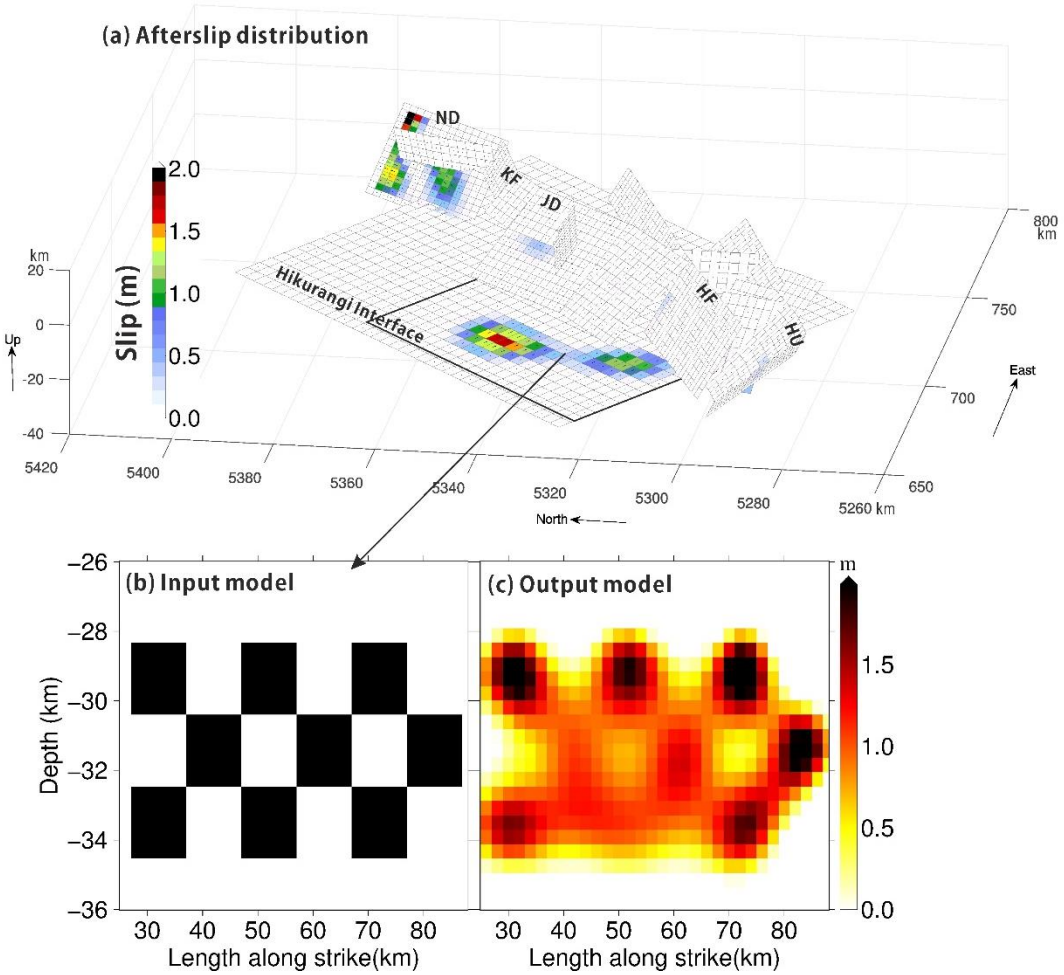

Figure 7.10 Best fit afterslip distributions for all faults. (b) and (c) are the input and output of the checkerboard test for slips on the Hikurangi subduction interface (2 m pure reverse slip input).

The second source is the slip on the subducting interface at depths from 25 to 35 km, reverse dominating with minor right-lateral components of up to ~ 2 m for one year. Unlike the co-seismic observations, the post-seismic observations provide clear evidence of triggered slips on the subduction interface, which were not mixed with the shallow crustal fault related surface displacements. We further conducted a checkerboard test around the main subducting region and validated that the simulated slips can be well recovered by our input observations.

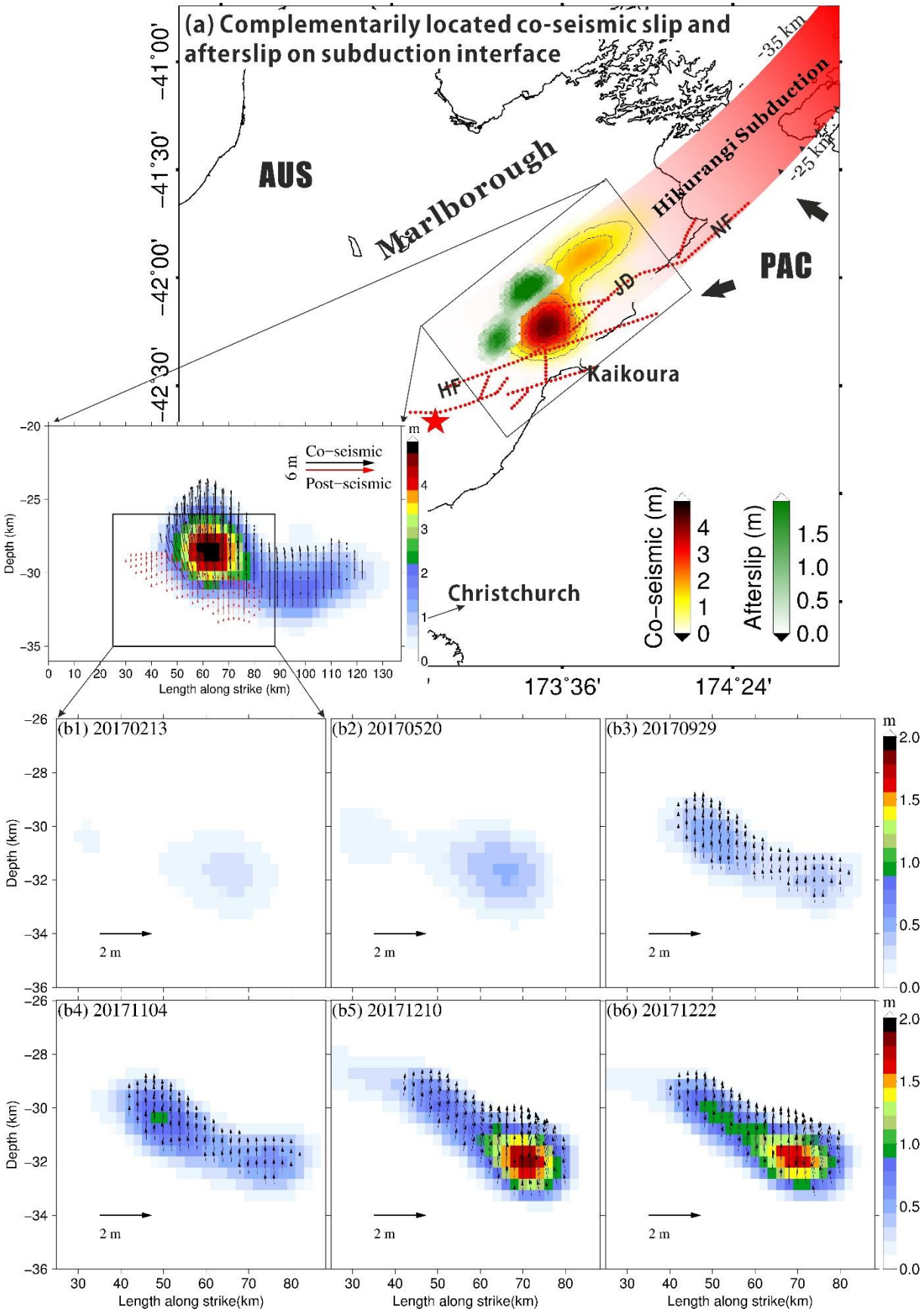

Figure 7.11 The time-dependent afterslip distribution on the Hikurangi subduction interface and the co-seismic slip distribution. (a) the cumulative afterslips; and (b) the slip time series, referenced from 15 November 2016.

The afterslip model evidenced a triggered subduction interface after the mainshock that was accommodating the regional oblique plate motion. It extended 50 km horizontally and 6 km vertically (equivalent to 22 km along the dipping direction), with a cumulative moment release that was equivalent to a Mw 6.9 earthquake on the interface. Our afterslip is complementarily located with the co-seismic subduction slip modelled by Hamling et al. (2017), who suggested a ~15% moment release on the subduction slab among the whole co-seismic energy. The slip distribution was a narrowed ellipsoid peaked below the co-seismic slip deficit area. The full afterslip history in Figure 7.11 shows that the afterslip started from the co-seismic deficit area and became substantial since May 2017. The overall slip history on the interface (co- and post-seismic) is rather homogeneous: the triggered co-seismic slips propagated mostly towards down-right, producing a slip deficit area where the up-leftward propagating afterslips centred. After the GACOS atmospheric correction, the two ascending tracks revealed more comprehensive surface displacements related to the subduction slip compared to the descending track used in Wallace et al. (2018), and therefore helped to precisely locate the actual afterslip source.

The afterslip may be underestimated because of the SAR satellite geometry and missing offshore observations. We neglected the potential contribution from poroelastic rebound and viscoelastic relaxation. Poroelasticity is mainly visible as uplift and subsidence in the near-field with shallow processes, and small spatial extent surface movements (Peltzer et al., 1996). It may have led to the small residuals near the Jordan thrust trace in Figure 7.9. After such a large event, the crust would consist of an initial elastic rebound followed by a transient element of deformation controlled by the viscosity (Nur and Mavko, 1974), which means the viscous deformation may be dominant over a decadal timescale, but is obscured by afterslip in the early stage of relaxation. To further distinguish the afterslip and viscoelastic deformation, additional data would be required.

7.6 Discussions

7.6.1 Features of the proposed atmospheric correction model

The spatial-temporal correlated atmospheric error is problematic in InSAR time series since the APS filters are only valid with random noise. The temporal deformation model (either linear or non-linear) also requires the atmospheric error to be temporally random. Within our proposed method, the long wavelength and topography related atmospheric errors are removed before filtering, leaving the residuals as small and random, which are removable both in space and in time. The key features of the proposed method are: (i) the individual atmospheric correction by GACOS (ECMWF) is globally anytime usable with a short time delay (< two days); (ii) it is suitable for both small and large areas as the APS estimation does not rely on strong spatial constraints after the GACOS correction; and (iii) temporal correlations of the atmospheric delay can be largely reduced. The performance of this method mainly relies on the accuracy of the GACOS correction map and its quality control by identifying out failed corrections. As the weather model used in GACOS is improving in both the spatial-temporal resolution and accuracy, we expect an improved performance of atmospheric corrections in the next few years.

7.6.2 Insights into the southern Hikurangi subduction slab

Detailed definition of the subducting plate and overlying plate in the MFS is problematic, as the plate boundary is broad and ~80% of the plate motion is accommodated by shallow crustal faults (Holt and Haines, 1995). The frequent seismic activities beneath the Hope and Clarence faults produced a broad boundary zone both horizontally and vertically. When coupled with complex shallow fault slips, the interface slip may be completely masked and hence indeterminable from surface geodetic observations. In the case of the 2016 Kaikoura earthquake, however, the interface afterslip can be clearly resolved mainly due to the limited contributions from the shallow crustal faults after the mainshock. After carefully calibrating the atmospheric effect, we obtained post-seismic surface displacements covering the whole MFS, especially the western and southwestern MFS which were not covered by previous studies. These observations offered valuable insights into the activities at the southern part of the Hikurangi subduction interface.

The southern margin of the Hikurangi subduction zone has long been considered as permanently locked and no longer accommodates the plate motions. There are decreased slip rate deficits from ~30 mm/year beneath the North Island to <10 mm/year beneath the MFS. Wallace et al. (2018) evidenced that the subduction plate boundary beneath the eastern MFS was indeed accommodating the plate motions with up to 5 cm early afterslip. Our resolved interface afterslip (up to 2 m in one year) extends their slip area towards the southwest with more wide-spreading surface displacements throughout the MFS. The slip source located at the edge of the broad seismic active zone beneath the Hope fault, where the subducting plate begins to bend downwards, is therefore valuable in the determination of the subducting plate thickness and shape.

7.6.2 Link between co-seismic slip and afterslip

Afterslips after large earthquakes are usually complementarily located with the co-seismic slip, compensating in magnitude and distribution with nearly the same direction, such as the 1999 Izmit earthquake (Wright et al., 2001a) and the 2004 Sumatra-Andaman earthquake (Chlieh et al., 2007). By comparing our afterslip model with the co-seismic interface slip proposed by Hamling et al. (2017), the afterslip peaked at a co-seismic slip deficit area and was distributed adjacently below the main co-seismic slip area. This implies the subduction interface may have already been triggered during the mainshock and continued to move afterwards in the same manner, but slightly below the main co-seismic slipping area. The total amount of the afterslip requires only a relatively low co-seismic moment release compared to the crustal faults, and is consistent with those proposed by Clark et al. (2017) and Wallace et al. (2018).

The co-seismic observations for the 2016 Kaikoura earthquake show that multi-faults can be triggered during a single large event and fault slips can propagate through fault step-overs and splays over a long distance (> 100 km, Hamling et al., 2017; Xu et al., 2018). When considering the co-seismic slip on the interface, the far-field subsidence and non-double-couple components of global moment tensors would be better explained. This implies a more complex event that undergoes slip along numerous faults, varied in orientation and direction, propagated from the mainshock both horizontally to adjacent fault segments and vertically to the underlying deep

crust.

7.7 Summary

This chapter detailed the recovery of the time-dependent afterslip distribution on the southwest Hikurangi Subduction Zone by the two tracks of Sentinel-1 data after mitigating the spatial-temporally correlated atmospheric error. A majority of interferograms (~94%) were considerably improved after applying GACOS atmospheric corrections, with its correction performing poorly for the remaining ~6%, whose corrections were estimated from a sub-network of the corrected interferograms. The residual atmospheric errors were then isolated from deformation by the SBAS+APS method. Validations showed that the resulting InSAR displacement has a good agreement against GPS (0.72 cm RMS), improved from the conventional SBAS (1.95 cm RMS). More improvements were found on the track with the larger spatial extent (>200 km) as larger atmospheric disturbances were observed.

The resultant InSAR displacement filled the data gap above the west and southwest MFS, and our resolved slip model clearly evidenced a triggered Hikurangi subduction slab by the 2016 Kaikoura earthquake. Despite afterslips and a slow slip event beneath the southern North Island and offshore South Island proposed by Wallace et al. (2017, 2018), our results identified considerable afterslips (up to 2 m in one year) beneath the southwest MFS that were complementarily located with the resolved co-seismic interface slip source by Hamling et al. (2017), implying that the interface probably has already moved during the mainshock. We also found a shallow slip source on the northern extension of the Needles fault, which may have induced large offshore surface displacements.

Chapter 8. Conclusions

8.1 Contributions of this Research

The accuracy of InSAR derived surface displacement is substantially affected by the spatial-temporal variations of atmospheric water vapour, which can cause errors comparable in magnitude to those associated with crustal deformation. It can not only mask the small magnitude tectonic displacement hence biasing the long-term velocity mapping (e.g., for post- or inter-seismic studies), but also mask some co-seismic signals when they are not dominant enough on an interferogram. The tremendous development of InSAR missions (e.g., Sentinel-1A/1B, ALOS-2, TerraSAR-X/TanDEM-X, COSMO-SkyMED, RADARSAT-2, Gaofen-3), as well as the planned future successors during 2018-2025, has posed more challenges for atmospheric corrections, with researchers being increasingly aware of the limitations of the existing correction models, including (i) the coupling effect of the tropospheric stratification and turbulence; (ii) the low spatial-temporal resolutions of weather models; and (iii) the lack of quality control indicators.

Inspired by the abovementioned research gap, several InSAR atmospheric correction models were developed in this thesis using GPS, ECMWF, and a combination of these two to achieve improved performance over mountainous areas or in the presence of tropospheric turbulence globally. Small magnitude co-seismic signals were detected from the atmospheric corrected InSAR measurements and used to invert for the fault geometry and slip distributions. The spatial-temporally correlated atmospheric delays in InSAR time series were reduced, after which InSAR and GPS were combined to recover the afterslip distribution and time-dependent slip history following a large earthquake, and to provide evidence of a downdip interface slip source.

8.1.1 Iterative tropospheric decomposition model

An iterative tropospheric decomposition model has been developed to generate high-resolution water vapour fields from GPS observations. Despite the importance of the elevation dependence of water vapour, addressed by several previous studies, it is often a challenge to separate elevation-dependent tropospheric delays from turbulent components. The ITD model

overcomes this by decoupling the elevation and turbulent tropospheric delay components, overcomes the spatial interpolation challenges over mountainous areas and/or in the presence of turbulence in the troposphere, and generates improved high-resolution water vapour maps compared with previous tropospheric turbulence- and elevation-dependent models.

The ITD model was validated on a 150 km × 150 km California study region, firstly using real-time mode ZTD estimates from precise point positioning at 41 GPS stations over 1 year. Cross validation yielded a ZTD RMS error of 4.6 mm with the ITD model, compared with 8.4 mm with the previous state-of art SKlm+Onn model. On converting the GPS ZWDs to PWV and interpolating to 1 km grid cells across the region, validations with the MODIS near-IR water vapour product for the year showed the RMS difference being improved from 1.96 mm by using the SKlm+Onn model to 1.71 mm by using ITD. Furthermore, the spatial PWV gradients using ITD and MODIS across a variety of topography were nearly identical to each other. The overall RMS difference between MODIS and ITD PWV profiles was 1.51 mm, and the RMS differences for mountain and flat areas were 1.57 mm and 1.47 mm, respectively. Such results were obtained without differencing the tropospheric delays or water vapour estimates in time or space, whilst the errors were similar over flat and mountainous terrains, as well as for both inland and coastal areas.

The generated near real-time mode PWV fields, high in spatial-temporal resolution, are beneficial to the InSAR atmospheric correction, numerical weather forecasting, and network RTK augmentation.

8.1.2 GPS-based InSAR atmospheric correction routine

Facilitated by the increased density of continuous GPS networks in different regions/countries, it becomes timely to integrate InSAR and GPS in a routine way aimed at precise deformation mapping, to tackle the binding of the stratified and turbulent tropospheric delays on InSAR interferograms without pre-defined local parameters. Based on ITD, we have implemented a framework to routinely use pointwise GPS data to reduce atmospheric effects on InSAR measurements systematically and automatically. Cross validation was introduced as a

performance indicator (exemplified through the station spacing tests in Section 4.3), to ensure the correction maps are appropriately applied (or potentially not applied) to InSAR measurements, and when. Ignoring this, there is a possibility of degrading InSAR measurements if such tropospheric corrections are applied.

The application of this framework to Sentinel-1A interferograms over the Southern California (USA) and Southern England (UK) regions showed approximately 45–78% of noise reduction even with a sparse (~ 50–80 km station spacing) GPS network and/or in the presence of strong and non-random tropospheric turbulence. This is about a 50% greater improvement than previous methods. The turbulent components can have a comparable magnitude to the stratified component and exhibit larger variations in the summer than in other seasons due to the atmosphere being able to hold more water vapour. By accounting for both the stratification and turbulence of the troposphere, ~ 1 cm precision of the corrected interferograms was achieved.

8.1.3 Generic atmospheric correction model

The vast development of InSAR has fulfilled a global coverage of surface movement measurements as continuous time series, which poses challenges for correcting interferograms for atmospheric effects that GPS alone cannot be used for due to its low availability and low spatial resolution. Inspired by newly published ECMWF data, we have developed a generic atmospheric correction model whose notable features comprise (i) global coverage, (ii) all-weather, all-time usability, (iii) with a short time delay of less than two days; and (iv) robust and easy to implement automatically, with quality control indicators.

Operational high-resolution ECMWF data (0.125° grid, 137 vertical levels, and 6-hour interval) and continuous GPS tropospheric delay estimates (every 5 min) were integrated using the modified ITD model, in which the relative weights between the two data types were determined iteratively by a cross test. Model performance was tested using eight globally distributed Sentinel-1 interferograms, encompassing both flat and mountainous topographies, midlatitude and near polar regions, and monsoon and oceanic climate systems. The average improvements in terms of phase StdDev resulting from the atmospheric correction maps applied were 47%,

49%, and 54% for GPS, ECMWF, and the integrated corrections, respectively. The corrected InSAR LOS displacements were also compared with the GPS displacements with average RMS improvements for the four interferograms of 55%, 45%, and 63% for GPS, ECMWF and the integrated corrections, respectively. Hence, the integrated model performed the best, with the combination of different data sources increasing the model's reliability, and the displacement StdDev and RMS difference arising for the corrected interferograms considered was approximately 1 cm.

Factors affecting the model performance were investigated in the scenario of an absent ground truth for validation. Then, a set of performance indicators including (i) GPS network and ECMWF cross RMS, (ii) phase versus estimated atmospheric delay correlations, (iii) ECMWF time differences, and (iv) topography variations were developed to enable the model's suitability for InSAR atmospheric correction application to be assessed, and we recommend their adoption as indicators to inform users when abnormal conditions occur and give insights of the confidence level into the correction results.

We made the proposed generic atmospheric correction model available among a wide audience by publishing a Generic Atmospheric Correction Online Service for InSAR (http://ceg-research.ncl.ac.uk/v2/gacos/). The service provides high-resolution atmospheric delay maps globally with two-day latency and benefits not only the InSAR community but GPS and meteorological researchers.

8.1.4 Co-seismic modelling using the atmospheric corrected InSAR measurement

While being extensively addressed in post- and inter-seismic studies requiring millimetre-level precision of velocity mapping, atmospheric delays are typically ignored in co-seismic models under the hypothesis that their magnitude is far smaller than co-seismic signals. However, there are indeed exceptions such as the co-seismic signal of the Nyingchi Mw 6.4 earthquake on 17 November 2017 which was surpassed and masked by the atmospheric delays, particularly those induced by local topographic variations. After applying the generic atmospheric correction model developed in Chapter 5, we successfully extracted the co-seismic surface displacements

from the Sentinel-1 interferograms. The phase standard deviation after correction for a seriously-contaminated interferogram dropped to 0.8 cm, largely improved from the traditional phase correlation analysis (1.13 cm) or bilinear interpolation (1.28 cm) methods. The co-seismic signal stood out only after applying the corrections, and the far-field observation noise was largely reduced, which facilitated the inversion of downdip fault slips.

Atmospheric corrections are essential for events with small magnitude ground displacements and the corrected interferograms for the Nyingchi Mw 6.4 event improved the inversion of the fault geometry and the reconstruction of the slip distribution. The seismogenic fault is a northwest–southeast striking back-thrust fault with a right-lateral strike-slip component. The maximum slip on the determined fault plane was 1.9 m, concentrated on the northwest part at a depth of 8 km. The proposed slip model reflected the strain partitioning of the northeast shortening and eastward movements of the Eastern Tibetan Plateau due to the oblique convergence between the Indian and Eurasian plates.

8.1.5 Afterslip modelling using InSAR and GPS time series

For longer term monitoring (e.g., post/inter-seismic motions, city subsidence) purposes, InSAR time series analysis allows for the separation of the atmospheric delay, DEM and orbital error from the deformation signal through temporal filters so that a 1 mm/year level of velocity precision is achievable. However, the temporal correlation of atmospheric delays (e.g., those induced by constant land covers or seasonal weather variations) would decrease the filter performance and mask or bias geophysical signals and hence introduce unpredictable errors on the velocity estimates. To overcome this, we have developed the SBAS+APS model applied after the generic atmospheric correction, which is capable of reducing atmospheric delay temporal correlations before applying temporal filters and is less dependent on atmospheric delay spatial correlations and therefore is applicable over large areas. The model was validated using a time series of InSAR measurements following the Mw 7.8 2016 Kaikoura earthquake and the resultant InSAR displacement series showed a good agreement against GPS (0.72 cm RMS), dramatically improved from the traditional stacking method (1.95 cm RMS). The larger the spatial extent, the more improvements were observed. Spectral analysis also implied that if

applying only the spatial-temporal filters without the generic atmospheric correction model, the biased high-frequency signals can still be dominating, probably due to atmospheric error temporal correlations.

The atmospheric corrected InSAR displacement series was combined with GPS to reconstruct the afterslip history following the 2016 Kaikoura earthquake. The InSAR time series filled the data gap above the west and southwest of the MFS where few GPS stations are installed. Despite the afterslips and the slow slip event beneath the southern North Island and offshore South Island, we have identified considerable afterslips (up to 2 m in one year) beneath the southwestern Marlborough Fault System located complementarily with the resolved co-seismic interface slip source. It clearly showed that the Hikurangi subduction slab has been triggered by the 2016 Kaikoura earthquake and was accommodating the plate motions. We also observed a shallow slip source on the northern extensions of the Needles fault, which may have induced large offshore surface displacements.

8.2 Research Innovations

The innovations and novelties of the research highlighted throughout the thesis are summarized as follows.

(R1) Proposed and developed an iterative tropospheric decomposition model for pointwise ZTD/PWV interpolation. The model deals with the ZTD/PWV in terms of the tropospheric stratification and turbulence, rather than traditionally dividing it into a hydrostatic component and a wet component, which is problematic for the spatial-temporally differenced InSAR measurements. High-resolution ZTD/PWV maps are generated and validated against MODIS near-IR water vapour fields, with equivalent interpolation performance over mountainous and flat terrain.

(R2) Proposed a framework to routinely use GPS for InSAR atmospheric correction. 45–79% improvements of InSAR displacements are obtainable with both sparse and dense GPS networks, and the impact of station spacing on atmospheric delay interpolation performances is quantitatively evaluated.

(R3) Developed a generic InSAR atmospheric correction model combining GPS and high-resolution ECMWF data with global availability at any time and in all weathers. A set of performance indicators for InSAR atmospheric correction quality control and model applicability evaluation is defined, and an atmospheric correction online service is released.

(R4) Detected small magnitude co-seismic deformation signals (< 10 cm)from InSAR observations contaminated by atmospheric errors. The proposed generic atmospheric correction model overperforms the traditional removal of signals exponentially related to the altitude, and the ITD model overperforms the bilinear interpolation method for the high-resolution ECMWF ZTDs.

(R5) Evidenced the triggered afterslips on the inactive southwestern Hikurangi subduction slab that accommodate regional plate motions using InSAR measurements. A SBAS+APS model is proposed to reduce spatial-temporally correlated atmospheric error in InSAR time series. The recovered afterslip sources suggest an existing but low co-seismic moment release on the Hikurangi subduction slab.

8.3 Future Work

Several InSAR atmospheric correction models were developed, either for individual interferograms or a stack of interferogram series, utilizing external datasets such as GPS and ECMWF. Room for improvement exists as the dataset itself is updated continuously. For example, the ECMWF model has improved its spatial resolution to ~9 km from ~16 km since its first release on 6th June 2017, and the GPS station coverage is steadily increasing, though gaps still remain. Conversely, new datasets will emerge in the next 2-5 years, such as the ERA-5 reanalysis product from ECMWF with ~30 km spatial and hourly temporal resolution (the next generation of ERA-Interim); the Sentinel-3 Ocean and Land Colour Instrument (OLCI) with a 300 m spatial resolution (the next generation of MERIS); and more and more local weather models with several kilometre spatial resolution and hourly temporal resolution. These developments will necessitate future work on validating the new datasets against each other thoroughly on a global scale, and including them in the GACOS system.

Conversely, when considering ground movement as a predictable parameter (e.g., linear background tectonic movements), it becomes possible to retrieve high-resolution water vapour maps from InSAR, perhaps providing more detail spatially than any other water vapour detection techniques, which is beneficial for studying the turbulence features of the troposphere (e.g., mountain waves) and can be fed into numerical weather models. This is already an on-going research topic, but our advantage is to use the models developed in this thesis to correct the first order atmospheric error on InSAR measurements so that the residual water vapour would be separable from the displacement signal without relying on strong linear deformation constraints. By doing this, we can estimate the atmospheric delay and the non-linear deformation signal simultaneously.

Appendix A: List of Publications

Yu, C., Penna, N. T., Li, Z., 2017. Generation of real-time mode high resolution water vapor fields from GPS observations. J. Geophys. Res. Atmos. 122(3), 2008-2025. doi:10.1002/2016JD025753.

Yu, C., Li, Z., Penna, N. T., 2018. Interferometric synthetic aperture radar atmospheric correction using a GPS-based iterative tropospheric decomposition model. Remote Sens. Environ. 204, 109-121. doi:10.1016/j.rse.2017.10.038.

Yu, C., Li, Z., Penna, N. T., Crippa, P., 2018. Generic atmospheric correction model for Interferometric Synthetic Aperture Radar observations. J. Geophys. Res. Solid Earth 123. doi:10.1029/2017JB015305.

Yu, C., Li, Z., Chen, J., Hu, J. C., 2018. Small magnitude co-seismic deformation of the 2017 Mw 6.4 Nyingchi earthquake revealed by InSAR measurements with atmospheric correction. Remote Sens. 10(5), 684. doi:10.3390/rs10050684.

Feng, W., Samsonov, S., Liang, C., Li, J., Charbonneau, F., **Yu, C.,** Li, Z., 2018. Source parameters of the 2017 Mw 6.2 Yukon earthquake doublet inferred from coseismic GPS and ALOS-2 deformation measurements. Geophys. J. Int. 216.3 (2018): 1517-1528. doi:10.1093/gji/ggy497.

Yao, Y., **Yu, C.,** Hu, Y., 2014. A new method to accelerate PPP convergence time by using a global zenith troposphere delay estimate model. J. Navig. 67, 899–910. doi:10.1017/S0373463314000265.

References

Ahmed, F., Václavovic, P., Teferle, F.N., Douša, J., Bingley, R., Laurichesse, D., 2016. Comparative analysis of real-time precise point positioning zenith total delay estimates. GPS Solut. 20, 187–199. doi:10.1007/s10291-014-0427-z

Altamimi, Z., Sillard, P., Boucher, C., 2002. ITRF2000: A new release of the International Terrestrial Reference Frame for earth science applications. J. Geophys. Res. Solid Earth 107, ETG 2-1-ETG 2-19. doi:10.1029/2001JB000561

Anber, U., Wang, S., Sobel, A., 2014. Response of atmospheric convection to vertical wind shear: cloud-system-resolving simulations with parameterized large-scale circulation. Part I: specified radiative cooling. J. Atmos. Sci. 71, 2976–2993. doi:10.1175/JAS-D-13-0320.1

Anzidei, M., Boschi, E., Cannelli, V., Devoti, R., Esposito, A., Galvani, A., Melini, D., Pietrantonio, G., Riguzzi, F., Sepe, V., Serpelloni, E., 2009. Coseismic deformation of the destructive April 6, 2009 L'Aquila earthquake (central Italy) from GPS data. Geophys. Res. Lett. 36. doi:10.1029/2009GL039145

Argus, D.F., Heflin, M.B., Peltzer, G., Crampé, F., Webb, F.H., 2005. Interseismic strain accumulation and anthropogenic motion in metropolitan Los Angeles. J. Geophys. Res. Solid Earth 110, 1–26. doi:10.1029/2003JB002934

Armijo, R., Tapponnier, P., 1989. Late Cenozoic right-lateral strike-slip faulting in southern Tibet. J. Geophys. Res. 94, 2787–2838. doi:10.1029/JB094iB03p02787

Armijo, R., Tapponnier, P., Mercier, J.L., Han, T.-L., 1986. Quaternary extension in southern Tibet: Field observations and tectonic implications. J. Geophys. Res. 91, 13803. doi:10.1029/JB091iB14p13803

Askne, J., Nordius, H., 1987. Estimation of tropospheric delay for microwaves from surface weather data. Radio Sci. 22, 379–386. doi:10.1029/RS022i003p00379

Bai, Y., Lay, T., Cheung, K.F., Ye, L., 2017. Two regions of seafloor deformation generated the tsunami for the 13 November 2016, Kaikoura, New Zealand earthquake. Geophys. Res. Lett. 44, 6597–6606. doi:10.1002/2017GL073717

Beavan, J., Samsonov, S., Denys, P., Sutherland, R., Palmer, N., Denham, M., 2010. Oblique slip on the Puysegur subduction interface in the 2009 July MW 7.8 Dusky Sound

earthquake from GPS and InSAR observations: Implications for the tectonics of southwestern New Zealand. Geophys. J. Int. 183, 1265–1286. doi:10.1111/j.1365-246X.2010.04798.x

Béjar-Pizarro, M., Socquet, A., Armijo, R., Carrizo, D., Genrich, J., Simons, M., 2013. Andean structural control on interseismic coupling in the North Chile subduction zone. Nat. Geosci. 6, 462–467. doi:10.1038/ngeo1802

Bekaert, D.P.S., Hooper, A., Wright, T.J., 2015a. A spatially variable power law tropospheric correction technique for InSAR data. J. Geophys. Res. Solid Earth 120, 1345–1356. doi:10.1002/2014JB011558

Bekaert, D.P.S., Segall, P., Wright, T.J., Hooper, A.J., 2016. A Network Inversion Filter combining GNSS and InSAR for tectonic slip modeling. J. Geophys. Res. Solid Earth 121, 2069–2086. doi:10.1002/2015JB012638

Bekaert, D.P.S., Walters, R.J., Wright, T.J., Hooper, A.J., Parker, D.J., 2015b. Statistical comparison of InSAR tropospheric correction techniques. Remote Sens. Environ. 170, 40–47. doi:10.1016/j.rse.2015.08.035

Bell, J.W., Amelung, F., Ferretti, A., Bianchi, M., Novali, F., 2008. Monitoring aquifer-system response to groundwater pumping and artificial recharge. First Break 26, 85–91. doi:10.1029/2007WR006152

Benevides, P., Catalao, J., Miranda, P.M.A., 2015. On the inclusion of GPS precipitable water vapour in the nowcasting of rainfall. Nat. Hazards Earth Syst. Sci. 15, 2605–2616. doi:10.5194/nhess-15-2605-2015

Benevides, P., Nico, G., Catalão, J., Miranda, P.M.A., 2016. Bridging InSAR and GPS tomography: a new differential geometrical constraint. IEEE Trans. Geosci. Remote Sens. 54, 697–702. doi:10.1109/TGRS.2015.2463263

Berrada Baby, H., Golé, P., Lavergnat, J., 1988. A model for the tropospheric excess path length of radio waves from surface meteorological measurements. Radio Sci. 23, 1023–1038. doi:10.1029/RS023i006p01023

Betts, R.A., Falloon, P.D., Goldewijk, K.K., Ramankutty, N., 2007. Biogeophysical effects of land use on climate: Model simulations of radiative forcing and large-scale temperature change. Agric. For. Meteorol. 142, 216–233. doi:10.1016/j.agrformet.2006.08.021

Bevis, M., Brown, A., 2014. Trajectory models and reference frames for crustal motion geodesy. J. Geod. 88, 283–311. doi:10.1007/s00190-013-0685-5

Bevis, M., Businger, S., Herring, T.A., Rocken, C., Anthes, R.A., Ware, R.H., 1992. GPS meteorology: Remote sensing of atmospheric water vapor using the global positioning system. J. Geophys. Res. 97, 15787. doi:10.1029/92JD01517

Beyerle, G., 2009. Carrier phase wind-up in GPS reflectometry. GPS Solut. 13, 191–198. doi:10.1007/s10291-008-0112-1

Biggs, J., Wright, T., Lu, Z., Parsons, B., 2007. Multi-interferogram method for measuring interseismic deformation: Denali Fault, Alaska. Geophys. J. Int. 170, 1165–1179. doi:10.1111/j.1365-246X.2007.03415.x

Blewitt, G., Kreemer, C., Hammond, W.C., Gazeaux, J., 2016. MIDAS robust trend estimator for accurate GPS station velocities without step detection. J. Geophys. Res. Solid Earth 121, 2054–2068. doi:10.1002/2015JB012552

Bock, O., Keil, C., Richard, E., Flamant, C., Bouin, M.N., 2005. Validation for precipitable water from ECMWF model analyses with GPS and radiosonde data during the MAP SOP. Q. J. R. Meteorol. Soc. 131, 3013–3036. doi:10.1256/qj.05.27

Boehm, J., Niell, A., Tregoning, P., Schuh, H., 2006. Global Mapping Function (GMF): A new empirical mapping function based on numerical weather model data. Geophys. Res. Lett. 33, L07304. doi:10.1029/2005GL025546

Boniface, K., Ducrocq, V., Jaubert, G., Yan, X., Brousseau, P., Masson, F., Champollion, C., Chéry, J., Doerflinger, E., 2009. Impact of high-resolution data assimilation of GPS zenith delay on Mediterranean heavy rainfall forecasting. Ann. Geophys. 27, 2739–2753. doi:10.5194/angeo-27-2739-2009

Bouin, M.N., Wöppelmann, G., 2010. Land motion estimates from GPS at tide gauges: A geophysical evaluation. Geophys. J. Int. 180, 193–209. doi:10.1111/j.1365-246X.2009.04411.x

Bourne, S.J., Árnadóttir, T., Beavan, J., Darby, D.J., England, P.C., Parsons, B., Walcott, R.I., Wood, P.R., 1998. Crustal deformation of the Marlborough Fault Zone in the South Island of New Zealand: Geodetic constraints over the interval 1982–1994. J. Geophys. Res. 103, 30147. doi:10.1029/98JB02228

Bürgmann, R., Rosen, P.A., Fielding, E.J., 2000. Synthetic aperture radar interferometry to measure earth's surface topography and its deformation. Annu. Rev. Earth Planet. Sci. 28, 169–209. doi:10.1146/annurev.earth.28.1.169

Cavalié, O., Pathier, E., Radiguet, M., Vergnolle, M., Cotte, N., Walpersdorf, A., Kostoglodov, V., Cotton, F., 2013. Slow slip event in the Mexican subduction zone: Evidence of shallower slip in the Guerrero seismic gap for the 2006 event revealed by the joint inversion of InSAR and GPS data. Earth Planet. Sci. Lett. 367, 52–60. doi:10.1016/j.epsl.2013.02.020

Chen, M., Tomás, R., Li, Z., Motagh, M., Li, T., Hu, L., 2016. Imaging land subsidence induced by groundwater extraction in Beijing (China) using satellite radar interferometry. Remote Sens. 1–21. doi:10.3390/rs8060468

Chen, Q., Liu, G., Ding, X., Hu, J.C., Yuan, L., Zhong, P., Omura, M., 2010. Tight integration of GPS observations and persistent scatterer InSAR for detecting vertical ground motion in Hong Kong. Int. J. Appl. Earth Obs. Geoinf. 12, 477–486. doi:10.1016/j.jag.2010.05.002

Chlieh, M., Avouac, J.P., Hjorleifsdottir, V., Song, T.R.A., Ji, C., Sieh, K., Sladen, A., Hebert, H., Prawirodirdjo, L., Bock, Y., Galetzka, J., 2007. Coseismic slip and afterslip of the great Mw 9.15 Sumatra-Andaman earthquake of 2004. Bull. Seismol. Soc. Am. 97, S152--S173. doi:10.1785/0120050631

Cho, J.Y.N., Newell, R.E., Anderson, B.E., Barrick, J.D.W., Thornhill, K.L., 2003. Characterizations of tropospheric turbulence and stability layers from aircraft observations. J. Geophys. Res. Atmos. 108. doi:10.1029/2002JD002820

Clark, K.J., Nissen, E.K., Howarth, J.D., Hamling, I.J., Mountjoy, J.J., Ries, W.F., Jones, K., Goldstien, S., Cochran, U.A., Villamor, P., Hreinsdóttir, S., Litchfield, N.J., Mueller, C., Berryman, K.R., Strong, D.T., 2017. Highly variable coastal deformation in the 2016 MW7.8 Kaikōura earthquake reflects rupture complexity along a transpressional plate boundary. Earth Planet. Sci. Lett. 474, 334–344. doi:10.1016/j.epsl.2017.06.048

Coleman, M., Hodges, K., 1995. Evidence for Tibetan plateau uplift before 14 Myr ago from a new minimum age for east-west extension. Nature 374, 49–52. doi:10.1038/374049a0

Cowan, H.A., 1990. Late Quaternary displacements on the Hope Fault at Glynn Wye, north

Canterbury. New Zeal. J. Geol. Geophys. 33, 285–293. doi:10.1080/00288306.1990.10425686

Crosetto, M., Tscherning, C.C., Crippa, B., Castillo, M., 2002. Subsidence monitoring using SAR interferometry: Reduction of the atmospheric effects using stochastic filtering. Geophys. Res. Lett. 29, 26-1-26–4. doi:10.1029/2001GL013544

Darby, D.J., Beanland, S., 1992. Possible source models for the 1855 Wairarapa Earthquake, New Zealand. J. Geophys. Res. 97, 12375. doi:10.1029/92JB00567

Dawson, J., Tregoning, P., 2007. Uncertainty analysis of earthquake source parameters determined from InSAR: A simulation study. J. Geophys. Res. Solid Earth 112, B09406. doi:10.1029/2007JB005209

Delacourt, C., Briole, P., Achache, J., 1998. Tropospheric corrections of SAR interferograms with strong topography. Application to Etna. Geophys. Res. Lett. 25, 2849–2852. doi:10.1029/98GL02112

DeMets, C., Gordon, R.G., Argus, D.F., Stein, S., 1990. Current plate motions. Geophys. J. Int. 101, 425–478. doi:10.1111/j.1365-246X.1990.tb06579.x

Ding, X.L., Li, Z.W., Zhu, J.J., Feng, G.C., Long, J.P., 2008. Atmospheric effects on InSAR measurements and their mitigation. Sensors 8, 5426–5448. doi:10.3390/s8095426

Ding, Z., Wang, Z., Lin, S., Liu, T., Zhang, Q., Long, T., 2017. Local fringe frequency estimation based on multifrequency InSAR for phase-noise reduction in highly sloped terrain. IEEE Geosci. Remote Sens. Lett. 14, 1527–1531. doi:10.1109/LGRS.2017.2720695

Doin, M.P., Lasserre, C., Peltzer, G., Cavalié, O., Doubre, C., 2009. Corrections of stratified tropospheric delays in SAR interferometry: Validation with global atmospheric models. J. Appl. Geophys. 69, 35–50. doi:10.1016/j.jappgeo.2009.03.010

Ehret, G., Hoinka, K.P., Stein, J., Fix, A., Kiemle, C., Poberaj, G., 1999. Low stratospheric water vapor measured by an airborne DIAL. J. Geophys. Res. Atmos. 104, 31351–31359. doi:10.1029/1999JD900959

Elliott, J.R., Biggs, J., Parsons, B., Wright, T.J., 2008. InSAR slip rate determination on the Altyn Tagh Fault, northern Tibet, in the presence of topographically correlated atmospheric delays. Geophys. Res. Lett. 35. doi:10.1029/2008GL033659

Emardson, T.R., Johansson, J.M., 1998. Spatial interpolation of the atmospheric water vapor content between sites in a ground-based GPS network. Geophys. Res. Lett. 25, 3347–3350. doi:10.1029/98GL02504

Emardson, T.R., Simons, M., Webb, F.H., 2003. Neutral atmospheric delay in interferometric synthetic aperture radar applications: Statistical description and mitigation. J. Geophys. Res. Solid Earth 108. doi:10.1029/2002JB001781

Farr, T.G., Rosen, P.A., Caro, E., Crippen, R., Duren, R., Hensley, S., Kobrick, M., Paller, M., Rodriguez, E., Roth, L., Seal, D., Shaffer, S., Shimada, J., Umland, J., Werner, M., Oskin, M., Burbank, D., Alsdorf, D.E., 2007. The shuttle radar topography mission. Rev. Geophys. 45, RG2004. doi:10.1029/2005RG000183

Fattahi, H., Amelung, F., 2015. InSAR bias and uncertainty due to the systematic and stochastic tropospheric delay. J. Geophys. Res. Solid Earth 120, 8758–8773. doi:10.1002/2015JB012419

Fattahi, H., Amelung, F., 2014. InSAR uncertainty due to orbital errors. Geophys. J. Int. 199, 549–560. doi:10.1093/gji/ggu276

Fattahi, H., Amelung, F., 2013. DEM error correction in InSAR time series. IEEE Trans. Geosci. Remote Sens. 51, 4249–4259. doi:10.1109/TGRS.2012.2227761

Fattahi, H., Amelung, F., Chaussard, E., Wdowinski, S., 2015. Coseismic and postseismic deformation due to the 2007 M5.5 Ghazaband fault earthquake, Balochistan, Pakistan. Geophys. Res. Lett. 42, 3305–3312. doi:10.1002/2015GL063686

Feng, W., Li, Z., Elliott, J.R., Fukushima, Y., Hoey, T., Singleton, A., Cook, R., Xu, Z., 2013. The 2011MW6.8 Burma earthquake: Fault constraints provided by multiple SAR techniques. Geophys. J. Int. 195, 650–660. doi:10.1093/gji/ggt254

Feng, W., Samsonov, S., Li, P., Omari, K., 2016. Coseismic and early-postseismic displacements of the 2015 MW8.3 Illapel (Chile) earthquaek imaged by Sentinel-1a and RADARSAT-2, in: International Geoscience and Remote Sensing Symposium (IGARSS). IEEE, pp. 5990–5993. doi:10.1109/IGARSS.2016.7730565

Ferretti, A., Fumagalli, A., Novali, F., Prati, C., Rocca, F., Rucci, A., 2011. A new algorithm for processing interferometric data-stacks: SqueeSAR, in: IEEE Transactions on Geoscience and Remote Sensing. pp. 3460–3470. doi:10.1109/TGRS.2011.2124465

Ferretti, A., Prati, C., Rocca, F., 2001. Permanent scatterers in SAR interferometry. IEEE Trans. Geosci. Remote Sens. 39, 8–20. doi:10.1109/36.898661

Fialko, Y., 2006. Interseismic strain accumulation and the earthquake potential on the southern San Andreas fault system. Nature 441, 968–971. doi:10.1038/nature04797

Fielding, E.J., Sangha, S.S., Bekaert, D.P.S., Samsonov, S. V., Chang, J.C., 2017. Surface deformation of north-central Oklahoma related to the 2016 Mw 5.8 Pawnee Earthquake from SAR interferometry time series. Seismol. Res. Lett. 88, 971–982. doi:10.1785/0220170010

Foster, J., Brooks, B., Cherubini, T., Shacat, C., Businger, S., Werner, C.L., 2006. Mitigating atmospheric noise for InSAR using a high resolution weather model. Geophys. Res. Lett. 33, L16304. doi:10.1029/2006GL026781

Foster, J., Kealy, J., Cherubini, T., Businger, S., Lu, Z., Murphy, M., 2013. The utility of atmospheric analyses for the mitigation of artifacts in InSAR. J. Geophys. Res. Solid Earth 118, 748–758. doi:10.1002/jgrb.50093

Fruneau, B., Sarti, F., 2000. Detection of ground subsidence in the city of Paris using radar interferometry: Isolation of deformation from atmospheric artifacts using correlation. Geophys. Res. Lett. 27, 3981–3984. doi:10.1029/2000GL008489

Fukahata, Y., Wright, T.J., 2008. A non-linear geodetic data inversion using ABIC for slip distribution on a fault with an unknown dip angle. Geophys. J. Int. 173, 353–364. doi:10.1111/j.1365-246X.2007.03713.x

Gao, B.-C., Kaufman, Y.J., 2003. Water vapor retrievals using Moderate Resolution Imaging Spectroradiometer (MODIS) near-infrared channels. J. Geophys. Res. Atmos. 108, 4389. doi:10.1029/2002JD003023

Gendt, G., Dick, G., Reigber, C., Tomassini, M., Liu, Y., Ramatschi, M., 2004. Near real time GPS water vapor monitoring for numerical weather prediction in Germany. J. Meteorol. Soc. Japan 82, 361–370. doi:10.2151/jmsj.2004.361

Genrich, J.F., Bock, Y., 2006. Instantaneous geodetic positioning with 10-50 Hz GPS measurements: Noise characteristics and implications for monitoring networks. J. Geophys. Res. Solid Earth 111, B03403. doi:10.1029/2005JB003617

Gili, J.A., Corominas, J., Rius, J., 2000. Using Global Positioning System techniques in

landslide monitoring. Eng. Geol. 55, 167–192.

Glowacki, T.J., Penna, N.T., Bourke, W.P., 2006. Validation of GPS-based estimates of integrated water vapour for the Australian region and identification of diurnal variability. Aust. Meteorol. Mag. 55, 131–148.

Goldstein, R., 1995. Atmospheric limitations to repeat-track radar interferometry. Geophys. Res. Lett. 22, 2517–2520. doi:10.1029/95GL02475

Goldstein, R.M., Zebker, H.A., Werner, C.L., 1988. Satellite radar interferometry: Two-dimensional phase unwrapping. Radio Sci. 23, 713–720. doi:10.1029/RS023i004p00713

Gomba, G., Parizzi, A., De Zan, F., Eineder, M., Bamler, R., 2016. Toward operational compensation of ionospheric effects in SAR interferograms: The split-spectrum method. IEEE Trans. Geosci. Remote Sens. 54, 1446–1461. doi:10.1109/TGRS.2015.2481079

Gomba, G., Rodriguez Gonzalez, F., De Zan, F., 2017. Ionospheric phase screen compensation for the Sentinel-1 TOPS and ALOS-2 ScanSAR modes. IEEE Trans. Geosci. Remote Sens. 55, 223–235. doi:10.1109/TGRS.2016.2604461

González, P.J., Fernández, J., 2011. Error estimation in multitemporal InSAR deformation time series, with application to Lanzarote, Canary Islands. J. Geophys. Res. Solid Earth 116, B10404. doi:10.1029/2011JB008412

Gourmelen, N., Amelung, F., 2005. Geophysics: Postseismic mantle relaxation in the Central Nevada Seismic Belt. Science 310, 1473–1476. doi:10.1126/science.1119798

Gray, A.L., Mattar, K.E., Sofko, G., 2000. Influence of ionospheric electron density fluctuations on satellite radar interferometry. Geophys. Res. Lett. 27, 1451–1454. doi:10.1029/2000GL000016

Gualandi, A., Avouac, J.P., Galetzka, J., Genrich, J.F., Blewitt, G., Adhikari, L.B., Koirala, B.P., Gupta, R., Upreti, B.N., Pratt-Sitaula, B., Liu-Zeng, J., 2017. Pre- and post-seismic deformation related to the 2015, Mw7.8 Gorkha earthquake, Nepal. Tectonophysics 714–715, 90–106. doi:10.1016/j.tecto.2016.06.014

Gundlich, B., Koch, K.R., 2002. Confidence regions for GPS baselines by Bayesian statistics. J. Geod. 76, 55–62. doi:10.1007/s001900100222

Habermann, R.E., Wyss, M., 1984. Earthquake triggering during preparation for great earthquakes. Geophys. Res. Lett. 11, 291–294. doi:10.1029/GL011i004p00291

Haddad, A.H., 1976. Applied optimal estimation. Proc. IEEE 64, 574–575. doi:10.1109/PROC.1976.10175

Hamling, I.J., Hreinsdóttir, S., Clark, K., Elliott, J., Liang, C., Fielding, E., Litchfield, N., Villamor, P., Wallace, L., Wright, T.J., D'Anastasio, E., Bannister, S., Burbidge, D., Denys, P., Gentle, P., Howarth, J., Mueller, C., Palmer, N., Pearson, C., Power, W., Barnes, P., Barrell, D.J.A., Van Dissen, R., Langridge, R., Little, T., Nicol, A., Pettinga, J., Rowland, J., Stirling, M., 2017. Complex multifault rupture during the 2016 Mw 7.8 Kaikōura earthquake, New Zealand. Science 356, eaam7194. doi:10.1126/science.aam7194

Hanssen, R., 2001. Radar interferometry: data interpretation and error analysis. Springer Science & Business Media, The Netherlands.

Hanssen, R., 1998. Atmospheric heterogeneities in ERS tandem SAR interferometry, DEOS Report 98.1. Delft University Press, The Netherlands.

Hinich, M.J., Wilson, G.R., 1990. Detection of non-Gaussian signals in non-Gaussian noise using the bispectrum. IEEE Trans. Acoust. 38, 1126–1131. doi:10.1109/29.57541

Holden, C., Kaneko, Y., D'Anastasio, E., Benites, R., Fry, B., Hamling, I.J., 2017. The 2016 Kaikōura Earthquake revealed by kinematic source inversion and seismic wavefield simulations: Slow rupture propagation on a geometrically complex crustal fault network. Geophys. Res. Lett. 44, 11,320-11,328. doi:10.1002/2017GL075301

Holt, W.E., Haines, A.J., 1995. The kinematics of northern South Island, New Zealand, determined from geologic strain rates. J. Geophys. Res. Solid Earth 100, 17991–18010. doi:10.1029/95JB01059

Hooper, A., Bekaert, D., Spaans, K., Arikan, M., 2012. Recent advances in SAR interferometry time series analysis for measuring crustal deformation. Tectonophysics 514–517, 1–13. doi:10.1016/j.tecto.2011.10.013

Hooper, A., Segall, P., Zebker, H., 2007. Persistent scatterer interferometric synthetic aperture radar for crustal deformation analysis, with application to Volcán Alcedo, Galápagos. J. Geophys. Res. Solid Earth 112, B07407. doi:10.1029/2006JB004763

Hooper, A., Zebker, H., Segall, P., Kampes, B., 2004. A new method for measuring deformation on volcanoes and other natural terrains using InSAR persistent scatterers. Geophys. Res. Lett. 31, 1–5. doi:10.1029/2004GL021737

Hopfield, H.S., 1971. Tropospheric effect on electromagnetically measured range: prediction from surface weather data. Radio Sci. 6, 357–367. doi:10.1029/RS006i003p00357

Houlie, N., Funning, G.J., Burgmann, R., 2016. Use of a GPS-Derived troposphere model to improve InSAR deformation estimates in the San Gabriel Valley, California. IEEE Trans. Geosci. Remote Sens. 54, 5365–5374. doi:10.1109/TGRS.2016.2561971

Hu, X., Wang, T., Liao, M., 2014. Measuring coseismic displacements with point-like targets offset tracking. IEEE Geosci. Remote Sens. Lett. 11, 283–287. doi:10.1109/LGRS.2013.2256104

Hussain, E., Wright, T.J., Walters, R.J., Bekaert, D., Hooper, A., Houseman, G.A., 2016. Geodetic observations of postseismic creep in the decade after the 1999 Izmit earthquake, Turkey: Implications for a shallow slip deficit. J. Geophys. Res. Solid Earth 121, 2980–3001. doi:10.1002/2015JB012737

Janssen, V., Ge, L., Rizos, C., 2004. Tropospheric corrections to SAR interferometry from GPS observations. GPS Solut. 8, 140–151. doi:10.1007/s10291-004-0099-1

Jarlemark, P.O.J., Emardson, T.R., 1998. Strategies for spatial and temporal extrapolation and interpolation of wet delay. J. Geod. 72, 350–355. doi:10.1007/s001900050174

Jarque, C.M., Bera, A.K., 1980. Efficient tests for normality, homoscedasticity and serial independence of regression residuals. Econ. Lett. 6, 255–259. doi:10.1016/0165-1765(80)90024-5

Jiang, M., Ding, X., Li, Z., Tian, X., Wang, C., Zhu, W., 2014. InSAR coherence estimation for small data sets and its impact on temporal decorrelation extraction. IEEE Trans. Geosci. Remote Sens. 52, 6584–6596. doi:10.1109/TGRS.2014.2298408

Jiang, Z., Huang, D., Yuan, L., Hassan, A., Zhang, L., Yang, Z., 2018. Coseismic and postseismic deformation associated with the 2016 Mw 7.8 Kaikoura earthquake, New Zealand: fault movement investigation and seismic hazard analysis. Earth, Planets Sp. 70, 62. doi:10.1186/s40623-018-0827-3

Jolivet, R., Agram, P.S., Lin, N.Y., Simons, M., Doin, M.P., Peltzer, G., Li, Z., 2014. Improving InSAR geodesy using Global Atmospheric Models. J. Geophys. Res. Solid Earth 119, 2324–2341. doi:10.1002/2013JB010588

Jolivet, R., Grandin, R., Lasserre, C., Doin, M.P., Peltzer, G., 2011. Systematic InSAR

tropospheric phase delay corrections from global meteorological reanalysis data. Geophys. Res. Lett. 38. doi:10.1029/2011GL048757

Jolivet, R., Simons, M., Agram, P.S., Duputel, Z., Shen, Z.K., 2015. Aseismic slip and seismogenic coupling along the central San Andreas Fault. Geophys. Res. Lett. 42, 297–306. doi:10.1002/2014GL062222

Jung, J., Kim, D.J., Park, S.E., 2014. Correction of atmospheric phase screen in time series InSAR using WRF model for monitoring volcanic activities. IEEE Trans. Geosci. Remote Sens. 52, 2678–2689. doi:10.1109/TGRS.2013.2264532

Kim, J.S., Papathanassiou, K.P., Scheiber, R., Quegan, S., 2015. Correcting distortion of polarimetric SAR data induced by ionospheric scintillation. IEEE Trans. Geosci. Remote Sens. 53, 6319–6335. doi:10.1109/TGRS.2015.2431856

Kouba, J., 2009. Testing of global pressure/temperature (GPT) model and global mapping function (GMF) in GPS analyses. J. Geod. 83, 199–208. doi:10.1007/s00190-008-0229-6

Koulali, A., Ouazar, D., Bock, O., Fadil, A., 2012. Study of seasonal-scale atmospheric water cycle with ground-based GPS receivers, radiosondes and NWP models over Morocco. Atmos. Res. 104–105, 273–291. doi:10.1016/J.ATMOSRES.2011.11.002

Lancaster, M., 1989. Summary for Policymakers, in: Climate Change 2013 - The Physical Science Basis. pp. 1–30. doi:10.1017/CBO9781107415324.004

Lau, N., Tymofyeyeva, E., Fialko, Y., 2018. Variations in the long-term uplift rate due to the Altiplano–Puna magma body observed with Sentinel-1 interferometry. Earth Planet. Sci. Lett. 491, 43–47. doi:10.1016/j.epsl.2018.03.026

Lauknes, T.R., Zebker, H.A., Larsen, Y., 2011. InSAR deformation time series using an L1-norm small-baseline approach. IEEE Trans. Geosci. Remote Sens. 49, 536–546. doi:10.1109/TGRS.2010.2051951

Leandro, R.F., Santos, M.C., Langley, R.B., 2006. UNB neutral atmosphere models: Development and performance. Proc. 2006 Natl. Tech. Meet. Inst. Navig. 564–573.

Lee, H.Y., Chung, S.L., Wang, J.R., Wen, D.J., Lo, C.H., Yang, T.F., Zhang, Y., Xie, Y., Lee, T.Y., Wu, G., Ji, J., 2003. Miocene Jiali faulting and its implications for Tibetan tectonic evolution. Earth Planet. Sci. Lett. 205, 185–194. doi:10.1016/S0012-821X(02)01040-3

Lee, W.J., Lu, Z., Jung, H.S., Ji, L., 2017. Measurement of small co-seismic deformation field

from multi-temporal SAR interferometry: application to the 19 September 2004 Huntoon Valley earthquake. Geomatics, Nat. Hazards Risk 8, 1241–1257. doi:10.1080/19475705.2017.1310764

Li, S., Freymueller, J., McCaffrey, R., 2016. Slow slip events and time-dependent variations in locking beneath Lower Cook Inlet of the Alaska-Aleutian subduction zone. J. Geophys. Res. Solid Earth 121, 1060–1079. doi:10.1002/2015JB012491

Li, X., Dick, G., Ge, M., Heise, S., Wickert, J., Bender, M., 2014. Real-time GPS sensing of atmospheric water vapor: Precise point positioning with orbit, clock, and phase delay corrections. Geophys. Res. Lett. 41, 3615–3621. doi:10.1002/2013GL058721

Li, X., Zus, F., Lu, C., Dick, G., Ning, T., Ge, M., Wickert, J., Schuh, H., 2015. Retrieving of atmospheric parameters from multi-GNSS in real time: Validation with water vapor radiometer and numerical weather model. J. Geophys. Res. 120, 7189–7204. doi:10.1002/2015JD023454

Li, Z., Fielding, E.J., Cross, P., 2009a. Integration of InSAR time-series analysis and water-vapor correction for emapping postseismic motion after the 2003 Bam (Iran) earthquake. IEEE Trans. Geosci. Remote Sens. 47, 3220–3230. doi:10.1109/TGRS.2009.2019125

Li, Z., Fielding, E.J., Cross, P., Muller, J.P., 2006a. Interferometric synthetic aperture radar atmospheric correction: GPS topography-dependent turbulence model. J. Geophys. Res. Solid Earth 111. doi:10.1029/2005JB003711

Li, Z., Fielding, E.J., Cross, P., Preusker, R., 2009b. Advanced InSAR atmospheric correction: MERIS/MODIS combination and stacked water vapour models. Int. J. Remote Sens. 30, 3343–3363. doi:10.1080/01431160802562172

Li, Z., Muller, J.P., Cross, P., 2003. Comparison of precipitable water vapor derived from radiosonde, GPS, and Moderate-Resolution Imaging Spectroradiometer measurements. J. Geophys. Res. Atmos. 108, 4651. doi:10.1029/2003JD003372

Li, Z., Muller, J.P., Cross, P., Albert, P., Fischer, J., Bennartz, R., 2006b. Assessment of the potential of MERIS near-infrared water vapour products to correct ASAR interferometric measurements. Int. J. Remote Sens. 27, 349–365. doi:10.1080/01431160500307342

Li, Z., Muller, J.P., Cross, P., Fielding, E.J., 2005. Interferometric synthetic aperture radar (InSAR) atmospheric correction: GPS, Moderate Resolution Imaging Spectroradiometer

(MODIS), and InSAR integration. J. Geophys. Res. Solid Earth 110, 1–10. doi:10.1029/2004JB003446

Li, Z.W., Ding, X.L., Huang, C., Zou, Z.R., Chen, Y.L., 2007. Atmospheric effects on repeat-pass InSAR measurements over Shanghai region. J. Atmos. Solar-Terrestrial Phys. 69, 1344–1356. doi:10.1016/j.jastp.2007.04.007

Li, Z.W., Ding, X.L., Liu, G.X., 2004. Modeling atmospheric effects on InSAR with meteorological and continuous GPS observations: Algorithms and some test results. J. Atmos. Solar-Terrestrial Phys. 66, 907–917. doi:10.1016/j.jastp.2004.02.006

Li, Z.W., Xu, W.B., Feng, G.C., Hu, J., Wang, C.C., Ding, X.L., Zhu, J.J., 2012. Correcting atmospheric effects on InSAR with MERIS water vapour data and elevation-dependent interpolation model. Geophys. J. Int. 189, 898–910. doi:10.1111/j.1365-246X.2012.05432.x

Liang, S., Gan, W., Shen, C., Xiao, G., Liu, J., Chen, W., Ding, X., Zhou, D., 2013. Three-dimensional velocity field of present-day crustal motion of the Tibetan Plateau derived from GPS measurements. J. Geophys. Res. Solid Earth 118, 5722–5732. doi:10.1002/2013JB010503

Libert, L., Derauw, D., D'Oreye, N., Barbier, C., Orban, A., 2017. Split-band interferometry-assisted phase unwrapping for the phase ambiguities correction. Remote Sens. 9, 879. doi:10.3390/rs9090879

Liou, Y., Teng, Y., Van Hove, T., Liljegren, J.C., 2001. Comparison of precipitable water observations in the near tropics by GPS, microwave radiometer, and radiosondes. J. Appl. Meteorol. 40, 5–15. doi:10.1175/1520-0450(2001)040<0005:COPWOI>2.0.CO;2

Liu, G.X., Ding, X.L., Li, Z.L., Li, Z.W., Chen, Y.Q., Yu, S.B., 2004. Pre- and co-seismic ground deformations of the 1999 Chi-Chi, Taiwan earthquake, measured with SAR interferometry. Comput. Geosci. 30, 333–343. doi:10.1016/j.cageo.2003.08.011

Liu, J., Ge, M., 2003. PANDA software and its preliminary result of positioning and orbit determination. Wuhan Univ. J. Nat. Sci. 8, 603–609. doi:10.1007/BF02899825

Liu, P., Li, Z., Hoey, T., Kincal, C., Zhang, J., Zeng, Q., Muller, J.P., 2012. Using advanced inSAR time series techniques to monitor landslide movements in Badong of the Three Gorges region, China. Int. J. Appl. Earth Obs. Geoinf. 21, 253–264.

doi:10.1016/j.jag.2011.10.010

Löfgren, J.S., Björndahl, F., Moore, A.W., Webb, F.H., Fielding, E.J., Fishbein, E.F., 2010. Tropospheric correction for InSAR using interpolated ECMWF data and GPS zenith total delay from the Southern California integrated GPS network, in: International Geoscience and Remote Sensing Symposium (IGARSS). IEEE, pp. 4503–4506. doi:10.1109/IGARSS.2010.5649888

Luzi, G., Pieraccini, M., Mecatti, D., Noferini, L., Guidi, G., Moia, F., Atzeni, C., 2004. Ground-based radar interferometry for landslides monitoring: Atmospheric and instrumental decorrelation sources on experimental data. IEEE Trans. Geosci. Remote Sens. 42, 2454–2466. doi:10.1109/TGRS.2004.836792

Lyard, F., Lefevre, F., Letellier, T., Francis, O., 2006. Modelling the global ocean tides: Modern insights from FES2004. Ocean Dyn. 56, 394–415. doi:10.1007/s10236-006-0086-x

Mahmood, R., Pielke, R.A., Hubbard, K.G., Niyogi, D., Dirmeyer, P.A., Mcalpine, C., Carleton, A.M., Hale, R., Gameda, S., Beltrán-Przekurat, A., Baker, B., Mcnider, R., Legates, D.R., Shepherd, M., Du, J., Blanken, P.D., Frauenfeld, O.W., Nair, U.S., Fall, S., 2014. Land cover changes and their biogeophysical effects on climate. Int. J. Climatol. 34, 929–953. doi:10.1002/joc.3736

Malenovský, Z., Rott, H., Cihlar, J., Schaepman, M.E., García-Santos, G., Fernandes, R., Berger, M., 2012. Sentinels for science: Potential of Sentinel-1, -2, and -3 missions for scientific observations of ocean, cryosphere, and land. Remote Sens. Environ. 120, 91–101. doi:10.1016/j.rse.2011.09.026

Massey, C., Townsend, D., Rathje, E., Allstadt, K.E., Lukovic, B., Kaneko, Y., Bradley, B., Wartman, J., Jibson, R.W., Petley, D.N., Horspool, N., Hamling, I., Carey, J., Cox, S., Davidson, J., Dellow, S., Godt, J.W., Holden, C., Jones, K., Kaiser, A., Little, M., Lyndsell, B., McColl, S., Morgenstern, R., Rengers, F.K., Rhoades, D., Rosser, B., Strong, D., Singeisen, C., Villeneuve, M., 2018. Landslides triggered by the 14 November 2016 Mw 7.8 Kaikoura Earthquake, New Zealand. Bull. Seismol. Soc. Am. doi:10.1785/0120170305

Massonnet, D., Briole, P., Arnaud, A., 1995. Deflation of Mount Etna monitored by spaceborne radar interferometry. Nature 375, 567–570. doi:10.1038/375567a0

Massonnet, D., Feigl, K., Rossi, M., Adragna, F., 1994. Radar interferometric mapping of deformation in the year after the Landers earthquake. Nature 369, 227–230. doi:10.1038/369227a0

Massonnet, D., Feigl, K.L., 1998. Radar interferometry and its application to changes in the earth's surface. Rev. Geophys. 36, 441–500. doi:10.1029/97RG03139

Massonnet, D., Rossi, M., Carmona, C., Adragna, F., Peltzer, G., Feigl, K., Rabaute, T., 1993. The displacement field of the Landers earthquake mapped by radar interferometry. Nature 364, 138–142. doi:10.1038/364138a0

McCarthy, D.D., 1996. IERS conventions (1996). IERS Tech. Note 21, 101. doi:10.1007/s00190-011-0444-4

Mears, C.A., Wang, J., Smith, D., Wentz, F.J., 2015. Intercomparison of total precipitable water measurements made by satellite-borne microwave radiometers and ground-based GPS instruments. J. Geophys. Res. Atmos. 120, 2492–2504. doi:10.1002/2014JD022694

Mengistu Tsidu, G., Blumenstock, T., Hase, F., 2015. Observations of precipitable water vapour over complex topography of Ethiopia from ground-based GPS, FTIR, radiosonde and ERA-Interim reanalysis. Atmos. Meas. Tech. 8, 3277–3295. doi:10.5194/amt-8-3277-2015

Michel, R., Avouac, J.P., Taboury, J., 1999. Measuring ground displacements from SAR amplitude images: Application to the Landers earthquake. Geophys. Res. Lett. 26, 875–878. doi:10.1029/1999GL900138

Molnar, P., Chen, W.P., 1983. Focal depths and fault plane solutions of earthquakes under the Tibetan plateau. J. Geophys. Res. 88, 1180–1196. doi:10.1029/JB088iB02p01180

Mora, O., Lanari, R., Mallorqui, J.J., Berardino, P., Sansosti, E., 2002. A new algorithm for monitoring localized deformation phenomena based on small baseline differential SAR interferograms, in: IEEE International Geoscience and Remote Sensing Symposium. pp. 1237–1239. doi:10.1109/IGARSS.2002.1025900

Nelder, J.A., Mead, R., 1965. A simplex method for function minimization. Comput. J. 7, 308–313. doi:10.1093/comjnl/7.4.308

Nico, G., Tomé, R., Catalao, J., Miranda, P.M.A., 2011. On the use of the WRF model to mitigate tropospheric phase delay effects in SAR interferograms. IEEE Trans. Geosci.

Remote Sens. 49, 4970–4976. doi:10.1109/TGRS.2011.2157511

Ning, T., Wang, J., Elgered, G., Dick, G., Wickert, J., Bradke, M., Sommer, M., Querel, R., Smale, D., 2016. The uncertainty of the atmospheric integrated water vapour estimated from GNSS observations. Atmos. Meas. Tech. 9, 79–92. doi:10.5194/amt-9-79-2016

Norris, R.J., Cooper, A.F., 2001. Late Quaternary slip rates and slip partitioning on the Alpine Fault, New Zealand. J. Struct. Geol. 23, 507–520. doi:10.1016/S0191-8141(00)00122-X

Norris, R.J., Koons, P.O., Cooper, A.F., 1990. The obliquely-convergent plate boundary in the South Island of New Zealand: implications for ancient collision zones. J. Struct. Geol. 12, 715–725. doi:10.1016/0191-8141(90)90084-C

Notebaert, B., Verstraeten, G., Govers, G., Poesen, J., 2009. Qualitative and quantitative applications of LiDAR imagery in fluvial geomorphology. Earth Surf. Process. Landforms 34, 217–231. doi:10.1002/esp.1705

Nur, A., Mavko, G., 1974. Postseismic viscoelastic rebound. Science 183, 204–206. doi:10.1126/science.183.4121.204

Ohtani, R., Naito, I., 2000. Comparisons of GPS-derived precipitable water vapors with radiosonde observations in Japan. J. Geophys. Res. Atmos. doi:10.1029/2000JD900362

Okada, Y., 1992. Internal deformation due to shear and tensile faults in a half-space. Bull. Seismol. Soc. Am. 82, 1018–1040.

Okada, Y., 1986. Surface deformation due to shear and tensile faults in a half-space. Int. J. Rock Mech. Min. Sci. Geomech. Abstr. 23, 128. doi:10.1016/0148-9062(86)90674-1

Onn, F., Zebker, H.A., 2006. Correction for interferometric synthetic aperture radar atmospheric phase artifacts using time series of zenith wet delay observations from a GPS network. J. Geophys. Res. Solid Earth 111, B09102. doi:10.1029/2005JB004012

Paoli, L.D.E., Flowers, G.E., 2007. Dynamics of a small surge-type glacier investigated using 1-D geophysical inversion. J. Glaciol. 00, 1–26. doi:10.3189/002214309790794850

Parker, A.L., Biggs, J., Walters, R.J., Ebmeier, S.K., Wright, T.J., Teanby, N.A., Lu, Z., 2015. Systematic assessment of atmospheric uncertainties for InSAR data at volcanic arcs using large-scale atmospheric models: Application to the Cascade volcanoes, United States. Remote Sens. Environ. 170, 102–114. doi:10.1016/j.rse.2015.09.003

Peltzer, G., Rosen, P., Rogez, F., Hudnut, K., 1996. Postseismic rebound in fault step-overs

caused by pore fluid flow. Science 273, 1202–1204. doi:10.1126/science.273.5279.1202

Pérez-Ruiz, M., Carballido, J., Agüera, J., Gil, J.A., 2011. Assessing GNSS correction signals for assisted guidance systems in agricultural vehicles. Precis. Agric. 12, 639–652. doi:10.1007/s11119-010-9211-4

Persson, A., 2015. User guide to ECMWF forecast products [WWW Document]. Ecmwf. URL http://cedadocs.ceda.ac.uk/1218/1/ECMWF_user_guide_2001.pdf (accessed 7.24.18).

Pettinga, J.R., Yetton, M.D., Van Dissen, R.J., Downes, G., 2001. Earthquake source identification and characterisation for the Canterbury Region, South Island, New Zealand. Bull. New Zeal. Soc. Earthq. Eng. 34, 282–317.

Pi, X., Freeman, A., Chapman, B., Rosen, P., Li, Z., 2011. Imaging ionospheric inhomogeneities using spaceborne synthetic aperture radar. J. Geophys. Res. Sp. Phys. 116, A04303. doi:10.1029/2010JA016267

Polcari, M., Montuori, A., Bignami, C., Moro, M., Stramondo, S., Tolomei, C., 2017. Using multi-band InSAR data for detecting local deformation phenomena induced by the 2016–2017 Central Italy seismic sequence. Remote Sens. Environ. 201, 234–242. doi:10.1016/j.rse.2017.09.009

Raucoules, D., De Michele, M., 2010. Assessing ionospheric influence on L-Band SAR data: Implications on coseismic displacement measurements of the 2008 Sichuan Earthquake. IEEE Geosci. Remote Sens. Lett. 7, 286–290. doi:10.1109/LGRS.2009.2033317

Reuveni, Y., Bock, Y., Tong, X., Moore, A.W., 2015. Calibrating interferometric synthetic aperture radar (InSAR) images with regional GPS network atmosphere models. Geophys. J. Int. 202, 2106–2119. doi:10.1093/gji/ggv253

Reyners, M., 1998. Plate coupling and the hazard of large subduction thrust earthquakes at the Hikurangi subduction zone, New Zealand. New Zeal. J. Geol. Geophys. 41, 343–354. doi:10.1080/00288306.1998.9514815

Rocken, C., Anthes, R., Exner, M., Hunt, D., Sokolovskiy, S., Ware, R., Gorbunov, M., Schreiner, W., Feng, D., Herman, B., Kuo, Y.-H., Zou, X., 1997. Analysis and validation of GPS/MET data in the neutral atmosphere. J. Geophys. Res. Atmos. 102, 29849–29866. doi:10.1029/97JD02400

Rodriguez, E., Martin, J.M., 1992. Theory and design of interferometric synthetic aperture

radars. IEE Proc. F Radar Signal Process. 139, 147. doi:10.1049/ip-f-2.1992.0018

Rogers, A.E.E., Ingalls, R.P., 1969. Venus: Mapping the surface reflectivity by radar interferometry. Science 165, 797–799. doi:10.1126/science.165.3895.797

Rosen, P., Werner, C., Fielding, E., Hensley, S., Buckley, S., Vincent, P., 1998. Aseismic creep along the San Andreas Fault northwest of Parkfield, CA measured by radar interferometry. Geophys. Res. Lett. 25, 825–828. doi:10.1029/98GL50495

Saastamoinen, J., 1972. Atmospheric correction for the troposphere and stratosphere in radio ranging satellites. American Geophysical Union (AGU), pp. 247–251. doi:10.1029/GM015p0247

Samieie-esfahany, S., Hanssen, R.F., Thienen-visser, K. Van, Muntendam-bos, A., Samiei-Esfahany, S., Hanssen, R.F., Thienen-visser, K. Van, Muntendam-bos, A., 2010. On the effect of horizontal deformation on InSAR subsidence estimates, in: Proceedings of Fringe 2009 Workshop.

Samsonov, S., d'Oreye, N., Smets, B., 2013. Ground deformation associated with post-mining activity at the French-German border revealed by novel InSAR time series method. Int. J. Appl. Earth Obs. Geoinf. 23, 142–154. doi:10.1016/j.jag.2012.12.008

Satriano, C., Kiraly, E., Bernard, P., Vilotte, J.P., 2012. The 2012 Mw 8.6 Sumatra earthquake: Evidence of westward sequential seismic ruptures associated to the reactivation of a N-S ocean fabric. Geophys. Res. Lett. 39, L15302. doi:10.1029/2012GL052387

Searle, M.P., Weinberg, R.F., Dunlap, W.J., 1998. Transpressional tectonics along the Karakoram fault zone, northern Ladakh: constraints on Tibetan extrusion. Geol. Soc. Spec. Publ. 135, 307–326. doi:10.1144/gsl.sp.1998.135.01.20

Serpelloni, E., Anzidei, M., Baldi, P., Casula, G., Galvani, A., 2005. Crustal velocity and strain-rate fields in Italy and surrounding regions: New results from the analysis of permanent and non-permanent GPS networks. Geophys. J. Int. 161, 861–880. doi:10.1111/j.1365-246X.2005.02618.x

Seymour, M.S., Cumming, I.G., 1994. Maximum likelihood estimation for SAR interferometry. Proc. IGARSS' 94 - 1994 IEEE Int. Geosci. Remote Sens. Symp. 4, 2272–2275. doi:10.1109/IGARSS.1994.399711

Shirzaei, M., Bürgmann, R., 2012. Topography correlated atmospheric delay correction in radar

interferometry using wavelet transforms. Geophys. Res. Lett. 39. doi:10.1029/2011GL049971

Shirzaei, M., Bürgmann, R., Fielding, E.J., 2017. Applicability of Sentinel-1 Terrain Observation by Progressive Scans multitemporal interferometry for monitoring slow ground motions in the San Francisco Bay Area. Geophys. Res. Lett. 44, 2733–2742. doi:10.1002/2017GL072663

Shoji, Y., Kunii, M., Saito, K., 2011. Mesoscale data assimilation of Myanmar Cyclone Nargis Part II: Assimilation of GPS-derived precipitable water vapor, in: Journal of the Meteorological Society of Japan. Meteorological Society of Japan, pp. 67–88. doi:10.2151/jmsj.2011-105

Short, N., LeBlanc, A.M., Sladen, W., Oldenborger, G., Mathon-Dufour, V., Brisco, B., 2014. RADARSAT-2 D-InSAR for ground displacement in permafrost terrain, validation from Iqaluit Airport, Baffin Island, Canada. Remote Sens. Environ. 141, 40–51. doi:10.1016/j.rse.2013.10.016

Simons, M., Fialko, Y., Rivera, L., 2002. Coseismic deformation from the 1999 Mw 7.1 Hector Mine, California, earthquake as inferred from InSAR and GPS observations. Bull. Seismol. Soc. Am. 92, 1390–1402. doi:10.1785/0120000933

Simons, M., Rosen, P.A., 2007. Interferometric synthetic aperture radar geodesy, in: Treatise on Geophysics. Elsevier, pp. 391–446. doi:10.1016/B978-044452748-6.00059-6

Sneed, M., Brandt, J.T., Solt, M., 2014. Land subsidence, groundwater levels, and geology in the Coachella Valley, California , 1993 – 2010. U.S. Geol. Surv. Sci. Investig. Rep. viii, 62. doi:10.3133/sir20145075

Sobrino, J.A., El Kharraz, J., Li, Z.L., 2003. Surface temperature and water vapour retrieval from MODIS data. Int. J. Remote Sens. 24, 5161–5182. doi:10.1080/0143116031000102502

Spits, J., Warnant, R., 2011. Total electron content monitoring using triple frequency GNSS: Results with Giove-A data. Adv. Sp. Res. 47, 296–303. doi:10.1016/j.asr.2010.08.027

Stafford, J. V., 2000. Implementing precision agriculture in the 21st century. J. Agric. Eng. Res. 76, 267–275. doi:10.1006/jaer.2000.0577

Tapponnier, P., Peltzer, G., Le Dain, A.Y., Armijo, R., Cobbold, P., 1982. Propagating extrusion

tectonics in Asia: new insights from simple experiments with plasticine. Geology 10, 611–616. doi:10.1130/0091-7613(1982)10<611:PETIAN>2.0.CO;2

Tarayre, H., Massonnet, D., 1996. Atmospheric Propagation heterogeneities revealed by ERS-1 interferometry. Geophys. Res. Lett. 23, 989–992. doi:10.1029/96GL00622

Teunissen, P.J.G., Odolinski, R., Odijk, D., 2014. Instantaneous BeiDou+GPS RTK positioning with high cut-off elevation angles. J. Geod. 88, 335–350. doi:10.1007/s00190-013-0686-4

Thomas, T., Phillips, M.R., Williams, A.T., 2010. Mesoscale evolution of a headland bay: Beach rotation processes. Geomorphology 123, 129–141. doi:10.1016/j.geomorph.2010.06.018

Tong, X., Sandwell, D.T., Fialko, Y., 2010. Coseismic slip model of the 2008 Wenchuan earthquake derived from joint inversion of interferometric synthetic aperture radar, GPS, and field data. J. Geophys. Res. 115, B04314. doi:10.1029/2009JB006625

Treuhaft, R.N., Lanyi, G.E., 1987. The effect of the dynamic wet troposphere on radio interferometric measurements. Radio Sci. 22, 251–265. doi:10.1029/RS022i002p00251

Wadge, G., Webley, P.W., James, I.N., Bingley, R., Dodson, A., Waugh, S., Veneboer, T., Puglisi, G., Mattia, M., Baker, D., Edwards, S.C., Edwards, S.J., Clarke, P.J., 2002. Atmospheric models, GPS and InSAR measurements of the tropospheric water vapour field over Mount Etna. Geophys. Res. Lett. 29, 11-1-11–4. doi:10.1029/2002GL015159

Wallace, L.M., Barnes, P., Beavan, J., Van Dissen, R., Litchfield, N., Mountjoy, J., Langridge, R., Lamarche, G., Pondard, N., 2012. The kinematics of a transition from subduction to strike-slip: An example from the central New Zealand plate boundary. J. Geophys. Res. Solid Earth 117, B02405. doi:10.1029/2011JB008640

Wallace, L.M., Beavan, J., McCaffrey, R., Berryman, K., Denys, P., 2007. Balancing the plate motion budget in the South Island, New Zealand using GPS, geological and seismological datas. Geophys. J. Int. 168, 332–352. doi:10.1111/j.1365-246X.2006.03183.x

Wallace, L.M., Beavan, J., McCaffrey, R., Darby, D., 2004. Subduction zone coupling and tectonic block rotations in the North Island, New Zealand. J. Geophys. Res. Solid Earth 109, 1–21. doi:10.1029/2004JB003241

Wallace, L.M., Hreinsdóttir, S., Ellis, S., Hamling, I., D'Anastasio, E., Denys, P., 2018. Triggered slow slip and afterslip on the Southern Hikurangi Subduction Zone following

the Kaikōura Earthquake. Geophys. Res. Lett. 45, 4710–4718. doi:10.1002/2018GL077385

Wallace, L.M., Kaneko, Y., Hreinsdóttir, S., Hamling, I., Peng, Z., Bartlow, N., D'Anastasio, E., Fry, B., 2017. Large-scale dynamic triggering of shallow slow slip enhanced by overlying sedimentary wedge. Nat. Geosci. 10, 765–770. doi:10.1038/ngeo3021

Walters, R.J., Elliott, J.R., Li, Z., Parsons, B., 2013. Rapid strain accumulation on the Ashkabad fault (Turkmenistan) from atmosphere-corrected InSAR. J. Geophys. Res. Solid Earth 118, 3674–3690. doi:10.1002/jgrb.50236

Wang, J., Zhang, L., Dai, A., 2005. Global estimates of water-vapor-weighted mean temperature of the atmosphere for GPS applications. J. Geophys. Res. Atmos. 110, 1–17. doi:10.1029/2005JD006215

Wang, Q., Zhang, P.Z., Freymueller, J.T., Bilham, R., Larson, K.M., Lai, X., You, X., Niu, Z., Wu, J., Li, Y., Liu, J., Yang, Z., Chen, Q., 2001. Present-day crustal deformation in China constrained by Global Positioning System measurements. Science 294, 574–577. doi:10.1126/science.1063647

Webley, P.W., Bingley, R.M., Dodson, A.H., Wadge, G., Waugh, S.J., James, I.N., 2002. Atmospheric water vapour correction to InSAR surface motion measurements on mountains: Results from a dense GPS network on Mount Etna. Phys. Chem. Earth 27, 363–370. doi:10.1016/S1474-7065(02)00013-X

Wei, M., Kaneko, Y., Shi, P., Liu, Y., 2018. Numerical modeling of dynamically triggered shallow slow slip events in New Zealand by the 2016 Mw7.8 Kaikoura Earthquake. Geophys. Res. Lett. 45, 4764–4772. doi:10.1029/2018GL077879

Weinberg, R.F., Searle, M.P., 1998. The Pangong Injection Complex, Indian Karakoram: a case of pervasive granite flowthrough hot viscous crust. J. Geol. Soc. London. 155, 883–891. doi:10.1144/gsjgs.155.5.0883

Williams, C.A., Eberhart-Phillips, D., Bannister, S., Barker, D.H.N., Henrys, S., Reyners, M., Sutherland, R., 2013. Revised interface geometry for the Hikurangi Subduction Zone, New Zealand. Seismol. Res. Lett. 84, 1066–1073. doi:10.1785/0220130035

Williams, H., Turner, S., Kelley, S., Harris, N., 2001. Age and composition of dikes in Southern Tibet: New constraints on the timing of east-west extension and its relationship to

postcollisional volcanism. Geology 29, 339–342. doi:10.1130/0091-7613(2001)029<0339:AACODI>2.0.CO;2

Williams, S., Bock, Y., Fang, P., 1998. Integrated satellite interferometry: Tropospheric noise, GPS estimates and implications for interferometric synthetic aperture radar products. J. Geophys. Res. Solid Earth 103, 27051–27067. doi:10.1029/98JB02794

Wood, J.C., Barry, D.T., 1992. Radon transformation of time-frequency distributions for analysis of multicomponent signals, in: ICASSP, IEEE International Conference on Acoustics, Speech and Signal Processing - Proceedings. pp. 257–260. doi:10.1109/ICASSP.1992.226437

Wright, T., Fielding, E., Parsons, B., 2001a. Triggered slip: Observations of the 17 August 1999 Izmit (Turkey) earthquake using radar interferometry. Geophys. Res. Lett. 28, 1079–1082. doi:10.1029/2000GL011776

Wright, T., Parsons, B., Fielding, E., 2001b. Measurement of interseismic strain accumulation across the North Anatolian Fault by satellite radar interferometry. Geophys. Res. Lett. 28, 2117–2120. doi:10.1029/2000GL012850

Wright, T.J., Parsons, B., England, P.C., Fielding, E.J., 2004. InSAR observations of low slip rates on the major faults of western Tibet. Science 305, 236–239. doi:10.1126/science.1096388

Xu, W., Feng, G., Meng, L., Zhang, A., Ampuero, J.P., Bürgmann, R., Fang, L., 2018. Transpressional rupture cascade of the 2016 Mw7.8 Kaikoura Earthquake, New Zealand. J. Geophys. Res. Solid Earth 123, 2396–2409. doi:10.1002/2017JB015168

Xu, W.B., Li, Z.W., Ding, X.L., Zhu, J.J., 2011. Interpolating atmospheric water vapor delay by incorporating terrain elevation information. J. Geod. 85, 555–564. doi:10.1007/s00190-011-0456-0

Yan, X., Ducrocq, V., Jaubert, G., Brousseau, P., Poli, P., Champollion, C., Flamant, C., Boniface, K., 2009. The benefit of GPS zenith delay assimilation to high-resolution quantitative precipitation forecasts: A case-study from COPS IOP 9. Q. J. R. Meteorol. Soc. 135, 1788–1800. doi:10.1002/qj.508

Yao, Y., Yu, C., Hu, Y., 2014. A new method to accelerate PPP convergence time by using a global zenith troposphere delay estimate model. J. Navig. 67, 899–910.

doi:10.1017/S0373463314000265

Yin, A., Harrison, T.M., 2000. Geologic evolution of the Himalayan-Tibetan orogen. Annu. Rev. Earth Planet. Sci. 28, 211–280. doi:10.1146/annurev.earth.28.1.211

Yokota, Y., Ishikawa, T., Watanabe, S.I., Tashiro, T., Asada, A., 2016. Seafloor geodetic constraints on interplate coupling of the Nankai Trough megathrust zone. Nature 534, 374–377. doi:10.1038/nature17632

Zebker, H.A., Goldstein, R.M., 1986. Topographic mapping from interferometric synthetic aperture radar observations. J. Geophys. Res. 91, 4993. doi:10.1029/JB091iB05p04993

Zebker, H.A., Rosen, P.A., Hensley, S., 1997. Atmospheric effects in interferometric synthetic aperture radar surface deformation and topographic maps. J. Geophys. Res. Solid Earth 102, 7547–7563. doi:10.1029/96JB03804

Zebker, H.A., Villasenor, J., 1992. Decorrelation in interferometric radar echoes. IEEE Trans. Geosci. Remote Sens. 30, 950–959. doi:10.1109/36.175330

Zhang, B., Wang, C., Ding, X., Zhu, W., Wu, S., 2018. Correction of ionospheric artifacts in SAR data: Application to fault slip inversion of 2009 Southern Sumatra Earthquake. IEEE Geosci. Remote Sens. Lett. 1–5. doi:10.1109/LGRS.2018.2844686

Zumberge, J.F., Heflin, M.B., Jefferson, D.C., Watkins, M.M., Webb, F.H., 1997. Precise point positioning for the efficient and robust analysis of GPS data from large networks. J. Geophys. Res. Solid Earth 102, 5005–5017. doi:10.1029/96JB03860